APRIL-JUNE 2022 VOL. 14 № 2 (53)

ISSN 2075-8251

ActaNaturae

The Evolution of Targeted Radionuclide Diagnosis of HER2-Positive Breast Cancer

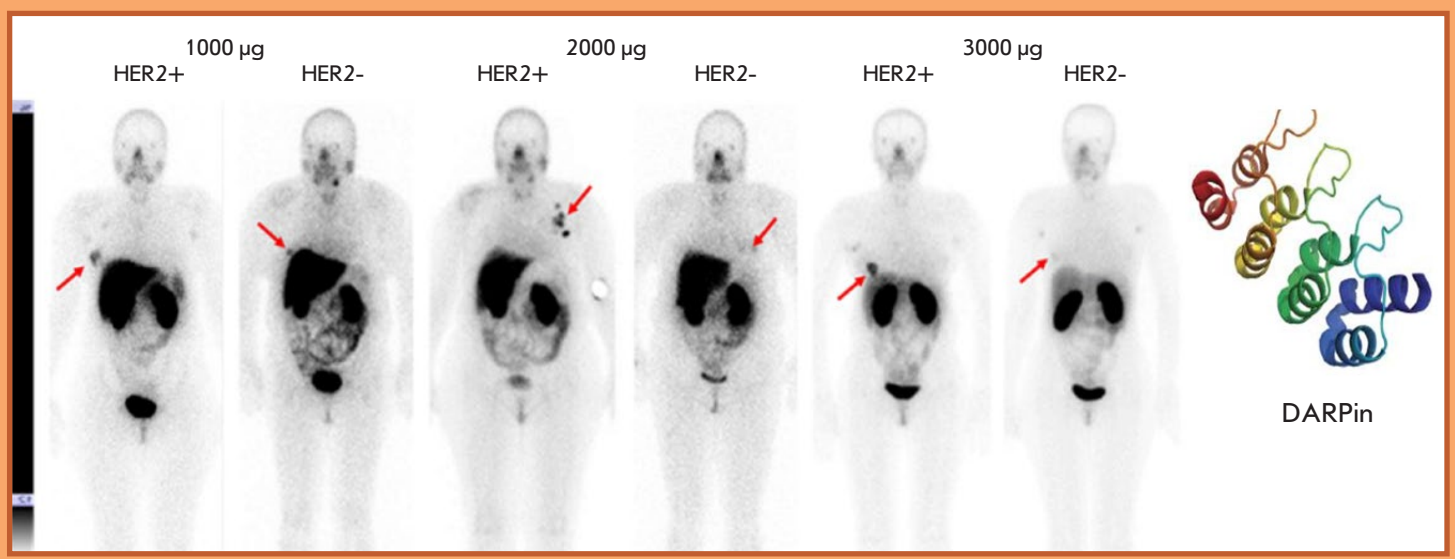

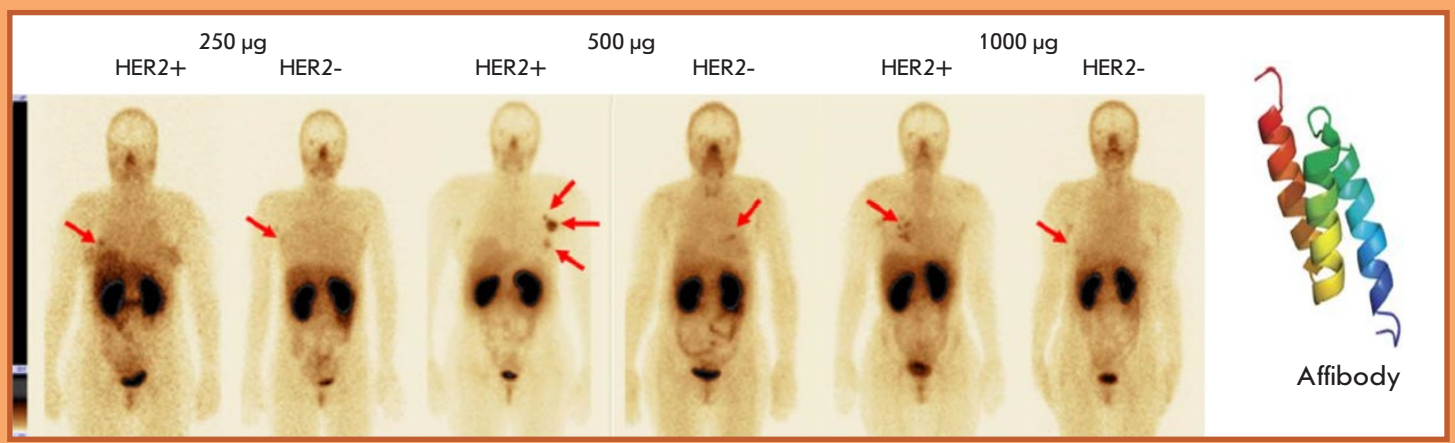

III JOINT LIFE SCIENCES FORUM

VII RUSSIAN CONGRESS ON BIOCHEMISTRY & MOLECULAR BIOLOGY

♦

X RUSSIAN SYMPOSIUM "PROTEINS AND PEPTIDES"

In Memory of Professor Vadim Ivanov

Sochi, Russia ***October 3–7, 2022***

We are happy to announce the Forum new dates and venue.
The Forum will be held on October 3–7 2022
in the Grand Hotel "Zhemchuzhina", one of the best hotels in Sochi.
To learn more, please visit our website at
http://rusbiochem.org/Page224.html

CONGRESS ORGANIZERS

- Russian Academy of Sciences
- Ivan Pavlov Russian Physiological Scoeity
- Russian Biochemical Society (National Committee of Russian Biochemists)
- Russian Science Foundation

with the involvement of

- CIS Union of Physiological Societies

PROGRAM COMMITTEE CO-CHAIRS

Full Members of the Russian Academy of Sciences
Alexander Gabibov, Mikhail Ostrovsky

ADDITIONAL APPLICATION FOR ORAL PRESENTATION ARE ACCEPTED
BEFORE JULY 15, 2022

ADDITIONAL APPLICATIONS FOR POSTER PRESENTATION AND
PARTICIPATION IN THE YOUNG SCIENTISTS' CONTEST ARE ACCEPTED
BEFORE JULY 20, 2022

Any questions? Please contact us by e-mail: info@rusbiochem.org

The preliminary scientific program is already published online at www.rusbiochem.org and www.physiology-cis.org. Upon receipt of additional applications, we will revise the program. The final version will be placed at our web sites before September 1, 2022.

WWW.RUSBIOCHEM.ORG

Eukaryotic Ribosome Biogenesis: The 60S Subunit

A. A. Moraleva, A. S. Deryabin, Yu. P. Rubtsov, M. P. Rubtsova, O. A. Dontsova

Ribosome biogenesis is consecutive coordinated maturation of ribosomal precursors in the nucleolus, nucleoplasm, and cytoplasm. Although the main features and stages of ribosome biogenesis are conservative among different groups of eukaryotes, this process in human cells has become more complicated due to the larger size of the ribosomes and pre-ribosomes and intricate regulatory pathways affecting their assembly and function.

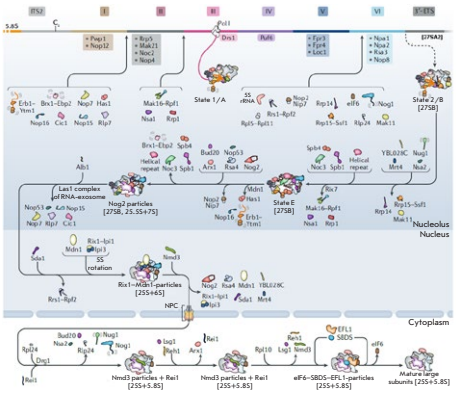

Large ribosomal subunit assembly in yeast

Citrobacter freundii Methionine γ-Lyase: The Role of Serine 339 in the Catalysis of γ- and β-Elimination Reactions

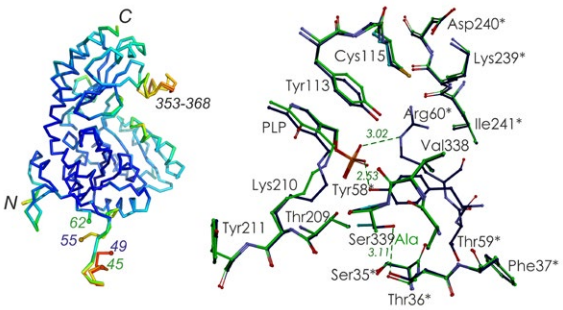

Superposition of the structures of the wild-type *C. freundii* MGL and Ser339Ala MGL

N. V. Anufrieva, E. A. Morozova, S. V. Revtovich, N. P. Bazhulina, V. P. Timofeev, Ya. V. Tkachev, N. G. Faleev, A. D. Nikulin, T. V. Demidkina

An analysis of the obtained kinetic and spectral data, as well as the known spatial structures of *C. freundii* MGL, indicates that serine 339 is necessary for efficient catalysis of γ- and β-elimination reactions at the stage of C-α-proton abstraction from the external aldimine, the γ-elimination reaction at the stages of coenzyme C4'-atom protonation, and C-β-proton abstraction from a ketimine intermediate.

Isolation and Biochemical Characterization of Recombinant Transketolase from *Mycobacterium tuberculosis*

T. A. Shcherbakova, S. M. Baldin, M. S. Shumkov, I. V. Gushchina, D. K. Nilov, V. K. Švedas

Using plasmid pET-19b carrying the Rv1449c gene of transketolase from *Mycobacterium tuberculosis* and an additional histidine tag, we isolated and purified recombinant transketolase and determined the conditions for obtaining the apoform of the protein. The authors found that the affinity of mycobacterial transketolase for thiamine diphosphate is by three orders of magnitude lower than that of the human enzyme. Analysis of the structural organization of the active centers of homologous enzymes showed that this difference is due to a replacement of lysine residues by less polar amino acid residues.

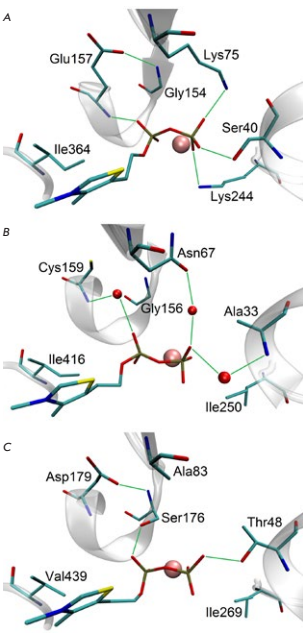

Interactions of the TDP cofactor with variable residues in the active sites of the homologous enzymes hTK (*A*), yTK (*B*), and mbTK (*C*)

ActaNaturae
APRIL–JUNE 2022 VOL. 14 № 2 (53)
since april 2009, 4 times a year

Founders
Acta Naturae, Ltd,
National Research University
Higher School of Economics

Adress: 101000, Moscow, Myasnitskaya Ulitsa, 13, str. 4
Phone/Fax: +7 (495) 727 38 60
E-mail: actanaturae@gmail.com

Номер подписан в печать 30 июня 2022 г.
Тираж 15 экз. Цена свободная.
Отпечатано в типографии: НИУ ВШЭ,
г. Москва, Измайловское шоссе, 44, стр. 2

Indexed in Pubmed, Web of Science, Scopus, and RISC

Impact Factor: 2.204

CONTENTS

REVIEWS

RESEARCH ARTICLES

SHORT REPORTS

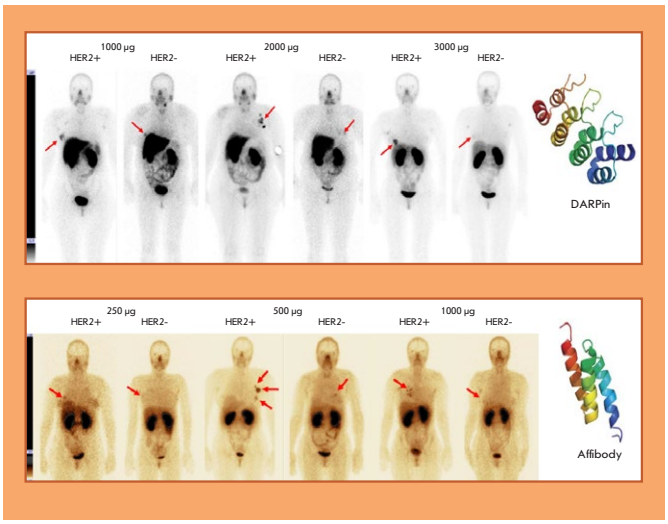

IMAGE ON THE COVER PAGE
(see the article by O. D. Bragina et al.)

The Evolution of Targeted Radionuclide Diagnosis of HER2-Positive Breast Cancer

O. D. Bragina[1,2], S. M. Deyev[2,3], V. I. Chernov[1,2], V. M. Tolmachev[2,4]
[1]Tomsk National Research Medical Center of the Russian Academy of Sciences Cancer Research institute, Tomsk, 634009 Russia
[2]National Research Tomsk Polytechnic University, Tomsk, 634050 Russia
[3]Shemyakin-Ovchinnikov Institute of Bioorganic Chemistry of the Russian Academy of Sciences, Moscow, 117997 Russia
[4]Uppsala University, Uppsala, Sweden
*E-mail: rungis@mail.ru
Received: October 20, 2021; in final form, March 18, 2022
DOI: 10.32607/actanaturae.11611

ABSTRACT **This review examines the evolution of the radionuclide diagnosis of HER2-positive breast cancer using various compounds as a targeting module in clinical practice: from full-length antibodies to a new group of small synthetic proteins called alternative scaffold proteins. This topic is of especial relevance today in view of the problems attendant to the detection of breast cancer with HER2/neu overexpression, which, in most cases, introduce errors in the treatment of patients. The results of clinical studies of radiopharmaceuticals based on affibody molecules, ADAPTs, and DARPins for SPECT and PET have demonstrated good tolerability of the compounds, their rapid excretion from the body, and the possibility to differentiate tumor sites depending on the HER2/neu status. This indicates that targeted radionuclide diagnosis holds promise and the need to continue research in this direction.**
KEYWORDS **breast cancer, HER2/neu, radionuclide diagnostics, monoclonal antibody, alternative scaffold proteins.**

INTRODUCTION

More than 10 million new cancer cases are diagnosed annually in the world, with about 7.6 million people dying from the pathology [1]. Breast cancer (BC) holds a stable, leading position among oncological diseases for women in terms of morbidity and mortality [2]. For instance, according to the ESMO (European Society for Medical Oncology) guidelines, about 2.1 million new BC cases were diagnosed worldwide (almost every fourth case) in 2018, while 630,000 patients died from the pathology [3]. A total of 70,682 BC cases (20.9% of all oncological diseases in women) with a mortality rate of 1.6% were recorded in the Russian Federation in 2019 [4]. BC also takes the first place (16.2%) among death causes in women [5].

Despite the widespread prevalence of BC, the life expectancy of patients diagnosed with it over the past five years or more (patients with or without disease signs) has been increasing since 2012. For instance, this parameter is 59.8% in the Russian Federation [6]. These results primarily have to do with the improvement achieved in diagnostic algorithms, as well as in both local and systemic treatment [7]. In particular, the concept of personalized medicine, which implies the administration of treatment based on the individual characteristics of a patient, with taking into account his/her expected response to it, has gained wide use in the treatment of oncological diseases in recent years [8]. The concept of personalized medicine has become conspicuous in oncological practice. One of the most rapidly developing areas of personalized medicine is theranostics; it combines such concepts as therapy and diagnosis and involves the use of agents and methods based on diagnostic imaging and targeted therapy [9]. The imaging stage of the theranostic approach consists in image processing, visualization of a biological target, and identification of a subgroup of patients in whom the planned treatment is expected to be at its most efficacious; the subsequent therapeutic stage includes the administration of a drug that acts on previously identified targets [10]. The main goals of this strategy are to increase therapy effectiveness, improve the survival rates of cancer patients, reduce adverse reactions and, as a result, decrease overall costs [11]. The rapid progress achieved in the development of theranostics is largely due to the accumulation of new data on the molecular basis of carcinogenesis, the creation of technologies

for the manufacture of new biological agents, and the improvement in the performance and accuracy of diagnostic devices [12].

EPIDERMAL GROWTH FACTOR RECEPTOR HER2/neu

One of the most studied molecular targets located on the surface of cancer cells is the human epidermal growth factor receptor 2 (HER2/neu). It belongs to the family of transmembrane receptors to EGF (epidermal growth factor receptor: ErbB1/HER1, ErbB2/HER2, ErbB3/HER3, and ErbB4/HER4) tyrosine kinases and regulates the processes of cell division, growth, differentiation, proliferation, migration, and apoptosis [13, 14]. HER2/neu overexpression, which is found in gastric, ovarian, prostate, lung, bladder and other cancers, is most common in invasive BC [15, 16]. In most cases, increased HER2/neu expression in a cancer cell is due to an amplification of the *ERBB2* gene located in the 17q12 locus of the chromosome and associated with specific changes in some loci of other chromosomes (11q13, 16q22–q24, and 18q21) [17].

Hyperexpression of HER2/neu and/or amplification of *ERBB2* is observed in 15–20% of BC cases; they are considered an unfavorable prognostic factor and are characterized by an aggressive disease course, as well as low rates of overall and disease-free survival [18, 19]. According to Russian and international clinical guidelines, tumors characterized by a high expression of this receptor require targeted treatment involving drugs used both as monotherapy and in combination with chemotherapy [20]. The targeted drug Herceptin, containing the humanized monoclonal antibody (mAb) trastuzumab, which the first compound capable of suppressing HER2/neu function approved by the FDA (Food and Drug Administration, USA) in 1998, remains the gold standard in the treatment of HER2-positive BC. The use of trastuzumab in combination with taxanes to treat metastatic BC has resulted in an increased response rate, progression-free survival (PFS), and overall survival (OS) [21]. Targeted therapy requires a careful selection of candidates [22]. To date, several methods have been developed to determine the HER2/neu status; they evaluate the protein, DNA, and RNA levels of marker expression. The FDA-approved immunohistochemistry (IHC) and fluorescence *in situ* hybridization (FISH) based methods are the most widespread among them [23].

The immunohistochemical study (IHC) is a widely used method used to evaluate HER2/neu expression on a cancer cell surface in formalin-fixed BC samples [24]. According to the 2018 American Society of Clinical Oncology (ASCO) guidelines, 0 and 1+ cases are considered negative, while cases scored as 3+ are considered positive. Targeted therapy is recommended for patients in whom the receptor overexpression corresponds to a score of 3+. Cases 2+ are considered equivocal and require a FISH analysis to verify *ERBB2* amplification [25].

Despite the availability and relatively low cost of the analysis, IHC results can be significantly affected by numerous factors, such as sample preparation method (duration of fixation and the fixative used), characteristics of the antibodies used (manufacturer), personnel qualifications, and interpretation of the results (mainly cases with a 2+ score) [26].

Fluorescent in situ hybridization (FISH) is a cytogenetic technique based on the use of fluorescently labeled probes to detect specific DNA sequences in formalin-fixed BC tissue samples. FISH is used to quantify the *ERBB2* copy number in the nuclei of BC cells; amplification is considered positive in the presence of an average number of *ERBB2* copies and an average number of chromosome 17 centromeres per cell of > 2.2. The undeniable advantages of FISH are more objective and quantitative results compared to IHC, which is probably due to greater DNA stability and the presence of internal controls consisting of non-amplified signals in the non-tumor cells (ductal epithelial and stromal cells) adjacent to the tumor [27].

FISH is a very reliable method for evaluating *ERBB2* amplification. However, it takes nine times longer (36 h vs 4 h); it is several times more expensive than standard ICH and requires expensive equipment to detect and recognize signals, as well as highly qualified personnel to analyze the obtained data [28].

From a clinical standpoint, a significant drawback of conventional methods for determining the HER2/neu status at the diagnostic stage is the impossibility to simultaneously assess tumor progression *in vivo* and analyze the molecular characteristics of identified tumor lesions prior to the administration of a specific treatment [29]. This fact is of particular importance in light of the increasingly discussed heterogeneity of HER2/neu expression in the primary tumor, local and distant metastatic lesions which can occur, according to various analysis data, in 6–48% of cases [30]. A discrepancy in the HER2/neu status between the primary tumor and affected lymph nodes was revealed in almost 20% of BC cases in [31]. In the case of metastatic lesions in distant organs and tissues, this discrepancy stood at 14.3%, according to Lower et al. but reached 34% in the study by Turner et al. [32, 33]. This fact is most significant in metastatic BC, which is characterized by a long and scallopy course requiring several stages and types of systemic treatment. At the same time, performing a biopsy and surgical sampling from existing and/or newly identified metastatic le-

sions to optimize the treatment strategy is sometimes either technically impossible or may lead to serious complications [30].

The problem of intratumoral heterogeneity, which is observed in 40% of BC cases and can be represented in the coexistence of many subpopulations of cells with different HER2/neu expression levels in the same tumor, remains unsolved [34, 35]. Recent studies have shown that the RFS and effectiveness of a targeted therapy with trastuzumab are reduced in HER2-positive BC patients with intratumoral heterogeneity of the receptor expression compared to tumors with homogeneous expression [36]. Despite this, the relationship between HER2 heterogeneity and long-term treatment outcomes in patients after surgery remains to be studied. All of this calls for the development of new additional diagnostic techniques in order to optimize the diagnosis of BC [37].

METHODS FOR RADIONUCLIDE DIAGNOSIS OF HER2-POSITIVE BREAST CANCER

In recent years, the possibility of diagnosing cancer using targeted radionuclide methods has become possible [38]. One of the most studied approaches based on binding to the HER2/neu receptor is the use of labeled monoclonal antibodies (mAbs) [39]. The diagnostic radiopharmaceuticals (RPs) used in oncological practice belong to the category of substances that contain radionuclides for single-photon-emission-computed tomography (SPECT) (γ-emitters with energies in the range of 100–200 keV and half-lives ranging from several minutes to several days) and positron emission tomography (PET) (β^+-emitters with half-lives ranging from several seconds to several hours) [40]. A comparative characterization of the radioisotopes used for radionuclide imaging is presented in *Table 1*.

Table 1. Radioisotopes for radionuclide diagnosis by PET and SPECT

Radioisotope	Half-life, $T_{1/2}$	Production method
Radioisotopes for SPECT		
^{99m}Tc	6.01 h	Generator
^{123}I	13.3 h	Cyclotron
^{111}In	2.8 days	Cyclotron
Radioisotopes for PET		
^{15}O	2.03 min	Cyclotron
^{13}N	9.97 min	Cyclotron
^{11}C	20.4 min	Cyclotron
^{68}Ga	67.7 min	Generator
^{18}F	109.8 min	Cyclotron
^{64}Cu	12.7 h	Cyclotron
^{76}Br	16.2 h	Cyclotron
^{89}Zr	78.4 h	Cyclotron
^{124}I	100 h	Cyclotron

SPECT has become widespread largely due to its low cost, while PET diagnostics, which is costlier, affords a significantly higher sensitivity, spatial resolution, and quantification accuracy. The recent introduction of scanners for SPECT diagnostics based on cadmium and zinc tellurides can significantly increase camera sensitivity and resolution [41, 42].

Radionuclide imaging of oncological diseases with HER2/neu overexpression has a number of significant advantages compared to invasive diagnostic methods. These advantages include the non-invasive nature of the study with a possibility to conduct repeated studies [43], the assessment of marker expression over time during treatment, simultaneous visualization of a patient's whole body with an evaluation of HER/neu receptor expression in the primary tumor and metastatic foci, as well as improvement of the diagnostic equipment in the form of developing devices that combine both modules for radionuclide studies and anatomical visualization of metastatic lesions (computed tomography (CT) and magnetic resonance imaging (MRI)) [44].

To date, several types of targeting modules that can be potentially used for radionuclide imaging of HER2/neu receptors are known: monoclonal antibodies; antibody fragments (Fab- and $(Fab)_2$-fragments), diabodies, minibodies, single-chain variable fragments of scFv and nanobodies, nucleic acid aptamers, rationally designed short peptides, and alternative scaffold proteins (ASPs, scaffolds) selected using the molecular display approach (*Table 2*) [45, 46].

Radionuclide diagnosis of HER2-positive breast cancer using full-length antibodies

Full-length monoclonal antibodies labeled with various radioisotopes were the first targeting modules used to evaluate HER2 expression [47]. The highly specific interaction between mAb and the corresponding antigen has become the starting point for preclinical and clinical studies aimed at exploring the possi-

Table 2. Radionuclide diagnosis of HER2-positive breast cancer (clinical studies)

Protein type	Agent name	Visualization technique	Patient population	Ref.
Full-length antibodies	^{111}In-trastuzumab	SPECT/CT	Metastatic breast cancer	[51–53]
	^{89}Zr-trastuzumab	PET/CT	Metastatic breast cancer	[54–56]
	^{64}Cu-trastuzumab	PET/CT	Primary metastatic breast cancer	[57, 58]
Antibody fragments	^{68}Ga-DOTA-F(ab′)$_2$-trastuzumab	PET/CT	Metastatic breast cancer	[59]
	^{68}Ga-HER2-Nanobody	PET/CT	Metastatic breast cancer	[60]
Alternative scaffold proteins	^{111}In-ABY-002 ^{68}Ga-ABY-002	SPECT/CT PET/CT	Metastatic breast cancer	[61]
	^{111}In-ABY-025	SPECT/CT	Locally advanced metastatic breast cancer	[62, 63]
	^{68}Ga-ABY-025	PET/CT	Locally advanced metastatic breast cancer	[63–65]
	^{99m}Tc-ADAPT6	SPECT	Operable locally advanced metastatic breast cancer	[66]
	^{99m}Tc-DARPinG3	SPECT	Operable locally advanced metastatic breast cancer	[67]

bility of using antibodies as a capture agent for either delivering radionuclides to tumor cells, visualizing them, or exerting a radiation cytotoxic effect on them. Long-term circulation of mAbs in a patient's body required the use of long-lived positron emitters such as ^{89}Zr (zirconium-89), ^{64}Cu (copper-64), ^{124}I (iodine-124), and ^{86}Y (yttrium-86) [48].

Since the creation of trastuzumab as a drug to treat BC patients with HER2/neu overexpression, drug molecules labeled with various radioisotopes have been extensively used to study the diagnostic efficiency of HER2 expression evaluation [49]. The drug ^{111}In-trastuzumab (^{111}In; a half-life of 2.8 days) was the first labeled monoclonal antibody clinically tested in HER2-positive BC patients [50]. At first, the cardiotoxicity of the compound for the most part. For instance, Behr et al. studied 20 patients with HER2-positive metastatic BC treated with trastuzumab in 2000. The authors evaluated a potential tumor response to therapy and the possibility to predict cardiotoxicity during treatment. Based on the study results, the authors concluded that the drug could be used as a tool to predict therapeutic efficacy and cardiotoxicity risk during targeted therapy (*Table 2*) [51].

Perik et al. used ^{111}In-trastuzumab in 17 patients with metastatic HER2-positive BC. Only one patient with severe cardiotoxicity showed weak uptake of the labeled protein; tumors overexpressing HER2 were detected in 45% of cases, which was an indication of an absence of diagnostic significance for ^{111}In-trastuzumab in predicting cardiotoxicity in these patients [52].

Sietske et al. studied ^{111}In-trastuzumab accumulation at the beginning of and 14 weeks after Herceptin therapy in 17 patients with HER2-positive BC. The study results revealed a stable uptake of the drug by all tumor lesions throughout the treatment course, with only a 20% decrease in uptake by the end of the therapy. This analysis showed that the number of HER2 receptor molecules on the cancer cell surface is sufficient for binding to targeted drugs; the decrease in the accumulation was largely due to a reduction in the tumor volume resulting from the combined chemotherapy, as well as competition between circulating "therapeutic" trastuzumab and labeled antibodies for binding to the target receptor. Apparently, the obtained result can be explained by an insufficient dosage of the mAb used and, therefore, incomplete blocking of HER2/neu receptors [53].

The first clinical study of ^{89}Zr-trastuzumab (^{89}Zr; half-life of 78.4 h) conducted in 14 patients with metastatic BC showed a high accumulation of the labeled antibody in the primary tumor and metastatic nodes with a positive HER2/neu status 4–5 days after their injection, according to PET data (anatomical localization of which was comparable to that established by CT and MRI). BC metastases to the brain due to dam-

age to the blood–brain barrier at the site of the metastasis have also been visualized [54].

The drug ^{89}Zr-trastuzumab was also studied by Ulaner et al. The authors conducted a prospective clinical analysis of 11 patients with HER2-negative BC who had at least one metastatic lesion at the time of the study. Metastatic lesions overexpressing HER2/neu were detected in four out of 11 patients (36%) 5–6 days after drug administration by PET/CT. However, subsequent ICH and FISH analysis of tumor tissue showed that the results were false-positive in three out of the four (75%) identified nodes. It is possible that such a high frequency of false-positive results could be due to nonspecific accumulation of the drug in tumor lesions, because of the large size of its molecules [55].

Gebhart et al. evaluated the possibility of using ^{89}Zr-trastuzumab- and ^{18}F-fluorodeoxyglucose-(^{18}F-FDG-) PET to assess the efficacy of trastuzumab emtansine (T-DM1) therapy in 56 patients with advanced HER2-positive BC in a multicentric clinical trial (the ZEPHIR study). A total of 16 (29%) patients (with high level of HER2/neu expression in tumor metastases that had been previously diagnosed by IHC) showed no signs of ^{89}Zr-trastuzumab accumulation, while co-administration of ^{89}Zr-trastuzumab and ^{18}F-FDG made it possible to predict the tumor response to treatment in all cases [56].

Tamura et al. and Mortimer et al studied the characteristics and efficacy of ^{64}Cu-trastuzumab (^{64}Cu; a half-life of 12.7 h). In the first case, a PET study of six patients with either operable or metastatic HER2-positive BC showed the safety of the good visualization of the primary tumor and brain metastases in two patients [57]. Drug effectiveness was confirmed in eight patients with metastatic HER2-positive BC in the study by Mortimer et al. Both the primary tumor and metastatic lesions in the bones, lymph nodes, liver, lungs, and pleura were well visible in all patients [58]. The main disadvantage of ^{64}Cu compounds is that their half-life is too short.

Despite the positive results that have been noted in numerous studies, the use of full-length antibodies as a targeting module also revealed some obvious drawbacks. These drawbacks are mainly related to the size of immunoglobulin molecules: slow excretion of mAb from the body, which significantly reduces imaging sensitivity and delays the start of research for 4–7 days after injection; a noticeably higher radiation exposure to patients through the use of long-lived radiation sources; slow extravasation and diffusion of drugs to the tumor interstitium, as well as nonspecific accumulation of labeled compounds in the tumor (intake of nonspecific antibodies by the tumor), which results in a high level of false-positive results [68].

Radionuclide diagnosis of HER2-positive breast cancer using antibody fragments

The obvious need to modify full-length antibodies (150 kDa) and improve their pharmacokinetics served as a starting point for the synthesis of Fab (~55 kDa) and $(Fab)_2$ (~110 kDa) antibody fragments obtained by enzymatic treatment of antibodies with pepsin and papain. These fragments lack an effector function (due to the absence of the Fc domain) and cannot recycle from lysosomes. Like the precursor immunoglobulin, the Fab and $(Fab)_2$ fragments are specific to a molecular target and preserve its spatial structure. Both fragments were used for radionuclide imaging of the tumors, which made it possible to evaluate their advantages over full-length antibodies: faster elimination from the bloodstream, compressed time between injection and imaging, decreased absorbed dose for patients, and better contrasting on the day of injection and the next day after injection. This allows for using relatively short-lived radionuclides such as ^{99m}Tc ($T_{1/2}$ = 6.0 h) and positron emitters with an average half-life: ^{55}Co ($T_{1/2}$ = 17.5), ^{64}Cu ($T_{1/2}$ = 12.7 h), ^{76}Br ($T_{1/2}$ = 16.2 h), and ^{86}Y ($T_{1/2}$ = 14.7 h) [69].

The only drug in this category that has passed phase I clinical trials is ^{68}Ga-DOTA-F(ab′)$_2$-trastuzumab, which was administered to 16 patients with metastatic and primary BC with different levels of HER2/neu expression. According to Beylergil et al., the compound was well tolerated by all patients, without pronounced adverse and allergic reactions and demonstrated low sensitivity (50%): the tumor was visualized only in four out of eight HER2-positive patients and not visualized in patients with HER2-negative tumors [59]. Preclinical and clinical studies revealed such shortcomings in this group of drugs as a decrease in the apparent binding affinity compared to monoclonal antibodies and significant sizes for effective extravasation, all things that significantly limit their use in clinical practice.

The discovery of camel heavy-chain-only antibodies (HCAbs) initiated the development of third-generation antibodies consisting of a single heavy chain variable domain (VHH; ~15 kDa) as the antigen-binding region; they were named nanobodies. One of the areas of nanobody application in clinical practice is the molecular imaging of tumors; in particular, their application in nuclear medicine [70, 71]. For instance, the possibility of using ^{68}Ga-HER2-Nanobody (half-life; 67.7 min) to detect HER2 receptor expression by PET/CT was evaluated in 20 patients with primary and metastatic BC in a phase I clinical study. Drug

safety and the absence of adverse effects at a radiation dose comparable to that of other commonly used PET tracers, as well as its rapid elimination from the bloodstream and accumulation mainly in the kidneys, liver, and intestines, with low accumulation in the area of mammary glands and regional lymph nodes, were shown [60]. Phase II clinical trials of ^{68}Ga-HER2-Nanobody aimed at determining HER2 expression in the brain metastases of BC patients are currently under way [72].

Radionuclide diagnosis of HER2-positive breast cancer using alternative scaffold proteins

The search for new effective agents capable of interacting with specific targets, as well as the rapid development of genetic engineering tools, has initiated an intensive effort to study and develop molecular compound alternatives to antibody-binding domains. These compounds must possess a number of necessary characteristics, such as being able to bind exclusively to the target antigen for a specific localization, lack immunogenicity, be stable and able to undergo rapid chemical modification during labeling, rapidly remove unbound molecules from the patient's body in order to make possible high-quality images of tumor lesions, and permit a reduction of the time interval between the injection and the start of research [73].

Over the past decade, a new class of target molecules called ASPs or scaffolds has gained increasing popularity. They meet all the requirements for optimal radionuclide delivery to tumor cells. The term "scaffold" was first introduced by Plyuktun et al. to designate a protein backbone that makes it possible to obtain various protein variants with different functions by slightly modifying their amino acid sequences and finding variants among them that effectively bind to specific targets [74]. The undeniable advantages of these compounds include their significantly smaller size compared to a conventional antibody, which increases substance penetration into the tumor, as well as their stable structure, additional functionalization and expression in the bacterial system that result in low production costs, and high thermal stability, which allows for long-term storage at room temperature, and the possibility to perform a direct chemical synthesis [75].

ASPs can be classified based on various criteria, such as size, synthesis method, origin, and biological function. One of the major classification systems divides scaffold proteins based on their structural elements, which has to do with the possibility of imparting their biological properties to new derivatives. The first class includes domain-sized compounds (6–20 kDa) such as affibody (Affibody, Inc.), albumin-binding-domain-derived affinity proteins (ADAPTs), affilins (Scil Proteins GmbH), anticalins (Pieris Pharmaceuticals Inc.), atrimers (Anaphore Inc.), DARPins (Dyax Inc., Shire Inc.), FN3 scaffolds (Molecular Partners Inc.), fynomer platforms (Janssen), Kunitz-type inhibitor domains and pronectins (Protelica Inc.), and FN3-based sequences (Protelica Inc.). The second class includes constrained peptides (2–4 kDa) such as avimers (Avidia Inc.), bicyclic peptides (Bicycle Therapeutics Inc.), and cysteine-containing peptides. To date, three scaffolds have been clinically tested for the diagnosis of HER2-positive BC: affibodies, ADAPTs, and DARPins (*Fig. 1*) [76].

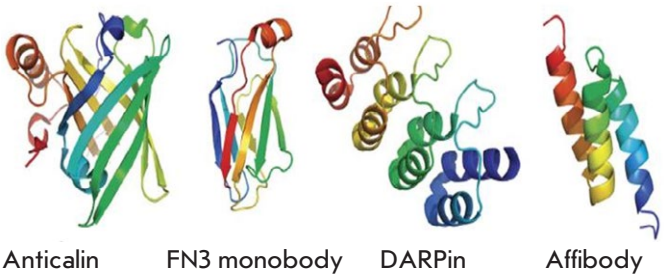

Fig. 1. Schematic representation of several alternative scaffold proteins

Affibodies. Affibody molecules are composed of three densely packed alpha helices stabilized by a hydrophobic core [77]. Affibodiies are small proteins with a molecular weight of 6–7 kDa that consist of 58 amino-acid residues. Affibodies display high affinity for HER3, IGF-1R, CAIX, and VEGFR2 receptors. Preclinical studies have revealed the high potential of affibodies as targeting modules for radionuclide diagnosis. The bulk of affibody studies were performed using a variant with high affinity for the HER2/neu receptor [78].

The ABY-002 molecule labeled with ^{111}In and ^{68}Ga was the first affibody variant studied in clinical practice. Baum et al. found that the drugs ^{111}In-ABY-002 and ^{68}Ga-ABY-002 are non-toxic in BC patients and characterized by rapid elimination from normal tissues. However, whole-body scanning 1, 2, and 4 h after administration of the labeled proteins revealed their high accumulation in the liver and kidneys [61].

The second-generation modified affibody molecule ABY-025 was created by re-engineering. Sorensen et al. showed that ^{111}In-ABY-025 is safe and can be used to differentiate the primary tumor and metastatic lesions based on the HER2/neu status in a phase I clinical trial of the compound in seven patients with local-

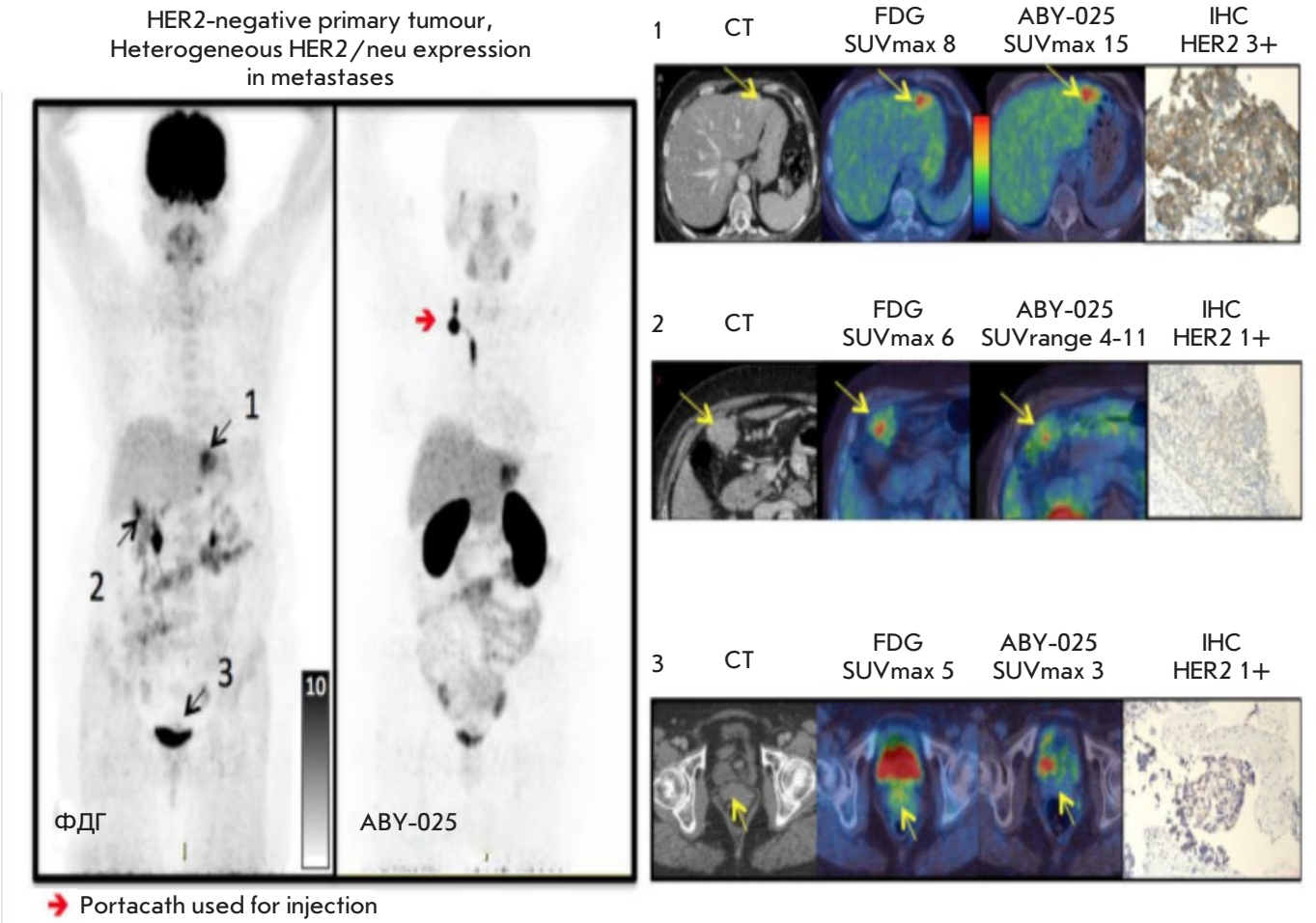

Fig. 2. A patient with HER2-negative primary breast cancer. FDG-PET/CT detected metastases in the left lobe of the liver, peritoneal lymph nodes, and the bladder neck. The study using ^{68}Ga-ABY-025 revealed its high additional accumulation level in hepatic metastasis and low level or no accumulation at other sites. According to IHC, the HER2/neu metastasis status is positive in the liver and negative at other sites

ly advanced and metastatic BC (five individuals with HER2/neu overexpression; two cases with no receptor expression) [62]. However, despite promising results, limited ability to visualize small lesions in HER2-positive patients was encountered for ^{111}In-ABY-025, which is probably due to low SPECT/CT resolution. Therefore, it was decided to study ^{68}Ga-ABY-025 use in PET/CT. A phase I clinical study showed no toxic effects by the compound in eight patients with metastatic BC. In addition, the importance of the drug dose was confirmed, since the use of 78 μg of the protein resulted in a statistically higher drug accumulation in the liver and kidneys compared to that when using 427 μg of the protein [63]. A subsequent analysis of 16 patients with metastatic BC (12 cases with HER2/neu overexpression; four individuals with no receptor expression) showed not only the possibility of visualizing metastatic nodes (metastases to regional lymph nodes and distant organs and tissues) in all cases but also their accurate differentiation depending on the HER2/neu status in patients with metastatic BC (*Fig. 2*) [64].

In addition, Sandberg et al. performed a study with 23 patients suffering from metastatic BC and showed that the spleen serves as the best reference organ in all modalities (followed by the blood pool and lungs) when using ^{111}In-ABY-025 and ^{68}Ga-ABY-025. At the same time, the tumor/spleen ratio attained a level of accuracy of 100% when separating tumor nodes, depending on the HER2/neu status 4 and 24 h after injection according to PET and SPECT, respectively [65].

The high efficiency of a labeled affibody molecule was confirmed by Xu Y. et al. In a preliminary clinical study performed in two patients, the authors showed

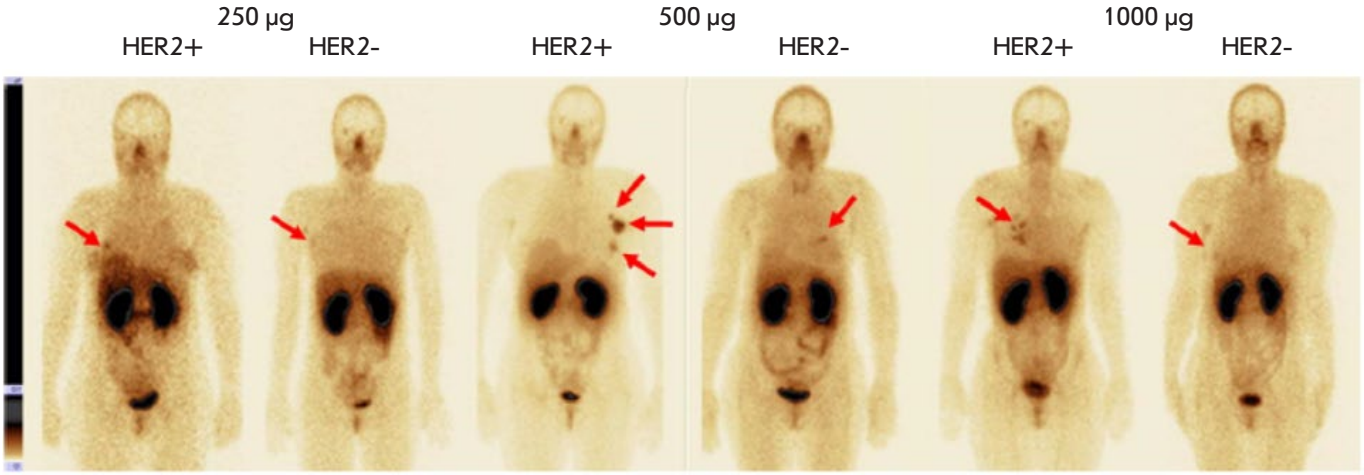

Fig. 3. Anterior projection of planar scintigraphy of breast cancer patients with positive (HER+) and negative (HER-) expression of HER2/neu 2 h after injection of 250, 500, and 1,000 μg of ^{99m}Tc-ADAPT6 (arrows indicate a breast tumor)

a higher accumulation level of ^{68}Ga-NOTA-MAL-Cys-MZHER$_{2:342}$ in a breast tumor overexpressing HER2/neu [79].

ADAPTs (ABD-Derived Affinity Proteins). These molecules were designed using a 46-amino acid scaffold derived from the albumin-binding domain (ABD), which folds spontaneously into a three-stranded structure and is independent of disulfide bridges. Hober's team (Royal Institute of Technology, Stockholm, Sweden) created a library that allows for synthesizing ABDs for various targets; molecules targeting various TNFα and HER3 receptors served as variants [80]. The ADAPT6 molecule, which has tropism for HER2/neu, was chosen because of its high affinity for HER2/neu (1 nM) and rapid elimination from the bloodstream thanks to low albumin binding [81].

Phase I clinical trials of ^{99m}Tc-ADAPT6 (^{9m}Tc; a half-life 6.01 h) included 22 BC patients with different HER2/neu expression levels in the primary tumor. Three dosages of the protein (250, 500, and 1,000 μg) were used in the study. All patients underwent whole-body planar scintigraphy and single-photon computed tomography of thoracic organs 2, 4, 6, and 24 h after administration of the labeled protein. The study results showed good tolerability of the drug and no changes in the vital organs. The most significant difference in drug distribution between the HER2/neu-positive and HER2/neu-negative tumors was observed 2 h after drug injection at a dose of 500 μg (mean tumor/background of 37 ± 19 for HER2-positive tumors and 5 ± 2 for HER2-negative tumors, $p < 0.05$, Mann–Whitney U test). The difference between the groups at other time intervals was not statistically significant. The tumor/background ratio in HER2-positive tumors was significantly higher in patients receiving the 500 μg dose than in those who received 250 and 1,000 μg ($p < 0.05$, Mann–Whitney U test). In addition, a relatively low radiation dose was set when administering 500 and 1,000 μg of the protein: 0.009 ± 0.002 and 0.010 ± 0.003 mSv/MBq, respectively, which is comparable to the data obtained in the studies of other ASPs (*Fig. 3*) [66, 82].

DARPins (Designed Ankyrin Repeat Proteins) are ASP members designed based on ankyrin proteins. Ankyrins are involved in the linking of membrane proteins to the cytoskeleton [83]. The DARPin backbone can include 4–6 ankyrin domains, each of which contains 33 amino acid residues; the domains are packed as two antiparallel alpha helices with a beta turn between them [84]. Considering that the molecular weight of a module is slightly over 3.5 kDa, and that DARPins consist of 4–6 modules, their molecular weight ranges from 14 to 21 kDa and is approximately a tenth the size of a conventional antibody (IgG) or a third the size of Fab [85]. Preclinical studies of DARPin variations have established their high tropism and specificity for the HER2/neu receptor [86, 87].

Phase I clinical trials of ^{99m}Tc-DARPinG3 at a dose of 1,000, 2,000, and 3,000 μg have been performed. They included 28 BC patients with different HER2/neu expression levels. Patients underwent whole-body planar scintigraphy and single-photon computed tomography of thoracic organs 2, 4, 6 and 24 h after drug administration. The drug ^{99m}Tc-DARPinG3

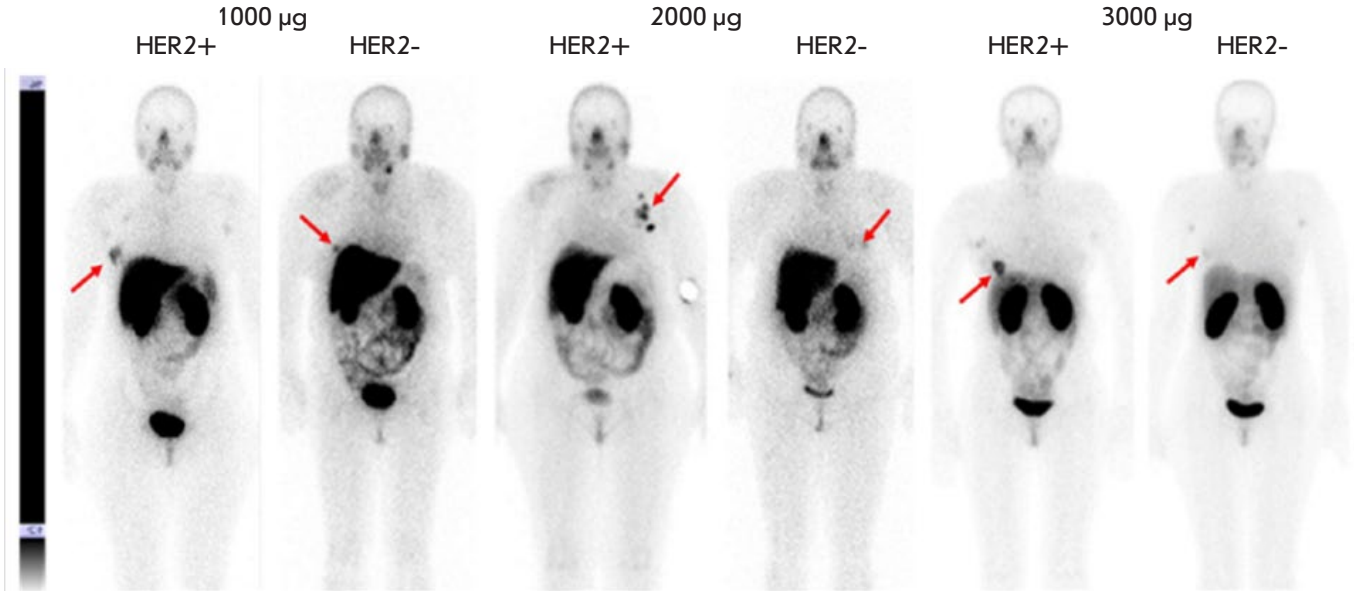

Fig. 4. Anterior projection of planar scintigraphy of breast cancer patients with positive (HER+) and negative (HER-) expression of HER2/neu 4 h after injection of 1,000; 2,000, and 3,000 μg of ^{99m}Tc-DARPinG3 (arrows indicate a breast tumor)

showed no toxic effects on the body over the entire observation period at the doses used, demonstrated rapid excretion with blood flow, and a relatively low radiation dose in patients (0.011 ± 0.001. 0.012 ± 0.006, and 0.012 ± 0.003 mSv/MBq, respectively) (*Fig. 4*). The best tumor/background ratio was observed in patients with HER2/neu overexpression in the tumor 2 and 4 h after the injection of 1,000 and 2,000 μg of the labeled protein; and 2, 4, and 6 h after the administration of 3,000 μg ($p < 0.05$; Mann–Whitney U test). At the same time, the dose of 3,000 μg turned out to be the most effective and made it possible to visualize liver metastases [67].

CONCLUSION

The diagnosis of HER2-positive BC remains a vexing issue in clinical oncology. None of the existing diagnostic methods can fully settle the question and usually requires additional, costly, invasive, and sometimes complicated manipulations [26, 28]. This problem becomes especially evident when determining the molecular characteristics of the identified tumor nodes (metastases) and choosing the optimal level of systemic treatment.

Currently, targeted radionuclide imaging methods, which expand the possibilities of cancer diagnosis, are rapidly developing [88]. The information presented in this review allows for a more detailed look at the evolution of the radionuclide diagnostics of HER2-positive BC using various compounds as a targeting module: from full-length antibodies to a new group of small synthetic proteins, namely alternative scaffold proteins, which are present in various molecular forms with different structures, charges, and lipophilicity of the amino acid residues exposed to a solvent. The numerous preclinical studies of labeled proteins have determined the optimal characteristics of the scaffolds needed for molecular imaging, as well as their high target specificity.

To date, clinical studies of compounds based on such proteins as affibodies, ADAPTs, and DARPins for SPECT and PET have shown good tolerance, rapid elimination from the body, and the possibility to differentiate tumor lesions depending on the status of human epidermal growth factor receptor 2 HER2/neu. An indisputable advantage of these methods over standard diagnostic approaches (FISH and IHC) is the possibility to perform simultaneous detection of additional tumor nodes and determine their molecular phenotype. The convincing results obtained in the first clinical trials point to the prospects of targeted radionuclide diagnosis and the need for further research in this direction. ●

This work was supported by the Ministry of Science and Higher Education of the Russian Federation (grant No. 075-15-2022-1103; "Development of target molecules based on scaffolds for cancer diagnosis and teratment: a theranostic approach").

REFERENCES

1. Kaprin A.D., Starinskii V.V., Petrova G.V. Malignant tumours in Russian Federation in 2019 (disease and mortality) M.: P.A. Herzen Moscow State Medical Research Institute – branch of the Federal State Budgetary Institution "NMIRC" of the Ministry of Health of Russia, 2020. 251 p.
2. Lambertini M., Viglietti G. // Oncotarget. 2019. V. 10. № 8. P. 803–804. doi: 10.18632/oncotarget.26611
3. Bray F., Ferlay J., Soerjomataram I., Siegel R.L., Torre L.A., Jemal A. // CA Cancer J. Clin. 2018. V. 68. № 6. P. 394–424. doi: 10.3322/caac.21492
4. Cardoso F., Kyriakides S., Ohno S., Penault-Llorca F., Poortmans P., Rubio I.T., Zackrisson S., Senkus E. // Ann. Oncol. 2019. V. 30. № 8. P. 1194–1220. doi: 10.1093/annonc/mdz173
5. Carioli G., Malvezzi M., Rodriguez T., Bertuccio P., Negri E., Vecchia C. // Breast. 2017. V. 36. P. 89–95. doi: 10.1016/j.breast.2017.06.003
6. Sachdev J.C., Sandoval A.C., Jahanzeb M. // Cancer Treat. Res. 2019. V. 178. P. 45–80. doi: 10.1007/978-3-030-16391-4_2
7. Arranja A.G., Pathak V., Lammers T., Shi Y. // Pharmacol. Res. 2017. V. 115. P. 87–95. doi: 10.1016/j.phrs.2016.11.014
8. Navalkissoor S., Gnanasegaran G., Baum R. // Br. J. Radiol. 2018. V. 91. № 1091. P. 20189004. doi: 10.1259/bjr.20189004
9. Turner J.H. // Br. J. Radiol. 2018. V. 91. № 1091. P. 20180440. doi: 10.1259/bjr.20180440
10. Langbein T., Weber W.A., Eiber M. // J. Nucl. Med. 2019. V. 60. № 9 (Suppl. 2). P. 13S–19S. doi:10.2967/jnumed.118.220566.
11. Lymperopoulos G., Lymperopoulos P., Alikari V., Dafogianni C., Zyga S., Margari N. // Adv. Exp. Med. Biol. 2017. V. 989. P. 119–128. doi: 10.1007/978-3-319-57348-9_10
12. Wiesing U. // Med. Hlth Care Philos. 2019. V. 22. № 4. P. 593–597. doi: 10.1007/s11019-019-09898-3.
13. Duffy M.J., Harbeck N., Nap M., Molina R., Nicolini A., Senkus E., Cardoso F. // Eur. J. Cancer. 2017. V. 75. P. 284–298. doi: 10.1016/j.ejca.2017.01.017
14. Nagini S. // Anticancer Agents Med. Chem. 2017. V. 17. P. 152–163. doi: 10.2174/1871520616666160502122724
15. Broughton M.N., Westgaard A., Paus E., Øijordsbakken M., Henanger K.J., Naume B., Bjoro T. // Tumour Biol. 2017. V. 39. № 6. P. 1010428317707436. doi: 10.1177/1010428317707436
16. Han L., Li L., Wang N., Xiong Y., Li Y., Gu Y. // Interferon Cytokine Res. 2018. V. 38. № 12. P. 578–582. doi: 10.1089/jir.2018.0085
17. Ahn S., Woo J.W., Lee K., Park S.Y. // J. Pathol. Transl. Med. 2020. V. 54. № 1. P. 34–44. doi: 10.4132/jptm.2019.11.03
18. Schwill M., Tamaskovic R., Gajadhar A.S., Kast F., White F.M., Pluckthun A. // Sci. Signal. 2019. V. 12. № 565. P. eaau2875. doi: 10.1126/scisignal.aau2875
19. Pareek A., Singh O.P., Yogi V., Ghori H.U., Tiwari V., Redhu P. // Cancer Res. Ther. 2019. V. 15. № 5. P. 971–975. doi: 10.4103/jcrt.JCRT_235_18
20. Waks A.G., Winer E.P. // J. Am. Med. Assoc. 2019. V. 321. № 3. P. 288–300. doi: 10.1001/jama.2018.19323
21. Slamon D.J., Clark G.M., Wong S.G., Levin W.J., Ullrich A., McGuire W.L. // Science. 1987. V. 235. № 4785. P. 177–182. doi: 10.1126/science.3798106.
22. Marshall D.A., Ferrusi I.L., Trudeau M., Leighl N.B., Hoch J.S., Grazziotin L.R., Khong H., Pullenayegum E., Earle G.C. // J. Oncol. Pharm. Pract. 2020. V. 26. № 2. P. 379–385. doi: 10.1177/1078155219850299
23. Pernas S., Tolaney S.M. // Ther. Adv. Med. Oncol. 2019. V. 11. P. 1758835919833519. doi: 10.1177/1758835919833519
24. Tsai Y.F., Tseng L.M., Lien P.J., Hsu C., Lin Y., King K., Wang Y., Chao T., Liu C., Chiu J., et al. // Histopathology. 2019. V. 74. № 4. P. 578–586. doi: 10.1111/his.13801
25. Stewart R.L., Caron J.E., Gulbahce E.H., Factor R.E., Geiersbach K.B., Downs-Kelly E. // Mod. Pathol. 2017. V. 30. № 11. P. 1561–1566. doi: 10.1038/modpathol.2017.65
26. Agersborg S., Mixon C., Nguyen T., Aithal S., Sudarsanam S., Blocker F., Weiss L., Gasparini R., Jiang S., Chen W., et al. // Breast Cancer Res. Treat. 2018. V. 170. № 2. P. 321–328. doi: 10.1007/s10549-018-4755-5
27. Bo W., Ding W., Sun K., Wang X., Xu L., Teng X.// Sci. Rept. 2019. V. 9. P. 16726. doi: 10.1038/s41598-019-53003-w
28. Furerr D., Jacobs S., Caron C., Sanschagrin F., Provencher L., Diorio C. // Anticancer Res. 2017. V. 37. P. 3323–3329. doi: 10.21873/anticanres.11701
29. Schrijver W., Suijkerbuijk K.P.M., van Gils C.H., van der Wall E., Moelans C.B., van Diest P.J. // J. Natl. Cancer Inst. 2018. V. 110. № 6. P. 568–580. doi: 10.1093/jnci/djx273.
30. Kroigard A.B., Larsen M.J., Thomassen M., Kruze T.A. // Breast J. 2016. V. 22. № 4. P. 420–430. https://doi.org/10.1111/tbj.12596
31. Raica M., Cimpean A.M., Ceasu R.A., Fulga V., Nica C., Rudico L., Sapefrati L. // Anticancer Res. 2014. V. 34. P. 1435–1440.
32. Lower E.E., Khan S., Kennedy D., Baughman R.P. // Breast Cancer – Targets and Therapy. 2017. V. 9. P. 515–520. doi: 10.2147/BCTT.S137709
33. Turner N.H., Di Leo A. // Cancer Treat. Rev. 2013. V. 39. № 8. P. 947–957. doi: 10.1016/j.ctrv.2013.05.003
34. Griguolo G., Pascual T., Dieci M.V., Guarneri V., Prat A. // J. Immunother. Cancer. 2019. V. 7. № 1. P. 90. doi.org/10.1186/s40425-019-0548-6
35. Ocaña A., Amir E., Pandiella A. // Breast Cancer Res. 2020. V. 22. № 1. P. 15. doi: 10.1186/s13058-020-1252-7
36. Muller K., Marotti J., Tafe L. // Am. J. Clin. Pathol. 2019. V. 152. № 1. P. 10. doi: 10.1093/ajcp/aqz010
37. Pekar G., Kasselaki I., Pekar-Lukacs A., Dekany C., Hellberg D., Tot T. // Histopathology. 2019. V. 74. № 2. P. 300–310. doi: 10.1111/his.13733
38. Jadvar H., Chen X., Cai W., Mahmood U. // Radiology. 2018. V. 286. № 1. P. 388–400. doi: 10.1148/radiol.2017170346
39. Stéen E.J.L., Edem P.E., Nørregaard K., Jorgensen J.T., Shalgunov V., Kjaer A., Herth M.M. // Biomaterials. 2018. V. 179. P. 209–245. doi: 10.1016/j.biomaterials.2018.06.021
40. Li L., Wu Y., Wang Z., Jia B., Hu Z., Dong C., Wang F. // J. Nucl. Med. 2017. V. 58. P. 821–826. doi: 10.2967/jnumed.116.183863
41. Ljungberg M., Pretorius P.H. // Br. J. Radiol. 2018. V. 91. № 1081. P. 20160402. doi: 10.1259/bjr.20160402
42. Massicano A.V.F., Marquez-Nostra B.V., Lapi S.E. // Mol. Imaging. 2018. V. 17. P. 1–11.
43. Gallivanone F., Valente M., Savi A., Canevari C., Castiglioni I. // Front. Biosci. (Landmark Ed). 2017. V. 22. P. 1750–1759. doi: 10.2741/4569
44. Pandit-Taskar N.J. // Med. Imaging Radiat. Sci. 2019. V. 50. № 4 (Suppl. 1). P. 41–44. https://doi.org/10.1016/j.jmir.2019.07.006
45. Tolmachev V., Orlova A., Sorensen J. // Semin Cancer Biol. 2021. V. 72. P. 185–197. doi: 10.1016/j.semcan-

cer.2020.10.005
46. Garousi J., Orlova A., Freid F.Y., Tolmachev V. // EJNMMI Radiopharmacy Chem. 2020. V. 5. P. 16. doi: 10.1186/s41181-020-00094-w
47. Hanack K., Messerschmidt K., Listek M. // Adv. Exp. Med. Biol. 2016. V. 917. P. 11–22. doi: 10.1007/978-3-319-32805-8_2
48. Ovacik M., Lin K. // Clin. Transl. Sci. 2018. V. 11. № 6. P. 540–552. doi: 10.1111/cts.12567
49. Mueller C., Haymond A., Davis J.B., Williams A., Espina V. // Expert Rev. Proteomics. 2018. V. 15. № 2. P. 131–152. doi: 10.1080/14789450.2018.1421071
50. Gebhart G., Flamen P., DeVries E.G.E., Jhaveri K., Wimana Z. // J. Nucl. Med. 2016. V. 57. № 2 (Suppl. 1). P. 81S–88S. doi 10.2967/jnumed.115.157941
51. Behr T.M., Behe M., Wormann B. // N. Engl. J. Med. 2001. V. 345. № 13. P. 995–996. doi: 10.1056/NEJM200109273451312
52. Perik P.J., Hooge M.L., Gietema J.A., Graaf W.T., Korte M.A., Jonkman S., Kosterink J.G., Veldhuisen D.J., Sleifer D.T., et al. // J. Clin. Oncol. 2006. V. 20. № 15. P. 2276–2282.
53. Sietske B.M., de Jong J., Perik P.J., Brouwers H., Schroder C.P., Munnink T., Bongaerts A.H.H., de Vries E.G.E., Hooge M.N. // Mol. Imaging. 2014. V. 13. P. 1–6. doi: 10.2310/7290.2014.00011
54. Dijekers E.C., Munnik T.H., Kosterink J.G., Brouwers A.H., Jager P.L., Jong J.R., Dongen G.A., Schroder C.P., Hooge M.N., Vries E.G. // Clin. Pharmacol. Ther. 2010. V. 87. № 5. P. 586–592. doi: 10.1038/clpt.2010.12
55. Ulaner G.A., Hyman D.M., Lyashchenko S.K., Lewis J.S., Carrasquillo J.A. // Clin. Nucl. Med. 2017. V. 42. P. 912–917. doi: 10.1097/RLU.0000000000001820
56. Gebhart G., Lamberts L.E., Wimana Z., Garcia C., Emonts P., Ameye L., Stroobants S., Huizing M., Aftimos P., Tol J., et al. // Ann. Oncol. 2016. V. 27. № 4. P. 619–624. doi: 10.1093/annonc/mdv577
57. Tamura K., Kurihara H., Yonemori K., Tsuda H., Suzuki J., Kona Y., Honda N., Kodaira M., Yamamoto H., Yunokawa M., et al. // J. Nucl. Med. 2013. V. 54. № 11. P. 1869–1875. doi: 10.2967/jnumed.112.118612
58. Mortimer J.E., Balding J.R., Colcher D.M., Conti P.S., Frankel P.H., Carrol M.I., Tong S., Poku E., Miles J.K., Shively J.E., et al. // J. Nucl. Med. 2014. V. 55. № 1. P. 23–29. doi: 10.2967/jnumed.113.122630
59. Beylergil V., Morris P.G., Smith-Jones P.M., Modi S., Solit D., Hudis C.A., Lu Y., O`Donoghue J., Lyashchenko S.K., Carrasquillo J.A., et al. // Nucl. Med. Commun. 2013. V. 34. № 12. P. 1157–1165 doi: 10.1097/MNM.0b013e328365d99b
60. Keyaerts M., Xavier C., Heemskerk J., Devoogdt N., Evaraert H., Ackaert C., Vanhoeij M., Duhoux F.P., Gevaert T., Simon P., et al. // J. Nucl. Med. 2016. V. 57. № 1. P. 27–33. doi: 10.2967/jnumed.115.162024
61. Baum R.P., Prasad V., Muller D., Schuchardt C., Orlova A., Wennborg A., Tolmachev V., Feldwisch J. // J. Nucl. Med. 2010. V. 51. № 6. P. 892–897. doi: 10.2967/jnumed.109.073239.
62. Sorensen J., Sandberg D., Sandstrom M., Wennborg A., Feldwisch J., Tolmachev V., Astrom G., Lubberink M., Garske-Roman U., Carlsson J., Lindman H. // J. Nucl. Med. 2014. V. 55. № 5. P. 730–735. doi: 10.2967/jnumed.113.131243
63. Sandstrom M., Lindskog K., Velikyan I., Wennborg A., Feldwisch J., Sandberg D., Tolmachev V., Orlova A., Sorensen J., Carlson J., et al. // J. Nucl. Med. 2016. V. 57. № 6. P. 86–71. doi: 10.2967/jnumed.115.169342
64. Sorensen J., Velikyan I., Sandberg D., Wennborg A., Feldwisch., Tolmachev V., Orlova A., Sandstrom M., Lubberink M., Olofsson H., Carlsson J., et al. // Theranostics. 2016. V. 6. № 2. P. 262–271. doi: 10.7150/thno.13502
65. Sandberg D., Tolmachev V., Velikyan I., Olofsson H., Wennborg A., Feldwisch J., Carlsson J., Lindman H., Sorensen J. // Eur. J. Nucl. Med. Mol. Imaging. 2017. V. 44. P. 1337–1346. doi: 10.1007/s00259-017-3650-3
66. Bragina O., von Witting E., Garousi J., Zelchan R., Sandstrom M., Orlova A., Medvedeva A., Doroshenko A., Vorobyeva A., Lindbo S., et al. // J. Nucl. Med. 2021. V. 62. № 4. P. 493–499. doi: 10.2967/jnumed.120.248799
67. Bragina O., Chernov V., Schulga A., Konovalova E., Garbukov E., Vorobyeva A., Orlova A., Tashireva L., Sorensen J., Zelchan R., et al. // J. Nucl. Med. 2021. V. 63. № 4. P. 528–535. doi: 10.2967/jnumed.121.262542
68. Sivelle C., Sierocki R., Ferreira-Pinto K., Simon S., Maillere B., Nozach H. // MAbs. 2018. V. 10. № 5. P. 720–729. doi: 10.1080/19420862.2018
69. Gebauer M., Skerra A. // Curr. Opin. Biotechnol. 2019. V. 60. P. 230–241. doi:10.1016/j.copbio.2019.05.007
70. Yang E.Y., Shan K. // Front. Oncol. 2020. V. 10. P. 1182. doi: 10.3389/fonc.2020.01182
71. Kijanka M., Dorresteijin B., Oliveira S., van Bergen P.M.P. // Nanomedicine. 2015. V. 10. №. 1. P. 161–174. doi: 10.2217/nnm.14.178
72. Keyaerts M., Xavier C., Everaet H., Vaneycken I., Fontaine C., Decoster L., Vanhoeij M., Cavelier V., Lahoutte T. // Ann. Oncol. 2019. V. 30. Suppl. 3. P. III25–III26. doi: 10.1093/annonc/mdz095.081
73. Shipunova V.O., Deyev S.M. // Acta Naturae. 2022. V. 14. № 1(52). P. 54–72. doi: 10.32607/actanaturae.11545
74. Martin H.L., Bedford R., Heseltine S.J., Tang A.A., Haza K.Z., Rao A., Mcpherson M.J., Tomlinson D.C. // Biotechnol. 2018. V. 45. P. 28–35. https://doi.org/10.1016/j.nbt.2018.02.008
75. Krasniqi A., D'Huyvetter M., Devoogdt N., Frejd F.Y., Sorensen J., Orlova A., Keyaerts M., Tolmachev V. // J. Nucl. Med. 2018. V. 59. P. 885–891. doi: 10.2967/jnumed.117.199901
76. Bragina O.D., Chernov V.I., Zeltchan R.V., Sinilkin I.G., Medvedeva A.A., Larkina M.S. // Bulletin of Siberian Medicine. 2019. V. 18. № 3. P. 125–133. https://doi.org/10.20538/1682-0363-2019-3-125-133
77. Tolmachev V., Tran T.A., Rosik D., Sjoberg A., Abrahmsen L. Orlova A. // J. Nucl. Med. 2012. V. 53. P. 953–960. doi: 10.2967/jnumed.111.101527
78. Tolmachev V., Gronroos T.J., Yim C.B., Garosi J., Yue Y., Grimm S., Rajander J., Perols A., Haaparanta-Solin M., Solin O., Ferdani R., Orlova A., Anderson C.J., Karlstrom A.E. // Sci. Rep. 2018. V. 8. P. 6542. doi:10.1038/s41598-018-24785-2
79. Xu Y., Wang L., Pan D., Yu C., Mi B., Huang Q., Sheng J., Yan J., Wang X., Yang R., Yang M. // Br. J. Radiol. 2019. V. 92. № 1104. P. 20190425. doi: 10.1259/bjr.20190425
80. Garousi J., Lindbo S., Borin J., von Witting E., Vorobyeva A., Oroujeni M., Mitran B., Orlova A., Buijs J., Tolmachev V., et al. // Eur. J. Pharm. Biopharm. 2019. V. 134. P. 37–48. doi: 10.1016/j.ejpb.2018.11.004
81. von Witting E., Garousi J., Lindbo S., Vorobyeva A., Altai M., Oroujeni M., Mitran B., Orlova A., Hober S., Tolmachev V. // Eur. J. Pharm. Biopharm. 2019. V. 140.

P. 109–120. doi: 10.1016/j.ejpb.2019.05.008
82. Bragina O.D., Chernov V.I., Garbukov E.Yu., Doroshenko A.V., Vorobyeva A.G., Orlova A.M., Tolmachev V.M. // Bulletin of Siberian Medicine. 2021. V. 20. № 1. P. 23–30. https://doi.org/10.20538/1682-0363-2021-1-23-30
83. Plückthun A. // Annu Rev. Pharmacol. Toxicol. 2015. V. 55. P. 489–511. doi: 10.1146/annurev-pharmtox-010611-134654
84. Stumpp M.T., Dawson K.M., Binz H.K. // BioDrugs. 2020. V. 34. № 4. P. 423–433. doi: 10.1007/s40259-020-00429-8
85. Shilova O.N., Deyev S.M. // Acta Naturae. 2019. V. 11. № 4. P. 42–53. doi: 10.32607/20758251-2019-11-4-42-53
86. Vorobyeva A., Garousi J., Tolmachev V., Shulga A., Konavalova E., Deyev S., Gulr R., Lofblom J., Sandstrom M., Chernov V., et al. // Sci. Rept. 2019. V. 9. № 1. P. 9405. doi: 10.1038/s41598-019-45795-8
87. Vorobyeva A., Bragina O., Altai M., Mitran B., Orlova A., Shulga A., Proshkina G., Chernov V., Tolmachev V., Deyev S. // Contrast Media Mol. Imaging. 2018. V. 2018. P. 6930425. doi: 10.1155/2018/6930425
88. Tolmachev V.M., Chernov V.I., Deyev S.M. // Rus. Chem. Rev. 2022. V. 91. RCR5034. https://doi.org/10.1070/RCR5034

Favipiravir and Its Structural Analogs: Antiviral Activity and Synthesis Methods

I. D. Konstantinova[1*], V. L.Andronova[1,2], I. V. Fateev[1], R. S. Esipov[1]
[1]Shemyakin and Ovchinnikov Institute of Bioorganic Chemistry, Russian Academy of Sciences, Moscow, 117997 Russia
[2]FSBI «National Research Centre for Epidemiology and Microbiology named after the honorary academician N.F. Gamaleya» of the Ministry of Health of Russia, Moscow, 123098 Russia
*E-mail: kid1968@yandex.ru
Received: December 08, 2021; in final form, April 27, 2022
DOI: 10.32607/actanaturae.11652

ABSTRACT **1,4-Pyrazine-3-carboxamide-based antiviral compounds have been under intensive study for the last 20 years. One of these compounds, favipiravir (6-fluoro-3-hydroxypyrazine-2-carboxamide, T-705), is approved for use against the influenza infection in a number of countries. Now, favipiravir is being actively used against COVID-19. This review describes the *in vivo* metabolism of favipiravir, the mechanism of its antiviral activity, clinical findings, toxic properties, and the chemical synthesis routes for its production. We provide data on the synthesis and antiviral activity of structural analogs of favipiravir, including nucleosides and nucleotides based on them.**

KEYWORDS **6-fluoro-3-oxopyrazine-2-carboxamide, favipiravir, pyrazine-2-carboxamide, influenza, SARS-CoV-2.**

ABBREVIATIONS **APRT – adenine phosphoribosyltransferase; Bz – benzoyl group; C – cytidine; CHIKV – Chikungunya virus; CC_{50} – 50% cytotoxic concentration; CT – computed tomography; DCI – 4,5-dicyanoimidazole; DENV – dengue virus; EBOV – Ebola virus; EC_{50} –50% effective concentration; GTP – guanosine 5'-triphosphate; G – guanosine; HCV – hepatitis C virus; HEK-293 cells – human embryonic kidney 293 cells; HGPRT – hypoxanthine-guanine phosphoribosyltransferase; HPRT – hypoxanthine phosphoribosyltransferase; HGXPRT – hypoxanthine guanine xanthine phosphoribosyltransferase; MDCK cells – Madin-Darby canine kidney cells; MV –mechanical ventilation; NAD – nicotinamide adenine dinucleotide; NCS – *N*-chlorosuccinimide; NMNAT – nicotinamide mononucleotide adenylyltransferase; PFU – plaque forming unit; PNP – purine nucleoside phosphorylase; PRPP – 5-phospho-ribosyl-1-alpha-pyrophosphate; RdRp – RNA-dependent RNA polymerase; RDP – ribose-5'-diphosphate; RMP – ribose 5'-monophosphate; RTP – ribose 5'-triphosphate; SARS – severe acute respiratory syndrome; SI – selectivity index (CC_{50}/EC_{50}); SOC – standard of care; T-1105 – 3-hydroxypyrazine-2-carboxamide; T-1106 – 3-oxo-4-(β-D-ribofuranosyl)-2-pyrazinecarboxamide; T-705 – 6-fluoro-3-hydroxypyrazine-2-carboxamide; $TCID_{50}$ – 50% tissue culture infectious dose; TSA – p-toluenesulfonamide; YFV – yellow fever virus.**

INTRODUCTION

Infectious diseases caused by both new, previously unknown viruses and re-emerging, known viruses, including their new variants, are one of the main causes of high mortality, mass epidemics, and pandemics. Three or four previously unknown viruses which are dangerous to humans are discovered annually [1]. The free movement of people increases the risk of a rapid spread of a viral infection among the population. In addition, viruses dangerous to humans can be transmitted by the insects or rodents that accompany our various goods. Furthermore, the ever-increasing interaction between humans and nature periodically leads to the emergence of diseases that are caused by zoonotic viruses capable of infecting humans: i.e., of overcoming the species barrier, or new variants of zoonotic viruses that have acquired the ability to infect humans through genetic variability. These viruses include the human immunodeficiency virus, influenza virus (H1N1), the highly pathogenic avian influenza virus (H5N1), Hendra virus (HeV), Zika, dengue, and yellow fever viruses, the Ebola virus (EBOV), severe acute respiratory syndrome coronavirus (SARS-CoV-1) [2], and COVID-19 (SARS-CoV-2) [3]. Viruses

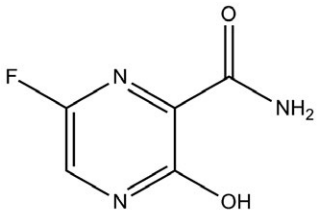

1

Fig. 1. Chemical structure of favipiravir (T-705, 6-fluoro-3-hydroxypyrazine-2-carboxamide)

that can not only infect but also effectively be transmitted from person to person can cause serious outbreaks and/or epidemics/pandemics [1].

Obviously, the development of safe and highly selective broad-spectrum antiviral agents is a must if we want to combat new, resistant forms of known viral infections. Of particular interest are synthetic analogs of natural nucleosides and nucleotides, because they have been used for a long time to diagnose and treat various infectious diseases and have also retain considerable biological and pharmaceutical potency [4, 5].

Favipiravir (6-fluoro-3-hydroxypyrazine-2-carboxamide, or T-705) (**1**) (*Fig. 1*) is a synthetic analog of 1,4-pyrazine-3-carboxamide. Its activity against the influenza virus A/PR/8/34 (H1N1) was discovered in the research laboratory of Toyama Chemical Co., Ltd [6].

Later, favipiravir was found to exhibit selective activity against a wide range of unrelated RNA viruses, including socially significant and especially dangerous pathogens, such as orthomyxoviruses (the influenza viruses A, B, and C), flaviviruses (yellow fever, West Nile, and Zika viruses), togaviruses (the Eastern, Western, and Venezuelan equine encephalitis viruses, the Chikungunya virus), arenaviruses (the Lassa fever and Junin viruses), filoviruses (the Ebola virus), paramyxoviruses (the respiratory syncytial virus and human metapneumovirus), rhabdoviruses (the rabies virus), etc., but not to be active against DNA viruses [7–10].

ANTI-INFLUENZA ACTIVITY OF FAVIPIRAVIR

Favipiravir is an effective inhibitor of the reproduction of the human influenza viruses A, B, and C and it exhibits activity against strains resistant to all anti-influenza drugs of practical importance: neuraminidase inhibitors (oseltamivir, zanamivir, laninamivir, peramivir); M2 protein inhibitors (amantadine and rimantadine with a 50% effective concentration (EC_{50}) in a range of 0.014 to 0.55 μg/mL [11–13] and against the pig viruses A/H2N2 and A/H4N2, the highly pathogenic avian virus A/H5N1, and the new virus A/H7N9. The toxic effect of favipiravir on a MDCK cell culture have proved insignificant, and the CC_{50} (50% cytotoxic concentration) was not achieved even at a concentration of 2,000 μg/mL, which is an indication of the compound's ability to highly selectively inhibit the replication of influenza viruses [12–15].

The high activity of favipiravir *in vivo* was confirmed in a model of lethal influenza infection in mice that had received the drug orally (*Table*). Administration of favipiravir to animals infected with type A influenza virus was shown to provide for a dose-dependent decrease in the pulmonary viral titer and animal mortality. The therapeutic efficacy of favipiravir varies depending on the influenza virus subtype and strain.

Importantly, the protective effect of favipiravir does not depend on the virus sensitivity to oseltamivir [14]. The potentiating effect of the interaction between favipiravir and oseltamivir has been shown in mice infected with the A/H1N, A/H3N2, and A/H5N1 virus subtypes [16, 17]. In addition, the combination of favipiravir and oseltamivir is also effective against infections caused by the highly-resistant-to-oseltamivir influenza virus strain A/Mississippi/03/2001 (H1N1) H274Y. In this case, oseltamivir was not effective even when it was used at a dose of 100 mg/kg/day (administered twice daily for 5 days). Upon simultaneous administration of oseltamivir (50 mg/kg/day) and favipiravir (12.5 mg/kg/day) at doses that were not protective when given alone (100% mortality), all the animals survived [18].

The synergistic effect of favipiravir and another inhibitor of influenza virus neuraminidase, piramivir, was also demonstrated in experiments in mice infected with the pandemic influenza virus A/California/04/2009 (H1N1) [19].

MECHANISM OF THE ANTIVIRAL ACTIVITY OF FAVIPIRAVIR

The mechanism of favipiravir action has been exhaustively studied in the influenza virus. Favipiravir has been shown to act on the RNA-dependent RNA polymerase (RdRp) of the influenza A virus, which comprises the virus-encoded proteins PB1, PB2, and PA. A metabolite of favipiravir, favipiravir-4-ribofuranosyl-5'-triphosphate (T-705-RTP), exhibits biological activity. The intracellular transformation of favipiravir resulting in the active metabolite involves only cellular enzymes. Favipiravir is first converted by hypoxanthinguanine phosphoribosyl transferase (HGPRT) to ribose 5'-monophosphate (T-705-RMP) and then metabolized to the triphosphate form by cellular kinases

The *in vivo* antiviral activity of favipiravir administered orally against some influenza virus strains

Influenza virus strain	Activity
A/Victoria/3/75 (H3N2)	Administration of favipiravir (30 and 100 mg/kg/day, 4 times a day for 5 days) produces a 70 and 100% survival rate in mice, respectively (100% lethality of mice in the control group). The pulmonary viral load in mice one day after the onset of treatment (100 mg/kg/day, 4 times a day) is reduced by more than 1 lg $TCID_{50}$/g. In the group treated with oseltamivir (20 mg/kg/day, 2 times a day for 5 days), the survival rate was 50% and the reduction in the pulmonary viral titer was 0.1–0.2 lg [11]
A/Duck/MN/1525/81 (H5N1)	Upon 100% lethality in the control group, administration of favipiravir (30 mg/kg/day, 4 times a day for 5 days) provides 100% survival rate of mice, and oseltamivir (20 mg/kg/day, 2 times a day for 5 days) provides a 20% survival rate in mice. The 100% protective effect of favipiravir at a dose of 300 mg/kg/day is fully preserved at a delay of 36 h in the onset of treatment and decreases to 90% at a delay of 48–72 h [11]
A/PR/8/34 (H1N1)	Increased survival rate of mice from 21.4 to 87.5% compared with that in the control, untreated group, a reduction in the pulmonary viral titer by 3 lg PFU/lung (100 mg/kg/day, 4 times a day within 5 days), and prevention of death of mice were achieved as the single dose (200 mg/kg/day) was increased; in 80% of mice, the pulmonary viral titer was below the detection threshold [6]
A/Vietnam/UT3040/04 (VN3040) (H5N1) highly pathogenic for mice	Mortality in the control group was 100%. Administration of favipiravir (300 mg/kg/day, 2 times a day) provided a 50 and 100% survival rate at a 5- and 8-day course, respectively. At an 8-day course, the infection was asymptomatic and the efficacy in animal protection was preserved even at a delay of 72 h in the first drug administration. As the dose of favipiravir was reduced to 100 mg/kg/day (8-day course), the survival rate of the animals decreased to 90%; and at a delay of 48 and 72 h in the onset of treatment, the survival rate of the animals decreased to 60 and 25%, respectively. Administration of favipiravir stops tracheitis and bronchitis, dose-dependently decreases the production of pro-inflammatory cytokines and the affected lung area, and significantly reduces the infectious titer of the virus in the lungs and brain [14]
VN1203-H274Y is a oseltamivir-resistant variant of the A/Vietnam/UT3040/04 (VN3040) virus that is highly pathogenic for mice	Administration of favipiravir to mice (100 and 300 mg/kg/day, 2 times a day) for 8 days provided a 50 and 100% survival rate of animals, respectively, with 100% lethality of the animals in the control group [14]

[20, 21]. T-705-RTP is recognized by viral RdRp, effectively competing with the natural substrates GTP and, to a lesser extent, ATP, and is included in the growing RNA chain [11, 14, 22]; it also inhibits RdRp activity, which leads to the total suppression of virus-specific RNA synthesis (transcription and replication of the viral genome). A scheme of metabolic transformations of favipiravir is shown in *Fig. 2* [20]. It is important to emphasize that favipiravir does not significantly affect DNA and cellular RNA synthesis, which is explained by a lack of the suppressive effect of T-705 on cellular DNA polymerases (α, β, and γ) and DNA-dependent RNA polymerase II [11].

Until recently, there had been only two reports of a slight decrease in the antiviral effect of T-705 against the influenza viruses A/H3N2 and A/H5N1 (1.8-fold and 1.5-fold) with the V43I mutation in the PB1 polymerase subunit (one of the proteins that form the ribonucleoprotein) [23, 24].

D. Goldhill et al. generated an A/H1N1 influenza strain highly resistant to favipiravir (the virus sensitivity decreased 30-fold) [25]. The decrease in the sensitivity was caused by a combination of two mutations in RdRp: K229R in the PB1 subunit and P653L in the PA subunit. The K229R mutation causes resistance to favipiravir, but critically (by a factor of 30) it reduces the activity of RdRp and the efficiency of virus reproduction. The P653L mutation in the PA subunit is compensatory and restores the polymerase activity associated with PB1 without reducing resistance, as well as normalizes the kinetics of mutant virus replication. The role of the combination of K229R + P653L mutations in the development of resistance to favipiravir was confirmed for two more influenza A virus subtypes (H3N2 and H7N9). Interestingly, the introduction of the K229R substitution in PB1 or a combination of PB1/K229R+PA/P653L substitutions reduces the mutagenic effect of favipiravir; i.e., the fidelity of RdRp in virus replication increases: the produced RNA contains significantly fewer mutations even in the presence of T-705 at a high concentration of 100 μM compared to wild-type RdRp; incorporation

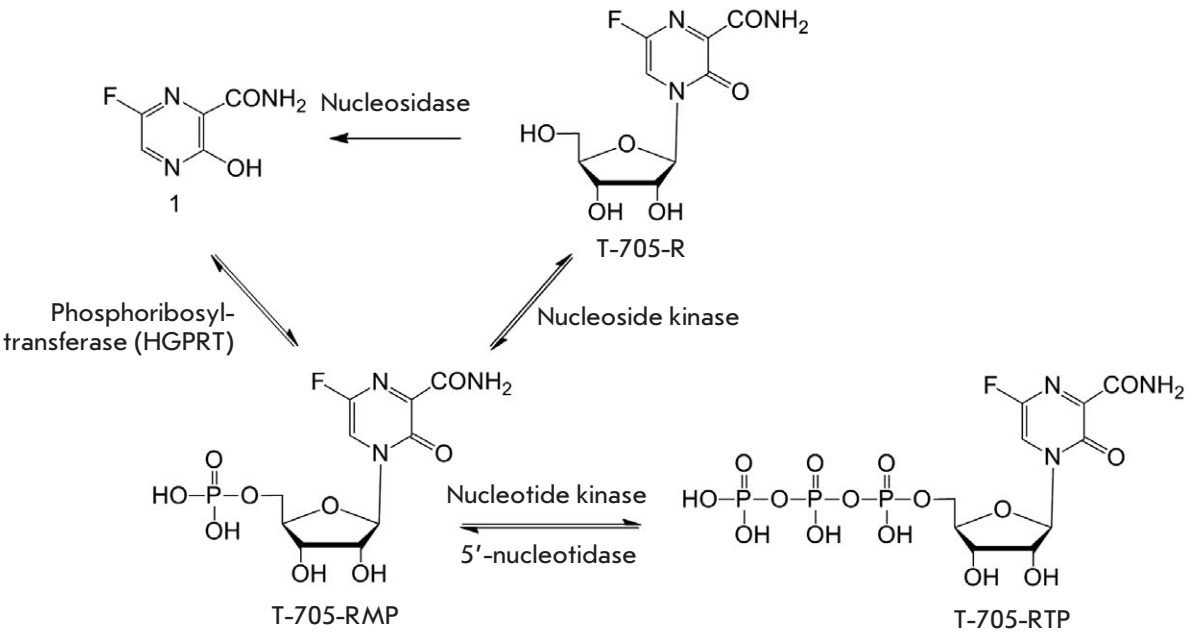

Fig. 2. Formation of the active form of favipiravir

of T-705 into the growing viral RNA during *in vitro* replication also decreases [25].

The antiviral effect of favipiravir against a large number of RNA viruses may be partially explained by its ability, after transformation into T-705-RTP, to integrate into the synthesized viral RNA and bind to conserved RdRp domains, thereby inhibiting virus replication. For example, the use of other viral models with an RNA-positive genome enabled the generation of virus strains resistant to favipiravir and identification of the molecular mechanism of drug resistance. The key mutation, K291R, in the Chikungunya virus (togavirus) was localized in nsP4 (RdRp) and, like the K229R mutation in the influenza virus, occurred in the highly conserved motif F of nsP4, which possesses RNA polymerase activity [26]. A similar genetically engineered K159R mutation in motif F of 3D (RdRp) in the Coxsackie B3 virus (picornavirus) fatally reduced the activity of the purified viral RdRp and was lethal. As in the influenza virus, a compensatory A239G mutation in RdRp was required to restore the viability of the mutant virus [27].

On the other hand, a number of researchers believe that at least two consecutive inclusions of T-705-RMP are required to stop RNA elongation. Therefore, the central mechanism of virus replication inhibition may be termination of RNA synthesis at high favipiravir concentrations and the ability to induce lethal mutagenesis at low favipiravir concentrations [28]. This has been shown in experiments with the influenza A(H1N1) [17, 29], hepatitis C [30], West Nile [31], dengue [32], and Ebola [33] viruses.

The mechanism of lethal mutagenesis is explained by the concept of error threshold: if the mutation rate during genome replication is above the error threshold, this is equivalent to a loss of hereditary information [34]. Most RNA-containing viruses are characterized by a high mutation rate, due to the lack of a mechanism that corrects errors during viral genome replication [35]. Hypermutability promotes rapid adaptation of viruses to certain adverse environmental changes; e.g., it allows rapid development of resistance to antiviral drugs. However, in the presence of a hypermutator during viral genome replication, the mutation rate exceeds the threshold level and defective genomes are synthesized, which leads to the formation of non-viable viral particles. Phenotypically, this is expressed as a significant decrease in the infectivity of a new virus generation (ratio of the titer of infectious viral particles to the number of viral genome copies) [36].

In vitro experiments have revealed that a decrease in the number of infectious particles of the influenza A/H1N1 virus in the presence of favipiravir does not correlate with a decrease in the number of RNA copies (viral genomes), which is an indication of preserved activity of the transcription complex and an

increase in the content (%) of defective viral particles in the population. Analysis of the *NP* gene sequence showed a dose-dependent increase in the rate of mutations, mainly transitions (G→A and C→U), and a shift in the nucleotide profiles of individual clones [29]. Hypervariability of the influenza A/H5N1 virus was also observed in experiments *in vivo* during an infection of mice treated with favipiravir compared with the control group and mice treated with oseltamivir [17].

EFFICACY OF FAVIPIRAVIR AGAINST THE SARS-CoV-2 CORONAVIRUS INFECTION

In 2014, favipiravir (under the brand name Avigan®) was approved in Japan for the treatment of new or re-emerging pandemic influenza virus infections, although its use was limited to cases where licensed influenza drugs were ineffective or insufficiently effective (http://www.toyama-chemical.co.jp/eng/news/news140324e.html) [37].

Since the outbreak of the novel coronavirus SARS-CoV-2 epidemic in China at the end of December 2019 and its rapid spread around the world, dozens of known pharmaceuticals with antiviral activity [38–40], including favipiravir [3, 41], have been tested as possible therapeutic agents for the treatment of patients infected with COVID-19.

In vitro, SARS-CoV-2 was significantly less sensitive to favipiravir than the influenza virus is. Favipiravir activity against the clinical isolate nCoV-2019BetaCoV/Wuhan/WIV04/2019 manifested itself when used at a concentration of 61.88 μM (EC50), and the maximum studied concentration of 400 μM was non-toxic to a Vero E6 cell culture (CC50 > 400 μM, selectivity index SI > 6.46) [42]. In another study, favipiravir proved ineffective against the SARS-CoV-2 clinical isolate BetaCoV/HongKong/VM20001061/2020 even at a concentration of 100 μM [43].

It is important to note that investigation of the effect of favipiravir on animals at doses equivalent to the proposed human treatment regimens revealed its embryotoxicity: in rats, there was fetal death in the early stages of embryogenesis, a decrease in the live fetal body weight and the number of live fetuses, decreased litter survival 4 days after birth, and reduced weight gain. In addition, favipiravir was found to be teratogenic in mice, rats, rabbits, and monkeys [3]. Given the high risk of teratogenicity and embryotoxicity of favipiravir, no human clinical trials have involved pregnant or lactating females and trial participants have been required to abstain from unprotected sex during trials and for 90 days after the last dose of the drug. Therefore, the risks to humans remain unknown and the use of favipiravir remains under strict supervision, which limits its use, especially in pregnant females [10].

The ribose-5'-triphosphate metabolite of favipiravir is known to be a substrate for human mitochondrial RNA polymerase [44]. *In vitro* incorporation of T-705-RTP into mitochondrial RNA was shown to have no toxic effect on human mitochondria; i.e., it did not lead to chain termination or inhibition of DNA-dependent RNA polymerase activity. However, favipiravir should be used with caution because it may exert an indirect toxic effect on mitochondria [44].

Forty-seven clinical trials (of which 17 are completed) on the efficacy of favipiravir for the treatment of COVID-19 had been registered on the clinicaltrials.gov site as of November 27, 2020. Trial protocols for the use of favipiravir in adult COVID-19 patients typically indicate the following dosage: a loading dose of 1,600 or 1,800 mg twice daily on day 1, then a maintenance dose of 1,200–2,000 mg daily in 2, 3, or 4 doses for the next 4–13 days. The results of several clinical trials of favipiravir for COVID-19 point at critical factors affecting the treatment outcome; in particular, loading doses <45 mg/kg per day, older age, and baseline disease severity.

We will describe the results of several clinical trials conducted in China and the Russian Federation.

An open-label, randomized, multicenter study of 236 adults with moderate, severe, or critical COVID-19 pneumonia was conducted in China (ChiCTR2000030254): 116 patients received favipiravir (1,600 mg orally, twice daily on day 1, then 600 mg orally twice daily for 7–10 days), and 120 patients received umifenovir (Arbidol®; 200 mg 3 times a day for 7–10 days). The rate of clinical recovery at day 7 in patients with moderate COVID-19 pneumonia was 61% (71/116) in the favipiravir group versus 52% (62/120) in the umifenovir group; in patients with severe or critical COVID-19, this rate was 16% versus 0%, respectively. Relief for pyrexia and cough was achieved faster in the favipiravir group [45].

An open-label, controlled trial of the efficacy of favipiravir for the treatment of COVID-19 was conducted at the Third People's Hospital of Shenzhen, China (Chinese Clinical Trials Registry, ID: ChiCTR2000029600), between January 30 and February 14, 2020 [46]. The trial included patients aged 16 to 75 years with a laboratory-confirmed diagnosis of coronavirus infection and clinical manifestations of the disease for no more than 7 days (N = 35). Patients who had initially received antiviral therapy with lopinavir/ritonavir before January 30, 2020, were included in the control group (N = 45). All baseline characteristics of the clini-

cal status of the patients in the groups were comparable. Favipiravir was used orally: 1,600 mg twice daily on day 1, then 600 mg twice daily on days 2 to 14 + α-interferon (5×10^6 IU twice daily as an aerosol inhalation). The patients in the control group received lopinavir/ritonavir (400 mg/100 mg twice daily for 14 days + α-interferon (5×10^6 IU twice daily as aerosol inhalation). In the favipiravir group, the mean viral clearance time (4 days) was shorter than that in the control group (11 days) and there was also a significant improvement in chest CT compared with that in the control group, 91% vs 62%, respectively. In this trial, favipiravir demonstrated the best therapeutic effect, as measured by COVID-19 progression and viral clearance.

In the Russian Federation, in an interim pilot phase of an open-label, randomized, multicenter phase II/III clinical trial comparing the efficacy of Avifavir (favipiravir) and standard treatment (SOC) in 60 hospitalized adult patients (aged 60 years and older) with moderate COVID-19 pneumonia (Russia, NCT04434248) the following dosage regimens were used: favipiravir 1,600 mg orally twice daily on day 1, then 600 mg twice daily on days 2–14 (group 1, N = 20) or 1,800 mg twice daily on day 1, then 800 mg twice daily on days 2–14 (group 2, N = 20). In group 3 (SOC, control), 15 patients received hydroxychloroquine or chloroquine, one patient received lopinavir/ritonavir, and four patients received no etiotropic treatment [47]. The virological response to favipiravir in groups 1 and 2 was as follows: viral clearance was achieved in 25/40 (63%) patients on day 4 and in 37/40 (93%) patients by day 10. The same indicators in group 3 (SOC) were 6/20 (30%) and 16/20 (80%) patients, respectively. The mean time to body temperature normalization (<37°C) was 2 days in groups 1 and 2 and 4 days in the SOC group. By day 15, chest CT findings had improved in 90% (36/40) of patients treated with favipiravir versus 80% (16/20) of patients treated with SOC. Mild to moderate adverse drug reactions to favipiravir (diarrhea, nausea, vomiting, chest pain, and elevated hepatic transaminases) were reported in 7/40 (18%) patients and resulted in discontinuation of the study drug in 2/40 (5%) patients. Thus, the mean duration of favipiravir administration was 10.9 ± 2.8 days.

Between May 21 and August 10, 2020, an open, randomized, multicenter phase 3 study was conducted in the Russian Federation [48] to evaluate the efficacy and safety of favipiravir tablets (Areplivir, PROMOMED RUS LLC, Russia) compared to the Standard of Medical Care in patients hospitalized with moderate COVID-19 pneumonia (ClinicalTrials.gov ID: NCT04542694). The study was conducted in four medical institutions: State Clinical Hospital No. 50 (Moscow), Regional Clinical Hospital (Ryazan), City Hospital No. 40 of Kurortny District (Saint-Petersburg), and Smolensk Clinical Hospital No. 1 (Smolensk).

Two hundred patients aged 18 to 80 years with an established diagnosis of moderate SARS-CoV-2 infection were randomized in a 1:1 ratio. The patients in group 1 received favipiravir 1,600 mg twice daily (8 tablets at a time, a total of 16 tablets per day) on day 1 and then 600 mg (3 tablets) twice daily (6 tablets per day) on days 2–14. The patients in group 2 received standard therapy, but not favipiravir (hydroxychloroquine with or without azithromycin, chloroquine, lopinavir/ritonavir, or other recommended regimens). The rate of clinical status improvement by day 10 evaluated using the WHO categorical ordinal scale of clinical status improvement was 27% in group 1 and 15% in group 2. The virus clearance rate by day 10 – the percentage of patients with COVID-19 elimination according to PCR – was 98% (group 1) and 79% (group 2). The CT extent of lung damage (decrease in the lesion size) compared with the baseline level was 60% in group 1 and 40% in group 2. Mortality in both groups was 0%. During the treatment in both groups (200 patients), there was no need to transfer patients to an intensive care unit or use non-invasive ventilation or mechanical ventilation (MV).

Despite the side effects, the efficacy and wide range of antiviral activity of favipiravir make it a promising antiviral compound.

These results led to the approval of favipiravir for the treatment of the coronavirus infection (COVID-19) in several countries, including China [49] and India [50].

In the Russian Federation, favipiravir has been used since 2020 as an etiotropic drug for a mild to moderate coronavirus infection (COVID-19) [51, 52]; it is also included in the List of Vital and Essential Medicines for Medical Use for 2021 [53] (https://mine-med.ru/archive/p2021p1.pdf). Favipiravir is produced in the form of film-coated tablets under the trade names Avifavir (Kromis), Areplivir (Promomed Rus), Favipiravir (Alium), Covidolek (Nanolek), Favibirin (Pharmasintez), and Coronavir (Technology of Medicines) [54]. In addition, in 2021, the first domestic drug for intravenous administration (Areplivir, Promomed Rus) received marketing authorization from the Ministry of Health of the Russian Federation [55].

Currently, structural analogs of favipiravir are under study for antiviral activity. This is especially important when many RNA virus diseases lack approved antiviral drugs or effective vaccines, and most interventions are limited to supportive care.

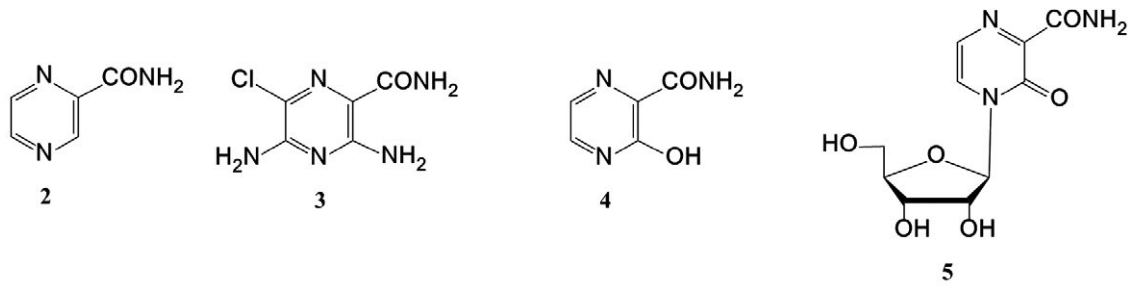

Fig. 3. Some structural analogs of favipiravir: **2** – 2-pyrazinecarboxamide; **3** – 3,5-diamino-6-chloro-2-pyrazinecarboxamide; **4** – 3-hydroxypyrazine-2-carboxamide (T-1105); **5** – 3-oxo-4-(β-*D*-ribofuranosyl)-2-pyrazinecarboxamide (T-1106)

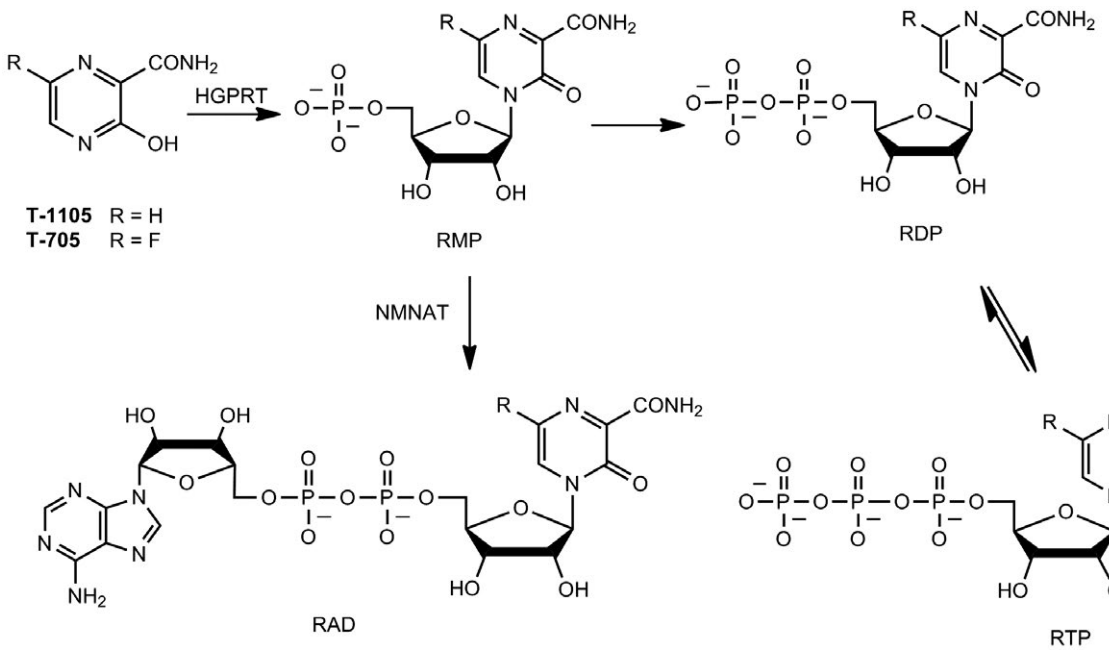

Fig. 4. Scheme for the conversion of T-705 and T-1105 to their active metabolites, ribose-5′-triphosphates (RTPs), and a parallel pathway in which monophosphate forms (RMPs) of T-705 and T-1105 are converted to the RAD metabolite

STRUCTURAL ANALOGS OF FAVIPIRAVIR EXHIBITING ANTIVIRAL ACTIVITY

Structural analogs of favipiravir include the following compounds (*Fig. 3*):

Of particular interest are T-1105 (**4**) and T-1106 (**5**), synthesized at the research laboratory of Toyama Chemical Co., Ltd. The antiviral activity of these analogs against influenza virus A/PR/8/34 (H1N1) was established in 2009 during *in vitro* screening of a chemical library of compounds [7].

Similar to favipiravir, T-1105, as the active nucleoside 5'-triphosphate (T-1105-RTP) form, inhibits viral RdRp. Compared with favipiravir, the efficiency of *in vitro* activation of 3-hydroxypyrazine-2-carboxamide to its ribose-5'-triphosphate form is more dependent on the cell line in which this activation occurs. For example, T-1105 showed higher antiviral activity in MDCK cells (the T-1105-RTP level was 841 and 1,228 pmol/10^6 cells after 24-hour incubation with 0.5 and 1 mM T-1105, respectively). In the control experiment in this cell line at equimolar favipiravir concentrations of 0.5 and 1 mM, the T-705-RTP level was 4-fold lower than the T-1105-RTP level. Antiviral activity of T-1105-RTP was not detected in A549 and Vero cells (less than 50 pmol/10^6 cells), as well as in HEK293T cells (65 and 171 pmol/10^6 cells after 24-hour incubation with 0.5 and 1 mM T-1105, respectively). In these three cell lines, T-1105 activation was hampered by an inefficient conversion of T-1105-RMP to T-1105-RDP. This phenomenon is associated with the fact that the main metabolic pathway is accompanied by a parallel reaction converting T-1105-RMP to the T-1105-RAD metabolite with nicotinamide mononucleotide adenylyltransferase (NMNAT) (*Fig. 4*) [56].

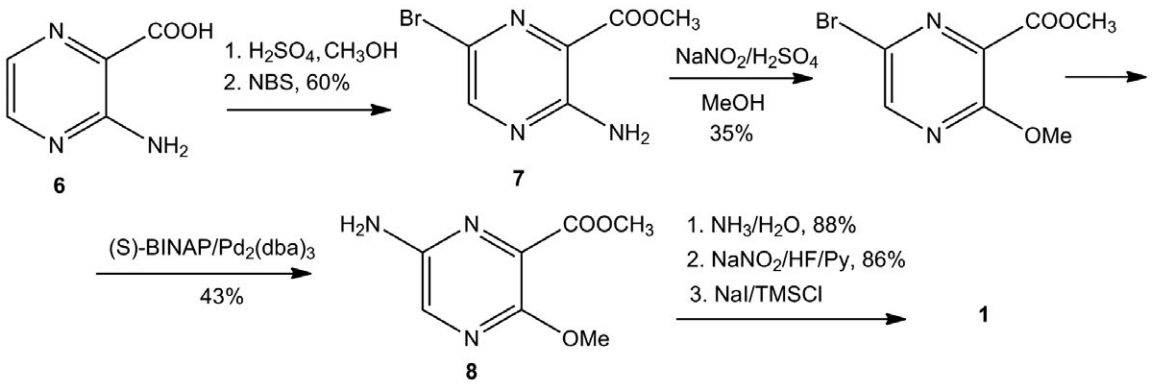

Fig. 5. Synthesis of favipiravir (**1**) according to the strategy developed by Y. Furuta (Toyama Company)

Because T-705-RAD and T-1105-RAD are found in all of the described cell lines, they are being studied as nicotinamide adenine dinucleotide (NAD) analogs.

The non-fluorinated analog of favipiravir, T-1105, was found to be active against the Chikungunya virus (CHIKV) *in vitro*. In that case, T-1105 was a selective inhibitor of the cytopathogenic effect induced by clinical isolates of CHIKV and other alphaviruses. The antiviral activity of T-1105 was 2- to 5-fold higher than that of favipiravir. For example, for the CHIKV Indian Ocean strain 899 (lab), the EC_{50} value was 25 ± 3 μmol/L for T-705 and 7.0 ± 1 μmol/L for T-1105 [27].

In *in vivo* experiments with the foot-and-mouth disease virus, T-1105 efficiently suppressed the clinical signs of the disease in infected pigs and reduced viremia and virus shedding (oral dose: 400 mg/kg/day for 6 days). The efficacy of 3-hydroxypyrazine-2-carboxamide and the prophylactic O_1 Manisa vaccine against the foot-and-mouth disease virus was also compared in a guinea pig model. The efficacy of prophylactic therapy with T-1105 (guinea pigs, 400 mg/kg/day orally for 5 days) was shown to be comparable to that of animal vaccination [57].

T-1106 proved more efficient than favipiravir against the yellow fever virus (YFV) in a Syrian hamster model with a minimum effective dose of 32 mg/kg/day administered intraperitoneally or orally. T-1106 had no antiviral activity in experiments on the cytopathic effect induced by the yellow fever virus in the Vero (EC_{50} more than 100 μg/mL) and CV-1 (EC_{50} more than 369 μmol/L) cell lines [58, 59].

Favipiravir was more efficient than T-1106 *in vitro* against several members of the Phlebovirus genus. At the same time, the efficacy of T-1106 in a model of Syrian hamsters infected with the Punta Toro virus, which is characterized by liver damage, was 9.4-fold higher than that of favipiravir (based on ED_{50}). In a mouse model, favipiravir showed the best antiviral activity [60].

The activity of the T-1105 and T-1106 nucleosides against the dengue virus (DENV) was compared *in vitro* [32]. The efficacy of T-1105 (EC_{50} 21 ± 0.7 μmol/L) was 5-fold higher than the EC_{50} of favipiravir. It exceeded the activity of T-1106 by almost the same factor (EC_{50} 113 ± 11 μmol/L for T-1106). In addition, both T-1105 and its nucleoside are capable of inducing lethal mutagenesis of the viral genome due to base mispairing during the formation of the RNA secondary structure.

Obviously, high activity against RNA viruses is inherent not only to favipiravir, but also to its structural analogs. A number of studies have shown an even higher efficacy of T-1105 and T-1106 compared to that of favipiravir both *in vitro* and *in vivo*, which points to the need for their clinical study for further use as antiviral drugs.

SYNTHESIS OF FAVIPIRAVIR AND ITS DERIVATIVES

Classical synthetic approaches to the production of favipiravir are described in detail in three recent reviews by Y. Titova [61], N. Al Bujug [62], and W. Hu [63].

The first version of favipiravir synthesis was patented and then published by Y. Furuta et al. from Toyama Chemical Company (*Fig. 5*) [64]. The starting 3-aminopyrazine-2-carboxylic acid (**6**) was first esterified and then brominated to yield aminocarboxylate (**7**). The formation of aminopyrazine (**8**) using an expensive Pd_2/diphenylphosphino-binaphthyl (BINAP) catalyst occurred with a low yield of 43%. The second bottleneck of this technology was the use of Olah's reagent (HF/Py) to introduce the F atom into position 6 of the base. The overall yield of favipiravir did not exceed 1%. This technology is very difficult to scale-up.

Another route of favipiravir synthesis was proposed by the same authors in 2001 (*Fig. 6*) [65].

The starting compound in that synthesis was the available aminomalonic acid diethyl ester (**9**) that was

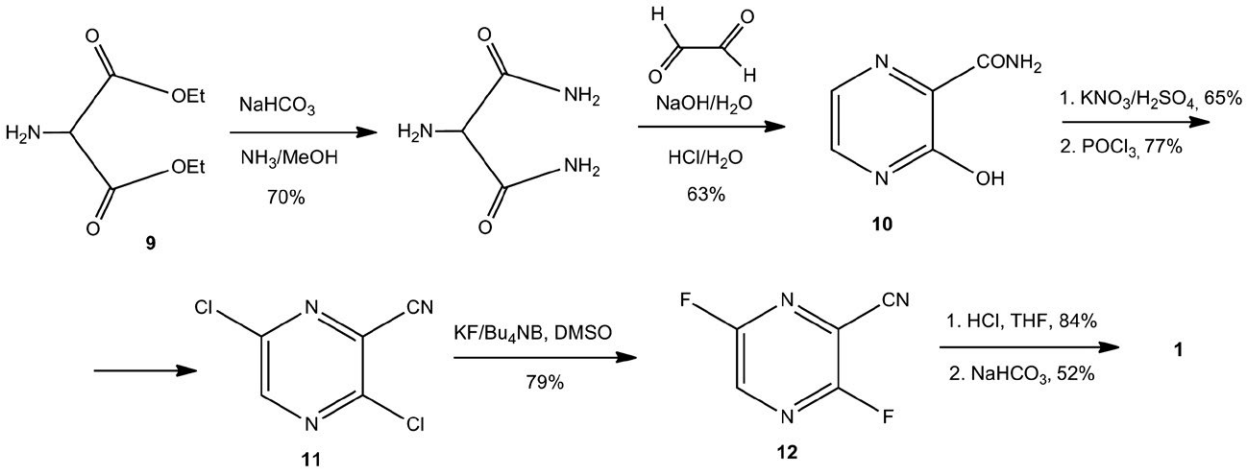

Fig. 6. Improved synthesis of favipiravir (**1**) following the Y. Furuta strategy (Toyama Company)

Fig. 7. Modified version of the synthesis of favipiravir (**1**) following the Nippon Soda & Toyama Company strategy (2011)

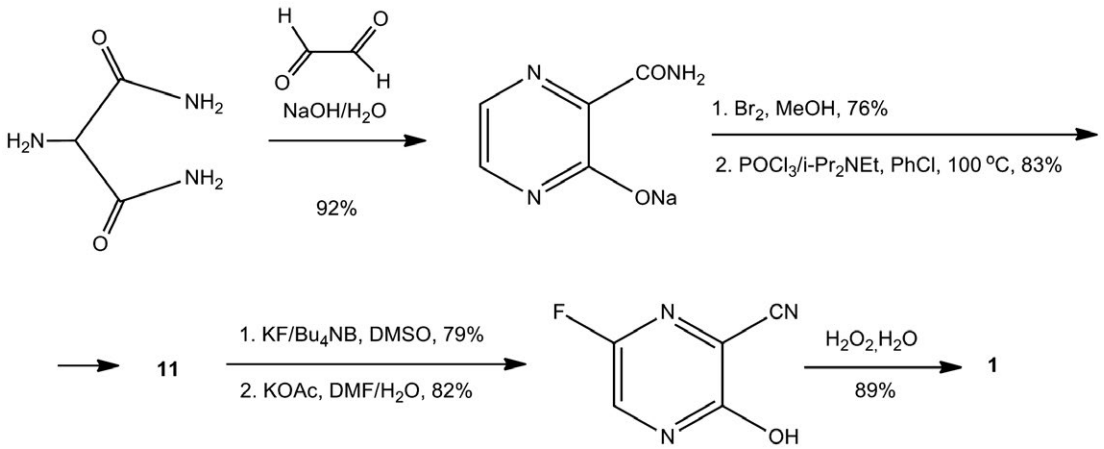

Fig. 8. Synthesis of favipiravir (**1**) according to the Liu Feng procedure

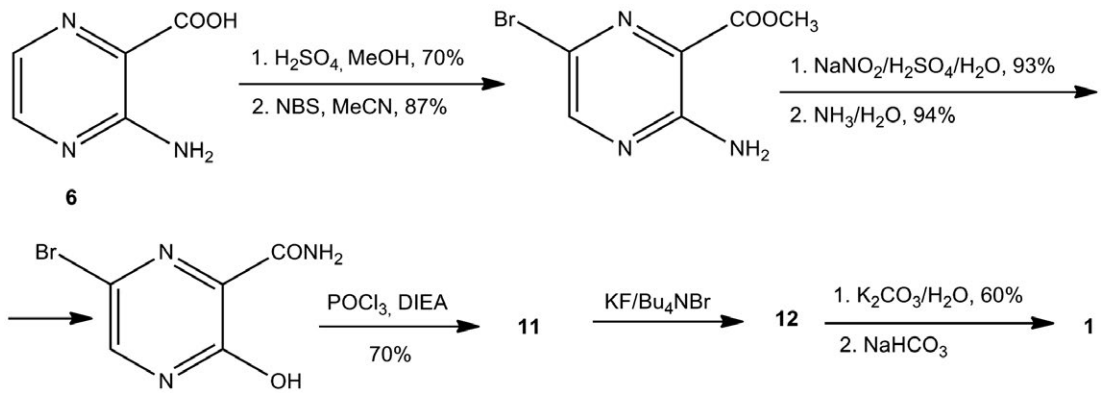

converted into 3-hydroxypyrazine-2-carboxamide (**10**) in two steps. The latter was converted into favipiravir (**1**) in a series of consecutive transformations of functional groups. The overall yield of the product was 17%.

A modified version of the latter synthesis of favipiravir was developed by Toyama in collaboration with Nippon Soda Corporation [66, 67] (*Fig. 7*). Using this method, it was possible to synthesize favipiravir with an overall yield of 33%.

The fourth version of favipiravir synthesis was proposed by Liu Feng et al. in 2017 [68] (*Fig. 8*). All intermediate products were purified by crystallization; the last step was performed in one pot; fa-

Fig. 9. Synthesis of 6-fluoro-3-hydroxypyrazine-2-carboxamide (**1**) according to the Zhang strategy

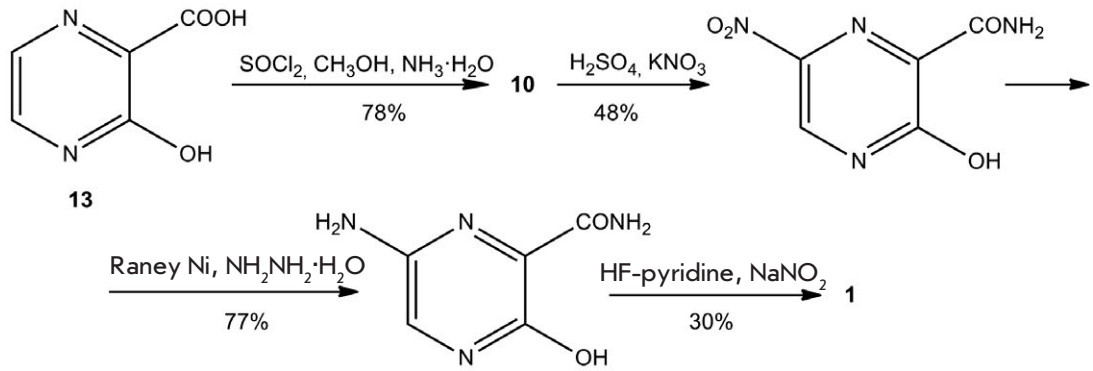

Fig. 10. Synthesis of favipiravir according to the Xie method (2019). NCS – N-chlorosuccinimide, TSA – *p*-toluenesulfonamide

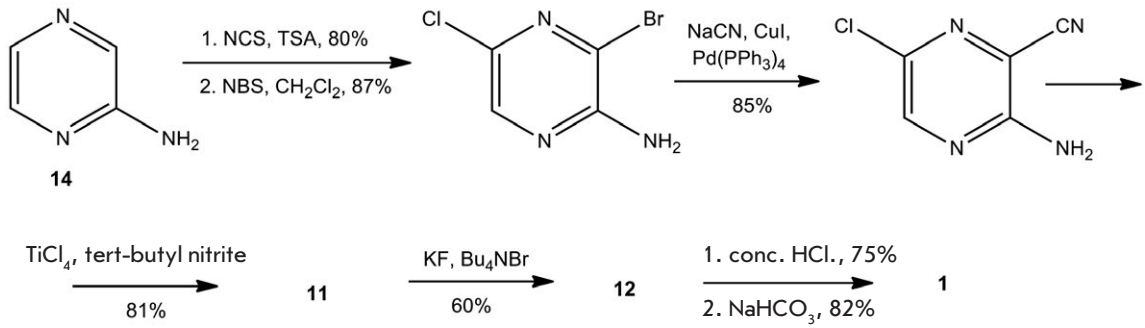

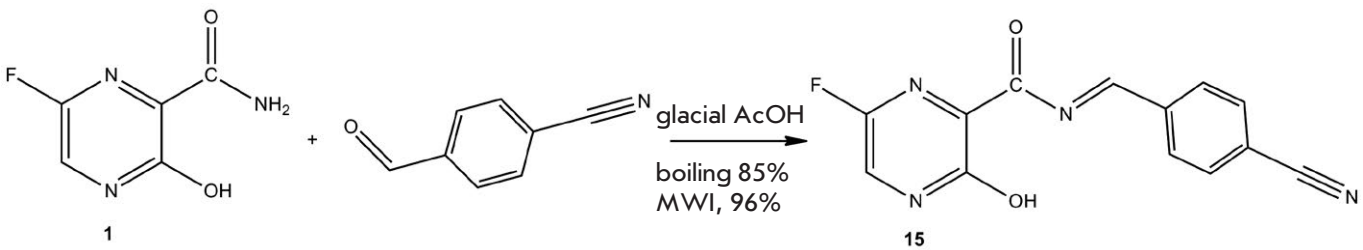

Fig. 11. Synthesis of the 4-cyanobenzylidene analog (**15**) of favipiravir. MWI – microwave irradiation

vipiravir (**1**) was easily isolated by recrystallization. However, this synthesis uses a large amount of phosphorus oxychloride, which constitutes a problem for the scaling up of the process, acting as an environmental pollution factor.

In addition, 3,6-dichloropyrazine-2-nitrile (**11**) is a strong allergen that causes skin irritation. Because of these factors, Liu Feng's technology was not scaled up to industrial production of favipiravir.

Favipiravir can be produced by the four-step method, proposed by Zhang et al., from commercially available 3-hydroxypyrazine-2-carboxylic acid (**13**) through amidation, nitration, reduction, and fluorination (*Fig. 9*) [69].

Another approach to favipiravir synthesis was proposed by Xie et al. [70]. This approach was to produce T-705 from inexpensive and widely available 2-aminopyrazine (**14**). A four-step synthesis of an intermediate compound, 3,6-dichloropyrazine-2-carbonitrile (**11**), was developed, which did not require the use of $POCl_3$ and afforded a good yield of the product (*Fig. 10*).

In 2021, synthesis of (E)-N-(4-cyanobenzylidene)-6-fluoro-3-hydroxypyrazine-2-carboxamide ((**15**), Cyanorona-20) was reported [71] (*Fig. 11*). The authors claimed it was the first selective SARS-CoV-2 RdRp inhibitor 209-fold more efficient than favipiravir *in vitro* (EC_{50} = 0.45 μM, $EC_{50\ (T\text{-}705)}$ = 94.09 μM).

Pre-synthesis computational studies predicted that compound (**15**) may act as an inhibitor of SARS-CoV-2 RdRp through the formation of riboside-5'-triphosphate via the mechanism described for favipira-

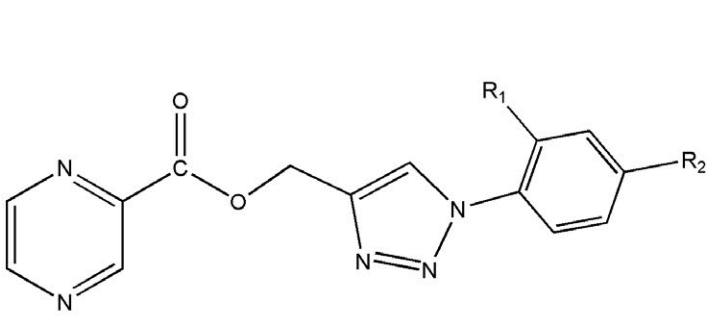

16

	IC_{50} мМ	CC_{50} мМ	$SI=CC_{50}/IC_{50}$
a: R^1=H, R^2= OMe	0.120	0.378	3.150
b: R^1=H, R^2= NO_2	0.477	4.916	10.306
c: R^1=Cl, R^2= H	0.952	3.508	3.685

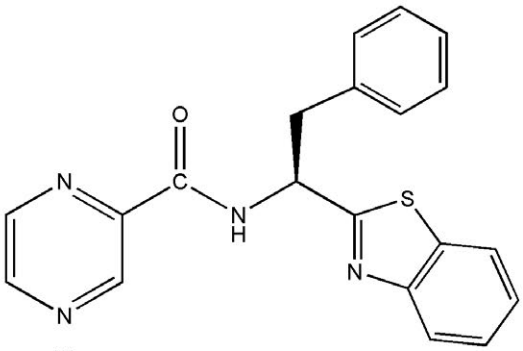

17

	IC_{50} мМ	CC_{50} мМ	$SI=CC_{50}/IC_{50}$
17	0.364	1.396	3.837
T-705	1.382	5.262	3.808

Fig. 12. Pyrazine-triazole (**16**) and pyrazinebenzothiazole (**17**) analogs of favipiravir, which exhibit antiviral activity against SARS-CoV-2

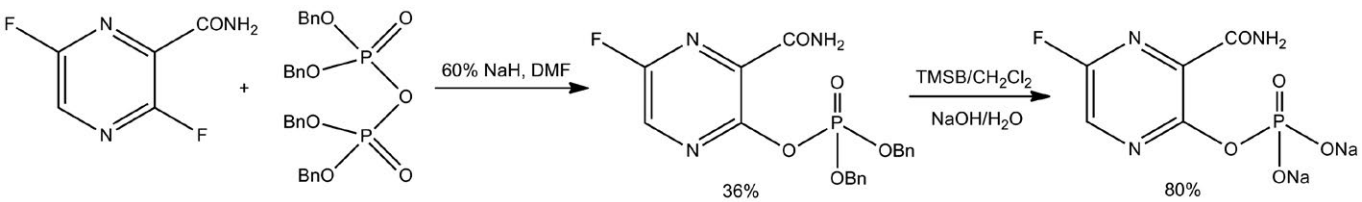

Fig. 13. Synthesis of favipiravir phosphate

vir. In addition, the cyano group is a zincophore; i.e., it can be a carrier of zinc ions, reducing its intracellular concentration. Zn^{2+} is a SARS-CoV-2 RdRp cofactor, and a decrease in its concentration drastically affects RdRp activity. The lipophilic benzylidene moiety of Cyanorona-20 promotes better transfer through the cytoplasmic membrane of the cell. However, the paper failed to report data on any changes in the solubility of the base (**15**) compared to that of T-705; it only stated that the results of Cyanorona-20 aqueous dissolution testing were excellent [71].

There were attempts to synthesize new analogs of 2-pyrazinecarboxamide to enhance antiviral activity against SARS-CoV-2 [72]. A series of seven pyrazine-triazole (**16**) and 11 pyrazine-benzothiazole (**17**) heterocyclic bases was synthesized. *Figure 12* shows analogs of favipiravir (**1**) with comparable or better antiviral properties.

An attempt was made to improve the solubility and bioavailability of favipiravir by a synthesis of its phosphate (*Fig. 13*) [73]. However, no data was offered on the antiviral activity of the produced compounds.

Another approach to improving the solubility of favipiravir was used by a group of Japanese researchers [74]. They tried to solubilize poorly soluble favipiravir using counterions of ethyl esters of L-proline (L-Pro-Et+) and beta-alanine (Beta-Ala-Et+), choline chloride, and tetramethylammonium hydrochloride (*Fig. 14*). The method is now used in pharma to produce poorly soluble active pharmaceutical substances or proteins balanced with various counterions [75]. According to NMR, the stoichiometric ratio of T-705 and the counterions was 1 : 1. The produced ionic liquid-based formulation of favipiravir were amorphous (according to X-ray diffraction analysis) and had significantly better water solubility compared with that of the original crystalline favipiravir: the choline counterion was characterized by the best solubility (739 mg/mL for Cho-T-705 versus 7.0 mg/mL for T-705, *Fig. 14*).

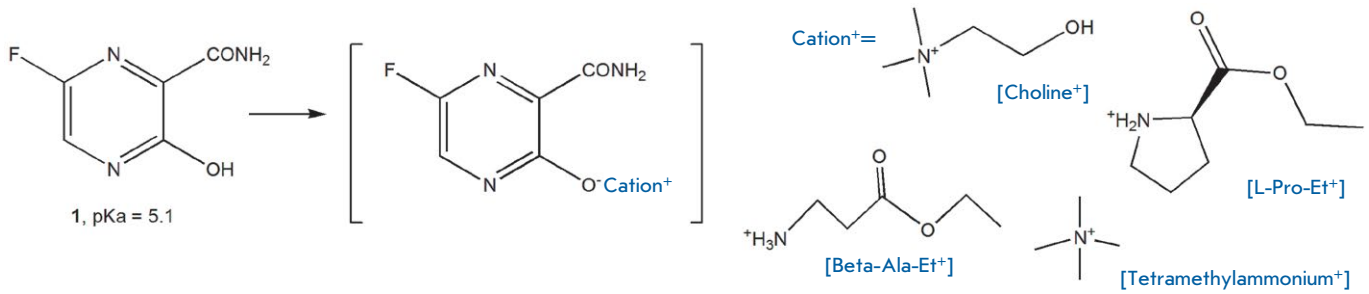

Fig. 14. Ionic liquid-based formulation of favipiravir (**1**)

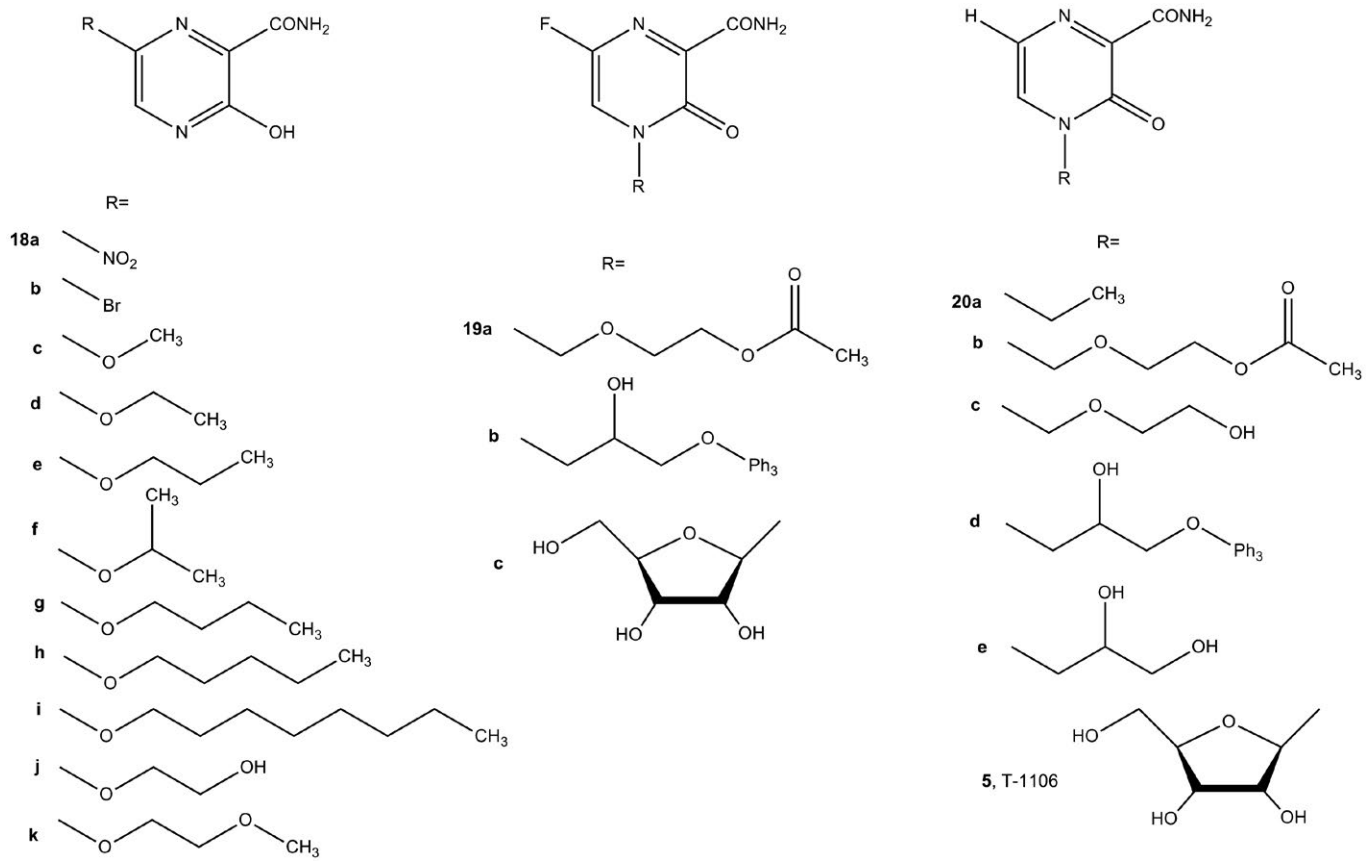

Fig. 15. Favipiravir analogs for studying activity against the Zika virus

In formulations *in vivo* experiments, all ionic liquid-based formulation of favipiravir had better pharmacokinetic and pharmacodynamic characteristics compared with those of the original favipiravir [74].

There have been attempts to synthesize effective drugs based on 3-oxopyrazine-2-carboxamide against the Zika virus (*Fig. 15*) [76]. 3-Hydroxypyrazine-2-carboxamide and favipiravir displayed antiviral activity against the Zika virus in the Vero cell line. T-1105 significantly reduced the level of cell death (EC_{50} = 97.5 ± 6.8 μmol/L).

Testing of analogs (**18**)–(**20**) showed very low (CC_{50} = 200–300 μmol/L for compounds (**18f–i**)) or no (CC_{50} >1000 μmol/L) antiviral activity [76].

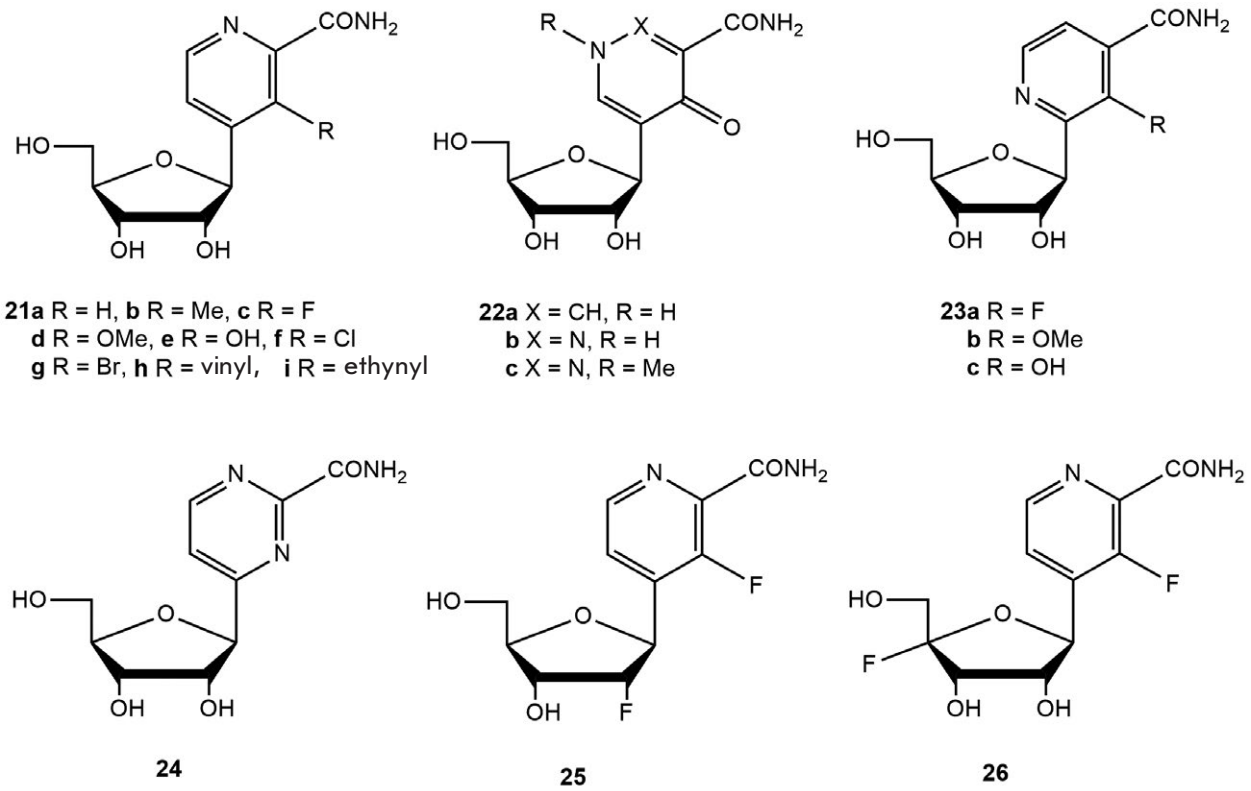

Fig. 16. C-nucleoside derivatives of pyridine, pyridazine, and pyrimidine

Wang et al. [77] synthesized a series of pyridine, pyridazine, and pyrimidine C-nucleosides, analogs of favipiravir (*Fig. 16*).

The antiviral activity of all the compounds was studied in MDCK cells infected with the influenza virus A/WSN/33 (H1N1). Compound (**21e**) exhibited the highest activity (EC_{50} = 1.3 μmol/L). At the same time, this compound had high cytotoxicity: the 50% cytotoxic concentration (CC_{50}) was 2.0 μmol/L. The antiviral activity of compound (**21c**) was comparable to that of T-705: the EC_{50} was 1.9 μmol/L, and the CC_{50} was more than 400 μmol/L. The remaining C-nucleosides showed low or weak antiviral activity; even compounds (**25**) and (**26**) with a modification at the positions of the 2'-OH and 4'-H-group of ribose had low activity [77].

The synthesis of acyclic nucleotide analogs of favipiravir as potential inhibitors of hypoxanthine-guanine-xanthine phosphoribosyltransferase (HGXPRT) from malarial *Plasmodium falciparum* was proposed [78]. HGXPRT catalyzes the magnesium-dependent synthesis of nucleoside 5'-monophosphates from purine bases (guanine or hypoxanthine). The acyclic nucleotide analogs (**27**) and (**28**) were synthesized from favipiravir via the Mitsunobu reaction. Alkylation occurred at positions N^4 or O^3 of the heterocyclic ring to form the N- (**28**) or O-regioisomer (**27**) (*Fig. 17*).

O-alkylated acyclic nucleotide derivatives of favipiravir (**27**) were produced according to the scheme shown in *Fig. 18*. Unfortunately, the N-alkylated derivatives of T-705 were unstable under deprotection conditions.

Investigation of the O-alkylated acyclic nucleotide derivatives of favipiravir as inhibitors of human HGPRT and *Pf*HGXPRT showed that none of the compounds inhibited any enzyme in the concentration range of 100 to 150 μmol/L. Acyclic nucleotide derivatives of guanine or hypoxanthine with the same substituents are efficient inhibitors of the HGPRT and *Pf*HGXPRT enzymes, with the inhibition constant ranging from 0.07 to 5 μmol/L [78].

Synthesis of nucleoside-based prodrugs is a modern approach to the production of new antiviral

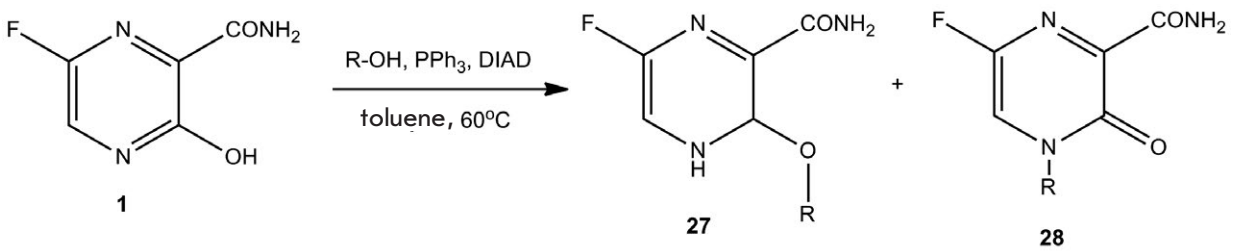

Fig. 17. General scheme of favipiravir alkylation under Mitsunobu reaction conditions. R-OH –hydroxyalkyl phosphonates

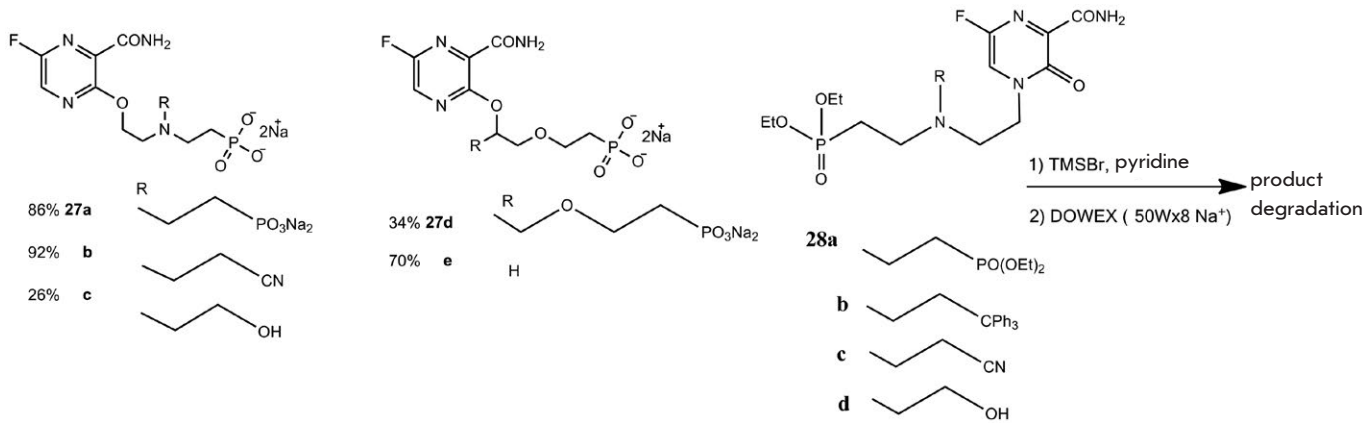

Fig. 18. Acyclic nucleotide derivatives of favipiravir

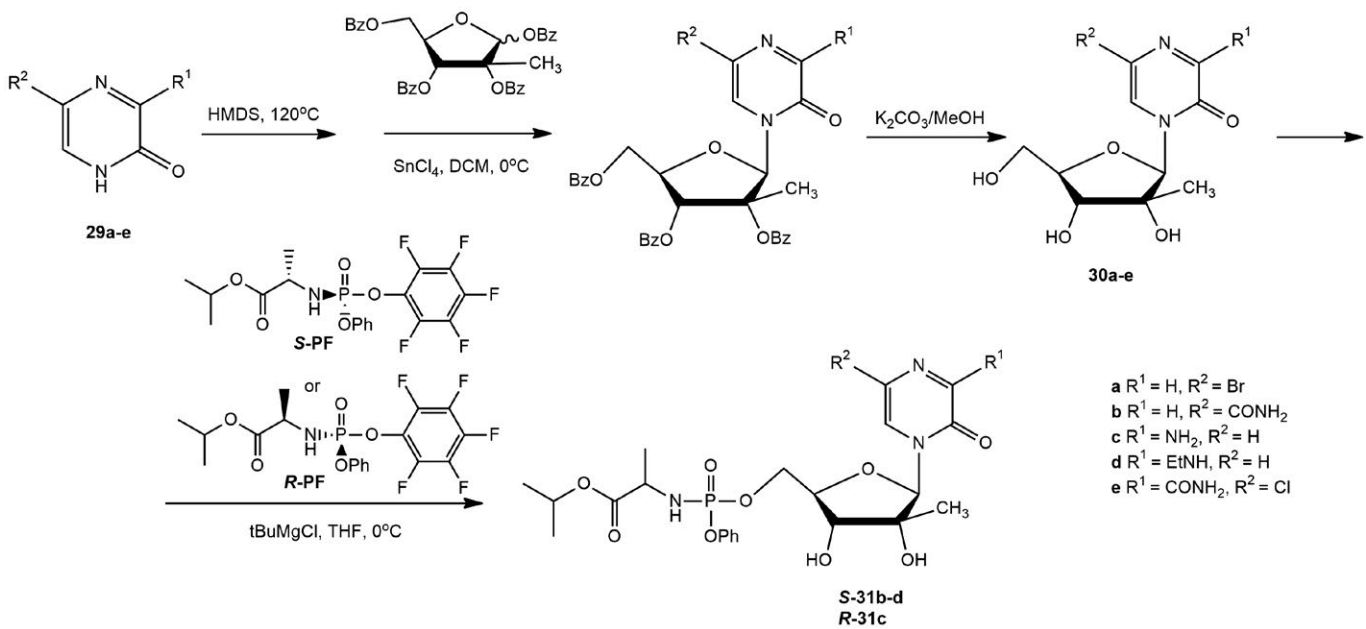

Fig. 19. Synthesis of 3-oxo-4-(2-C-methyl-β-*D*-ribofuranosyl)-pyrazines and their 5′-phosphoramidate prodrugs

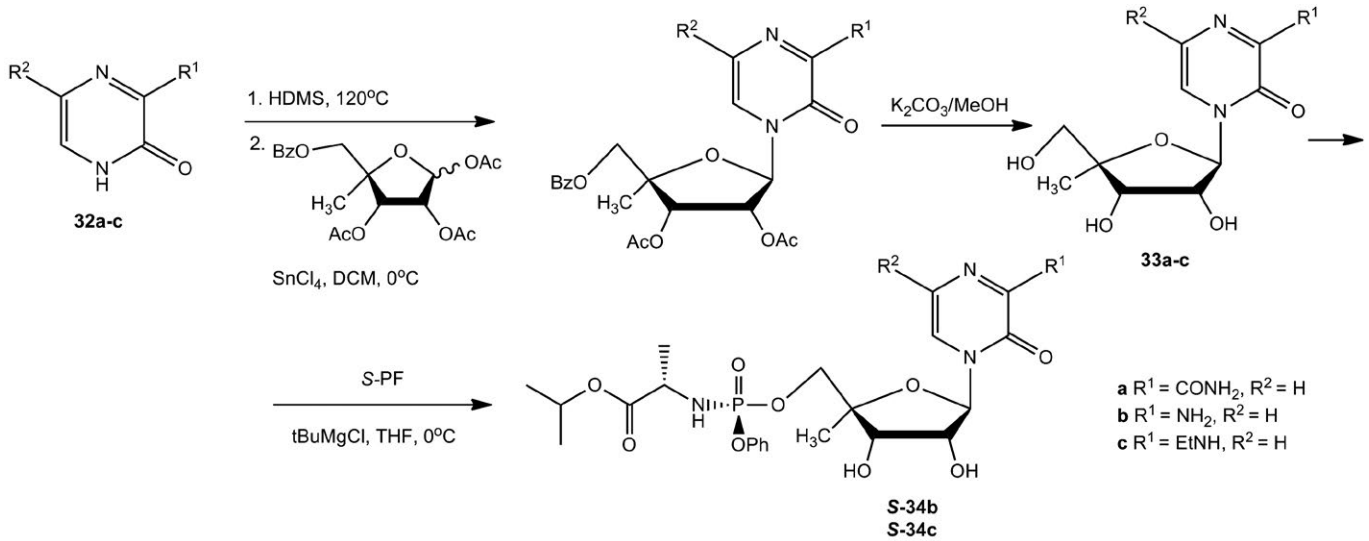

Fig. 20. Synthesis of 3-oxo-4-(4-C-methyl-β-*D*-ribofuranosyl)-pyrazines and their 5′-phosphoramidate prodrugs

Fig. 21. Synthesis of 3-oxo-4-(β-*D*-ribofuranosyl)-2-pyrazinecarboxamide. BSA – N,O-bis(trimethylsilyl) acetamide

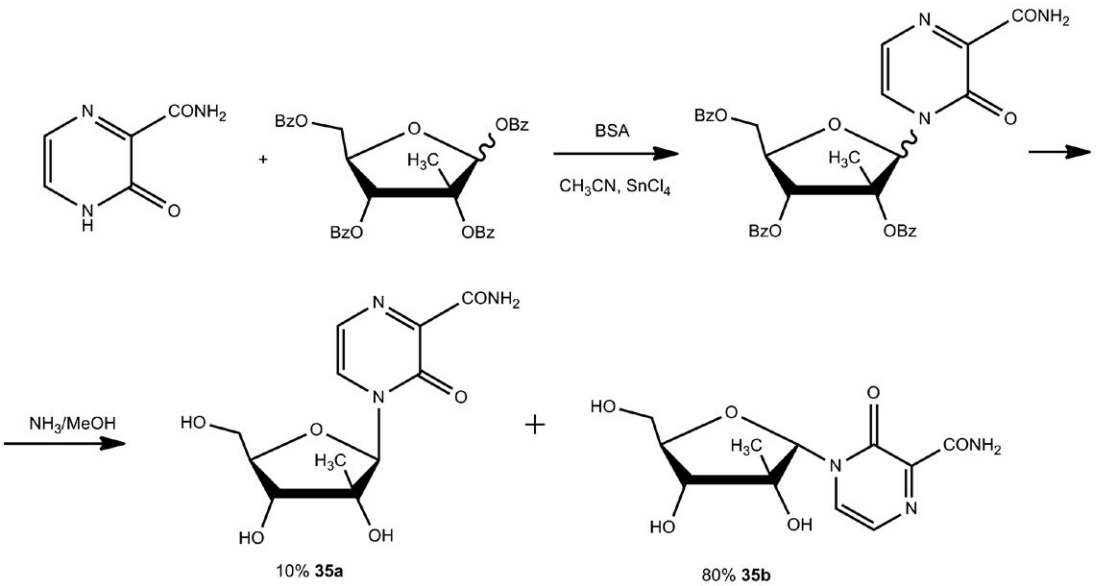

drugs [79]. Synthesis of several pyrazine nucleosides and their phosphoramidate prodrugs was described in (*Fig. 19*) [80]. The activity of these nucleosides against the hepatitis C virus (HCV) was evaluated. 3-oxo-4-(2-C-methyl-β-*D*-ribofuranosyl)-pyrazines and their 5'-phosphoramidate prodrugs were synthesized using the silyl method by glycosylation of the bases (**29a–e**) with 1,2,3,5-tetra-O-benzoyl-2-C-methyl-β-D-ribofuranose in the presence of tin tetrachloride ($SnCl_4$). After removal of benzoyl (Bz) protecting groups, phosphoramidate derivatives were synthesized by reacting with *S*-PF or the (*R*)-2-((*R*)-(2,3,4,5,6-pentafluorophenoxy)phenoxyphosphorylamino) propionic acid isopropyl ester (*R*-PF).

3-Oxo-4-(4-C-methyl-β-D-ribofuranosyl)-pyrazines and their 5'-phosphoramidate prodrugs were similarly synthesized from the corresponding bases (*Fig. 20*).

In vitro investigation of the activity of synthesized compounds against HCV showed that among the compounds (**30a–d**), only (**30c**) demonstrated a low inhibition rate of 22.3% at a concentration of 100 μmol/L. The ethylamine group at position C3 of the heterocyclic ring caused a loss of the antiviral activity of compound (**30d**) and its (*S*)-phosphoramidate (**S-31d**).

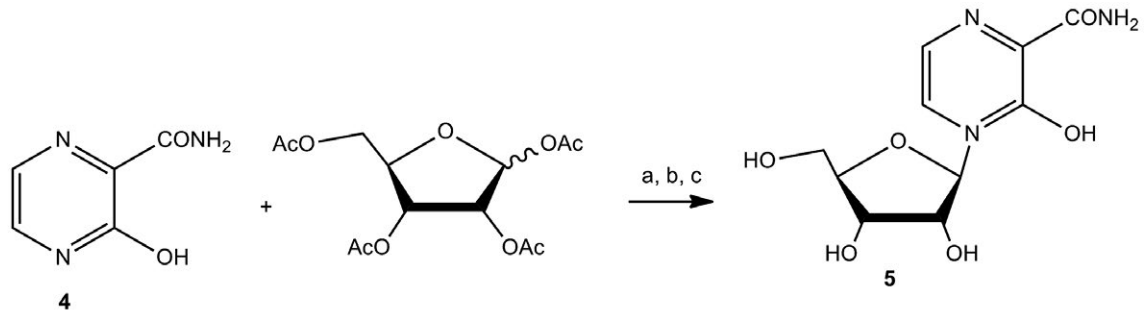

Fig. 22. Synthesis of 3-oxo-4-(β-*D*-ribofuranosyl)-2-pyrazinecarboxamide (***5***). a) 1,2,3,5-tetra-O-acetyl-β-*D*-ribofuranose, N,O-bis(trimethylsilyl)acetamide, acetonitrile, 30 min, rt; b) trimethylsilyl trifluoromethanesulfonate, acetonitrile, 44 h, rt; c) methanol, water, triethylamine, 6 h, rt

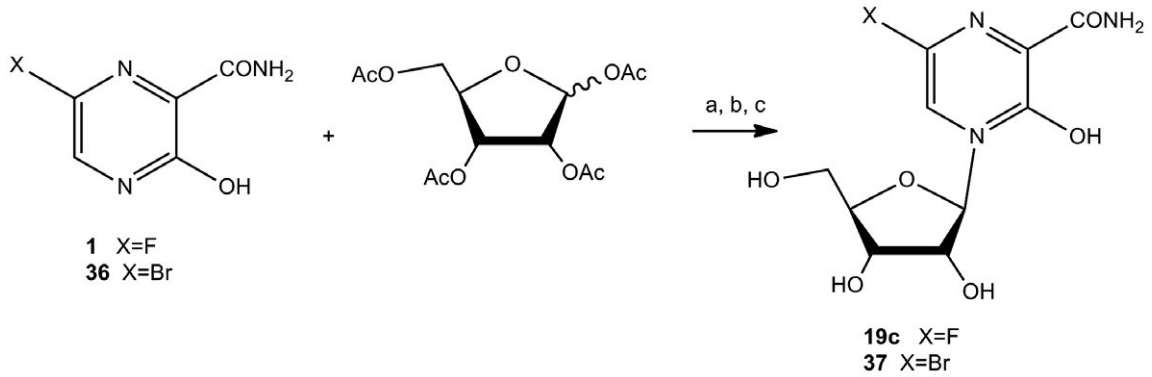

Fig. 23. Synthesis of 6-fluoro-3-oxo-4-(β-*D*-ribofuranosyl)-2-pyrazinecarboxamide (**19c**) and 6-bromo-3-oxo-4-(β-*D*-ribofuranosyl)-2-pyrazinecarboxamide (**37**). a) hexamethyldisilazane, $(NH_4)_2SO_4$, 140°C; b) $SnCl_4$, acetonitrile, rt; c) Bu_2SnO, methanol, 80°C

Compound (**30e**) showed good activity with an EC_{50} value of 7.3 μmol/L; however, attempts to convert it to a phosphoramidate prodrug failed [80].

It was presumed that changing the position of the methyl group in the ribose moiety (compounds (**33a–c**)) may reduce their cytotoxicity. However, among these compounds, only the (*S*)-isomer phosphoramidate prodrug (**S-34b**) was not cytotoxic at a concentration of 100 μmol/L, but it showed weak activity (EC_{50} = 19.5 μM) [80].

The nonfluorinated base T-1105 was used to synthesize 3-oxo-4-(2-C-methyl-β-D-ribofuranosyl)-2-pyrazinecarboxamide (*Fig. 21*) as an α/β-anomeric mixture. After ammonolysis of the benzoyl (Bz) protecting groups, the desired β-anomeric product (**35a**) was isolated at a yield of 10% only and the α-anomer (**35b**) was also isolated at a yield of 58% [81].

Unfortunately, the nucleosides (**35a**) and (**35b**) showed neither antiviral activity against RNA viruses nor cytotoxicity *in vitro* at concentrations up to 100 μmol/L [81].

Typically, classical chemical glycosylation methods are used in the synthesis of modified nucleosides and nucleotides based on T-705 and T-1105. For example, 3-oxo-4-(β-*D*-ribofuranosyl)-2-pyrazinecarboxamide (**5**) (*Fig. 22*) is synthesized following the Vorbruggen procedure by treating 3-hydroxypyrazine-2-carboxamide (T-1105) with 1,2,3,5-tetra-O-acetyl-β-*D*-ribofuranose in anhydrous acetonitrile (CH_3CN) in the presence of N,O-bis(trimethylsilyl)acetamide at room temperature, followed by the addition of trimethylsilyl trifluoromethanesulfonate. The yield of the desired product in this procedure is 55% [82].

Chemical synthesis of 6-fluoro-3-oxo-4-(β-D-ribofuranosyl)-2-pyrazine-carboxamide (**19c**) (*Fig. 23*) can be performed by treating C6-substituted 3-hydroxypyrazine-2-carboxamide with ammonium sulfate $(NH_4)_2SO_4$ in hexamethyldisilazane at 140°C.

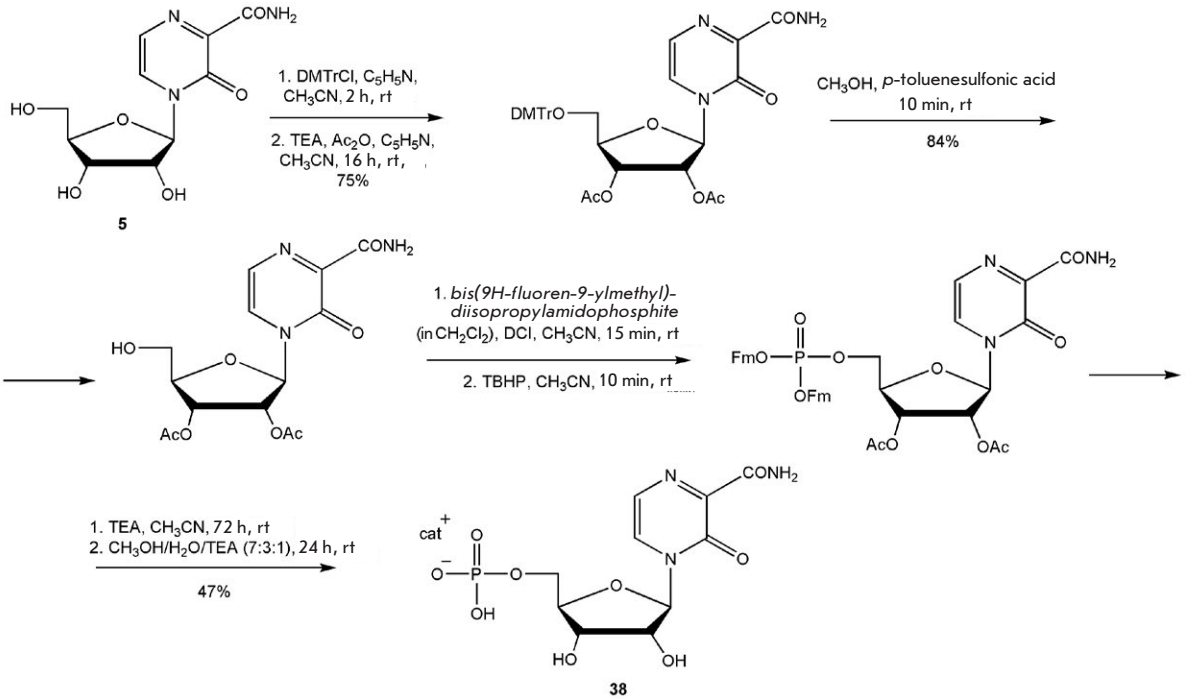

Fig. 24. Synthesis of T-1105 riboside phosphate. DCI – dicyanoimidazole; TEA – triethylamine

The resulting silylated pyrazinecarboxamide is reacted with peracylated ribofuranose in the presence of tin tetrachloride ($SnCl_4$). The yield of pure nucleoside after chromatographic purification is 40%. Transfer of optimized conditions for the synthesis of 6-fluoro-3-oxo-4-(β-D-ribofuranosyl)-2-pyrazinecarboxamide to the 6-bromo-substituted analog of favipiravir provided compound (**37**) in a yield of 68% [82].

In 2018, J. Huchting presented a scheme for the synthesis of T-1105 riboside phosphate (**38**) (*Fig. 24*) and a similar method for the synthesis of the favipiravir nucleotide [83]. Huchting et al. were able to chemically synthesize nucleoside 5'-monophosphate, diphosphate, and triphosphate of T-1105.

The most efficient route for the synthesis of 3-oxo-4-(β-*D*-ribofuranosyl-5'-phosphate)-2-pyrazinecarboxamide (**33**) was by phosphorylation of compound (**5**) with preliminary protection of the 2'- and 3'-OH groups of ribose. The yield in the target compound (**38**) was 47% [83].

Nucleoside 5'-diphosphate and triphosphate of T-1105 were prepared by sequential two-step synthesis using fluorenylmethyl (Fm) protecting groups (*Fig. 25*).

To improve lipophilicity and screen negatively charged groups of the T-1105 and T-705 nucleotides, depot forms of *cyclo*Sal-pronucleotides, Di*PP*ro, and Tri*PPP*ro were synthesized (*Fig. 26*). *Cyclo*Sal-pronucleotides are prodrugs; controlled release of active nucleotides occurs in a pH-dependent manner. They were produced using phosphoramidite synthesis. Activation of the Di*PP*ro and Tri*PPP*ro prodrugs includes a major and minor pathway. The major pathway is activation of these compounds by esterases and subsequent efficient release of nucleotides [83].

The minor metabolic pathway involves hydrolytic cleavage of phosphoanhydride in the pronucleotide, which leads to the formation of an undesired nucleotide [83]. The antiviral activity of these compounds was tested in MDCK and MDCK-TG^{res} (HGPRT-deficient cell line) cells using two influenza strains: A/X-31 (A/H3N2 subtype) and B/Ned/537/05. The cytotoxicity of these compounds was evaluated in uninfected cells. Compound (**36**) exhibited the highest antiviral activity and minimal toxicity. The mean EC_{50} was 0.91 μmol/L in MDCK cells. All Di*PP*ro and Tri*PPP*ro compounds retained antiviral activity in MDCK-TG^{res} cells. For example, the mean EC_{50}

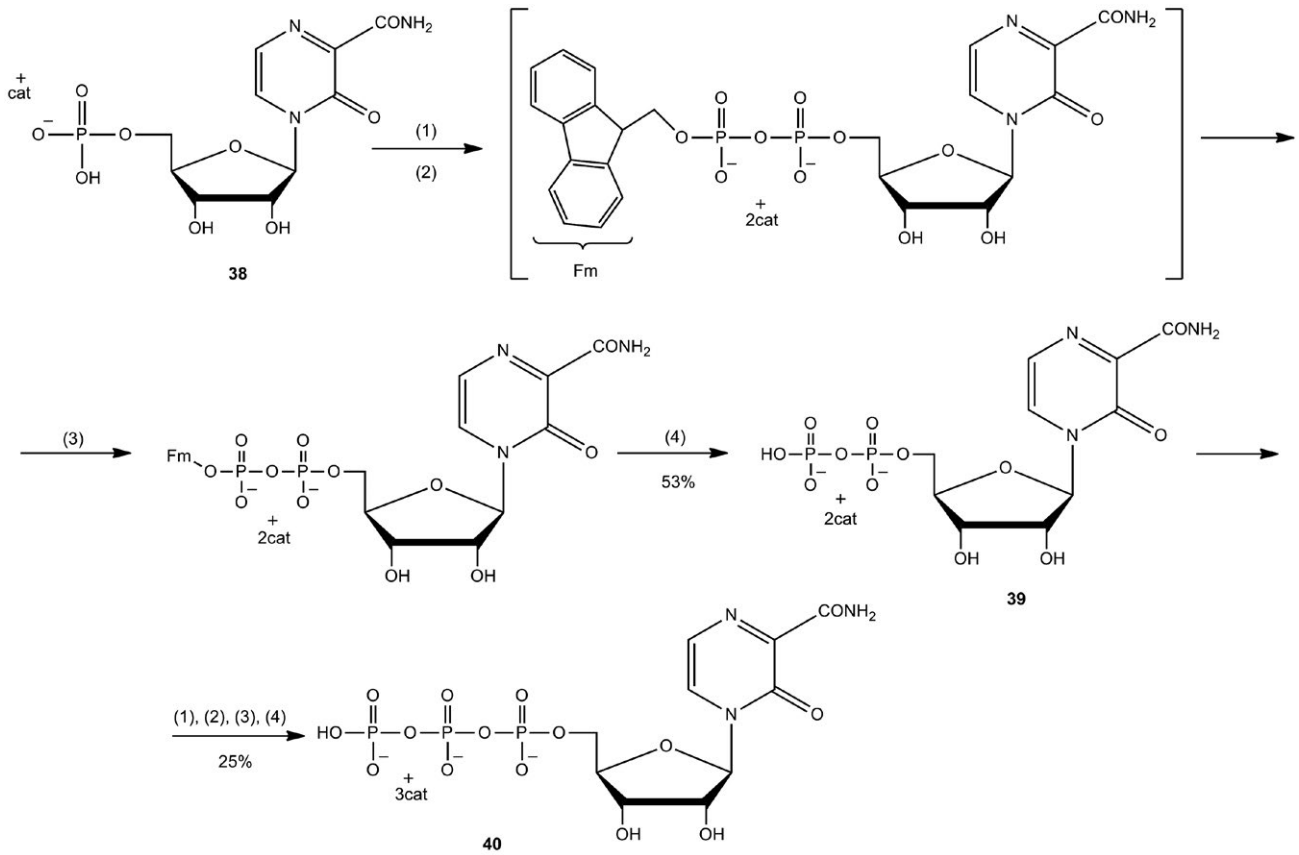

Fig. 25. Synthesis of 3-oxo-4-(β-*D*-ribofuranosyl-5′-diphosphate)-2-pyrazinecarboxamide (**39**) and 3-oxo-4-(β-*D*-ribofuranosyl-5′-triphosphate)-2-pyrazinecarboxamide (**40**). (1) bis(9H-fluoren-9-ylmethyl)-diisopropylaminophosphoramidite in CH_2Cl_2, dicyanoimidazole, DMF; (2) *tert*-butyl hydroperoxide (TBHP), DMF; (3) TEA, CH_3CN; (4) TEA, H_2O, CH_3CN

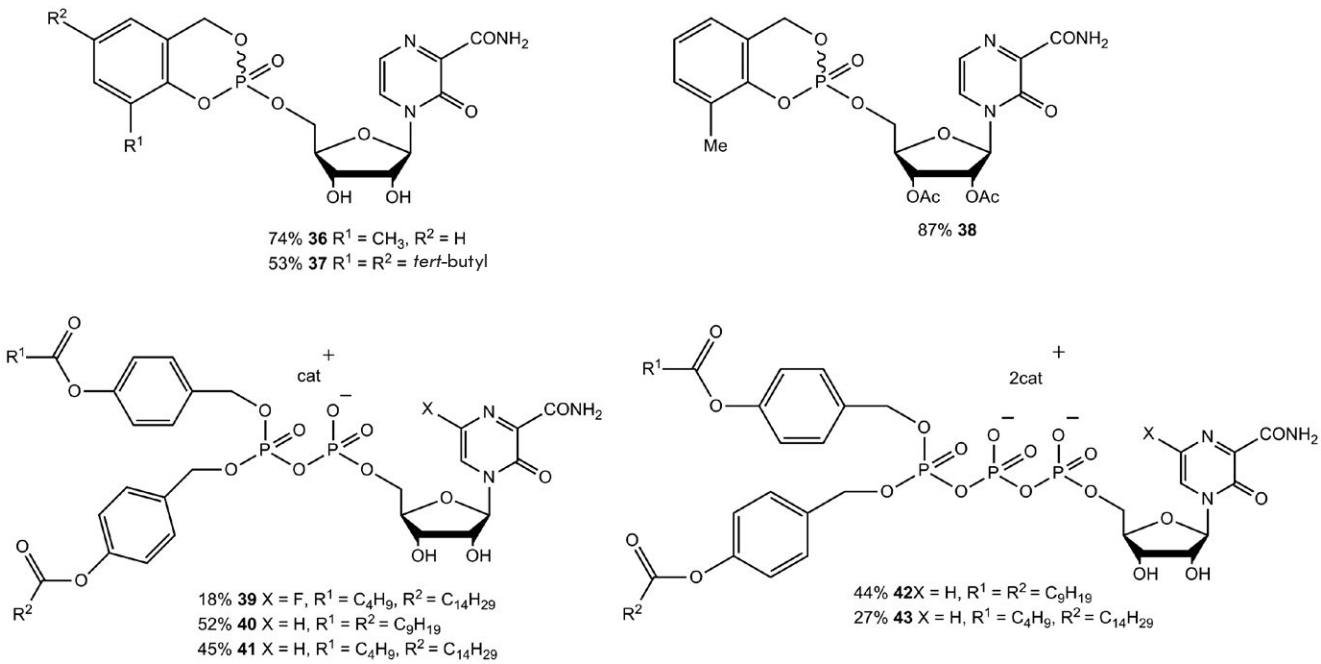

Fig. 26. Structural formulas of *cyclo*Sal pronucleotides (**28**)–(**30**) and Di*PPP*ro and Tri*PPP*ro of compounds (**31**)–(**35**)

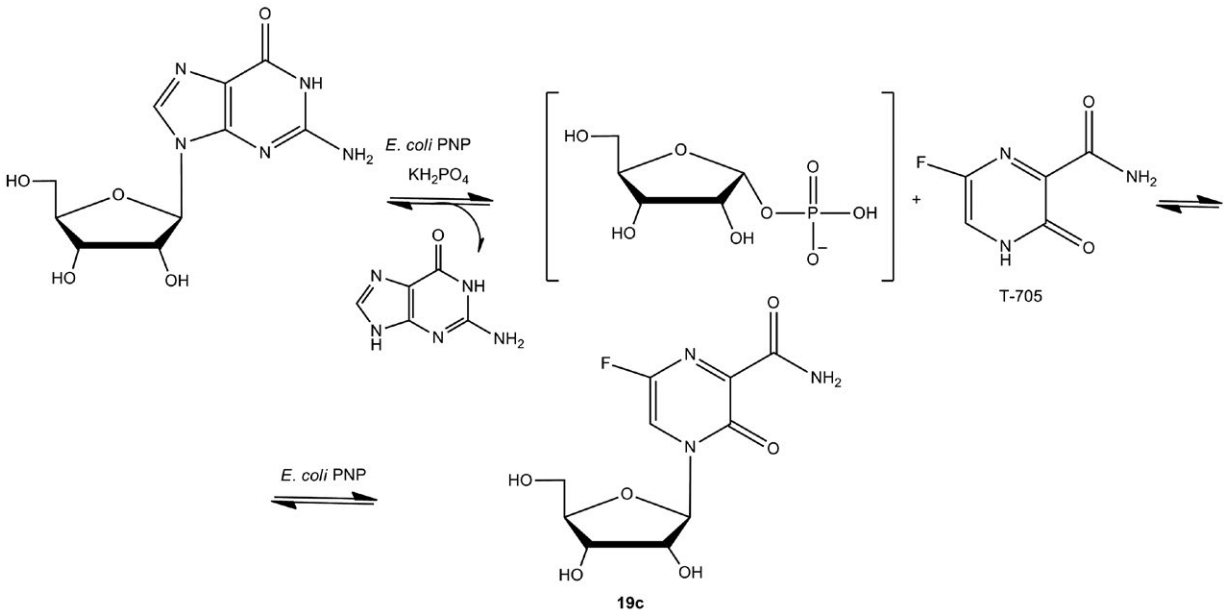

Fig. 27. Enzymatic synthesis of T-705 riboside

value for compound (**36**) in MDCK-TG^{res} cells was 0.80 μmol/L [83].

Obviously, the development of simple and efficient enzymatic methods for the synthesis of modified nucleosides and nucleotides based on 3-hydroxypyrazine-2-carboxamide and its 6-fluoro-substituted analog is extremely important.

To date, there exists only one short communication on the enzymatic synthesis of modified nucleosides based on substituted 3-hydroxypyrazine-2-carboxamides using *E. coli* purine nucleoside phosphorylase (PNP) [84]. The efficiency in the transfer of the T-705 base to the ribose moiety reached 43% in 4 h (*Fig. 27*). However, the study did not provide the yield and spectral characteristics of the product.

Ribosyltransferases are involved in the formation of all C-N-glycosidic bonds in nucleoside monophosphates via the *de novo* biosynthetic pathway. Purine phosphoribosyltransferases catalyze a reversible transfer of the 5-phosphoribosyl group from PRPP to nitrogen at position 9 in 6-amino- or 6-oxopurines in the presence of Mg^{2+} to form the corresponding ribose-5'-monophosphate [85].

According to substrate specificity, there are 6-aminopurine and 6-oxopurine purine phosphoribosyltransferases, (APRTs) and (HPRTs, HGPRTs, etc.), respectively. APRTs are strictly specific to 6-aminopurines, such as adenine, 2-fluoroadenine, or 2-chloroadenine. 6-oxopurine PRTs can recognize various 6-oxopurines, such as hypoxanthine, guanine, xanthine, and other 6-oxo- and 6-mercaptopurine analogs [85].

The active metabolite of favipiravir and 3-hydroxypyrazine-2-carboxamide is their ribose-5'-triphosphate form that is involved in the suppression of the activity of RNA viruses. Naesens et al. [21] found that in the cell, human HGPRT first phosphorylates T-705 into 6-fluoro-3-oxo-4-(β-*D*-ribofuranosyl-5'-phosphate)-2-pyrazinecarboxamide (T-705-RMP) and T-1105 into 3-oxo-4-(β-*D*-ribofuranosyl-5'-phosphate)-2-pyrazinecarboxamide (T-1105-RMP) (*Fig. 28*). However, T-705 and T-1105 show low affinity for the HGPRT active site under both synthesis and intracellular phosphoribosylation conditions. Human APRT was found to catalyze T-705 and T-1105 phosphoribosylation 40-fold less efficiently than HGPRT under similar conditions. In addition, these researchers found that T-705 and T-1105 were poor substrates for human PNP [21].

An extract of MDCK cells is known to be used to assess the metabolic activation profiles of favipiravir and 3-hydroxypyrazine-2-carboxamide [83]. Phosphoribosylation of favipiravir in a MDCK cell extract is less efficient than that of 3-hydroxypyrazine-2-carboxamide. The formation of the T-705-RMP metabolite in the MDCK cell extract upon incubation of T-705 with 5-phosphoribosyl-α-1-pyrophosphate (PRPP) was 35% after 25 h of incubation. The yield of the T-1105-RMP metabolite

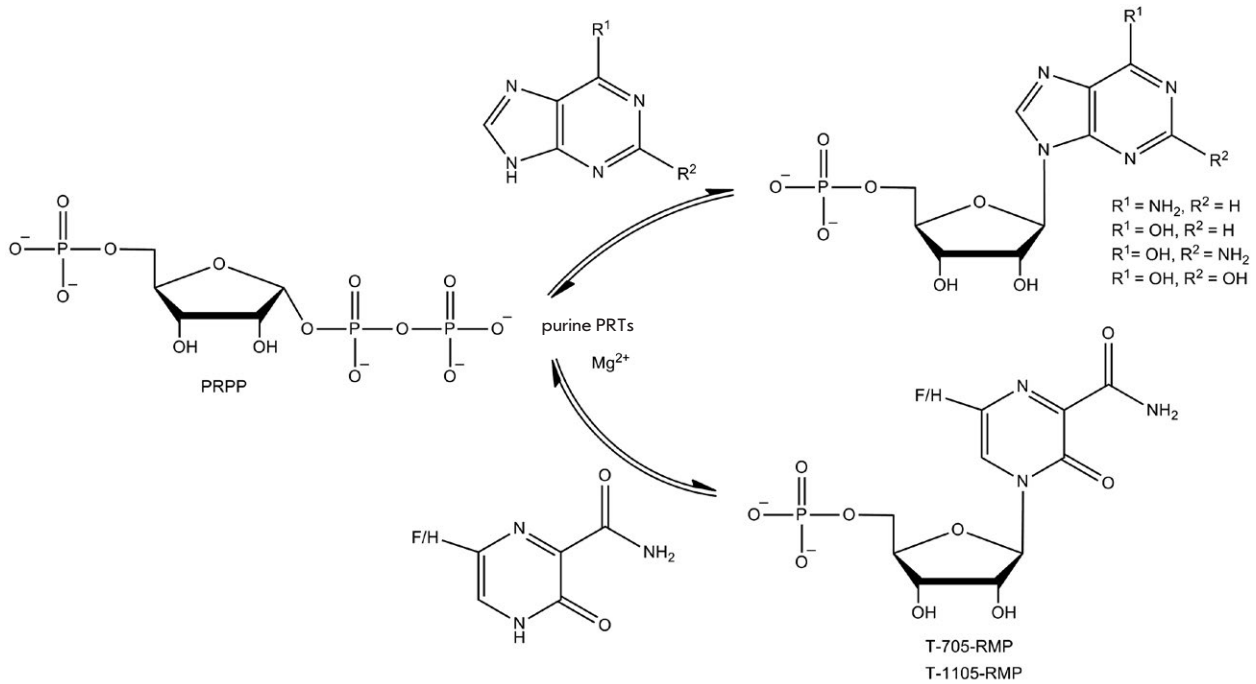

Fig. 28. Enzymatic synthesis of ribose-5′-monophosphates catalyzed by phosphoribosyl transferases (PRTs)

in the MDCK cell extract during the incubation of T-1105 with PRPP was 90% after 19 h of incubation. Further incubation of T-1105-RMP with the MDCK cell extract for 15 h did not result in the formation of either T-1105-RDP or T-1105-RTP, even with the addition of a high concentration of ATP (phosphate donor). However, incubation of T-1105-RDP with a 10-fold higher ATP concentration led to its effective phosphorylation: T-1105-RTP formed 2 min after incubation and remained the main metabolite for the next 2 h.

Single examples of the biosynthesis of pyrazinecarboxamide nucleosides and nucleotides indicate that classical chemical methods remain the main routes for their synthesis.

CONCLUSION

Favipiravir T-705 and some of its structural analogs exert a significant antiviral effect against RNA viruses. However, a high dose load (up to 3.6 g of favipiravir per day in the treatment of COVID-19), poor bioavailability due to low solubility, high systemic toxicity, and the teratogenic activity of the drug encourage researchers to continue synthesizing more and more new structural analogs in an effort to increase the selectivity of the active molecule and reduce its toxicity.

Most likely, the use of the nucleosides of favipiravir and its structural analogs may reduce the dose load on the human body and reduce the toxic effect of the drug. To date, many pyrazinecarboxamide nucleosides modified in the heterocyclic base and carbohydrate moiety have been synthesized. A series of acyclic linear analogs and nucleosides modified in the ribose 5′-hydroxyl group has been produced. However, the efficacy of these compounds in the treatment of human viral infections has yet to be proven.

Therefore, the structural analogs of 1,4-pyrazine-3-carboxamide may become the basis for the development of new selective and highly effective antiviral drugs to be used during viral pandemics and, in some cases, extremely severe viral infections. ●

This study was financially supported by the Russian Science Foundation (project No. 21-13-00429).
The authors declare no conflict of interest.

REFERENCES

1. Woolhouse M., Scott F., Hudson Z., Howey R., Chase-Topping M. // Philosophical Transactions Royal Soc. B-Biol. Sci. 2012. V. 367. № 1604. P. 2864–2871. doi: 10.1098/rstb.2011.0354
2. Carrasco-Hernandez R., Jácome R., López Vidal Y., Ponce de León S. / ILAR J. 2017. V. 58 № 3. P. 343–358. doi: 10.1093/ilar/ilx026
3. Pilkington V., Pepperrell T., Hill A. // J. Virus Eradication. 2020. V. 6(2). P. 45–51. doi: 10.1016/S2055-6640(20)30016-9
4. Kolb V.M. // Progress Drug Res. 1997. V. 48. P. 195–232. doi: 10.1007/978-3-0348-8861-5_8
5. Mahmoud S., Hasabelnaby S., Hammad S., Sakr T. // J. Adv. Pharmacy Res. 2018. V. 2. № 2. P. 73–88. doi: 10.21608/aprh.2018.5829
6. Furuta Y., Takahashi K., Fukuda Y., Kuno M., Kamiyama T., Kozaki K., Nomura N., Egawa H., Minami S., Watanabe Y., et al. // Antimicrob. Agents Chemother. 2002. V. 46. № 4. P. 977–981. doi: 10.1128/AAC.46.4.977-981.2002
7. Furuta Y., Takahashi K., Shiraki K., Sakamoto K., Smee D.F., Barnard D.L., Gowen B.B., Julander J. G., Morrey J. D.// Antiviral Res. 2009. V. 82. P. 95–102. doi: 10.1016/j.antiviral.2009.02.198
8. Furuta Y., Komeno T., Nakamura T. // Proc. Jpn. Acad. Ser. B Phys. Biol. Sci. 2017. V. 93. № 7. P. 449–463. doi: 10.2183/pjab.93.027
9. De Clercq E., Li G. // Clin. Microbial. Rev. 2016. V. 29. № 3. P. 695–747. doi: 10.1128/CMR.00102-15
10. Delang L., Abdelnabi R., Neyts J. // Antiviral Res. 2018. V. 153. P. 85–94. doi: 10.1016/j.antiviral.2018.03.003
11. Furuta Y., Gowen B.B., Takahashi K., Shiraki K., Smee D.F., Barnard D.L. // Antiviral Res. 2013. V. 100. № 2. P. 446–454. doi: 10.1016/j.antiviral.2013.09.015
12. L'Huillier A.G., Abed Y., Petty T.J., Cordey S., Thomas Y., Bouhy X., Schibler M., Simon A., Chalandon Y., van Delden C., et al. // J. Infect. Dis. 2015. V. 212. № 1. P. 1726–1734. doi: 10.1093/infdis/jiv288
13. Sleeman K., Mishin V.P., Deyde V.M., Furuta Y., Klimov A.I., Gubareva L.V. // Antimicrob. Agents Chemother. 2010. V. 54. № 6. P. 2517–2524. doi: 10.1128/AAC.01739-09
14. Kiso M., Takahashi K., Sakai-Tagawa Y., Shinya K., Sakabe S., Le Q.M., Ozawa M., Furuta Y., Kawaoka Y. // Proc. Natl. Acad. Sci. USA. 2010. V. 107. № 2. P. 882–887. doi: 10.1073/pnas.0909603107
15. Watanabe T., Kiso M., Fukuyama S., Nakajima N., Imai M., Yamada S., Murakami S., Yamayoshi S., Iwatsuki-Horimoto K., Sakoda Y., et al. // Nature. 2013. V. 501. № 7468. P. 551–555. doi: 10.1038/nature12392
16. Smee D.F., Hurst B.L., Wong M.H., Bailey K.W., Tarbet E.B., Morrey J.D., Furuta Y. //Antimicrob. Agents Chemother. 2010. V. 54. № 1. P. 126–133. doi: 10.1128/AAC.00933-09
17. Marathe B., Wong S.S., Vogel P., Garcia-Alcalde F., Webster R.G., Webby R.J., Najera I., Govorkova E.A. // Sci. Rep. 2016. V. 6. P. 26742. doi: 10.1038/srep26742
18. Smee D.F., Tarbet E.B., Furuta Y., Morrey J.D., Barnard D.L. // Future Virol. 2013. V. 8. № 11. P. 1085–1094. doi: 10.2217/fvl.13.98
19. Tarbet E.B., Maekawa M., Furuta Y., Babu Y.S., Morrey J.D., Smee D.F. // Antiviral Res. 2012. V. 94. № 1. P. 103–110. doi: 10.1016/j.antiviral.2012.03.001
20. Furuta Y., Takahashi K., Kuno-Maekawa M., Sangawa H., Uehara S., Kozaki K., Nomura N., Egawa H., Shiraki K. // Antimicrob. Agents Chemother. 2005. V. 49. № 3. P. 981–986. doi: 10.1128/AAC.49.3.981-986.2005
21. Naesens L., Guddat L.W., Keough D.T., van Kuilenburg A.B., Meijer J., Vande Voorde J., Balzarini J. // Mol. Pharmacol. 2013. V. 84. № 4. P. 615–629. doi: 10.1124/mol.113.087247
22. Sangawa H., Komeno T., Nishikawa H., Yoshida A., Takahashi K., Nomura N., Furuta Y. // Antimicrob. Agents Chemother. 2013. V. 57. № 11. P. 5202–5208. doi: 10.1128/AAC.00649-13
23. Davidson S. // Front. Immunol. 2018. V. 9. P. 1946. doi: 10.3389/fimmu.2018.01946
24. Cheung P.P.H., Watson S.J., Choy K.-T., Sia S.F., Wong D.D.Y., Poon L.L.M., Kellam P., Guan Y., Peiris J.S.M., Yen H.-L. // Nat. Commun. 2014. V. 5. № 1. P. 1–13. doi: 10.1038/ncomms5794
25. Goldhill D.H., Te Velthuis A.J., Fletcher R.A., Langat P., Zambon M., Lackenby A., Barclay W.S. // Proc. Natl. Acad. Sci. USA. 2018. V. 115. № 45. P. 11613–11618. doi: 10.1073/pnas.1811345115
26. Delang L., Segura Guerrero N., Tas A., Querat G., Pastorino B., Froeyen M., Dallmeier K., Jochmans D., Herdewijn P., Bello F., et al. // J. Antimicrob. Chemother. 2014. V. 69. № 10. P. 2770–2784. doi: 10.1093/jac/dku209
27. Abdelnabi R., Morais A.T.S., Leyssen P., Imbert I., Beaucourt S., Blanc H., Froeyen M., Vignuzzi M., Canard B., Neyts J., et al. // J. Virol. 2017. V. 91. № 1–2. pii: e00487-17. doi: 10.1128/JVI.00487-17
28. Jin Z., Smith L.K., Rajwanshi V.K., Kim B., Deval J. // PLoS One. 2013. V. 8. № 7. P. e68347. doi: 10.1371/journal.pone.0068347
29. Baranovich T., Wong S.S., Armstrong J., Marjuki H., Webby R.J., Webster R.G., Govorkova E. A.// J. Virol. 2013. V. 87. P. 3741–3751. doi: 10.1128/JVI.02346-12
30. de Avila A.I., Gallego I., Soria M.E., Gregori J., Quer J., Esteban J.I., Rice C.M., Domingo E., Perales C. // PLoS One. 2016. V. 11. № 10. P. e0164691. doi: 10.1371/journal.pone.0164691
31. Escribano-Romero E., Jimenez de Oya N., Domingo E., Saiz J.C. // Antimicrob. Agents Chemother. 2017. V. 61. № 11. pii: e01400-17. doi: 10.1128/AAC.01400-17
32. Qiu L., Patterson S.E., Bonnac L.F., Geraghty R.J. // PLoS Neglected Trop. Dis. 2018. V. 12. № 4. P. e0006421. doi: 10.1371/journal.pntd.0006421
33. Guedj J., Piorkowski G., Jacquot F., Madelain V., Nguyen T.H.T., Rodallec A., Gunther S., Carbonnelle C., Mentre F., Raoul H., et al. // PLoS Med. 2018. V. 15. № 3. P. e1002535. doi: 10.1371/journal.pmed.1002535
34. Schuster P. // Curr. Top. Microbiol. Immunol. 2016. V. 392. P. 61–120. doi: 10.1007/82_2015_469
35. Pauly M.D., Procario M.C., Lauring A.S. // Elife. 2017. V. 6. e26437. doi: 10.7554/eLife.26437.001
36. Perales C., Martin V., Domingo E. // Curr. Opin. Virol. 2011. V. 1. P. 419–422. doi: 10.1016/j.coviro.2011.09.001
37. Hayden F.G., Shindo N. // Curr. Opin. Infect. Dis. 2019. V. 32. № 2. P. 176–186. doi: 10.1097/QCO.0000000000000532
38. de Almeida S.M.V., Soares J.C.S., dos Santos K.L., Alves J.E.F., Ribeiro A.G., Jacob Í.T.T., da Silva Ferreira C.J., dos Santos J.C., de Oliveira J.F., de Carvalho Junior L.B., // Bioorganic & Med. Chem. 2020. V. 28. № 23. P. 115757. doi: 10.1016/j.bmc.2020.115757
39. Lima W.G., Brito J.C.M., Overhage J., da Cruz Nizer W.S. // Arch. Virol. 2020. V. 165. P. 1729–1737. doi: 10.1007/s00705-020-04693-5

40. Danta C.C. // ACS Chem. Neurosci. 2020. V. 11. № 15. P. 2137–2144. doi: 10.1021/acschemneuro.0c00335
41. Konstantinidou S.K., Papanastasiou I.P. // Exp. Ther. Med. 2020. V. 20. P. 1845–1855. doi: 10.3892/etm.2020.8905
42. Wang M., Cao R., Zhang L., Yang X., Liu J., Xu M., Shi Z., Hu Z., Zhong W., Xiao G. // Cell Res. 2020. V. 30. № 3. P. 269–271. doi: 10.1038/s41422-020-0282-0
43. Choy K.-T., Wong A.Y-L., Kaewpreedee P., Sia S.F., Chen D., Hui K.P.Y., Chu D.K.W., Chan M.C.W., Cheung P.P.-H., Huang X., et al. // Antiviral. Res. 2020. V. 178. P. 104786. doi: 10.1016/j.antiviral.2020.104786
44. Jin Z., Kinkade A., Behera I., Chaudhuri S., Tucker K., Dyatkina N., Rajwanshi V.K., Wang G., Jekle A., Smith D.B. // Antiviral Res. 2017. V. 143. P. 151–161. doi: 10.1016/j.antiviral.2017.04.005
45. Chen C., Zhang Y., Huang J., Yin P., Cheng Z., Wu J., Chen S., Zhang Y., Chen B., Lu M., et al. // Front. Pharmacol. 2021. V. 21. Art. 683296. doi: 10.3389/fphar.2021.683296
46. Cai Q., Yang M., Liu D., Chen J., Shu D., Xia J., Liao X., Gu Y., Cai Q., Yang Y., et al. // Engineering. 2020. V. 6. P. 1192–1198. doi: 10.1016/j.eng.2020.03.007
47. Ivashchenko A.A., Dmitriev K.A., Vostokova N.V., Azarova V.N., Blinow A.A., Egorova A.N., Gordeev I.G., Ilin A.P., Karapetian R.N., Kravchenko D.V., et al. // Clin. Infect. Dis. 2021. V. 73. P. 531–534. doi: 10.1093/cid/ciaa1176
48. https://clinicaltrials.gov/ct2/show/results/NCT04542694?term=favipiravir&draw=2&rank=47
49. https://www.pharmaceutical-technology.com/news/china-approves-favilavir-covid-19/
50. Agrawal U., Raju R., Udwadia Z.F. // Med. J. Armed. Forces India. 2020. V. 76. № 4. P. 370–376. doi: 10.1016/j.mjafi.2020.08.004
51. Interim Guidelines for Prevention, Diagnosis, and Treatment of the New Coronavirus Infection (COVID-19). 7th Edition. Moscow, Ministry of Health of the Russian Federation, 2020, 166 p. http://edu.rosminzdrav.ru MR_COVID-19_v7.pdf.
52. Interim Guidelines for Prevention, Diagnosis, and Treatment of the New Coronavirus Infection (COVID-19), Issue 13.1, Moscow, Ministry of Health of the Russian Federation, 2021, 236 p. https://static-0.minzdrav.gov.ru BMP-13.1-from-17-11-2021.pdf
53. «List of Vital and Essential Medicines for Medical Use for 2021» (https://mine-med.ru/archive/p2021p1.pdf)
54. State Register of Medicines. https://grls.rosminzdrav.ru/GRLS.aspx?RegNumber=&MnnR=фавипиравир&lf=таблетки&TradeNmR=&OwnerName=&MnfOrg=&MnfOrgCountry=&isfs=0&regtype=1%2c6&pageSize=10&order=RegDate&orderType=desc&pageNum=1
55. https://lenta.ru/news/2021/11/12/lecheniecovid/
56. Huchting J., Vanderlinden E., van Berwaer R., Meier C., Naesens L. // Antiviral Res. 2019. V. 167. P. 1–5. doi: 10.1016/j.antiviral.2019.04.002
57. De Vleeschauwer A.R., Lefebvre D.J., Willems T., Paul G., Billiet A., Murao L.E., Neyts J., Goris N., De Clercq K. // Transboundary Emerging Diseases 2016. V. 63. № 2. P. e205–e212. doi: 10.1111/tbed.12255
58. Julander J.G., Furuta Y., Shafer K., Sidwell R.W. // Antimicrob. Agents Chemother. 2007. V. 51. № 6. P. 1962–1966. doi: 10.1128/AAC.01494-06
59. Julander J.G., Shafer K., Smee D.F., Morrey J.D., Furuta Y. // Antimicrob. Agents Chemother. 2009. V. 53. № 1. P. 202–209. doi: 10.1128/AAC.01074-08
60. Gowen B.B., Wong M.-H., Jung K.-H., Smee D.F., Morrey J.D., Furuta Y. // Antiviral Res. 2010. V. 86. № 2. P. 121–127. doi: 10.1016/j.antiviral.2009.10.015
61. Titova Y.A., Fedorova O.V. // Chem. Heterocycl. Comp. 2020. V. 56. № 6. P. 659–662. doi: 10.1007/s10593-020-02715-3
62. Al Bujuq N. // Synthesis. 2020. V. 52. № 24. P. 3735–3750. doi: 10.1055/s-0040-1707386
63. Qin N., Min Q., Hu W. // J. Compar. Chem. 2020. V. 4. № 1. C. 1–11. doi: 10.12677/CC.2020.41001
64. Furuta Y., Egava H. Patent № WO2000/010569. Japan. C07D 237/24 2006.1. 2000.
65. Egawa H., Furuta Y., Sugita J., Uehara S., Hamamoto S., Yonesawa K. Patent № WO 2001/060834. Japan. C07H 19/04 2006.1. 2001.
66. Hara H., Norimatsu N., Kurushima H., Kano T. Patent № 2011.0275817A1. USA. C07D 241/16 2006.1. 2011.
67. Takamatsu T., Yonezawa K. Patent № WO 2009/041473. Japan. C07D 241/24 2006.1. 2009.
68. Liu F.-L., Li C.-Q., Xiang H.-Y., Feng S. // Chem. Papers. 2017. V. 71. № 11. P. 2153–2158. doi: 10.1007/s11696-017-0208-6
69. Shi F., Li Z., Kong L., Xie Y., Zhang T., Xu W. // Drug Discov. Therapeut. 2014. V. 8. № 3. P. 117–120. doi: 10.5582/ddt.2014.01028
70. Guo Q., Xu M., Guo S., Zhu F., Xie Y., Shen J. // Chem. Papers. 2019. V. 73. № 5. P. 1043–1051. doi: 10.1007/s11696-018-0654-9
71. Rabie A.M. // Chem. Papers. 2021. V. 75. № 9. P. 4669–4685. doi: 0.1007/s11696-021-01640-9
72. Seliem I.A., Girgis A.S., Moatasim Y., Kandeil A., Mostafa A., Ali M.A., Panda S.S. // ChemMedChem. 2021. V. 16. № 22. P. 3418–3427. doi: 10.1002/cmdc.202100476
73. Wu Y. Patent № 105884827. China. C07F 9/6509 2006.1. 2016.
74. Moshikur R.M., Ali M.K., Wakabayashi R., Moniruzzaman M., Goto M. // Mol. Pharmaceut. 2021. V. 18. № 8. P. 3108–3115. doi: 10.1021/acs.molpharmaceut.1c00324
75. Moshikur R.M., Chowdhury M.R., Wakabayashi R., Tahara Y., Moniruzzaman M., Goto M. // Internat. J. Pharmaceut. 2018. V. 546. № 1–2. P. 31–38. doi: 10.1016/j.ijpharm.2018.05.021
76. Cai L., Sun Y., Song Y., Xu L., Bei Z., Zhang D., Dou Y., Wang H. // Arch. Virol. 2017. V. 162. № 9. P. 2847–2853. doi: 10.1007/s00705-017-3436-8
77. Wang G., Wan J., Hu Y., Wu X., Prhavc M., Dyatkina N., Rajwanshi V.K., Smith D.B., Jekle A., Kinkade A. // J. Med. Chem. 2016. V. 59. № 10. P. 4611–4624. doi: 10.1021/acs.jmedchem.5b01933
78. Klejch T., Pohl R., Janeba Z., Sun M., Keough D.T., Guddat L.W., Hocková D. // Tetrahed. 2018. V. 74. № 40. P. 5886–5897. doi: 10.1016/j.tet.2018.08.014
79. Pertusati F., Serpi M., McGuigan C. // Antiviral Chem. Chemother. 2012. V. 22. № 5. P. 181–203. doi: 10.3851/IMP2012
80. Guo S., Xu M., Guo Q., Zhu F., Jiang X., Xie Y., Shen J. // Bioorg. Med. Chem. 2019. V. 27. № 5. P. 748–759. doi: 10.1016/j.bmc.2019.01.007
81. Pierra C., Counor C., Storer R., Gosselin G. // Collect. Czech. Chem. Com. 2011. V. 76. № 11. P. 1327–1333. doi: 10.1135/cccc2011089
82. Huchting J., Winkler M., Nasser H., Meier C. // ChemMedChem. 2017. V. 12. № 9. P. 652–659. doi: 10.1002/cmdc.201700116
83. Huchting J., Vanderlinden E., Winkler M., Nasser H., Naesens L., Meier C. // J. Med. Chem. 2018. V. 61. № 14.

P. 6193–6210. doi: 10.1021/acs.jmedchem.8b00617
84. Bulatovski A., Zinchenko A. // Biotehnologii moderne-soluții pentru provocările lumii contemporane. 2021. C. 133–133. doi.org/10.52757/imb21.075
85. Arco J.D., Fernandez-Lucas J. // Cur. Pharm. Des. 2017. V. 23. № 45. P. 6898–6912. doi: 10.2174/1381612823666171017165707

Eukaryotic Ribosome Biogenesis: The 60S Subunit

A. A. Moraleva[1], A. S. Deryabin[1*], Yu. P. Rubtsov[1], M. P. Rubtsova[2*], O. A. Dontsova[1,2,3]
[1]Shemyakin-Ovchinnikov Institute of Bioorganic Chemistry of the Russian Academy of Sciences, Moscow, 117997 Russia
[2]Lomonosov Moscow State University, Faculty of Chemistry, Moscow, 119991 Russia
[3]Skolkovo Institute of Science and Technology, Moscow, 121205 Russia
*E-mail: deryabin95@mail.ru, mprubtsova@gmail.com
Received: July 29, 2021; in final form, February 11, 2022
DOI: 10.32607/actanaturae.11541

ABSTRACT **Ribosome biogenesis is consecutive coordinated maturation of ribosomal precursors in the nucleolus, nucleoplasm, and cytoplasm. The formation of mature ribosomal subunits involves hundreds of ribosomal biogenesis factors that ensure ribosomal RNA processing, tertiary structure, and interaction with ribosomal proteins. Although the main features and stages of ribosome biogenesis are conservative among different groups of eukaryotes, this process in human cells has become more complicated due to the larger size of the ribosomes and pre-ribosomes and intricate regulatory pathways affecting their assembly and function. Many of the factors involved in the biogenesis of human ribosomes have been identified using genome-wide screening based on RNA interference. A previous part of this review summarized recent data on the processing of the primary rRNA transcript and compared the maturation of the small 40S subunit in yeast and human cells. This part of the review focuses on the biogenesis of the large 60S subunit of eukaryotic ribosomes.**
KEYWORDS **nucleolus, ribosome biogenesis, ribosomopathy.**

INTRODUCTION

The first part of this review describes in detail the mechanisms of formation and processing of the common 90S precursor, biogenesis of the small 40S subunit, and the nucleolus as a special intranuclear structure necessary for the formation and early maturation of ribosome precursors. In this second part, we continue with a discussion of the details of ribosome biogenesis as exemplified by the formation of the large 60S ribosomal subunit in human and yeast cells.

BIOGENESIS OF THE 60S SUBUNIT PRECURSOR

The 25S ribosomal RNA (rRNA) of the 60S yeast subunit consists of six conserved domains (I–VI) that are more closely intertwined than the 18S rRNA domains in the small subunit (SSU) (*Fig. 1*). Domains I and II of 25S and 5.8S rRNAs are located on the outer surface of the large subunit (LSU), and domains IV and V are involved in the functional centers. Domains III and IV connect the small and large subunits. In this case, rRNA domain III binds to other rRNA domains in the lower part of the 60S subunit, the 5.8S rRNA is located between domains I and III, and the 5S rRNA is anchored at the top of domains II and V (*Fig. 1*). Domain VI is connected to domains I and II and 5.8S rRNA.

In 2017, three research groups published high-resolution cryo-EM structures of pre-60S from yeast nuclei. Six types of pre-60S particles have been identified in these structures. They differ in the packing density of RNA and the composition of ribosomal proteins (RPs) [1, 6–8] (*Fig. 1*). The secondary structure of LSU rRNA comprises six domains; however, these domains cannot be clearly distinguished in the 3D structure, in contrast to the four domains of the SSU 18S rRNA. During transcription, domains I and II of the 25S rRNA bind 5.8S and ITS2 to form a structural scaffold for further assembly (*Fig. 1*) [1, 7, 8]. Immediately after transcription by RNA polymerase I (Pol I), domain VI folds into an ordered structure, while the central domains (III, IV, and V) remain disordered, interacting with the ribosome assembly factors (RAFs) that prevent contacts with 5'-terminal domains. In mature LSU, domains I–V form the peptide exit tunnel, domains II and VI form the GTPase center, and domain V forms the peptidyl transferase center (PTC) comprising the A and P sites. Coordinated binding and dissociation of various RAFs ensure a consecutive formation of these key structures. For example, a series of consecutive interactions with RAFs (Nog1, Rei1, and Reh1), which

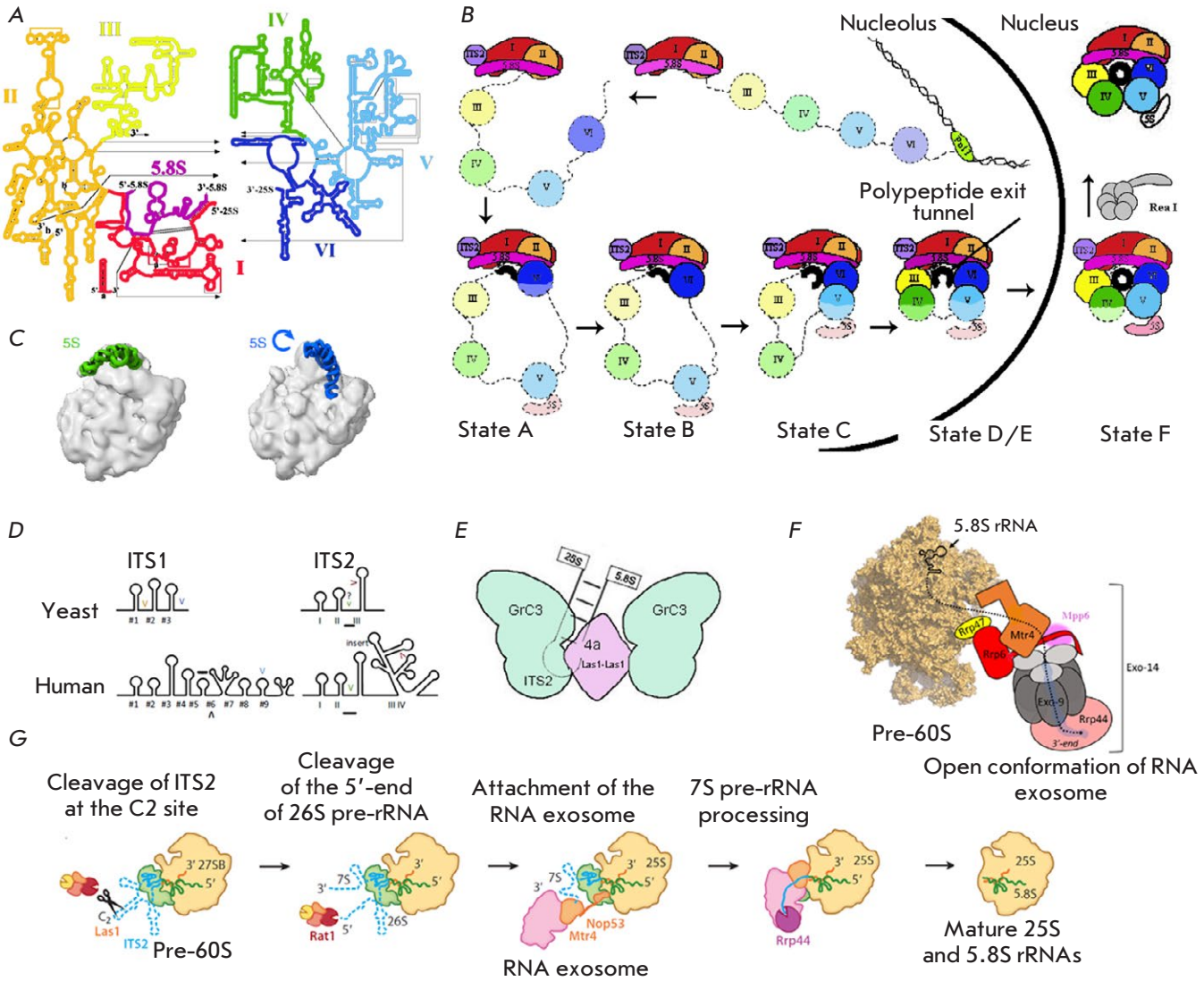

Fig. 1. Structure and maturation of yeast pre-rRNA. (*A*) 25S rRNA contains six secondary structure domains (I–VI). 5.8S rRNA (shown in black) forms a complementary interaction with domain I of 25S rRNA (adapted from https://crw-site.chemistry.gatech.edu/). (*B*) Scheme of assembly of pre-60S pre-rRNA domains. The color coding of 25S rRNA domains is the same as in (*A*). Attachment of ribosomal proteins and biogenesis factors to the 35S rRNA precursor. The formation of the polypeptide exit tunnel (black circle) begins with binding of domain VI to domains I and II and a 5.8S region of the rRNA precursor. Folding of rRNA domains occurs in the following order: VI, V, III, and IV. In the F (final) state, domain V is completely folded [1]. (*C*) 5S rRNA turn [2]. (*D*) Secondary structures of yeast and human ITS1 and ITS2. Cleavage sites are marked with "V". The predicted sites are indicated by question marks, and human exonuclease binding sites are underscored [3]. (*E*) Model of ITS2 processing by PNK RNase [4]. (*F*) Scheme of the interaction between the nuclear RNA exosome and pre-60S [5]. (*G*) Removal of ITS2 from the pre-60S particle by RNA processing enzymes. Intermediates formed during ITS2 removal are shown [6]

occur immediately after the formation of the polypeptide exit tunnel, promote the completion of folding [9–13]. Domain VI, which corresponds to the 3'-end of 25S rRNA, is stably incorporated into the particle, closing the rRNA ring and leaving domains III–V free [1, 7, 8] (*Fig. 2*). They are consecutively assembled around the polypeptide exit tunnel, leaving the PTC in an immature conformation. This sequence of events differs from 40S biogenesis, where rRNA folding occurs consecutively from the 5'- to the 3'-end of 18S rRNA. Notably, the essential condition for the formation of these ring rRNA intermediates in the 60S subunit is the removal of the internal transcribed spacer 1 (ITS1) and external transcribed spac-

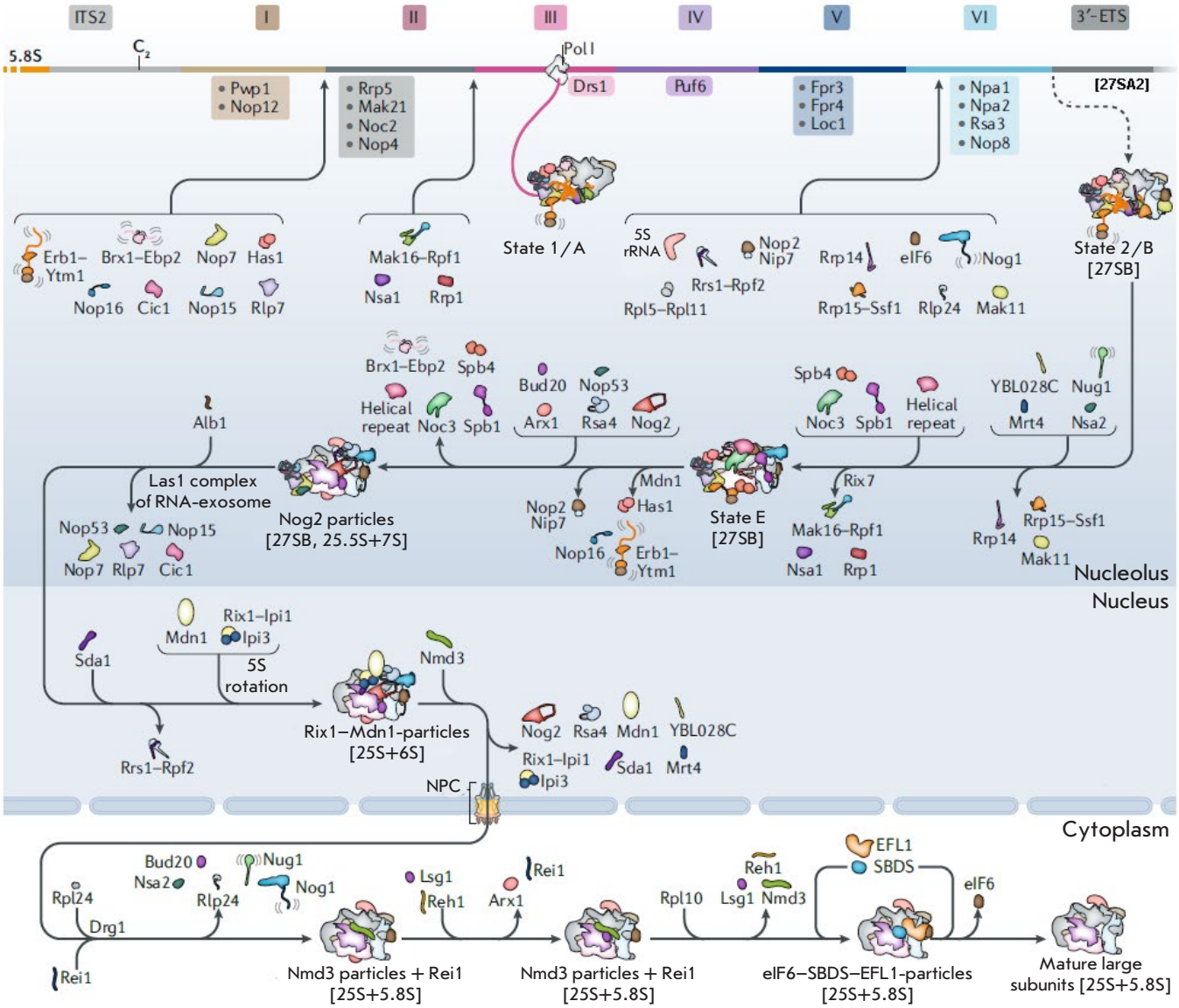

Fig. 2. Large ribosomal subunit assembly in yeast. Consecutive stages of large ribosomal subunit (60S) maturation are shown, starting with the earliest stages in the nucleolus, through stages in the nucleoplasm, and finally in the cytoplasm. rDNA regions giving rise to 5.8S rRNA, ITS2, domains I–VI of 25S rRNA, and 3′-ETS are indicated. Adapted from [14]. Assembly factors and complexes with known structures are depicted as cartoons; those whose structures are not known are indicated with text only

er (3'-ETS) (*Fig. 3*), because these sequences sterically prevent the association of rRNA domain VI with other domains. The ring intermediate comprises both the 5'- and 3'-ends of rRNA and can protect rRNA from degradation but does not interfere with the modification of heterocyclic bases. Anchoring of the 5'- and 3'-ends probably facilitates the assembly of mobile neighboring domains, forming a kind of scaffold. Domain V especially benefits from the preassembly of other rRNA domains, because its regions should form contacts with several domains, including 5S rRNA (*Fig. 1, 2*). During this process, the conformation of this complex changes three times (*Fig. 1, 2*).

Some RAFs, such as Rrp5, Mak21, Noc2, and Nop4, seem to promote rRNA compaction at the earliest co-transcriptional stages of LSU biogenesis, forming a rigid support for coordinated RNA folding [14–19]. The structures of pre-ribosomal particles in mutants deficient in these RAFs have a looser structure [14, 18]. Early RAFs (Npa1, Npa2, Rsa3, and Nop8) and

RNA helicase Dbp6 form a stable complex capable of performing a structural function [19, 20]. Six other RNA helicases (Dbp2, Dbp3, Dbp7, Dbp9, Mak5, and Prp43) are also required at the initial assembly stages that involve the remodeling of RNA structures (for review, see [20, 21]). Interestingly, cleavage of ITS1 at A2 and A3 is associated with the transcription and processing of sequences that are separated from each other by several thousand nucleotides in the primary structure. Co-transcriptional cleavage at site A2 occurs after synthesis of 25S rRNA domains I and II [22, 23]. Hydrolysis at A3 occurs after the completion of 3'-ETS transcription and processing [24]. Probably, protein-mediated RNA folding results in the formation of structures that can interact with RAFs and nucleases. For example, Rrp5 binding to ITS1 both in the SSU processome (site A2) and in pre-60S particles (site A3) [25–27] can regulate cleavage at these sites and coordinate the assembly of both subunits [16, 18, 28, 29].

Early nucleolar pre-60S particles contain approximately 30 RAFs and 30 ribosomal proteins (*Table*). Most of them seem to stabilize the structure, and some exhibit enzymatic activity that controls the transition between key steps in the 60S assembly process. For example, the Nop2 and Spb1 factors are important for snoRNP-independent RNA methylation. The substrate and function of helicase Has1 have not been identified. The functions of GTPases Nog1 and Nug1, which are likely required for the release of Nop2 and Spb1 from later pre-60S subunits, have not been identified. Interestingly, Brix family proteins and their partner proteins [31–34] probably fold rRNA by bringing different domains together. For example, the Ssf1–Rrp15 dimer binds rRNA domains III and VI; the Brx1–Ebp2 complex binds the junction of domains I and II; Rpf1–Mak16 comes into contact with 5.8S rRNA and domains I, II, and VI. Brix family proteins, Rpf2 and Rrs1, interact with 5S rRNA and domain V in the pre-60S Nog2 particle [13], and the Imp4–Mpp10 complex binds 5'-ETS and the nascent 3'-domain in the 90S particle.

Isolation of the Nsa1–pre-60S complex revealed that, during LSU formation, the Nsa1–Rpf1–Mak16–Rrp1 complex stabilizes the surface exposed to the solvent; the Rlp24–Nog1–Mrt4–Mak16–Tif6–Nsa2 complex interacts predominantly with domains V and VI; and the Nsa3–Nop15–Rlp3–Nop7–Erb1–Ytm1 complex organizes ITS2 during foot formation. Like several RAFs of the 90S subunit, Erb1 has a long N-terminus that meanders over the pre-60S surface, contacting distant factors, including the Brx1–Ebp2 dimer, Has1 helicase, Nop16, and foot factor Nop7 [1, 7, 8]. Furthermore, the β-propeller domain of Erb1 interacts stably with the Ytm1 factor that is a substrate for the Rea1 ATPase [35]. At a certain stage, Rea1 creates a mechanochemical force to remove Ytm1 and the deep-rooted Erb1. Notably, other protein complexes also contain proteins (Nsa1, Rlp24) dissociation of which requires AAA-ATPases such as Rix7 and Drg1 [35, 36].

It is not yet clear when and how the 5S RNP (5S rRNA, uL18/Rpl5, uL5/Rpl11) is incorporated into the earliest pre-60S particles. The interaction occurs with the 5S RNP in a folded conformation, and, therefore, it requires a 180° conformational rotation at later stages of 60S maturation [6, 13, 37]. This stage combines with the formation of PTC correct occurrence, which is checked through removal of Rsa4 by the huge Rea1 AAA-ATPase and GTP-dependent dissociation of Nug2 [38, 39]. Binding of nuclear export factors to pre-60S and subsequent transport occur after passing the assembly quality control stages [39]. Despite a strict system for assembly accuracy control in the nucleus, pre-60S particles containing ITS2 and related factors can enter the cytoplasm and even participate in translation [40–42].

Transport of pre-60S into the cytoplasm and quality control of subunit precursors

Transport from the nucleolus to the nucleoplasm is accompanied by the exchange of protein factors that promote remodeling and subsequent export of precursors from the nucleus. In the cytoplasm, pre-60S ribosomes undergo the final stages of maturation; in particular, removal of RAFs, attachment of the last few RPs, and quality control of the functional centers.

The nuclear export adaptor protein Nmd3 controls the interaction between Crm1/Xpo1 exportin and the 60S subunit, which facilitates transport of the subunit into the cytoplasm [6, 43–46]. The interaction between 60S subunits and noncanonical export factors has been reported [6, 46].

In the cytoplasm, the pre-40S precursor binds to several RAFs, which block access to the mRNA channel and P-site for initiator tRNA binding, and undergoes quality control. Subsequently, 40S binds to the 60S large subunit using the Fab7 ATPase and eukaryotic translation initiation factor 5B (eIF5B). In this case, the GTPase center of eIF5B should be in an active conformation. The formation of the complex ensures the ability of mature 40S to hydrolyze GTP. The formation of the mature 3'-end of 18S rRNA by endonuclease Nob1 is accompanied by a dissociation of the remaining RAFs from 40S and dissociation of the 40S–60S complex, which is an indication that the small subunit is ready for the final stage of processing [12, 47–49].

Human ribosome biogenesis is far more complex than yeast ribosome biogenesis

The main stages and molecular events of ribosome biogenesis are conserved. For a long time, it was believed that most stages of subunit formation in human and *Saccharomyces cerevisiae* cells are identical, but this turned out to be an oversimplification of the situation. Human nucleoli have three compartments, instead of two in yeast's nucleoli, are involved in a greater number of cellular processes [50, 51], and contain at least 20-fold more proteins than yeast (up to 300 in yeast; 6,000 in humans) [52]. The complexity of the physiological processes in multicellular organisms determines the need for new modes for regulating ribosome formation, which is evidenced in particular by the dependence of 40S subunit synthesis on circadian rhythms in mice [53, 54].

Human ribosomes are larger than yeast ribosomes. They contain more ribosomal proteins that are often larger than yeast proteins. Human rRNAs are comparable in size to yeast rRNAs, except for the 28S rRNA that is 1.5-fold larger. ETS and ITS sizes differ most significantly: in humans, they contain many mono- and dinucleotide repeats that may have arisen due to replication errors. The more complex ribosomal structure in higher eukaryotes and, accordingly, the rRNA structure inevitably affect ribosome biogenesis [26], which is reflected in a larger number of precursors [55]. Biogenesis of human 40S subunits is accompanied by the formation of at least two additional precursors containing 30S and 21S pre-rRNAs (*Fig. 3*) [15, 56]. In yeast, 70–80% of nascent pre-rRNA transcripts undergo co-transcriptional cleavage in ITS1, while the primary transcript in mammals is usually cleaved post-transcriptionally [23, 57]. ITS1 processing in human cells has been shown to be more complex than that in yeast cells and require both endo- and exonucleolytic activity [57–59].

A distinctive feature of eukaryotic ribosome biogenesis is the modular assembly of pre-ribosomal complexes. Both in yeast and in humans, the UTP-A, UTP-B, UTP-C, U3 snoRNA, RCL1–BMS1 heterodimers, and IMP3–IMP4–MPP10 and EMG1 complexes are assembled on the newly synthesized pre-rRNA transcript and form the core of the so-called SSU processome. Some complexes, such as human PeBoW (Nop7–Erb1–Ytm1 in yeast) [60] and PELP1–TEX10–WDR18 (Rix1–Ipi3–Ipi1 in yeast) [61], act similarly during the biogenesis of pre-60S subunits. Despite their evolutionary conservatism, their composition is different in various species; in humans, several additional RNA helicases, e.g., DDX21 for UTP-B and DDX27 for PeBoW, have been identified [62, 63]. All these facts indicate additional remodeling steps at the early stages of pre-ribosome assembly in humans.

Production of 18S rRNA in mammalian cells can occur upon suppression of 28S rRNA synthesis [64–67]. Depletion of several human LSU ribosomal proteins [57] does not prevent the formation of both 18S rRNA and its direct precursor, 18S-E pre-rRNA, despite a serious decrease in 28S rRNA synthesis. These data support a model in which early assembly events in each ribosomal subunit control proximal cleavage in ITS1. Notably, this mode of splitting the SSU and LSU precursors does not preclude the existence of factors that may be involved in both ITS1 cleavages. In mammalian cells, separation of the SSU and LSU precursors occurs simultaneously, which complicates the analysis of processing stages. Depletion of various mouse SSU and LSU assembly factors leads to the inhibition of one of the two ITS1 cleavages [68]. It is hypothesized that cleavage in mouse pre-rRNA at two ITS1 sites, which correspond to human E and C sites, is coordinated with early assembly in the SSU or LSU. As a result, each subunit remains attached to ITS1 until it reaches the maturation stage and is capable of cleaving the ITS1 [68].

In the absence of several assembly factors, the LSU inhibits cleavage at the A2 site, which leads to the accumulation of aberrant 35S pre-rRNAs [69–71] and processing arrest. In contrast to yeast, transcript cleavage in mammalian cells occurs at either of two ITS1 sites, which leads to the generation of major precursors that mature to 18S and 5.8S/28S rRNAs (*Fig. 3*). Defects in the early steps of LSU assembly in mammalian cells inhibit cleavage in the 3'-region of ITS1. Separation of RNA ribosomal subunits in mammals involves cleavage of ITS1 at two sites, as opposed to one in yeast.

Quite little is known about the structure of human pre-ribosomes, because there are no reliable methods for their isolation and purification. Many human ribosome synthesis factors have been identified using high-throughput small interfering RNA screening capable of detecting defects in the production of pre-rRNA intermediates and accumulation of ribosomes or pre-ribosome components in the nucleolus or nucleoplasm [30, 72]. Such screening has identified 286 proteins, including yeast RAF orthologues, as well as 74 human-specific proteins and snoRNAs which may be RAFs [30, 73] (*Table*). Recently, 139 potential RAFs have been identified by screening for factors that affect the amount or morphology of nucleoli [74]. However, the role of individual human RAFs has barely been studied. The composition, activity, and structure of intermediate complexes are also not well understood, because most data have been obtained by

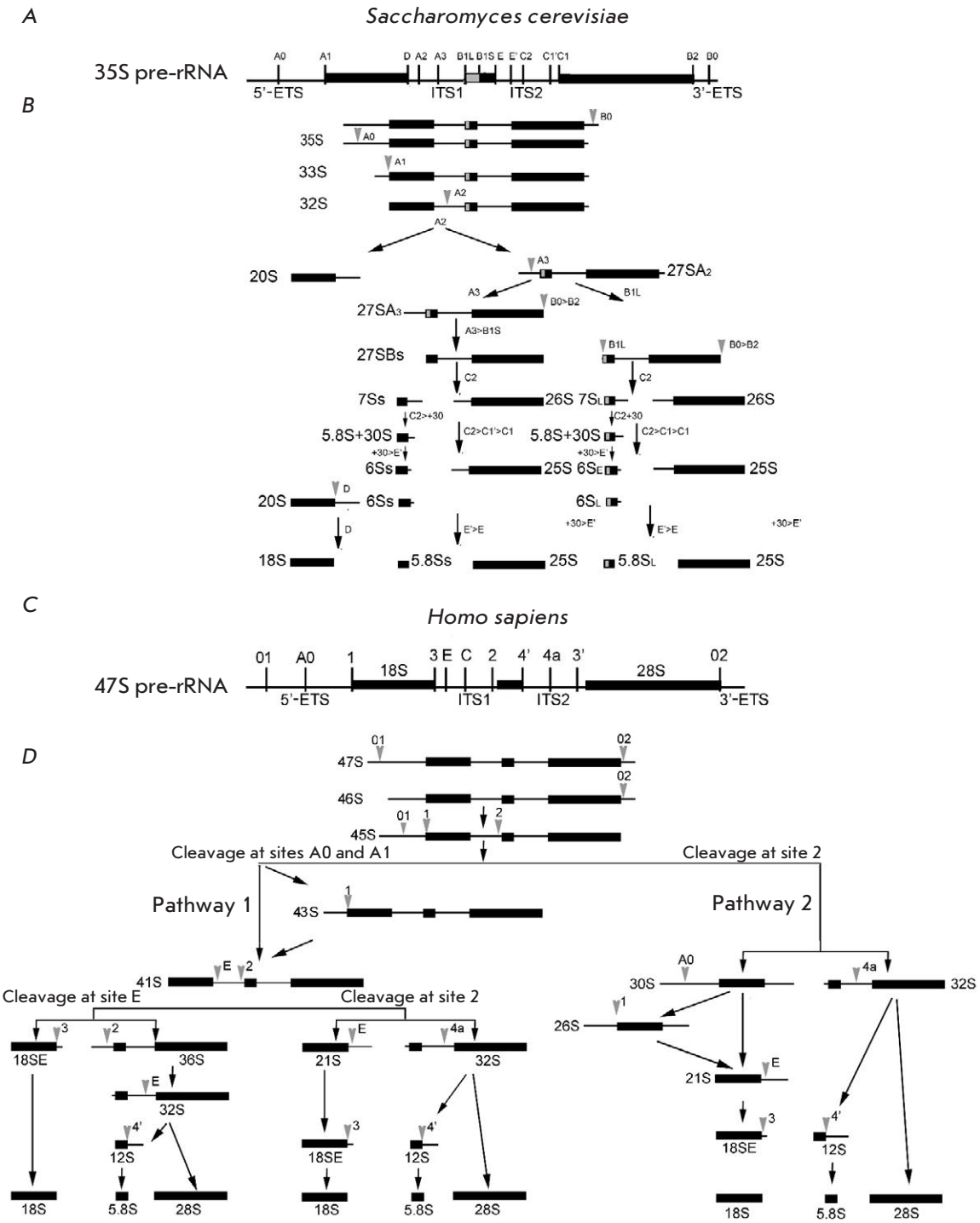

Fig. 3. Maturation pathways of the 35S pre-rRNA transcript in *Saccharomyces cerevisiae* (*A*) and the 47S pre-RNA transcript in *Homo sapiens* (*C*). Three of the four rRNAs (18S, 5.8S, and 25S (in yeast)/28S (in humans)) are synthesized by Pol I as a single long transcript. The coding sequences of mature rRNAs are flanked by 5′- and 3′-ETS, ITS1, and ITS2 non-coding spacers. The schematic shows the relative position of known and predicted cleavage sites. (*B*) Processing of pre-rRNA in budding yeast. (*D*) A simplified schematic of human pre-rRNA processing. The primary transcript, 47S pre-rRNA, is initially cleaved at both ends at sites 01 and 02 to form the 45S precursor that is processed via two alternative pathways [51]. ">" (e.g., C2>C1′>C1) denotes consecutive shortening of the appropriate 3′- or 5′-ends of the pre-rRNA by nucleases

Large ribosomal subunit assembly factors [20, 30]

Ribosome biogenesis factors; LSU components in *Saccharomyces cerevisiae*					
Cluster number			Homo sapiens	S. cerevisiae	Function
8	8	4	PDCD11	Rrp5	Structural
	4		RBM28	Nop4	Structural
1			DDX51	Dbp6	DEAD-box-helicase
	1		DDX50	Dbp3	«
1	1		DDX31	Dbp7	«
1	4		DDX56	Dbp9	«
1	1		DDX24	Mak5	«
			DDX54	Dbp10	«
	2		GAR1	Gar1	Pseudouridine synthase cofactor
2	2		NHP2	Nhp2	Pseudouridine synthase cofactor
	8		NOP10	Nop10	Pseudouridine synthase cofactor
6	6	6	DKC1	Cbf5	Pseudouridine synthase
2	2	2	NOP56	Nop56	Main component of C/D Box snoRNP
			NOP58	Nop58	Same
2	2	2	FBL	Nop1	«
2	2	11	NHP2L1	Snu13	«
			KIAA0020	Puf6	Structural
1			PWP1	Pwp1	Structural
			RBM34	Nop12	Structural
4	4	4	DDX27	Drs1	DEAD-box-helicase
6	11	11	PAK1IP1	Mak11	Structural
			PPAN	Ssf1	«
			PPAN	Ssf2	«
4	4	4	RRP15	Rrp15	«
9	11		SURF6	Rrp14	«
4	4	4	WDR74	Nsa1	«
4	4	4	RRP1/NOP52	Rrp1	«
4	10	10	RPF1	Rpf1	«
4	4	4	MAK16	Mak16	«
			NVL	Rix7	AAA-ATPase
4	4	4	EBNA1BP2	Ebp2	Structural
4	4	4	BRIX1	Brx1	«
4	4	4	BOP1	Erb1	«
		4	WDR12	Ytm1	«
8	8	8	DDX18	Has1	DEAD-box-helicase
4	4	11	NOC2L	Noc2	Structural
1			FTSJ3	Spb1	rRNA methyltransferase
			DDX55	Spb4	DEAD-box-helicase
1			NOP2	Nop2	rRNA methyltransferase
1			NIP7	Nip7	Structural
			NOC3L	Noc3	«
4	4	4	PES1	Nop7	«
4	4	4	MKI67IP	Nop15	«
				Cic1	«
	8		eIF6	eIF6	«
11	11	11	GLTSCR2	Nop53	Structural, binding of RNA-exosome
2			RSL24D1	Rlp24	Structural
4	4	4	GTPBP4	Nog1	GTPase
			MRTO4	Mrt4	Structural
4	1	1	NSA2	Nsa2	Structural
1			GNL3	Nug1	GTPase
11		11	RRS1	Rrs1	Structural
		1	RPF2	Rpf2	Structural
11		11	GNL2	Nog2	GTPase
			NLE1	Rsa4	Structural
			WDR18	Ipi3	Structural
			MDN1	Mdn1	AAA-ATPase
11	11		SDAD1	Sda1	Structural
			Nmd3-containing particles		
2			NMD3	Nmd3	«
		2	ZNF622	Rei1	«
			ZNF622	Reh1	«
	6		LSG1	Lsg1	ATPase

extrapolating data from the analysis of yeast pre-ribosomes. In some cases, the functions of even homologous ribosome synthesis factors may differ; for example, yeast Nip7 and Spb1 are required for the maturation of 5.8S and 25S rRNAs, and their homologues, human NIP7 and FTSJ3, are involved in the synthesis of 18S rRNA [75]. A separate issue is the difficulty in identification of RAFs directly involved in subunit assembly and how they differ from the proteins/signaling pathways that indirectly affect the production of ribosomes.

A high-throughput screening of the functions of human nucleolar proteins was performed by reducing their level using small interfering RNAs. According to the results of such screening, nucleolar proteins may be divided into 12 functional clusters, depending on their influence on certain stages of pre-rRNA processing. Similar defects were observed in different cell types, including primary cell lines [30]. For example, UTP18-depleted cells accumulate aberrant 34S pre-rRNA due to the inhibition of early cleavages of the rRNA precursor (at sites 01, A0, and 1). RPS11-depleted cells accumulate significant amounts of 30S pre-rRNA due to the lack of processing at sites A0 and 1. NOL9 is primarily involved in ITS2 processing, because 32S pre-rRNA accumulates in its absence. 43S and 26S pre-rRNAs are present in higher amounts in RPS3-depleted cells than in control cells, which indicates that this protein is involved in the cleavage at the A0 and A1 sites. RPS3-depleted cells accumulate a truncated 21S-21S-C form (*Fig. 3*).

The human MDN1, NVL2, and AFGH2 proteins are homologues of the three yeast AAA-ATPases (Rea1/Mdn1, Rix7, and Drg1, respectively) involved in the release of specific biogenesis factors from pre-60S particles [76]. The presence of MDN1 in the pre-60S and PELP1–TEX10–WDR18 complexes (Rix1 complex in yeast) suggests that this enzyme acts similarly in different species, from yeast to humans [77]. Some RNA helicases also play common roles. For example, yeast Dhr1 and human DHX37 mediate the release of U3 snoRNA [78–81]. In this case, several human RNA helicases have additional functions associated with ribosome biogenesis. For example, DDX51 is required for the release of U8 snoRNA, which is specific to multicellular organisms, from pre-LSU complexes [82], while DDX21 coordinates pre-rRNA processing with transcription, facilitating access of late snoRNA pre-40S to the complexes [63, 78, 83].

Several new pre-ribosomal mini-complexes have been identified in human cells [82]. For example, the anti-apoptotic transcription factor AATF, neurohydin (NGDN), and NOL10 form a nucleolar subcomplex (ANN) [84]. These proteins interact with early pre-ribosomes, and the lack of any of the ANN components leads to impaired pre-rRNA cleavage in the early stages of biogenesis. XND, a nucleolar complex consisting of the NF-kB repressing factor (NKRF), RNA helicase DHX15, and 5'–3'-exonuclease XRN2, is also involved in the early stages of human ribosome assembly [85]. NKRF recruits XRN2 to pre-ribosomal complexes, where it is involved in pre-rRNA processing and removal of excised pre-rRNA fragments. NKRF also stimulates the ATPase and helicase activities of DHX15 [85]; i.e., these proteins seem to function in tandem in the early stage of pre-rRNA remodeling. A yeast homologue of DHX15, Prp43, is involved in snoRNA release from pre-60S particles and promotes cleavage of the 3'-end of 18S rRNA [86, 87]. The NF45–NF90 heterodimer, a transcription factor, binds double-stranded RNA within pre-60S. The lack of these factors does not affect rRNA processing, but it causes nucleolar morphology changes and accumulation of pre-60S complexes [88].

Recently, cryo-EM structures of late nuclear and cytoplasmic complexes of the human pre-40S subunits were obtained in the Beckman laboratory [89]. The structure of one of the intermediate states revealed the position of the biogenesis factor RRP12 and two methyltransferases (BUD23 and TRM112) in the head of the 40S subunit. The later human cytoplasmic pre-40S particle is very similar to yeast pre-40S, with conserved RAFs in identical positions. Thus, the pre-40S structure and the final 18S rRNA processing mechanism are evolutionarily conserved [89].

Ribosomal proteins and their role in the formation of the rRNA structure and subunit maturation

The main role of ribosomal proteins is to maintain the structure and function of ribosomes and the production of active ribosomes. Mathematical modeling has shown a great advantage in assembling elaborate complexes – in particular ribosomes – from numerous small ribosomal proteins, rather than bundling a small number of larger polypeptides [90]. Most human RPs are known to have a single variant, while many yeast RPs have two isoforms. Surprisingly, ~50% of the transcripts synthesized by human RNA polymerase II are RP mRNAs [91] and concentrations of 80 RPs in the cell are carefully maintained at levels optimal for ribosome assembly. Most RP genes comprise one or more common promoter elements (GABP, Sp1, YY1) to synchronize transcription. The mRNAs of all RPs contain a 5'-terminal oligopyrimidine tract (5'-TOP), which also enables co-regulation of their translation [92]. Ribosomal proteins are usually positively charged and prone to aggregation and degradation. Chaperones bind (often co-translationally) to

newly synthesized RPs, stabilize them, and facilitate import into the nucleus and attachment to pre-ribosomal complexes [93, 94]. Homologues of many yeast RP chaperones have been found in human cells: the Bcp1/BCCIP, Syo1/HEATR3, Rrb1/GRWD1, Sqt1/AMMP, and Tsr2/TSR2 proteins. However, others, such as Acl4 and Yar1, apparently were not preserved in multicellular organisms [78, 93, 95–98]. Notably, the ribosomal proteins RPL5 (uL18) and RPL11 (uL5) bind to pre-ribosomes as a subcomplex together with 5S rRNA [99]. Pre-5S rRNA is synthesized by RNA polymerase III, and maturation of its 3'-end requires the REX1, REX2, and REX3 exonucleases, as well as RPL5 [100–102]. In both yeast and humans, Rrs1/RRS1 and Rpf2/BXDC1 are required for 5S RNP integration into pre-60S complexes and the tumor suppressor protein PICT1/GLTSCR2 is an additional factor in human cells [102, 103]. The interaction of many RPs with pre-ribosomes is initially unstable, but the correct folding and formation of tertiary structures in rRNAs gradually lead to their stable incorporation into ribosomal complexes. A distinctive feature of ribosome assembly, which is preserved not only in eukaryotes, but also occurs during the synthesis of prokaryotic ribosomes [104], is the hierarchical incorporation of RPs, which promotes the sequential organization of individual subunit domains. First, proteins of the 5'-, central, and 3'-minor domains of 18S rRNA form the SSU body, and then the head and beak are assembled [105]. Similarly, RPs located on the LSU surface exposed to the solvent are incorporated in the structure at the first stages of assembly, while the proteins that bind to the intersubunit interface and central prominence are incorporated later [106]. The universal nature of the hierarchical incorporation of RPs suggests that the stepwise assembly, stabilization, and compaction of various ribosomal subunit domains are an important mechanism that ensures correct progression along the assembly pathway.

CONCLUSIONS AND OUTLOOK

For many years, the complex biogenesis pathway of the eukaryotic ribosome had been studied mostly in yeast cells, where the simplicity of genetic manipulations and the possibility of isolating large amounts of pre-ribosomal complexes for compositional and structural analysis provided a wealth of data on the fundamentals of ribosome assembly. Recent studies have confirmed that many stages of ribosome assembly in yeast and humans are important information about the specific biogenesis stages that have undergone adaptation during evolution. Although many of the factors necessary for human ribosome biogenesis have been identified, it is likely that the list of RAFs will significantly expand. The main challenge is to determine which of the factors necessary for ribosome synthesis are directly associated with pre-ribosomal complexes and to analyze the individual roles of such proteins during subunit assembly. Recent cryo-EM structures of yeast pre-ribosomes have provided a wealth of information on the temporal order, distribution, and molecular functions of many RAFs. Structural analyses of pre-ribosomes should significantly improve our understanding of human ribosome assembly. ●

This study was supported by the Russian Foundation for Basic Research (grant No. 20-04-00796 A "Analysis of the protein-nucleic composition of ribosomal subunit assembly intermediates in genetically modified human cells").

REFERENCES

1. Kater L., Thoms M., Barrio-Garcia C., Cheng J., Ismail S., Ahmed Y.L., Bange G., Kressler D., Berninghausen O., Sinning I., et al. // Cell. 2017. V. 171. № 7. P. 1599–1610.
2. Thoms M., Mitterer V., Kater L., Falquet L., Beckmann R., Kressler D., Hurt E. // Nat. Commun. 2018. V. 9. № 1. P. 1–13.
3. Coleman A.W. // Trends Genet. 2015. V. 31. № 3. P. 157–163.
4. Pillon M.C., Hsu A.L., Krahn J.M., Williams J.G., Goslen K.H., Sobhany M., Borgnia M.J., Stanley R.E. // Nat. Struct. Mol. Biol. 2019. V. 26. № 9. P. 830–839.
5. Pillon M.C., Lo Y.-H., Stanley R.E. // DNA Repair (Amst.). 2019. V. 81. e102653.
6. Baßler J., Hurt E. // Annu. Rev. Biochem. 2019. V. 88. № 1. P. 281–306.
7. Zhou D., Zhu X., Zheng S., Tan D., Dong M.-Q., Ye K. // Protein Cell. 2019. V. 10. № 2. P. 120–130.
8. Sanghai Z.A., Miller L., Molloy K.R., Barandun J., Hunziker M., Chaker-Margot M., Wang J., Chait B.T., Klinge S. // Nature. 2018. V. 556. № 7699. P. 126–129.
9. Greber B.J., Gerhardy S., Leitner A., Leibundgut M., Salem M., Boehringer D., Leulliot N., Aebersold R., Panse V.G., Ban N. // Cell. 2016. V. 164. № 1–2. P. 91–102.
10. Ma C., Wu S., Li N., Chen Y., Yan K., Li Z., Zheng L., Lei J., Woolford J.L., Gao N. // Nat. Struct. Mol. Biol. 2017. V. 24. № 3. P. 214–220.
11. Greber B.J., Boehringer D., Montellese C., Ban N. // Nat. Struct. Mol. Biol. 2012. V. 19. № 12. P. 1228–1233.
12. Correll C.C., Bartek J., Dundr M. // Cells. 2019. V. 8. № 8. e869.
13. Wu S., Tutuncuoglu B., Yan K., Brown H., Zhang Y., Tan D., Gamalinda M., Yuan Y., Li Z., Jakovljevic J., et al. // Nature. 2016. V. 534. № 7605. P. 133–137.
14. Klinge S., Woolford J.L. // Nat. Rev. Mol. Cell Biol. 2019. V. 20. № 2. P. 116–131.

15. Mullineux S.-T., Lafontaine D.L.J. // Biochimie. 2012. V. 94. № 7. P. 1521–1532.
16. Venema J., Tollervey D. // EMBO J. 1996. V. 15. № 20. P. 5701–5714.
17. Young C.L., Karbstein K. // RNA. 2011. V. 17. № 3. P. 512–521.
18. Lebaron S., Segerstolpe Å., French S.L., Dudnakova T., de lima Alves F., Granneman S., Rappsilber J., Beyer A.L., Wieslander L., Tollervey D. // Mol. Cell. 2013. V. 52. № 5. P. 707–719.
19. Granneman S., Petfalski E., Tollervey D. // EMBO J. 2011. V. 30. № 19. P. 4006–4019.
20. Sloan K.E., Bohnsack M.T. // Trends Biochem. Sci. 2018. V. 43. № 4. P. 237–250.
21. Rodríguez-Galán O., García-Gómez J.J., De la Cruz J. // Biochim. Biophys. Acta – Gene Regul. Mech. 2013. V. 1829. № 8. P. 775–790.
22. Turowski T.W., Tollervey D. // Wiley Interdiscip. Rev. RNA. 2015. V. 6. № 1. P. 129–139.
23. Koš M., Tollervey D. // Mol. Cell. 2010. V. 37. № 6. P. 809–820.
24. Allmang C., Tollervey D. // J. Mol. Biol. 1998. V. 278. № 1. P. 67–78.
25. Chaker-Margot M., Hunziker M., Barandun J., Dill B.D., Klinge S. // Nat. Struct. Mol. Biol. 2015. V. 22. № 11. P. 920–923.
26. Zhang L., Wu C., Cai G., Chen S., Ye K. // Genes Dev. 2016. V. 30. № 6. P. 718–732.
27. Barandun J., Chaker-margot M., Hunziker M., Molloy K.R., Chait B.T., Klinge S. // Nat. Struct. Mol. Biol. 2017. V. 24. № 11. P. 944–953.
28. Eppens N.A., Rensen S., Granneman S., Raué H.A., Venema J. // RNA. 1999. V. 5. № 6. P. 779–793.
29. Hierlmeier T., Merl J., Sauert M., Perez-Fernandez J., Schultz P., Bruckmann A., Hamperl S., Ohmayer U., Rachel R., Jacob A., et al. // Nucl. Acids Res. 2013. V. 41. № 2. P. 1191–1210.
30. Tafforeau L., Zorbas C., Langhendries J.-L., Mullineux S.-T., Stamatopoulou V., Mullier R., Wacheul L., Lafontaine D.L.J. // Mol. Cell. 2013. V. 51. № 4. P. 539–551.
31. Madru C., Lebaron S., Blaud M., Delbos L., Pipoli J., Pasmant E., Réty S., Leulliot N. // Genes Dev. 2015. V. 29. № 13. P. 1432–1446.
32. Baßler J., Ahmed Y.L., Kallas M., Kornprobst M., Calviño F.R., Gnädig M., Thoms M., Stier G., Ismail S., Kharde S., et al. // Protein Sci. 2017. V. 26. № 2. P. 327–342.
33. Asano N., Kato K., Nakamura A., Komoda K., Tanaka I., Yao M. // Nucl. Acids Res. 2015. V. 43. № 9. P. 4746–4757.
34. Kharde S., Calviño F.R., Gumiero A., Wild K., Sinning I. // Nucl. Acids Res. 2015. V. 43. № 14. P. 7083–7095.
35. Baßler J., Kallas M., Pertschy B., Ulbrich C., Thoms M., Hurt E. // Mol. Cell. 2010. V. 38. № 5. P. 712–721.
36. Hiraishi N., Ishida Y., Sudo H., Nagahama M. // Biochem. Biophys. Res. Commun. 2018. V. 495. № 1. P. 116–123.
37. Leidig C., Thoms M., Holdermann I., Bradatsch B., Berninghausen O., Bange G., Sinning I., Hurt E., Beckmann R. // Nat. Commun. 2014. V. 5. P. 3491–3499.
38. Baßler J., Paternoga H., Holdermann I., Thoms M., Granneman S., Barrio-Garcia C., Nyarko A., Stier G., Clark S.A., Schraivogel D., et al. // J. Cell Biol. 2014. V. 207. № 4. P. 481–498.
39. Matsuo Y., Granneman S., Thoms M., Manikas R.G., Tollervey D., Hurt E. // Nature. 2014. V. 505. № 7481. P. 112–116.
40. Sarkar A., Thoms M., Barrio-Garcia C., Thomson E., Flemming D., Beckmann R., Hurt E. // Nat. Struct. Mol. Biol. 2017. V. 24. № 12. P. 1107–1115.
41. Biedka S., Micic J., Wilson D., Brown H., Diorio-Toth L., Woolford J.L. // J. Cell Biol. 2018. V. 217. № 7. P. 2503–2518.
42. Rodríguez-Galán O., García-Gómez J.J., Kressler D., de la Cruz J. // RNA Biol. 2015. V. 12. № 8. P. 838–846.
43. Thomas F., Kutay U. // J. Cell Sci. 2003. V. 116. № 12. P. 2409–2419.
44. Trotta C.R., Lund E., Kahan L., Johnson A.W., Dahlberg J.E. // EMBO J. 2003. V. 22. № 11. P. 2841–2851.
45. Gadal O., Strauß D., Kessl J., Trumpower B., Tollervey D., Hurt E. // Mol. Cell. Biol. 2001. V. 21. № 10. P. 3405–3415.
46. Nerurkar P., Altvater M., Gerhardy S., Schütz S., Fischer U., Weirich C., Panse V.G. // Int. Rev. Cell Mol. Biol. 2015. V. 319. P. 107–140.
47. Ghalei H., Trepreau J., Collins J.C., Bhaskaran H., Strunk B.S., Karbstein K. // Mol. Cell. 2017. V. 67. № 6. P. 990–1000.
48. Lebaron S., Schneider C., van Nues R.W., Swiatkowska A., Walsh D., Böttcher B., Granneman S., Watkins N.J., Tollervey D. // Nat. Struct. Mol. Biol. 2012. V. 19. № 8. P. 744–753.
49. Strunk B.S., Novak M.N., Young C.L., Karbstein K. // Cell. 2012. V. 150. № 1. P. 111–121.
50. Hernandez-Verdun D., Roussel P., Thiry M., Sirri V., Lafontaine D.L.J. // Wiley Interdiscip. Rev. RNA. 2010. V. 1. № 3. P. 415–431.
51. Boisvert F.-M., van Koningsbruggen S., Navascués J., Lamond A.I. // Nat. Rev. Mol. Cell Biol. 2007. V. 8. № 7. P. 574–585.
52. Andersen J.S., Lam Y.W., Leung A.K.L., Ong S.-E., Lyon C.E., Lamond A.I., Mann M. // Nature. 2005. V. 433. № 7021. P. 77–83.
53. Preußner M., Heyd F. // Pflugers Arch. Eur. J. Physiol. 2016. V. 468. № 6. P. 983–991.
54. Sinturel F., Gerber A., Mauvoisin D., Wang J., Gatfield D., Stubblefield J.J., Green C.B., Gachon F., Schibler U. // Cell. 2017. V. 169. № 4. P. 651–663.
55. Fernández-Pevida A., Kressler D., de la Cruz J. // Wiley Interdiscip. Rev. RNA. 2015. V. 6. P. 191–209.
56. Stępiński D. // Histochem. Cell Biol. 2018. V. 150. № 6. P. 607–629.
57. Carron C., O'Donohue M.F., Choesmel V., Faubladier M., Gleizes P.E. // Nucl. Acids Res. 2011. V. 39. № 1. P. 280–291.
58. Preti M., O'Donohue M.F., Montel-Lehry N., Bortolin-Cavaillé M.L., Choesmel V., Gleizes P.E. // Nucl. Acids Res. 2013. V. 41. № 8. P. 4709–4723.
59. Sloan K.E., Mattijssen S., Lebaron S., Tollervey D., Pruijn G.J.M., Watkins N.J. // J. Cell Biol. 2013. V. 200. № 5. P. 577–588.
60. Hölzel M., Rohrmoser M., Schlee M., Grimm T., Harasim T., Malamoussi A., Gruber-Eber A., Kremmer E., Hiddemann W., Bornkamm G.W., et al. // J. Cell Biol. 2005. V. 170. № 3. P. 367–378.
61. Finkbeiner E., Haindl M., Muller S. // EMBO J. 2011. V. 30. № 6. P. 1067–1078.
62. Kellner M., Rohrmoser M., Forné I., Voss K., Burger K., Mühl B., Gruber-Eber A., Kremmer E., Imhof A., Eick D. // Exp. Cell Res. 2015. V. 334. № 1. P. 146–159.
63. Sloan K.E., Leisegang M.S., Doebele C., Ramírez A.S.,

Simm S., Safferthal C., Kretschmer J., Schorge T., Markoutsa S., Haag S., et al. // Nucl. Acids Res. 2015. V. 43. № 1. P. 553–564.
64. Lapik Y.R., Fernandes C.J., Lau L.F., Pestov D.G. // Mol. Cell. 2004. V. 15. № 1. P. 17–29.
65. Strezoska Ž., Pestov D.G., Lau L.F. // Mol. Cell. Biol. 2000. V. 20. № 15. P. 5516–5528.
66. Strezoska Z., Pestov D.G., Lau L.F. // J. Biol. Chem. 2002. V. 277. № 33. P. 29617–29625.
67. Robledo S., Idol R.A., Crimmins D.L., Ladenson J.H., Mason P.J., Bessler M. // RNA. 2008. V. 14. № 9. P. 1918–1929.
68. Wang M., Anikin L., Pestov D.G. // Nucl. Acids Res. 2014. V. 42. № 17. P. 11180–11191.
69. Saveanu C., Namane A., Gleizes P.-E., Lebreton A., Rousselle J.-C., Noaillac-Depeyre J., Gas N., Jacquier A., Fromont-Racine M. // Mol. Cell. Biol. 2003. V. 23. № 13. P. 4449–4460.
70. Talkish J., Campbell I.W., Sahasranaman A., Jakovljevic J., Woolford J.L. // Mol. Cell. Biol. 2014. V. 34. № 10. P. 1863–1877.
71. Kallstrom G., Hedges J., Johnson A. // Mol. Cell. Biol. 2003. V. 23. № 12. P. 4344–4355.
72. Badertscher L., Wild T., Montellese C., Alexander L.T., Bammert L., Sarazova M., Stebler M., Csucs G., Mayer T.U., Zamboni N., et al. // Cell Rep. 2015. V. 13. № 12. P. 2879–2891.
73. Nieto B., Gaspar S.G., Moriggi G., Pestov D.G., Bustelo X.R., Dosil M. // Nat. Commun. 2020. V. 11. P. 156–173.
74. Farley-Barnes K.I., McCann K.L., Ogawa L.M., Merkel J., Surovtseva Y.V., Baserga S.J. // Cell Rep. 2018. V. 22. № 7. P. 1923–1934.
75. Morello L.G., Coltri P.P., Quaresma A.J.C., Simabuco F.M., Silva T.C.L., Singh G., Nickerson J.A., Oliveira C.C., Moore M.J., Zanchin N.I.T. // PLoS One. 2011. V. 6. № 12. e29174.
76. Kressler D., Hurt E., Bergler H., Baßler J. // Biochim. Biophys. Acta – Mol. Cell Res. 2012. V. 1823. № 1. P. 92–100.
77. Raman N., Weir E., Müller S. // Mol. Cell. 2016. V. 64. № 3. P. 607–615.
78. Bohnsack K.E., Bohnsack M.T. // EMBO J. 2019. V. 38. № 13. e100278.
79. Choudhury P., Hackert P., Memet I., Sloan K.E., Bohnsack M.T. // RNA Biol. 2019. V. 16. № 1. P. 54–68.
80. Sardana R., Liu X., Granneman S., Zhu J., Gill M., Papoulas O., Marcotte E.M., Tollervey D., Correll C.C., Johnson A.W. // PLoS Biol. 2015. V. 13. № 2. e1002083.
81. Martin R., Straub A.U., Doebele C., Bohnsack M.T. // RNA Biol. 2013. V. 10. № 1. P. 4–18.
82. Srivastava L., Lapik Y.R., Wang M., Pestov D.G. // Mol. Cell. Biol. 2010. V. 30. № 12. P. 2947–2956.
83. Calo E., Flynn R.A., Martin L., Spitale R.C., Chang H.Y., Wysocka J. // Nature. 2015. V. 518. № 7538. P. 249–253.
84. Bammert L., Jonas S., Ungricht R., Kutay U. // Nucl. Acids Res. 2016. V. 44. № 20. P. 9803–9820.
85. Memet I., Doebele C., Sloan K.E., Bohnsack M.T. // Nucl. Acids Res. 2017. V. 45. № 9. P. 5359–5374.
86. Bohnsack M.T., Martin R., Granneman S., Ruprecht M., Schleiff E., Tollervey D. // Mol. Cell. 2009. V. 36. № 4. P. 583–592.
87. Pertschy B., Schneider C., Gnädig M., Schäfer T., Tollervey D., Hurt E. // J. Biol. Chem. 2009. V. 284. № 50. P. 35079–35091.
88. Wandrey F., Montellese C., Koos K., Badertscher L., Bammert L., Cook A.G., Zemp I., Horvath P., Kutay U. // Mol. Cell. Biol. 2015. V. 35. № 20. P. 3491–3503.
89. Ameismeier M., Cheng J., Berninghausen O., Beckmann R. // Nature. 2018. V. 558. № 7709. P. 249–253.
90. Reuveni S., Ehrenberg M., Paulsson J. // Nature. 2017. V. 547. № 7663. P. 293–297.
91. Li B., Nierras C.R., Warner J.R. // Mol. Cell Biol. 1999. V. 8. P. 5393–5404.
92. Mayer C., Grummt I. // Oncogene. 2006. V. 25. P. 6384–6391.
93. Pillet B., Mitterer V., Kressler D., Pertschy B. // BioEssays. 2017. V. 39. № 1. P. 1–12.
94. Landry-Voyer A.M., Bergeron D., Yague-Sanz C., Baker B., Bachand F. // Nucl. Acids Res. 2020. V. 48. № 22. P. 12900–12916.
95. Pausch P., Singh U., Ahmed Y.L., Pillet B., Murat G., Altegoer F., Stier G., Thoms M., Hurt E., Sinning I., et al. // Nat. Commun. 2015. V. 6. e7494.
96. Pillet B., García-Gómez J.J., Pausch P., Falquet L., Bange G., de la Cruz J., Kressler D. // PLoS Genet. 2015. V. 11. № 10. e1005565.
97. Schütz S., Fischer U., Altvater M., Nerurkar P., Peña C., Gerber M., Chang Y., Caesar S., Schubert O.T., Schlenstedt G., et al. // Elife. 2014. V. 3. e03473.
98. Wyler E., Wandrey F., Badertscher L., Montellese C., Alper D., Kutay U. // FEBS Lett. 2014. V. 588. № 20. P. 3685–3691.
99. Calviño F.R., Kharde S., Ori A., Hendricks A., Wild K., Kressler D., Bange G., Hurt E., Beck M., Sinning I. // Nat. Commun. 2015. V. 6. P. 6510.
100. van Hoof A., Lennertz P., Parker R. // EMBO J. 2000. V. 19. № 6. P. 1357–1365.
101. Ciganda M., Williams N. // Wiley Interdiscip. Rev. RNA. 2011. V. 2. № 4. P. 523–533.
102. Sloan K.E., Bohnsack M.T., Watkins N.J. // Cell Rep. 2013. V. 5. № 1. P. 237–247.
103. Zhang J., Harnpicharnchai P., Jakovljevic J., Tang L., Guo Y., Oeffinger M., Rout M.P., Hiley S.L., Hughes T., Woolford J.L. // Genes Dev. 2007. V. 21. № 20. P. 2580–2592.
104. Chen S.S., Williamson J.R. // J. Mol. Biol. 2013. V. 425. № 4. P. 767–779.
105. O'Donohue M.F., Choesmel V., Faubladier M., Fichant G., Gleizes P.E. // J. Cell Biol. 2010. V. 190. № 5. P. 853–866.
106. Nicolas E., Parisot P., Pinto-Monteiro C., De Walque R., De Vleeschouwer C., Lafontaine D.L.J. // Nat. Commun. 2016. V. 7. e11390.

Dedicated to the 120th anniversary of Academician Alexander Evseevich Braunstein's birth

Citrobacter freundii Methionine γ-Lyase: The Role of Serine 339 in the Catalysis of γ- and β-Elimination Reactions

N. V. Anufrieva[1], E. A. Morozova[1], S. V. Revtovich[1], N. P. Bazhulina[1], V. P. Timofeev[1], Ya. V. Tkachev[1], N. G. Faleev[2], A. D. Nikulin[3], T. V. Demidkina[1*]

[1]Engelhardt Institute of Molecular Biology of the Russian Academy of Sciences, Moscow, 119991 Russia

[2]Nesmeyanov Institute of Organoelement Compounds of the Russian Academy of Sciences, Moscow, 119991 Russia

[3]Institute of Protein Research of the Russian Academy of Sciences, Pushchino, Moscow Region, 142290 Russia

*E-mail: tvdemidkina@yandex.ru

Received: October 22, 2020; in final form, July 21, 2021

DOI: 10.32607/actanaturae.11242

ABSTRACT **Serine 339 of the active site of *Citrobacter freundii* methionine γ-lyase (MGL) is a conserved amino acid in most pyridoxal 5'-phosphate-dependent enzymes of the cystathionine β-lyase subclass, to which MGL belongs. The reaction mechanism of the MGL-catalyzed γ-elimination reaction is poorly explored. We replaced serine 339 with alanine using site-directed mutagenesis. The replacement of serine 339 with alanine led to a significant (by two orders of magnitude) decrease in efficiency in the catalysis of the γ- and β-elimination reactions by the mutant form of the enzyme. The exchange rates of the C-α- and C-β-protons in the amino acids in complexes consisting of the enzyme and competitive inhibitors decreased by one-two orders of magnitude. The spectral characteristics of the mutant form indicated that the replacement did not lead to significant changes in the conformation and tautomerism of MGL internal aldimine. We crystallized the holoenzyme and determined its spatial structure at 1.7 Å resolution. The replacement of serine 339 with alanine did not affect the overall course of the polypeptide chain of the MGL subunit and the tetrameric enzyme structure. An analysis of the obtained kinetic and spectral data, as well as the known spatial structures of *C. freundii* MGL, indicates that serine 339 is necessary for efficient catalysis of γ- and β-elimination reactions at the stage of C-α-proton abstraction from the external aldimine, the γ-elimination reaction at the stages of coenzyme C4'-atom protonation, and C-β-proton abstraction from a ketimine intermediate.**

KEYWORDS **methionine γ-lyase, pyridoxal 5'-phosphate, Ser339, mutant form, kinetic parameters, spectral characteristics, spatial structure.**

ABBREVIATIONS **MGL – methionine γ-lyase; PLP – pyridoxal 5'-phosphate; Ser339Ala – a mutant form of the enzyme with Ser339 replaced by Ala; LDH – lactate dehydrogenase; HOHxoDH – D-2-hydroxyisocaproate dehydrogenase; NADH – reduced nicotinamide adenine dinucleotide.**

INTRODUCTION

Pyridoxal 5'-phosphate (PLP)-dependent enzymes underlie the vital activity of most pro- and eukaryotic organisms. These biocatalysts are characterized by the ability to perform a wide range of the chemical transformations of amino acids and amines with the involvement of the coenzyme. The substrate and reaction specificity of each particular enzyme is ensured by the interaction of the cofactor and substrate with the apoenzyme. Studies of PLP-dependent enzymes and data on X-ray analysis have significantly improved our knowledge of the structure–function relationship in enzymatic catalysis and enabled, as early as 1995, the use of a rational de-

sign for changing the substrate specificity in PLP-dependent catalysis [1]. Our ability to determine the crystal structures of PLP-dependent enzymes belonging to different classes has expanded our knowledge about critical residues for chemically different enzymatic reactions and engendered a number of basic ideas about biocatalysis. Replacement of the coenzyme-binding protein matrix by a matrix of the immunoglobulin superfamily has demonstrated the relevance of our main conclusions about the mechanisms of amino acid conversion by these enzymes and the possibility of predicting the changes taking place in the enzymatic activity [2–5].

Methionine γ-lyase (MGL, EC 4.4.1.11) is a PLP-dependent enzyme that catalyzes the γ-elimination reaction of L-methionine, the β-elimination reaction of L-cysteine, and their S-substituted derivatives, as well as the γ- and β-replacement reactions of L-methionine, L-cysteine, and their analogs [6, 7]. The enzyme is found in pathogenic protozoa eukaryotes [8, 9], a number of bacteria, in particular pathogenic ones [10–14], fungi [15], and plants [16].

Recently, we showed that MGL catalyzes the β-elimination reaction of S-substituted cysteine sulfoxide derivatives to form thiosulfinates [17, 18]. Thiosulfinates produced by a "pharmacological pair" MGL/S-substituted L-cysteine sulfoxide exhibited antibacterial activity against a number of bacteria *in vitro* [18–20] and *Pseudomonas aeruginosa in vivo* [21]. The applicability of the enzyme as an antitumor agent has been demonstrated *in vitro* and *in vivo* [22–25].

The mechanisms of the MGL-catalyzed physiological reaction, the β-elimination reaction, and replacement reactions are poorly understood. Aside from its contribution to basic enzymology, investigation of these mechanisms is necessary for the development of new antibacterial and anticancer drugs.

MGL belongs to a cystathionine β-lyase subclass with fold type I of PLP-dependent enzymes [26]. In a tetrameric MGL molecule formed by four identical polypeptide chains, two subunits form two so-called "catalytic dimers", each of which contains two active centers composed of amino acid residues from two subunits [27, 28].

Determination of the three-dimensional structures of the complexes between MGL and the competitive inhibitors, glycine [29], cycloserine [30], and norleucine [31, 32] has showed that the active site residue Ser339, which is conserved in the cystathionine β-lyase subclass, is most likely involved in the catalytically optimal orientation of the Lys210 side chain that binds the coenzyme.

To investigate the role of Ser339 in the catalysis of γ- and β-elimination reactions, a mutant form of the enzyme, with replacement of the serine residue with alanine (Ser339Ala MGL), was prepared by site-directed mutagenesis and the spatial holoenzyme structure, the steady- state kinetic parameters of the γ- and β-elimination reactions of several substrates, the exchange rates of the C-α- and C-β-protons in the complexes of Ser339Ala MGL with the inhibitors, and the spectral characteristics of the mutant form were determined.

EXPERIMENTAL

Reagents and materials

In this study, we used L-methionine, L-norvaline, L-norleucine, L-α-aminobutyric acid, glycine, L-alanine, L-homoserine, L-homocysteine, L-phenylalanine, DL-penicillamine, phenylmethylsulfonyl fluoride, lactate dehydrogenase (LDH) from rabbit muscle, dithiothreitol (DTT), reduced nicotinamide adenine dinucleotide (NADH), and D_2O (Sigma, USA); pyridoxal 5'-phosphate (Merck, Germany); S-ethyl-L-cysteine, S-methyl-L-cysteine, S-benzyl-L-cysteine, ethylenediaminetetraacetic acid (EDTA), protamine sulfate, sodium dodecyl sulfate (SDS) (Serva, USA); lactose (Panreac, Spain); glucose, glycerin, magnesium sulfate, ammonium sulfate, monobasic potassium phosphate, dibasic sodium phosphate, acetic acid, acetic anhydride, triethanolamine, $HClO_4$ (Reakhim, Russia); yeast extract, tryptone (Difco, USA); DEAE-cellulose (Whatmann, UK), superdex 200 (Amersham Biosciences, Sweden); Bluescript II SK(+/–) and pET28 plasmids (Novagen, USA); a DNA isolation kit and Bsp119I and BveI restriction enzymes (Fermentas, Lithuania). O-acetyl-L-homoserine was obtained by acetylation of L-homoserine [33]; D-2-hydroxyisocaproate dehydrogenase (HOHxoDH) was produced as described in [34].

Site-directed mutagenesis

Site-directed mutagenesis was performed using the polymerase chain reaction (PCR). The mglBlue plasmid produced by cloning the MGL gene into the Bluescript II SK(+/–) vector was used as a template in PCR. The replacement of Ser339 with alanine was performed using the following synthetic oligonucleotides (F is a forward primer, and R is a reverse primer):

(F) TATCAGCTTCGAATCGCTGGC
(RS339/A) GTATCACCGAGAGCGACCGCGA
(FS339/A) TCGCGGTCGCTCTCGGTGATAC
(R) ATACCTGCTTTAAGCCGCTCTTCTGGCGCA

After PCR, the amplicon was isolated from the reaction mixture using a DNA isolation kit. The purified DNA sample was treated with the restriction en-

donucleases Bsp119I and BveI and ligated with the mglBlue vector treated with the same enzymes. The resulting mixture was transformed by electroporation into *Escherichia coli* DH10B cells and grown on a solid medium (1.8% agar in Luria–Bertani (LB) medium with ampicillin). Grown colonies were transferred into a liquid LB medium supplemented with ampicillin and grown for 15–18 h. Plasmid DNA was isolated using a plasmid isolation kit and identified by analytical restriction. The fragment containing the Ser339Ala substitution was re-cloned from the mglBlue plasmid into the pET28 plasmid. The cloning accuracy was controlled by sequencing the DNA insert (Genome Center for Collective Use, Moscow). *E. coli* BL21 (DE3) cells were transformed with a plasmid containing the required insert.

Bacterial mass cultivation and enzyme purification

Cultivation of *E. coli* BL21 (DE3) cells containing the plasmid with the mutant gene and enzyme purification were performed as described previously [35]. The concentration of the purified enzyme was determined by absorption at 278 nm using the absorption coefficient $A_{1cm}^{0.1\%} = 0.8$ [36].

The homogeneity of samples was examined by PAGE electrophoresis under denaturing conditions [37]. During purification, activity was determined in the β-elimination reaction; activity of the final sample was determined in β- and γ-elimination reactions. The reaction mixture contained a 100-mM potassium phosphate buffer, pH 8.0, 0.1 mM PLP, 1 mM DTT, 0.2 mM NADH, 10 U LDH, and 30 mM S-ethyl-L-cysteine (the β-elimination reaction) or 70 μg HOHxoDH and 30 mM L-methionine (the γ-elimination reaction). The amount of enzyme that catalyzes the formation of 1.0 μM/min of keto acid was defined as the unit of enzymatic activity. Enzyme samples of 95% purity had a specific activity of 0.31 U/mg in the γ-elimination reaction of L-methionine and 1.03 U/mg in the β-elimination reaction of S-ethyl-L-cysteine.

Kinetic studies

The kinetic parameters of the γ- and β-elimination reactions were determined at 30°C in the conjugate reaction with HOHxoDH or LDH based on a decrease in NADH absorbance at 340 nm ($\Delta\varepsilon = 6{,}220\ M^{-1}cm^{-1}$). The reaction mixtures contained a 100-mM potassium phosphate buffer, pH 8.0, 0.1 mM PLP, 1 mM DTT, 0.2 mM NADH, 70 μg HOHxoDH or 10 U LDH, and variable amounts of the substrate in a total volume of 1 mL. The reaction was initiated by the addition of 10 μg of the enzyme.

Inhibition of the γ-elimination reaction of L-methionine by various amino acids was investigated under the conditions described above, with varying amounts of an inhibitor in the samples.

The kinetic parameters were calculated according to the Michaelis–Menten equation using the EnzFitter software [38]. In the calculations, an enzyme subunit molecular weight of 43 kDa was used. The inhibition constants were also determined using the EnzFitter software [38].

Isotope exchange of the C-α- and C-β-protons in the enzyme complexed with the inhibitors

The kinetics of isotope exchange reactions of the C-α- and C-β-protons for deuteron in inhibitors, catalyzed by the mutant form, was detected using ^{1}H NMR spectroscopy. The reaction was conducted in D_2O containing 50 mM potassium phosphate (pD = 7.6), 0.1 mM PLP, and an inhibitor in a total volume of 0.5 mL at 30°C at L-alanine and L-norleucine concentrations of 144.23 mM and 98.04 mM, respectively. The reaction was initiated by adding 0.3–0.7 mg of the enzyme. ^{1}H NMR spectra were recorded at fixed time intervals on a Bruker AMXIII-400 spectrometer at an operating frequency of 400 MHz. The signals of the C-α- and C-β-protons were integrated using the modified Enzkin computer program, which is a part of the XWIN-NMR programs. The kinetic curves of the yields of deuterated products were processed according to the method described in [39].

Isotopic exchange of glycine protons was performed in D_2O, pD 7.6, containing 50 mM potassium phosphate, 0.1 mM PLP, 60 mg glycine, and 3.6 mg of the enzyme. After incubation at 30°C for 72 h, the enzyme was inactivated by heating (90°C, 5 min) and separated by centrifugation. The solvent was removed on a rotary evaporator. To determine the configuration at the Cα-atom, the deuterated product was converted into a dipeptide, L-phenylalanyl-[D]-glycine, in the reaction with Boc-L-Phe-ONp [40, 41]. The dipeptide was dissolved in 0.5 mL of D_2O, and the ^{1}H NMR spectrum was collected on a Bruker AMX III-400 spectrometer at an operating frequency of 400 MHz.

Spectral studies

The absorption spectra of the holoenzyme in a complex with methionine were acquired at 25°C on a Cary-50 spectrophotometer (Varian, USA) in a 50-mM potassium phosphate buffer, pH 8.0, containing 1 mM DTT, 1 mM EDTA, and 20 mM L-methionine at an enzyme concentration of 1 mg/mL.

Preparation of the holoenzyme and apoenzyme

The apoenzyme and holoenzyme were prepared in a 50-mM potassium phosphate buffer, pH 8.0, containing 1 mM DTT and 1 mM EDTA. The holoenzyme

was prepared by adding a 50-fold molar excess of PLP. The mixture was incubated at 25°C for 1 h. The excess PLP was removed by dialysis. The apoenzyme was prepared by adding a 100-fold molar excess of DL-penicillamine to the sample [42]. The mixture was incubated at 25°C for 1 h. DL-Penicillamine was removed by dialysis. The procedure was repeated until the enzyme activity decreased to 1% of the initial activity. The PLP content in the sample was determined in 100 mM NaOH using the molar extinction coefficient of PLP at 390 nm (ε = 6,600 $M^{-1}cm^{-1}$ [43]).

Determination of the coenzyme dissociation constant

The PLP dissociation constant was determined by ultrafiltration [44]. Varying amounts of PLP (in a range of 5×10^{-3} to 1.2×10^{-1} mM) were added to the 8×10^{-3} mM apoenzyme in a 50-mM potassium phosphate buffer, pH 8.0, containing 1 mM DTT and 1 mM EDTA. After incubation at 30°C for 30 min, free PLP was separated by centrifugation in a Centricon-30 microconcentrator (Amicon, United States) at 5,000 rpm and 4°C for 5 min. The PLP content in each sample was determined in 100 mM NaOH. The data were processed in Scatchard coordinates [45].

Crystallization and data collection

Ser339Ala MGL crystals were produced by vapor diffusion in a hanging drop under the conditions presented in [28]. Crystals suitable for the acquisition of diffraction data formed within 10 days and had a rhombic shape. Diffraction data were recorded on a synchrotron radiation source at BESSY BEAMLINE 14.1 (Berlin, Germany) using a MARMOSAIC 225 mm CCD detector at 100 K and processed in the XDS software package [46] (*Table 1*).

Determination and refinement of the Ser339Ala MGL spatial structure

The structure of Ser339Ala MGL was solved by molecular replacement using the CCP4 software package [47]. As a model, we used the previously determined structure of *C. freundii* MGL (1.35 Å, PDB code 2RFV) where mobile enzyme regions, water molecules, and the coenzyme were excluded. An electron density map was calculated for the produced model. To further calculate the structure, we used the Phenix refinement protocols [48] with energy minimization and optimization of the model's geometry, followed by manual rebuilding in the COOT program [49]. To control the refinement process, we used the model reliability factor R_{free} calculated from 5% of the reflections excluded from the refinement. The final model was refined to a resolution of 1.70 Å with the R_{work} and R_{free} parameters of 17.3% and 20.5%, respectively. The model contained 2,879 non-hydrogen atoms and 393 water molecules; the Lys210 side chain was covalently linked to PLP. An excess electron density was present near the sulfur atom in three cysteines (Cys4, Cys193, and Cys245), indicating their oxidized states, after which they were replaced with 3-sulfenoalanines. The structure was deposited into the protein data bank (PDB code 5D5S); the statistics of structure refinement are shown in *Table 1*.

Table 1. X-ray data collection and refinement statistics of Ser339Ala MGL

Space group	I222
Unit cell parameters, Å	a = 56.66, b = 123.09, c = 128.79 $\alpha = \beta = \gamma = 90°$
Wavelength, Å	0.91841
Resolution, Å	30.0–1.70 (1.79–1.70)
Completeness, %	99.4 (97.5)
Redundancy	7.0 (6.3)
R_{merge}, %	4.5 (34.9)
Disordered amino acid residues in the protein	1, 46–61, 398
Number of non-hydrogen atoms in the protein	2,879
Number of water molecules	393
Number of unique reflections	49,574 (7,001)
R/R_{free}	0.173/0.205 (0.243/0.285)
Average temperature B-factor, Å solvent macromolecule	 29.28 27.51 41.64
Root mean deviation	
bond lengths	0.007 Å
bond angles	1.095°
chiral angles	0.047°
planar angles	0.005°
Ramachandran plot, residues in	
most favorable regions, %	98.64
additional allowed regions, %	1.36
outlier region, %	0.0

Values in parentheses are for the highest resolution shell.

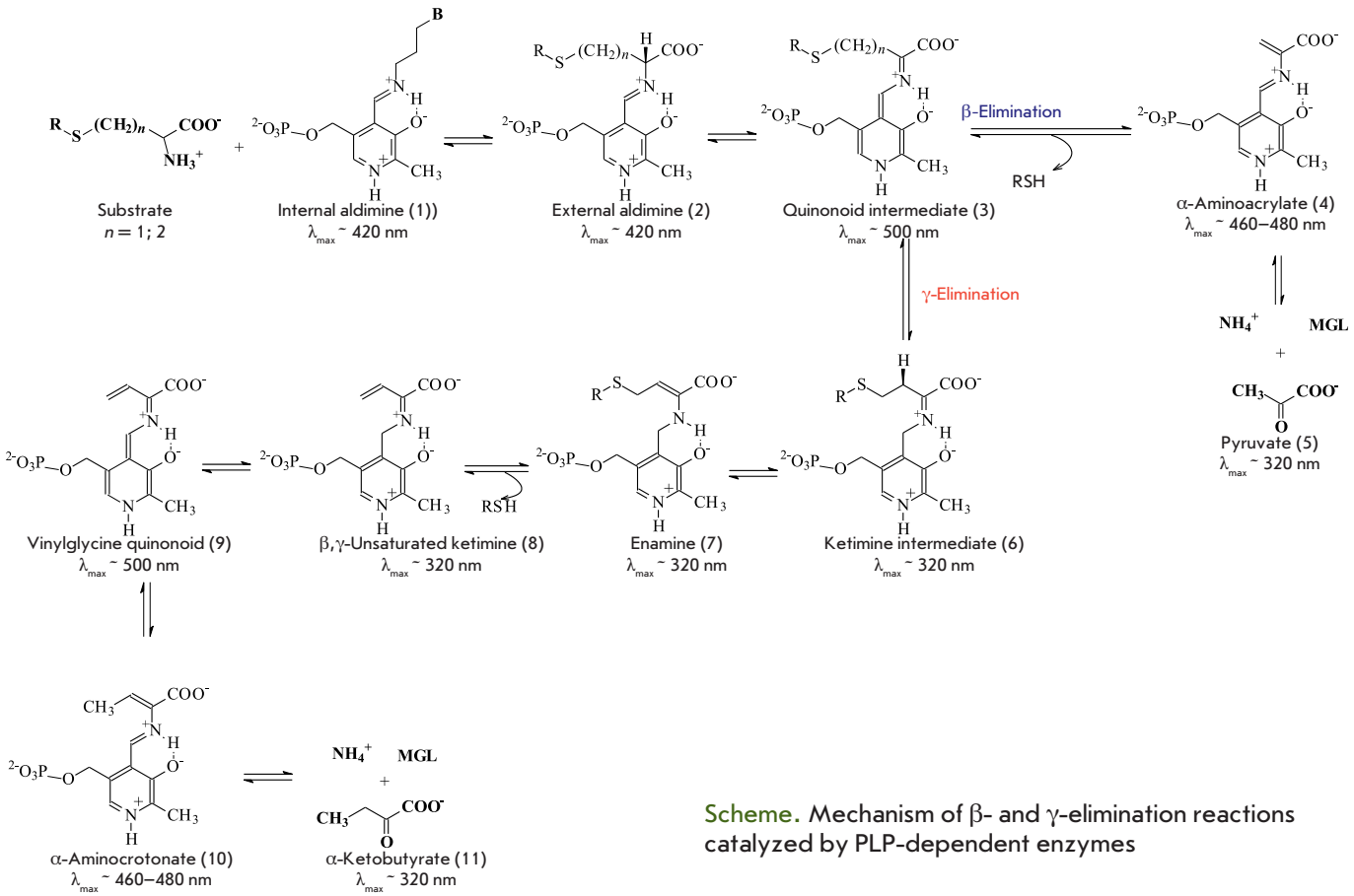

Scheme. Mechanism of β- and γ-elimination reactions catalyzed by PLP-dependent enzymes

RESULTS AND DISCUSSION

The mechanism of the γ- and β-elimination reactions, shown in Scheme 1, was proposed in [50] and [51]. Because of the presence of the coenzyme, PLP-dependent enzymes have unique spectral properties that enable the identification of the reaction intermediates. The main absorption bands of an internal aldimine and intermediates of the γ- and β-elimination reactions are shown in *Scheme* according to [52].

In PLP-dependent enzymes catalyzing various reactions that start with C-α-proton abstraction in the external aldimine, the lysine residue that binds the coenzyme is the base accepting this proton. In the β-elimination reaction of sulfur-containing amino acids, which is catalyzed by cystathionine γ-lyase subclass enzymes, the coenzyme-binding lysine residue was supposed to be also a general acid catalyst at the stage of leaving group elimination [51, 53].

In [54], the coenzyme-binding the lysine residue of cystathionine γ-lyase was thought to transfer a proton from the Cα-atom to the C4'-atom of PLP. Given the obtained structural data, the authors concluded that the side chain of this residue "swings like a liana" to either the Cα-, C4'-, or Cβ-atoms of the substrate, and that its ε-amino group is also a base that accepts the C-β-proton.

An analysis of the spatial structure of *C. freundii* MGL complexed with glycine, which models the structure of an external aldimine, suggested that the PLP-binding Lys210 provides both the 1,3-prototropic shift of the C-α-proton and abstraction of the C-α-proton [29]. Investigation of a *Pseudomonas putida* MGL mutant form with substitution of active site tyrosine 114 with phenylalanine showed that Tyr114 most likely acted as a general acid catalyst at the stage of leaving group elimination [50].

In [56], the authors analyzed the spatial structures of four intermediates formed during the interaction of *Entamoeba hystolytica* MGL with L-methionine and proposed a γ-elimination reaction mechanism different from the above scheme, which excluded the stages of two quinonoid intermediates (*Scheme 1*, intermediates 3 and 9). This mechanism assumes the formation of α-aminocrotonate following β,γ-unsaturated ketimine due to a 1,5-sigmatropic proton shift from the C4'-atom to the Cγ-atom, which does not require catalysis.

Table 2. Kinetic parameters of γ- and β-elimination reactions

Substrate	MGL, wild type			MGL, Ser339Ala		
	k_{cat}, s^{-1}	K_M, mM	k_{cat}/K_M, $M^{-1}s^{-1}$	k_{cat}, s^{-1}	K_M, mM	k_{cat}/K_M, $M^{-1}s^{-1}$
L-Met	6.2 ± 0.42*	0.7 ± 0.11*	8.85×10^3	0.21 ± 0.002	1.84 ± 0.15	1.77×10^2
DL-Hcy	8.51 ± 0.41*	0.97 ± 0.15*	8.77×10^3	0.28 ± 0.009	3.39 ± 0.34	8.25×10^1
S-Et-L-Hcy	6.78 ± 0.02*	0.54 ± 0.01*	1.25×10^4	0.16 ± 0.0016	0.54 ± 0.037	2.92×10^2
O-Ac-L-Hse	2.1 ± 0.053**	2.91 ± 0.18**	7.21×10^2	0.77 ± 0.011	2.07 ± 0.22	3.73×10^2
S-Met-L-Cys	4.6 ± 0.29*	0.71 ± 0.11*	6.48×10^3	0.41 ± 0.018	21.8 ± 2.25	1.88×10^1
S-Et-L-Cys	5.03 ± 0.16*	0.17 ± 0.02*	2.96×10^4	0.67 ± 0.024	6.47 ± 0.54	1.04×10^2
S-Bzl-L-Cys	8.16 ± 0.23*	0.18 ± 0.02*	4.53×10^4	1.81 ± 0.094	5.76 ± 0.59	3.14×10^2
O-Ac-L-Ser	2.13 ± 0.037***	4.28 ± 0.33***	4.98×10^2	0.047 ± 0.001	16.36 ± 1.09	2.87

*Data from [35].
**Data from [36].
***Data from [57].

Table 3. Inhibition of the γ-elimination reaction of L-methionine and the kinetic parameters of isotopic exchange of the C-α- and C-β-protons in inhibitors

Amino acid	MGL, wild type			MGL, Ser339Ala			Number of exchanged C-α- and C-β-protons
	K_I, mM	k_{ex}, s^{-1} $K_M = K_P$, mM		K_I, mM	k_{ex}, s^{-1} $K_M = K_P$, mM		
		α-H	β-H		α-H	β-H	
Gly	48.49 ± 4.37*	20.2*	–	22.87 ± 2.84	0.078	–	1, *pro*-(R) proton**
L-Ala	3.41 ± 0.40*	2.71*	2.63*	1.25 ± 0.32	0.387	0.116	1; 3
L-α-Abu	8.01 ± 0.76*	–	–	4.66 ± 0.51	–	–	
L-Nva	4.60 ± 0.43*	–	–	1.7 ± 0.32	–	–	
L-Nle	0.6 ± 0.06*	41.8*	4.74*	0.89 ± 0.09	0.46	0.12	1; 2

K_I is the inhibition constant; K_M is the Michaelis constant; K_P is the product inhibition constant which characterizes the binding of the enzyme to the product of the isotope exchange.
*Data from [36].
**Data from [40].

Steady-state kinetic parameters, inhibition of the γ-elimination reaction, and exchange of C-α- and C-β-protons in Ser339Ala MGL complexes with inhibitors

Table 2 shows the steady-state kinetic parameters of γ- and β-elimination reactions catalyzed by the wild-type MGL [35, 36, 57] and mutant form. Compared with the wild-type enzyme, substitution of Ser339 with Ala led to a decrease in the rates of β-elimination by 5- to 10-fold and γ-elimination by 30- to 40-fold. The K_M values increased more for substrates containing a leaving group in the β-position, and, as a result, the catalytic efficiency for both reactions decreased equally by two orders of magnitude, on average. In the case of substrates with a good leaving group, the catalytic efficiency of the mutant form in the γ-elimination reaction is comparable to that of the wild-type MGL but the k_{cat}/K_M parameter is two orders of magnitude lower in the β-elimination reaction of O-Ac-L-Ser.

Glycine, L-alanine, L-α-aminobutyric acid, L-norvaline, and L-norleucine are competitive inhibitors of the physiological reaction for both the mutant enzyme and the wild-type enzyme. The inhibition constants were found to be comparable to those of the wild-type MGL (*Table 3*).

The data of isotopic exchange of substrate and inhibitor protons enable an assessment of the contribution of individual stages to the enzymatic reaction and the elucidation of the stereochemistry of the proton exchange. *Table 3* summarizes the rates of C-α- and C-β-proton exchange in the inhibitors, which was

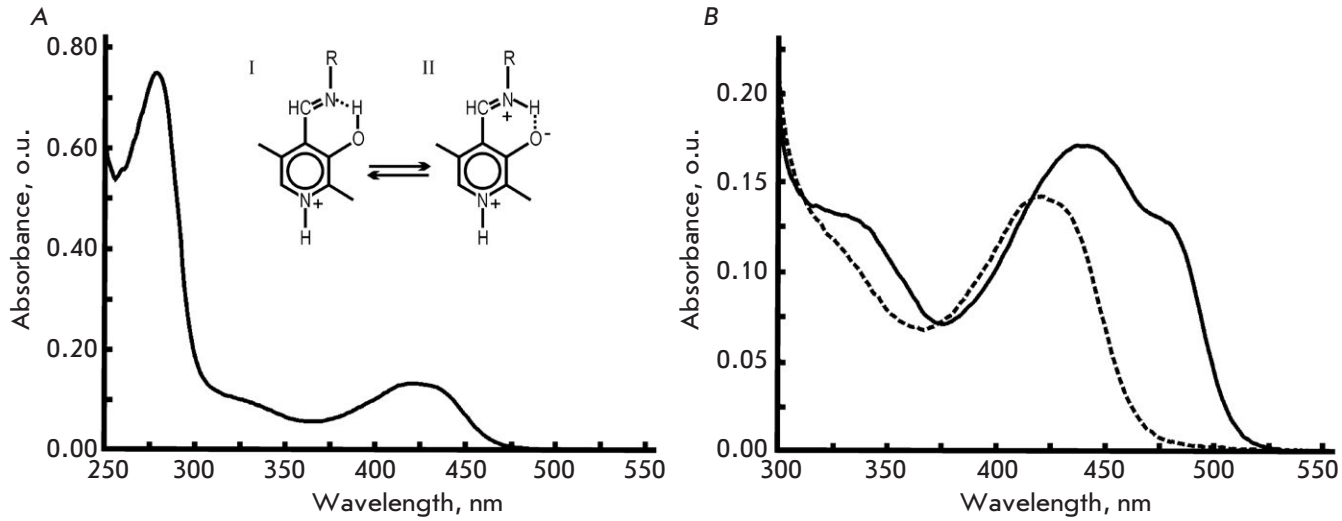

Fig. 1. Absorption spectra: (*A*) Ser339Ala MGL holoenzyme; (*B*) MGL–L-methionine complexes: wild-type MGL (solid line), and Ser339Ala MGL (dashed line). The spectra were acquired in a 50-mM potassium phosphate buffer, pH 8.0, containing 1 mM DTT, 1 mM EDTA, and 1 mg/mL of the enzyme

catalyzed by Ser339Ala MGL, compared to those of the wild-type MGL. The substitution led to a slowdown in the rates of C-α- and C-β-proton exchange in the inhibitors. A decrease in the exchange rate of the C-α-proton in the complexes of mutant enzyme with glycine and norleucine compared with those of the wild-type enzyme was two orders of magnitude; the exchange rates of C-β-protons decreased by an order of magnitude.

An investigation of the stereospecificity of the glycine proton exchange in the wild-type enzyme showed that the ratio of exchange rates of the *pro*-(R) and *pro*-(S) protons was 14,000 : 1 [40]. The ^{1}H NMR spectrum of a dipeptide L-phenylalanylglycine (data not shown) containing glycine, which was isolated after incubation of the mutant enzyme with glycine in D_2O, had a signal at 3.4 ppm characteristic of the methylene *pro*-(R) proton of glycine [41].

We were unable to detect any exchange of the *pro*-(S) proton after incubation of the mutant form with glycine for a long period of time, because it led to the inactivation of Ser339Ala MGL. The obtained data showed that both the wild-type enzyme and the mutant MGL predominantly exchanged the *pro*-(R) proton.

Spectral studies

Figure 1 shows the absorption spectra of the Ser339Ala holoenzyme and its complex with L-methionine. The absorption spectrum of the mutant enzyme has a form typical of PLP aldimines, with the main band at 420 nm and a band at 320 nm.

The results of lognormal deconvolution of the holoenzyme spectrum, which was carried out as described for the wild-type enzyme [37], are shown in *Table 4*. The internal aldimine of the mutant form is described by four structures: ketoenamine, its tautomer, enolimine (*Fig. 1A*; structures II and I), and two ketoenamine conformers, a conformer whose aldimine group is in a plane perpendicular to the pyridine ring plane (*Table 4*, structure II$^{\perp}$), and a conformer whose aldimine bond is out of the coenzyme ring plane but retains conjugation with π-electrons of the coenzyme ring and a hydrogen bond between the aldimine nitrogen atom and the coenzyme 3'-hydroxy group (*Table 4*, structure II$^{\perp}$). The absorption band parameters obtained from spectral deconvolution are summarized in *Table 4*.

The discovered structures and the parameters of their absorption bands turned out to be almost identical to those of the wild-type enzyme [36]. The dissociation constant of the PLP complex for the wild-type MGL was 6.24×10^{-4} mM [57]. The PLP dissociation constant for the mutant enzyme was 1.01×10^{-3} mM. Thus, the substitution did not significantly affect the apoenzyme affinity for the coenzyme and the conformation and tautomerism of the internal aldimine. The substitution led to some change in the quantitative composition of the tautomers and conformers of the internal aldimine. The reactive form of internal aldimine is ketoenamine. Its content is 67.6% in the wild-type holoenzyme [36] and 52.9% in the mutant holoenzyme (*Table 4*).

Table 4. Parameters of the absorption spectrum of the Ser339Ala MGL internal aldimine

Structure	E, eV	$\nu \times 10^{-3}$, cm^{-1}	λ, nm	$\varepsilon \times 10^{-3}$, $M^{-1}cm^{-1}$	$W \times 10^{-3}$, cm^{-1}	ρ	f	n, %
II^{1}	2.92	23.58	424.1	10.46	3.58	1.55	0.18	52.9
$II^{\angle}$	3.24	26.10	383.1	8.27	3.87	1.37	0.03	10.4
I	3.63	29.26	341.8	9.75	3.65	1.23	0.06	20.0
$II^{\perp}$	3.80	30.67	326.1	8.50	3.47	1.29	0.05	16.7
II^{2*}	4.28	34.52	289.7	12.20	5.06	1.20	0.29	
*	4.55	36.56	272.8	23.10	4.56	1.39	0.79	

E is the electronic transition energy; ν is the wave number; λ is the wavelength; ε is the molar absorption coefficient; *W* is the half-width; ρ is the asymmetry; *f* is the oscillator strength; *n* is the content of tautomers and conformers. The PLP content in the enzyme is 97%.
*Experimental information on these bands is insufficient.
Superscripts (1, 2) refer to the first and second electronic transitions in structure II. Superscripts ($^{\perp}$ and $^{\angle}$) refer to two conformers of structure II (a conformer with an aldimine bond located in a plane perpendicular to the pyridine ring plane, and a conformer with an aldimine bond that is partially out of the pyridine ring plane but retains conjugation with the π-electrons of the cofactor ring and the hydrogen bond between the aldimine nitrogen and the 3′-oxy group of the coenzyme).

Absorption and the circular dichroism spectra of the wild-type MGL complexed with L-methionine display bands with maxima at 440 nm and 480 nm [36]. These bands in the spectra of PLP-dependent enzymes are assigned to β- and γ-elimination reaction intermediates: α-aminocrotonate or α-aminoacrylate [54]. The presence of α-aminocrotonate in the spectrum of the wild-type MGL associated with L-methionine and the kinetic data on the interaction between the wild-type enzyme and a number of substrates and inhibitors suggest that the rate-limiting stage of the physiological reaction follows the stage of α-aminocrotonate formation [36]. There is no absorption at 440–480 nm in the absorption spectrum of the mutant enzyme associated with L-methionine. Consequently, the substitution of Ser339 with Ala led to the inhibition of the γ-elimination reaction at the stage(s) following the stage of the external aldimine.

Spatial structure of the mutant holoenzyme

The spatial structure of Ser339Ala MGL was determined at a resolution of 1.7 Å. The substitution of serine 339 with alanine did not affect the spatial structure of the enzyme. The course of the polypeptide chain was almost identical to that of the wild-type MGL holoenzyme (*Fig. 2A*). The root-mean-square deviation of the Cα-atom positions of Ser339Ala MGL compared to their positions in the wild-type enzyme (PDB code 2RFV) is 0.29 $Å^2$. As in the previously determined structures of *C. freundii* MGL [29–31] and the structures of MGL from other microorganisms, the Ser339Ala MGL structure is characterized by a flexibility of the N- and C-terminal fragments of the polypeptide chain (*Fig. 2A*) [28]. The high flexibility of the N-terminal fragment in Ser339Ala MGL precluded the localization of a long segment consisting of sixteen amino acids (46–61), including Tyr58 and Arg60, whose side groups form hydrogen bonds with the O2P atom of the phosphate "handle" of the coenzyme (*Fig. 2B*).

The average temperature B-factor of the amino acid residues from the flexible C-terminal fragment (54.02 $Å^2$, residues 353–368) is two-fold higher than that of the stable regions of the enzyme. This flexibility may be associated with removal of γ- and β-elimination products from the active center [30]. The substitution of Ser339 with alanine led to the loss of the hydrogen bond between it and Thr36 of the neighboring subunit of the catalytic dimer (*Fig. 2B*), but this did not affect the tetrameric structure of Ser339Ala MGL.

Spatial structures of the covalent and non-covalent complexes of MGL with inhibitors and the role of Ser339 in the catalysis of the γ- and β-elimination reactions

In the spatial structure of the *C. freundii* wild-type MGL holoenzyme (PDB code 2RFV), the Ser339 side

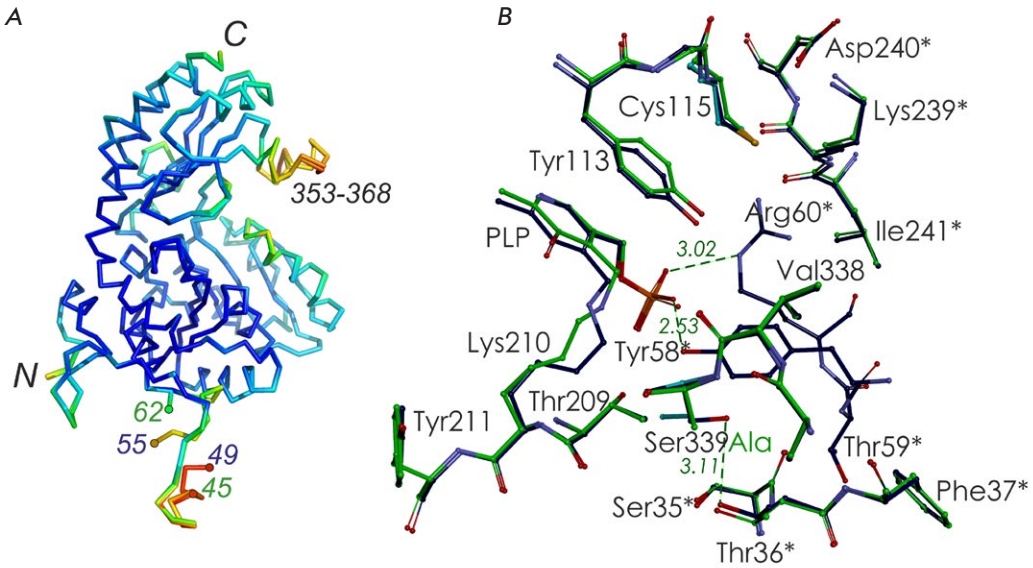

Fig. 2. Superposition of the structures of the wild-type *C. freundii* MGL (code PDB 2RFV; green) and Ser339Ala MGL (code PDB 5D5S; dark blue): (*A*) the polypeptide chain is colored according to the B-factor, varying from dark blue to red as the value increases; (*B*) fragments of active centers; asterisks indicate residues belonging to the neighboring subunit of the catalytic dimer

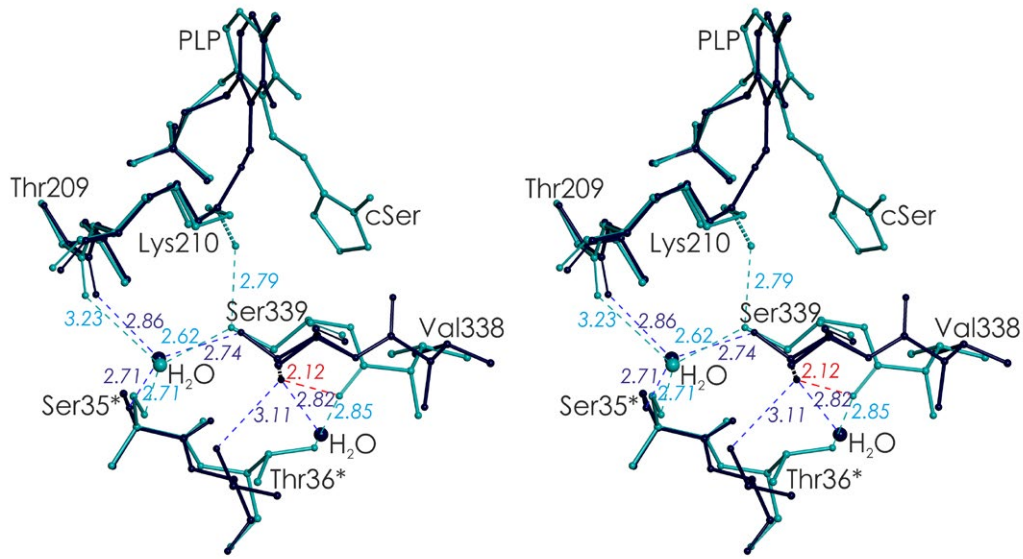

Fig. 3. Stereoview of the superposition of active center fragments of *C. freundii* MGL: the wild-type holoenzyme (PDB code 2RFV, dark blue) and its complex with L-cycloserine (PDB code 4OMA, blue). Asterisks indicate residues belonging to the neighboring subunit of the catalytic dimer. The alternative positions of the amino acid residues are shown by dashed lines

chain occurs in two equally probable positions (*Fig. 3*). In one of them, it is located in the active site, next to Lys210; in the second position, it is located in the region of intersubunit interaction with the N-terminal domain of the neighboring subunit of the catalytic dimer. Both positions of the Ser339 side chain are stabilized by hydrogen bonds and are clearly visible on the electron density map.

In the spatial structures of MGL complexes with inhibitors, which model the Michaelis complex, external aldimine, and the ketimine intermediate, the Ser339 side chain occupies the only position in which its Oγ-atom is directed towards Lys210 [29–32]. When MGL binds inhibitors, their carboxyl groups push the carbonyl group of the peptide bond between Ser339 and Val338 from the active center cavity into the region of intersubunit contacts and the C=O-group is rotated by 180° [29, 32]. Upon this rotation, the distance between the Oγ-atom of Ser339 and the oxygen atom of the Val338 main chain drops to 2.12 Å, which leads to the thrusting of the Oγ-atom of Ser339 into the enzyme active site region (*Fig. 3*). This ensures the only position of the Ser339 side chain in which its Oγ-atom forms a hydrogen bond with the Nζ-atom of Lys210. The bond length is 2.85 Å in the Cys115His MGL–L-norleucine complex modeling the external aldimine [31] and 2.79 Å in the wild-type MGL–L-cycloserine complex modeling the ketimine intermediate [30] (*Fig. 3*).

As noted above, the MGL N-terminal fragment is flexible both in the wild-type holoenzyme and in the Ser339Ala MGL holoenzyme. Binding of inhibi-

tors by wild-type MGL leads to a stabilization of this fragment [30, 32]. Probably, this stabilization also occurs upon binding of substrates and inhibitors by Ser339Ala MGL.

Figure 4 shows the active center fragments of the *C. freundii* MGL–L-cycloserine complex, which represent two positions of the Lys210 side chain.

In one position, which is analogous to the Lys210 side chain position in the mutant form–norleucine complex [31] modeling an external aldimine, the Lys210 Nζ-atom is stabilized by hydrogen bonds with the hydroxyl groups of the Ser339 and Tyr58* side chains (2.79 Å and 2.82 Å, respectively; *Fig. 4A*). The side chain of Lys210 is almost perpendicular to the coenzyme ring plane and occurs at a distance of 3.28 Å from the C-α-*pro*-(R)-proton and 3.15 Å from the Cβ-atom of L-cycloserine (*Fig. 4B*). This position is favorable to the abstraction of the C-α-*pro*-(R)-proton or C-β-proton by the side amino group of Lys210.

In another position, the Nζ-atom of Lys210 is located at a hydrogen bond distance from the hydroxyl groups of the Ser207 and Tyr58* side chains (3.30 Å and 2.96 Å, respectively; *Fig. 4A*). In this position, the Nζ-atom of Lys210 is closest (3.23 Å) to the C4'-atom of PLP, while the distance to the Cα-atom of the substrate increases by 0.43 Å (*Fig. 4B*). This position of the Lys210 side chain is favorable to a transfer of the C-α-proton to the C4'-atom of the coenzyme.

Therefore, if Tyr58* is involved in the stabilization of both positions of the Lys210 Nζ-atom, then the Ser339 and Ser207 side chains, located on opposite sides of Lys210, provide the optimal position for the Lys210 ε-amino group at the stages of C-α-proton abstraction in the external aldimine, protonation of the C4'-atom of PLP, and abstraction of the C-β-proton in the ketimine intermediate.

In the mutant form complexed with substrates and inhibitors, the Lys210 group can form only one hydrogen bond with the Tyr58* hydroxyl group. This leads to a disruption of the Lys210 side chain conformation optimal for the abstraction of the C-α-proton and to a decrease in its pK_a. Obviously, this explains the decrease in the observed exchange rate of the C-α-proton of inhibitors. The exchange of C-β-protons was previously thought to occur via the configuration inversion mechanism when the first proton is abstracted by the Lys210 side chain, and the second proton comes from the opposite side: from the Tyr113 side chain. As a result, both C-β-protons are exchanged at the same rate [29]. In the Ser339Ala enzyme, the rate of isotopic exchange of C-β-protons decreases and both β-protons undergo exchange at the same rate.

Probably, the hydrogen bond between the Nζ-atom of Lys210 and the Oγ-atom of Ser339 ensures both a

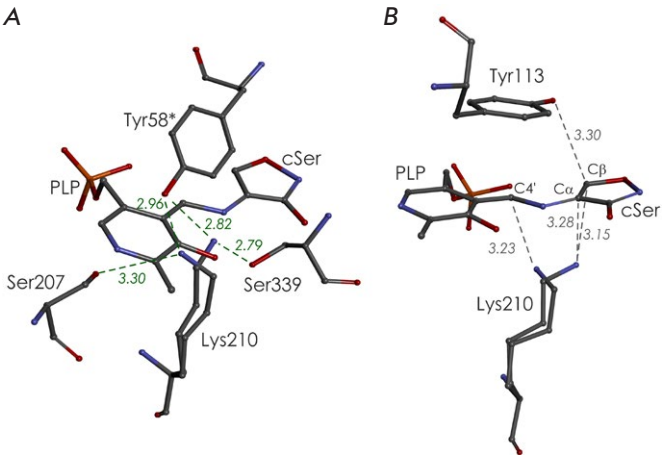

Fig. 4. (*A*) Environment of Lys210 in the active center of the *C. freundii* MGL–L-cycloserine complex (PDB code 4OMA). Asterisks indicate amino acid residues belonging to the second subunit of the catalytic dimer. (*B*) Position of the Nζ-atom of the Lys210 side chain relative to the C4′-atom of PLP and Cα- and Cβ-atoms of the inhibitor

Lys210 amino group position optimal for abstraction of the C-α- and C-β-protons, and stabilization of its ammonium form for the 1,3-prototropic shift of the C-α-proton to the C4'-atom of the coenzyme and effective exchange of C-α- and C-β-protons in complexes with substrates and inhibitors. The absorption band of an external aldimine in the absorption spectrum of the Ser339Ala–L-methionine complex also suggests that the substitution of Ser339 with alanine leads to inhibition of the physiological reaction at the stage of C-α-proton abstraction from the external aldimine.

If α-aminocrotonate formation occurs via the mechanism proposed in [50], the ε-amino group of Lys210 can participate as a base or an acid in the physiological reaction stages that follow the elimination of methyl mercaptan and the substitution of Ser339 can slow these stages of the physiological reaction.

In the β-elimination reaction, the substitution of serine 339 with alanine leads to inhibition at the stage of abstraction of the C-α-proton of the external aldimine. Because Lys210 is postulated as a general acid catalyst in PLP-dependent β-elimination reactions of sulfur-containing amino acids [54], the hydroxyl group of Ser339 probably provides a position and basicity of Lys210 that are optimal for catalysis.

Earlier, a similar role for a serine residue corresponding to MGL Ser339 was proposed for two enzymes from the structural subclass to which MGL belongs: cystathionine γ-synthase [58] and cystathionine β-lyase [59].

CONCLUSION

In this study, we have demonstrated the importance of the Ser339 residue in the mechanism of γ- and β-elimination reactions catalyzed by *C. freundii* MGL. Kinetic, spectral, and X-ray data revealed that Ser339 is necessary to ensure an optimal position of the Lys210 side chain at the stage of C-α-proton abstraction from the substrate in the β-elimination reaction and at the stages of C-α- and C-β-proton abstraction from the substrate in the γ-elimination reaction. In the γ-elimination reaction, the Ser339 residue is supposed to ensure the necessary basicity of the Lys210 side chain at the stage of the 1,3-prototropic shift of the C-α-proton of the substrate to the C4'-atom of the coenzyme. Along with the contribution to basic enzymology, understanding the mechanisms of γ- and β-elimination reactions catalyzed by MGL is necessary for the development of new antibacterial and antitumor drugs based on changing/improving the substrate and reaction specificity of the enzyme. ●

This study was supported by the Program for Basic Research of State Academies of Sciences (No. 01201363820) and the Russian Foundation for Basic Research (projects No. 14-04-00349 and No. 14-04-31398).

REFERENCES

1. Onuffer J.J., Kirsch J.F. // Protein Sci. 1995. V. 4. № 9. P. 1750–1757.
2. Vacca R.A., Giannattasio S., Capitani G., Marra E., Christen P. // BMC Biochem. 2008. V. 9. P. 17.
3. Golinelli-Pimpaneau B., Lüthi C., Christen P. // J. Biol. Chem. 2006. V. 281. № 33. P. 23969–23977.
4. Belogurov A. Jr., Kozyr A., Ponomarenko N., Gabibov A. // Bioessays. 2009. V. 31. № 11. P. 1161–1171.
5. Durova O.M., Vorobiev I.I., Smirnov I.V., Reshetnyak A.V., Telegin G.B., Shamborant O.G., Orlova N.A., Genkin D.D., Bacon A., Ponomarenko N.A., et al. // Mol. Immunol. 2009. V. 47. № 1. P. 87–95.
6. Tanaka H., Esaki N., Soda K. // Enzyme Microb. Technol. 1985. V. 7. P. 530–537.
7. Faleev N.G., Troitskaya M.V., Ivoylov V.S., Karpova V.V., Belikov V.M. // Applied Biochemistry and Microbiology. 1994. V. 30. № 3. P. 458–463.
8. Tokoro M., Asai T., Kobayashi S., Takeuchi T., Nozaki T. // J. Biol. Chem. 2003. V. 278. № 43. P. 42717–42727.
9. Lockwood B., Coombs G. // Biochem. J. 1991. V. 279. № 3. P. 675–682.
10. Kreis W., Hession C. // Cancer Res. 1973. V. 33. № 8. P. 1862–1865.
11. Yoshimura M., Nakano Y., Yamashita Y., Oho T., Saito T., Koga T. // Infection Immunity. 2000. V. 68. № 12. P. 6912–6916.
12. Nakayama T., Esaki N., Lee W.-J., Tanaka I., Tanaka H., Soda K. // Agric. Biol. Chem. 1984. V. 48. P. 2367–2369.
13. Revtovich S.V., Morozova E.A., Anufrieva N.V., Kotlov M.I., Bely Yu.F., Demidkina T.V. // Proceedings of the Russian Academy of Sciences. 2012. V. 445. № 2. P. 214–220.
14. Kulikova V.V., Morozova E.A., Revtovich S.V., Kotlov M.I., Anufrieva N.V., Bazhulina N.P., Raboni S., Faggiano S., Gabellieri E., Cion, P., et al. // IUBMB Life. 2017. V. 69. № 9. P. 668–676.
15. El-Sayed A.S. // Appl. Microbiol. Biotechnol. 2010. V. 86. № 2. P. 445–467.
16. Goyer A., Collakova E., Shachar-Hill Y., Hanson A.D. // Plant Cell Physiol. 2007. V. 48. № 2. P. 232–242.
17. Morozova E.A., Revtovich S.V., Anufrieva N.V., Kulikova V.V., Nikulin A.D., Demidkina T.V. // Acta Crystallogr. D Biol. Crystallogr. 2014. V. 70. № 11. P. 3034–3042.
18. Anufrieva N.V., Morozova E.A., Kulikova V.V., Bazhulina N.P., Manukhov I.V., Degtev D.I., Gnuchikh E.Yu., Rodionov A.N., Zavilgelsky G.B., Demidkina T.V. // Acta Naturae. 2015. V. 7. № 4 (27). P. 141–148.
19. Kulikova V.V., Anufrieva N.V., Revtovich S.V., Chernov A.S., Telegin G.B., Morozova E.A., Demidkina T.V. // IUBMB Life. 2016. V. 68. № 10. P. 830–835.
20. Morozova E.A., Kulikova V.V., Rodionov A.N., Revtovich S.V., Anufrieva N.V., Demidkina T.V. // Biochimie. 2016. V. 128–129. P. 92–98.
21. Kulikova V.V., Chernukha M.Yu., Morozova E.A., Revtovich S.V., Rodionov A.N., Koval V.S., Avetisyan L.R., Kulyastova D.G., Shaginyan I.A., Demidkina T.V. // Acta Naturae. 2018. V. 10. № 3 (38). P. 83–87.
22. Yoshioka T., Wada T., Uchida N., Maki H., Yoshida H., Ide N., Kasai H., Hojo K., Shono K., Maekawa R., et al. // Cancer Res. 1998. V. 58. № 12. P. 2583–2587.
23. Miki K., Al-Refaie W., Xu M., Jiang P., Tan Y., Bouvet M., Zhao M., Gupta A., Chishima T., Shimada H., et al. // Cancer Res. 2000. V. 60. № 10. P. 2696–2702.
24. Tan Y., Xu M., Hoffman R.M. // Anticancer Res. 2010. V. 30. № 4. P. 1041–1046.
25. Hoffman R.M. // Expert Opin. Biol. Ther. 2015. V. 15. № 1. P. 21–31.
26. Käck H., Sandmark J., Gibson K., Schneider G., Lindqvist Y. // J. Mol. Biol. 1999. V. 291. № 4. P. 857–876.
27. Mamaeva D.V., Morozova E.A., Nikulin A.D., Revtovich S.V., Nikonov S.V., Garber M.B., Demidkina T.V. // Acta Crystallogr. Sect. F Struct. Biol. Cryst. Commun. 2005. V. 61. № 6. P. 546–549.
28. Nikulin A., Revtovich S., Morozova E., Nevskaya N., Nikonov S., Garber M., Demidkina T. // Acta Crystallogr. Sect. D. 2008. V. D64. № 2. P. 211–218.
29. Revtovich S.V., Faleev N.G., Morozova E.A., Anufrieva N.V., Nikulin A.D., Demidkina T.V. // Biochimie. 2014. V. 101. P. 161–167.
30. Kuznetsov N.A., Faleev N.G., Kuznetsova A.A., Morozova E.A., Revtovich S.V., Anufrieva N.V., Nikulin A.D., Fedorova O.S., Demidkina T.V. // J. Biol. Chem. 2015. V. 290. № 1. P. 671–681.
31. Revtovich S.V., Morozova E.A., Kulikova V.V., Anufrieva N.V., Osipova T.I., Koval V.S., Nikulin A.D., Demidkina T.V. // BBA-Proteins Proteom. 2017. V. 1865. № 9. P. 1123–1128.
32. Revtovich S.V., Morozova E.A., Khurs E.N., Zakomyrdina L.N., Nikulin A.D., Demidkina T.V., Khomutov R.M. // Biochemistry (Moscow). 2011. V. 76. №. 5. P. 690–698.
33. Nagai S., Flavin M. // J. Biol. Chem. 1967. V. 242. № 17.

P. 3884–3895.
34. Morneau D.J.K., Abouassaf E., Skanes J.E., Aitken S.M. // Anal. Biochem. 2012. V. 423. № 1. P. 78–85.
35. Manukhov I.V., Mamaeva D.V., Morozova E.A., Rastorguev S.M., Faleev N.G., Demidkina T.V., Zavilgelsky G.B. // Biochemistry (Moscow). 2006. V. 71. № 4. P. 454–463.
36. Morozova E.A., Bazhulina N.P., Anufrieva N.V., Tkachev Ya.V., Streltsov S.A., Timofeev V.P., Faleev N.G., Demidkina T.V. // Biochemistry (Moscow). 2010. V. 75. № 10. P. 1435–1445.
37. Laemmli U.K. // Nature. 1970. V. 227. № 5259. P. 680–685.
38. Cleland W.W. // Methods Enzymol. 1979. V. 63. P. 103–138.
39. Faleev N.G., Ruvinov S.B., Bakhmutov V.I., Demidkina T.V., Myagkikh I.V., Belikov V.M. // Mol. Biol. 1987. V. 21. P. 1636–1644.
40. Koulikova V.V., Zakomirdina L.N., Gogoleva O.I., Tsvetikova M.A., Morozova E.A., Komissarov V.V., Tkachev Y.V., Timofeev V.P., Demidkina T.V., Faleev N.G. // Amino Acids. 2011. V. 41. № 5. P. 1247–1256.
41. Kainosho M., Ajisaka K., Kamisaku M., Murai A., Kyogoku Y. // Biochem. Biophys. Res. Commun. 1975. V. 64. № 1. P. 425–432.
42. Morino Y., Snell E.E. // J. Biol. Chem. 1967. V. 242. № 23. P. 5591–5601.
43. Peterson E.A., Sober H.A. // J. Am. Chem. Soc. 1954. V. 76. P. 169–175.
44. Osterman A.L., Brooks H.B., Rizo J., Phillips M.A. // Biochemistry. 1997. V. 36. № 15. P. 4558–4567.
45. Scatchard G. // Ann. N.Y. Acad. Sci. 1949. V. 51. P. 660–672.
46. Kabsch W. // Acta Crystallogr. Sect. D Biol. Crystallogr. 2010. V. 66. № 2. P. 125–132.
47. Winn M.D., Ballard C.C., Cowtan K.D., Dodson E.J., Emsley P., Evans P.R., Keegan R.M., Krissinel E.B., Leslie A.G., McCoy A., et al. // Acta Crystallogr. Sect. D Biol. Crystallogr. 2011. V. 67. № 2. P. 235–242.
48. Adams P.D., Grosse-Kunstleve R.W., Hung L.-W., Ioerger T.R., McCoy A.J., Moriarty N.W., Read R.J., Sacchettini J.C., Sauter N.K., Terwilliger T.C. // Acta Crystallogr. Sect. D Biol. Crystallogr. 2002. V. 58. № 11. P. 1948–1954.
49. Emsley P., Lohkamp B., Scott W., Cowtan K. // Acta Crystallogr. Sect. D Biol. Crystallogr. 2010. V. 66. № 4. P. 486–501.
50. Brzovic P., Holbrook E.L., Greene R.C., Dunn M.F. // Biochemistry. 1990. V. 29. № 2. P. 442–451.
51. Clausen T., Huber R., Laber B., Pohlenz H.D., Messerschmidt A. // J. Mol. Biol. 1996. V. 262. № 2. P. 202–224.
52. Davis L., Metzler D. The Enzymes. 3rd Edn. V. 7 / Ed. Boyer P.D. N.Y.: Acad. Press, 1972. P. 33–74. https://www.elsevier.com/books/the-enzymes/boyer/978-0-12-122707-4
53. Clausen T., Huber R., Prade L., Wahl M.C., Messerschmidt A. // EMBO J. 1998. V. 17. № 23. P. 6827–6838.
54. Messerschmid, A., Worbs M., Steegborn C., Wahl M. C., Huber R., Laber B., Clausen T. // Biol. Chem. 2003. V. 384. № 3. P. 373–386.
55. Inou H., Inagaki K., Adachi N., Tamura T., Esaki N., Soda K., Tanaka H. // Biosci. Biotechnol. Biochem. 2000. V. 64. № 11. P. 2336–2343.
56.Sato D., Shiba T., Karaki T., Yamagat W., Nozaki T., Nakazawa T., Harada S. // Sci. Rep. 2017. V. 7. № 1. P. 4874.
57. Anufrieva N.V., Faleev N.G., Morozova E.A., Bazhulina N.P., Revtovich S.V., Timofeev V.P., Tkachev Y.V., Nikulin A.D., Demidkina T.V. // Biochim. Biophys. Acta. 2015. V. 1854. № 9. P. 1220–1228.
58. Jaworski A.F., Lodha P.H., Manders A.L., Aitken S.M. // Protein Sci. 2012. V. 21. № 11. P. 1662–1671.
59. Lodha P.H., Aitken S.M. // Biochemistry. 2011. V. 50. № 45. P. 9876–9885.

The Signaling Pathways Controlling the Efficacy of Glioblastoma Therapy

N. S. Vasileva*, A. B. Ageenko, V. A. Richter, E. V. Kuligina
Institute of Chemical Biology and Fundamental Medicine SB RAS, Novosibirsk, 630090 Russia
*E-mail: nataly_vas@bk.ru
Received: October 29, 2021; in final form, March 16, 2022
DOI: 10.32607/actanaturae.11623

ABSTRACT **The resistance of glioblastoma to existing therapies puts limits on quality-of-life improvements and patient survival with a glioblastoma diagnosis. The development of new effective glioblastoma therapies is based on knowledge about the mechanisms governing tumor resistance to therapeutic agents. Virotherapy is one of the most actively developing approaches to the treatment of malignant neoplasms: glioblastoma in particular. Previously, we demonstrated that the recombinant vaccinia virus VV-GMCSF-Lact exhibits *in vitro* cytotoxic activity and *in vivo* antitumor efficacy against human glioblastoma. However, the studied glioblastoma cell cultures had different sensitivities to the oncotoxic effect of the virus. In this study, we investigated cancer stem cell (CSC) surface markers in glioblastoma cells with different sensitivities to VV-GMCSF-Lact using flow cytometry and we assessed the levels of proteins affecting viral entry into cells and virus infection efficiency by western blotting. We showed that cell cultures more sensitive to VV-GMCSF-Lact are characterized by a greater number of cells with CSC markers and a lower level of activated Akt kinase. Akt probably inhibits lactaptin-induced apoptosis in virus-resistant cells. Hence, we suggest that the sensitivity of glioblastoma cells to the oncotoxic effect of VV-GMCSF-Lact is determined by the nature and extent of the disturbances in cell death regulation in various cultures. Further investigation of the factors affecting glioblastoma resistance to virotherapy will test this hypothesis and identify targets for antitumor therapy, combined with VV-GMCSF-Lact.**
KEYWORDS **glioblastoma, oncolytic viruses, VV-GMCSF-Lact, cancer stem cells, mechanisms of glioblastoma resistance.**
ABBREVIATIONS **CSC – cancer stem cell; Akt – serine/threonine kinase 1; GM-CSF – granulocyte-macrophage colony-stimulating factor; PI3K – phosphoinositide 3-kinase; PAK1 – p21-activated kinase; MEM – Minimum Essential Medium; FBS – fetal bovine serum; CD15 (Lewis X) – 3-fucosyl-N-acetyllactosamine; CD171 – neural cell adhesion molecule L1 (L1CAM); PE – phycoerythrin; IC_{50} – virus concentration causing 50% cell death; CD133 – prominin-1; CD44 – integral cellular glycoprotein; VACV – vaccinia virus.**

INTRODUCTION

Glioblastoma is the most malignant tumor of the central nervous system, which is characterized by a low patient survival rate. Standard glioblastoma therapy, which involves maximal surgical resection followed by radiation therapy and/or chemotherapy, neither improves the quality of life nor increases the survival rate of patients with this diagnosis.

The key challenge to effective glioblastoma treatment is tumor resistance to existing therapies. Today, the scientific and medical community is developing and promoting various approaches to glioblastoma therapy that are based on the inhibition of target molecules, immunotherapy, and other methods. Therapy with oncolytic viruses, an approach to the immunotherapy of tumors, and gliomas in particular, is being actively developed [1].

Previously, a team of researchers from the Institute of Chemical Biology and Fundamental Medicine SB RAS and State Research Center of Virology and Biotechnology VECTOR designed a recombinant vaccinia virus strain, VV-GMCSF-Lact. VV-GMCSF-Lact contains deletions of the thymidine kinase and growth factor genes in whose regions the GM-CSF and oncotoxic protein lactaptin genes are inserted. Deletion of these genes reduces the virus virulence for healthy cells and significantly increases its selectivity for tumor cells. Expression of GM-CSF promotes an antitumor immune response, whereas expression of lactaptin, a fragment of human milk kappa-casein, in-

duces the apoptotic death of tumor cells. VV-GMCSF-Lact was previously shown to exhibit high cytotoxic activity against human tumor cells of different histogenesis *in vitro* and significant antitumor activity against human breast cancer and glioblastoma *in vivo* [2, 3].

However, different glioblastoma cell cultures, both immortalized and derived from patient tumor samples (patient-derived cell cultures), have different sensitivities to VV-GMCSF-Lact. Glioblastoma is known to be characterized by intertumor and intratumor heterogeneity. Some molecular glioblastoma subtypes, such as proneural, are more sensitive to radiotherapy and temozolomide chemotherapy; however, certain glioblastoma subtypes, and the mesenchymal molecular subtype in particular, are resistant to standard therapy [4, 5]. In this case, the issue of tumor cell resistance to viral therapy remains open [6, 7].

The vaccinia virus, which was used to design VV-GMCSF-Lact, is able to penetrate target cells via fusion with the cell membrane or (at low pHs) endosomal membranes [8, 9]. Furthermore, phosphatidylserine present on the membrane of viral particles was shown to facilitate virus entry into the cell via macropinocytosis by mimicry of apoptotic bodies [10]. These entry pathways require rearrangement of the target cell cytoskeleton; therefore, their efficiency may depend on the status of various cellular signaling pathways: e.g., the PI3K/Akt pathway. In addition, all macropinocytosis stages require p21-activated kinase (PAK1) that is involved in cytoskeleton reorganization and microtubule dynamics [11].

In this study, we investigated the factors that control the cytotoxic effect of VV-GMCSF-Lact against glioblastoma cells with different sensitivities to the virus. We assessed the abundance of glioblastoma cancer stem cell (CSC) markers in immortalized U87 MG and U343 MG cell lines and patient-derived BR1.20 and BR3.20 cell cultures and measured the levels of proteins affecting the viral infection efficiency in tumor cells – elements of the PI3K/Akt signaling pathway, and PAK1. Glioblastoma cell cultures sensitive to the oncotoxic effect of VV-GMCSF-Lact were shown to be characterized by a greater number of cells carrying CSC markers and a lower (compared to resistant cells) level of activated Akt protein kinase capable of inhibiting lactaptin-induced apoptosis.

EXPERIMENTAL

Glioblastoma cell culture

The human glioblastoma cell cultures U87 MG, U343 MG, BR1.20, and BR3.20 were taken from the cell culture collection of the Institute of Chemical Biology and Fundamental Medicine SB RAS (Novosibirsk, Russia).

Cells of immortalized U87 MG and U343 MG cultures were cultured in an alpha-MEM medium supplemented with 10% FBS, 2 mM *L*-glutamine, and an antibiotic/antimycotic solution (100 U/mL penicillin, 100 mg/mL streptomycin sulfate, and 0.25 μg/mL amphotericin).

Cells of patient-derived BR1.20 and BR3.20 cultures were cultured in a DMEM/F12 medium supplemented with 10% FBS, 4 mM *L*-glutamine, and an antibiotic/antimycotic solution (200 U/mL penicillin, 200 mg/mL streptomycin sulfate, and 0.5 μg/mL amphotericin).

All the cell cultures were maintained in a CO_2 incubator at 37.0 ± 1.0°C in an atmosphere of 5.0 ± 0.5% CO_2.

Flow cytometry

The cells that had reached 60–80% confluence were harvested from the culture dish and incubated with anti-human CD15 monoclonal antibodies conjugated to Alexa Fluor 647 (R&D Systems, USA) and anti-human CD171 monoclonal antibodies conjugated to PE (R&D Systems), according to the manufacturer's protocol. Analysis was performed using a FACSCanto II flow cytometer (BD Biosciences, USA). Data were analyzed using the FACSDiva software (BD Biosciences).

Western blot analysis

The levels of the p85α, p110α, $pAkt^{Ser473}$, $pAkt^{Thr308}$, and $pPAK1^{Ser199/204}$ proteins, before and after exposure to the virus (after 0.5, 1, 2, 6, and 12 h), were assessed using the Western blot analysis. The multiplicity of infection was 1 PFU/cell.

The cells were incubated with the virus. Then, cell lysates were produced using a RIPA buffer (1% NP40, 150 mM NaCl, 0.1% SDS, 50 mM Tris-HCl, pH 7.4) in the presence of protease and phosphatase inhibitors (Pierce Phosphatase Inhibitor Mini Tablets, Thermo Scientific, USA) and a cOmplete™ Protease Inhibitor Cocktail (Sigma-Aldrich, USA). The protein concentration in the resulting lysates was measured using a commercial Modified Lowry Protein Assay Kit (Thermo Scientific), according to the manufacturer's protocol. The proteins were separated by denaturing 10% polyacrylamide gel electrophoresis using a vertical electrophoresis chamber. "Wet" transfer of the proteins from a gel onto a nitrocellulose membrane (0.45 μm) was performed in a NuPAGE Transfer Buffer (Invitrogen, USA) at a direct current of 400 mA for 1 h. Membranes were treated with antibodies using an IBind Western Device (Bio-Rad, USA). The proteins were detected using a Novex®

ECL Chemiluminescent Substrate Reagent Kit (Invitrogen) and an Amersham™ Imager 600 System. For normalization, the membranes were stained with anti-β-actin recombinant rabbit monoclonal antibodies.

RESULTS AND DISCUSSION

CD15- and CD171-positive cells in U87 MG, U343 MG, BR1.20, and BR3.20 human glioblastoma cultures

Previously, we demonstrated that the recombinant vaccinia virus VV-GMCSF-Lact with deletions of the viral thymidine kinase and growth factor genes in whose regions the human GM-CSF and oncotoxic protein lactaptin gene are inserted exhibited high cytotoxic activity and antitumor efficacy against both immortalized and patient-derived cell–cultures. In that case, the studied cells had different sensitivities to the virus [3].

In this study, we investigated some factors that can influence the effect of the virus on tumor cells. U87 MG and U343 MG immortalized glioblastoma cell lines and BR1.20 and BR3.20 cell cultures derived from patient tumor samples (patient-derived cell cultures) were used for this purpose. The analyzed cells exhibit different sensitivities to the oncolytic virus VV-GMCSF-Lact (*Table*).

The differences in the cytotoxic effect of the virus on the cells may be associated primarily with the diversity of the origin of the studied cell cultures. Glioblastoma is known to belong to a heterogeneous group of malignancies with different responses to therapy [12]. In addition, these neoplasms are characterized by intratumoral heterogeneity at the molecular level and a complex cellular organization [13]. According to the hierarchical model, glioblastoma CSCs are at the top of the hierarchy and significantly contribute to tumor therapy resistance [14]. Thus, the Notch signaling pathway, which plays an important role in maintaining the CSC phenotype, promotes the development of radiotherapy resistance by these cells via the activation of the PI3K/AKT and Bcl-2 pathways, which are important regulators of cell growth and survival [15]. Previously, we showed that glioblastoma cell cultures more sensitive to VV-GMCSF-Lact contain more CD133+ and CD133+/CD44+ cells (*Fig. 1*) [3].

Cytotoxic activity of VV-GMCSF-Lact against glioma cells

Cell culture	IC_{50}*, PFU/cell
U87 MG	0.1
U343 MG	0.06
BR1.20	0.006
BR3.20	0.02

*IC_{50} is the virus concentration causing 50% cell death.

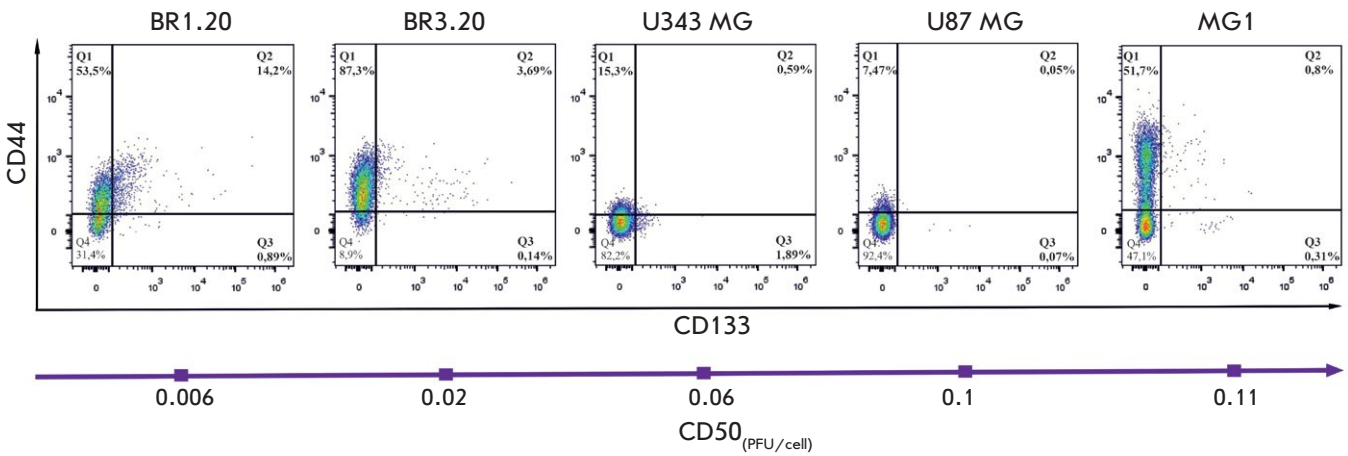

Fig. 1. The expression profiles of CD133 and CD44 and their co-expression in MG1, BR1.20, BR3.20, U343 MG, and U87 MG cell cultures. Cell suspensions were incubated with PE-conjugated anti-CD133 and APC-conjugated anti-CD44 antibodies and analyzed by flow cytometry. The CD44-positive cell population is displayed in the upper quadrants (Q1, Q2); The CD133-positive population is represented in the right quadrants (Q2, Q3). Cells positive for both markers are presented in the upper right quadrant (Q2). The purple arrow indicates a decrease in the sensitivity of the studied cell cultures to VV-GMCSF-Lact [3]

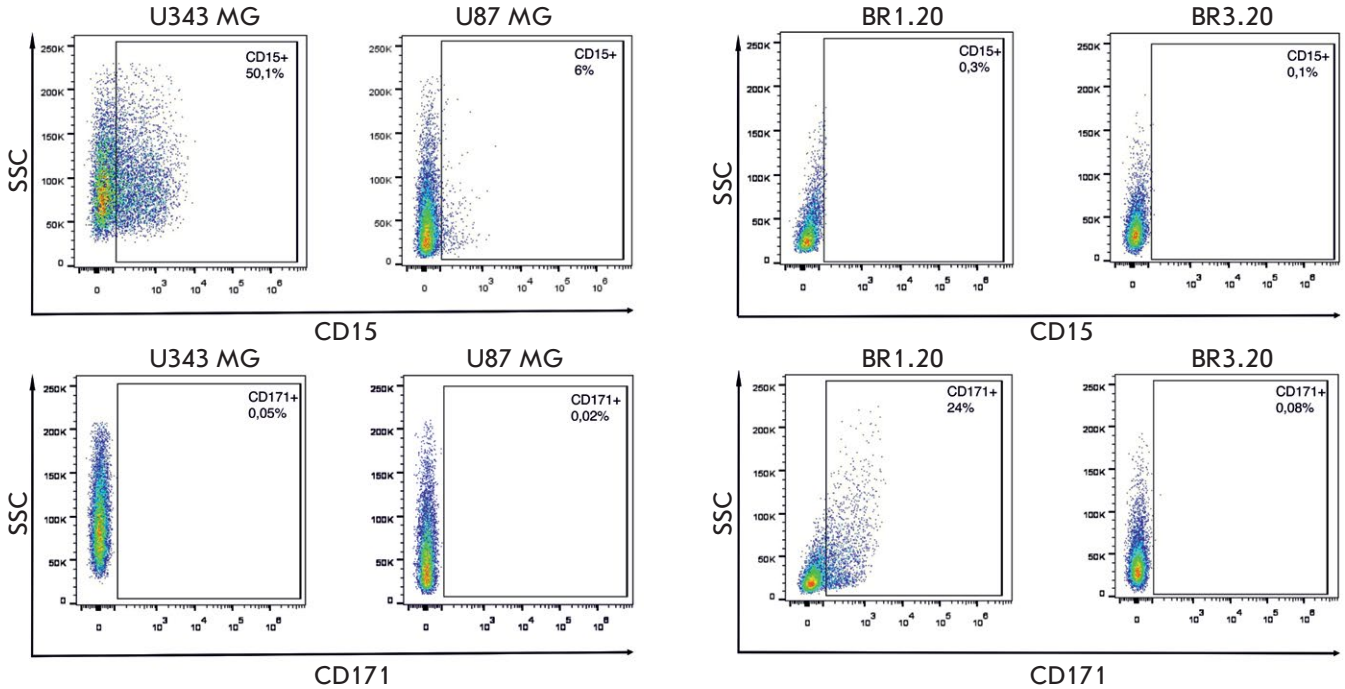

Fig. 2. Expression profiles of the CD15 and CD171 markers in U87 MG, U343 MG, BR1.20, and BR3.20 cell cultures. Cell suspensions were incubated with PE-conjugated anti-CD171 and FITC-conjugated anti-CD15 antibodies and analyzed by flow cytometry

Using flow cytometry, we assessed the abundance of other CSC markers, CD15 and CD171 [16, 17], in U87 MG, U343 MG, BR1.20, and BR3.20 cell cultures with different sensitivities to VV-GMCSF-Lact (*Fig. 2*).

CD15, also known as SSEA-1 or Lewis X, is a carbohydrate adhesion molecule usually present on many types of pluripotent stem cells [18]. In the present study, CD15-positive cells were present in U87 MG and U343 MG immortalized cell cultures (6 and 50.1%, respectively). In this case, the number of CD133-positive cells in these cultures was significantly lower, or no such cells were detected [3]. In 2009, M. Son et al. showed that patient-derived glioblastoma cell cultures may not contain CD133-positive cancer stem cells. However, these cultures contained cells that had properties similar to those of stem cells and exhibited a tumorigenic potential when transplanted to immunodeficient mice [19]. Hence, CD15 can be considered an alternative to CD133 in the isolation and characterization of glioblastoma stem cells.

CD171, or L1CAM, belongs to the family of immunoglobulin-like cell adhesion molecules and plays an important role in the development of neural cells, survival, and migration of tumor cells [20, 21]. CD171 mediates the development of radio- and chemoresistance in glioblastoma cells [22, 23]. It should be noted that BR1.20 is the only cell culture in this study containing CD171-positive cells.

Thus, the BR1.20 cell culture was the most sensitive to VV-GMCSF-Lact. Its cells are characterized by a higher content not only of CD133 and CD44, but also CD171 that is involved in maintaining the survival and clonogenicity of CD133-positive CSCs due to positive regulation of Olig2, thus leading to a reduced expression of the tumor suppressor p21 [24]. CD133, known as prominin-1, plays an important role in cell growth, proliferation and the pathophysiology of tumors [25]. CD133+ cells were shown to be radiotherapy resistant due to a more efficient repair system [26]. Phosphorylation of the CD133 cytoplasmic domain results in its binding to p85 (the PI3K regulatory subunit), followed by the activation of the PI3K/Akt signaling pathway [27]. According to the literature, activation of the PI3K/Akt signaling pathway is one of the leading processes controlling the entry of VACV viral particles into the cell and virus replication at the early stages of infection [28–30].

p85α, p110α, pAkt^{Ser473}, pAkt^{Thr308}, and pPAK1$^{Ser199/204}$ protein levels in U87 MG and U343 MG cells before and after exposure to the virus

The vaccinia virus is able to enter the host cell both via complete membrane fusion and pH-dependent

endocytosis and via macropinocytosis through the interaction between phosphatidylserine residues on the viral membrane and the G-protein-coupled receptors of the cell, leading to the activation of downstream signaling pathways, such as PI3K/Akt, reorganization of the host cell cytoskeleton, and subsequent virus entry into the cell. Inhibition of PI3K was shown to decrease the number of virions entering the cell [10]. In addition, all macropinocytosis stages involve P21-activated kinase PAK1, whose transfer to the plasma membrane leads to the activation of many of the effectors necessary for macropinosome formation [11].

Assessment of the levels of p85α and p110α (the PI3K regulatory and catalytic subunits) in U87 MG and U343 MG cells showed that the relative levels of these proteins both at the point of control and at different virus incubation times are higher in U343 MG cells that are more sensitive to VV-GMCSF-Lact (*Fig. 3, 4*). Higher p85α and p110α levels are probably associated with the formation of a larger number of PI3K heterodimers and, accordingly, the activation of the PI3K/Akt signaling cascade that, according to published data, is involved not only in vaccinia virus entry into the cell, but also in the early stages of viral replication [28]. In addition, the U343 MG cells most sensitive to the virus have a higher level of pAkt^{Ser473} and pPAK1$^{Ser199/204}$ (PAK1 autophosphorylation at these sites prevents the kinase from being converted to an inactive conformation [31]). At the same time, the levels of these proteins rose with the duration of the incubation of both cell lines with the virus. PAK1 is involved in cytoskeleton reorganization and microtubule dynamics, mediating cell membrane blebbing [32]; inhibition of this enzyme reduces the efficiency of cell infection with the vaccinia virus [10]. Akt is phosphorylated at serine 473 by the mTORC2 complex [33]. The conserved poxvirus protein F17 is known to sequester Raptor and Rictor and disrupt mTOR regulation, which leads to mTORC2 overactivation [34]. Therefore, a higher level of pAkt^{Ser473} in U343 MG cells sensitive to VV-GMCSF-Lact may be indicative of a more efficient virus entry into cells, which is mediated by PI3K and PAK1. However, it should be noted that Akt phosphorylation at threonine 308 is required for its complete activation. The interaction between phosphatidylserine residues located on the viral membrane and the G protein-coupled receptors of the host cell gives rise to p85–p110 heterodimers (PI3K). Then, PI3K converts phosphatidylinositol 4,5-bisphosphate (PIP2) to phosphatidylinositol 3,4,5-trisphosphate (PIP3). After binding of the Akt plextrin homology domain to PIP3, Akt is phosphorylated at Thr308 by PDK1 kinase [35, 36]. The level of phosphorylated Akt was higher in U87 MG cells, which are more resistant to VV-GMCSF-Lact, both at the control point and at different incubation times with the virus, which may indicate that there is a higher level of fully activated Akt in these cells. Akt phosphorylated at the two sites activates the mTORC1 complex both indirectly, via TSC2 inactivation, and directly, via PRAS40 phosphorylation [37]. These processes lead to enhancement of protein synthesis and inhibition of the apoptosis system. Akt regulates apoptotic processes by inhibiting caspases-9 and -3 [38]. In this case, VV-GMCSF-Lact-expressed lactaptin induces apoptotic cell death via the mitochondrial pathway. Incubation of MCF-7 human breast adenocarcinoma cells with the recombinant lactaptin analog RL2 was shown to increase the level of active caspase-9 in the cells [39]. Thus, the resistance of U87 MG glioblastoma cells to VV-GMCSF-Lact can be related to the activity of the Akt kinase that inhibits lactaptin-induced apoptosis.

p85α, p110α, pAkt^{Ser473}, pAkt^{Thr308}, and pPAK1$^{Ser199/204}$ protein levels in BR1.20 and BR3.20 cells before and after exposure to the virus

The levels of the p85α and p110α proteins in BR1.20 and BR3.20 cells varied with virus incubation time (*Fig. 5, 6*). In BR1.20 cells, the p85α level slightly increased at 12 h of incubation. In BR3.20 cells, it increased at 6 h of incubation and then decreased after 12 h of incubation. The p110α level in BR1.20 cells remained unchanged, on average, for 12-h incubation. In BR3.20 cells, it decreased at 12 h. Meanwhile, the p110α level in BR3.20 cells, which are more resistant to VV-GMCSF-Lact, was higher at the control point (cells not exposed to the virus). The PAK1 level in more sensitive BR1.20 cells increased at 0.5 h of incubation with the virus, then decreased after 1 h, and increased again after 12 h. In contrast, the PAK1 level in BR3.20 cells decreased by 1 h of incubation with VV-GMCSF-Lact, increased by 2 h, and decreased again after 12 h. The amount of pAKT^{Ser473} in the cells of both cultures increased after 1 h of incubation, decreased at 2 h, and increased again after 12 h. On the contrary, the pAkt^{Thr308} level in cells of both cultures decreased at 1 h of incubation, increased after 2 h, and decreased after 12 h (*Fig. 3, 4*). However, by 2 and 12 h of incubation with VV-GMCSF-Lact, the pAkt^{Thr308} level was significantly higher in BR3.20 cells, which are more resistant to the virus. Thus, the levels of p85α, p110α (PI3K regulatory and catalytic subunits, respectively), pAkt^{Ser473}, and pPAK1$^{Ser199/204}$ change with incubation time, but do not vary considerably in BR1.20 and BR3.20 cells. However, it is important to note that the pAkt^{Thr308} level in BR3.20 cells,

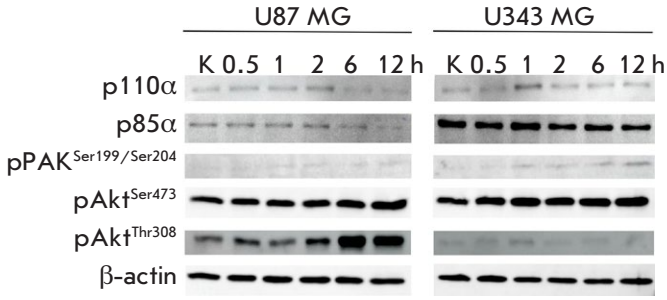

Fig. 3. Analysis of the p85α, p110α, pAKT^{Ser473}, pAKT^{Thr308}, and pPAK1$^{Ser199/204}$ proteins in the cells of immortalized cultures U87 MG and U343 MG. Western blot. Lanes: K – lysates of control cells; 0.5, 1, 2, 6, and 12 h – lysates of cells incubated with VV-GMCSF-Lact for different periods of time

which are more resistant to the virus, was higher and significantly differed from that in BR1.20 cells by 2 h and 12 h of incubation with the virus.

Therefore, the molecular mechanisms regulating PI3K and PAK1 activation and subsequent virus entry into tumor cells may vary significantly in different cellular models of glioblastoma: in immortalized and patient-derived cell cultures. The processes controlling the efficiency of vaccinia virus entry into the cell can also involve other molecular events. For example, glioblastoma cells often contain deletions or mutations in the gene of the tumor suppressor PTEN, which, in turn, inhibits Akt activation [40, 41]. Glioblastoma cells are also characterized by a high expression of PDK1 that is able to activate PAK1 and is involved in cytoskeleton reorganization processes [42–44].

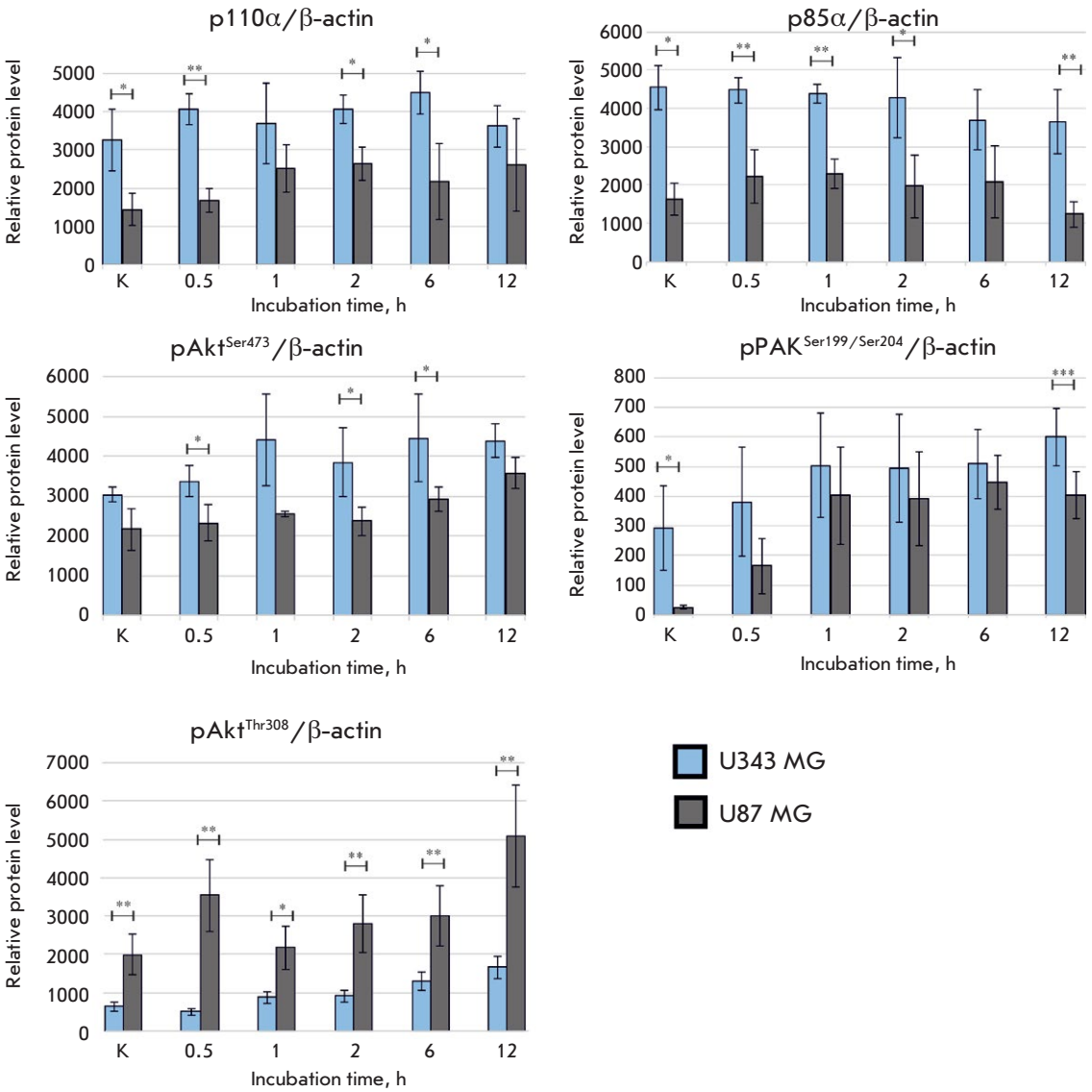

Fig. 4. The relative levels of the p85α, p110α, pAKT^{Ser473}, pAKT^{Thr308}, and pPAK1$^{Ser199/204}$ proteins in the cells of immortalized cultures U87 MG and U343 MG before and after incubation with VV-GMCSF-Lact ($^{*}p < 0.05$, $^{**}p < 0.01$, $^{***}p < 0.001$)

In addition, the efficiency of VV-GMCSF-Lact entry into glioblastoma cells does not mean that the virus would exhibit pronounced oncotoxic activity, because the virus needs to successfully replicate in the cell to achieve the cytotoxic effect. VV-GMCSF-Lact contains deletions in the viral thymidine kinase and growth factor genes, which prevents it from replicating in healthy, normally dividing cells. However, tumor cells may also differ in levels of growth factors and other proteins required for viral DNA replication and subsequent assembly of new viral particles, which determines the antitumor efficacy of VV-GMCSF-Lact towards different tumors.

Given these findings, we may suggest that human glioblastoma cells resistant to VV-GMCSF-Lact are characterized by an increased level of activated Akt

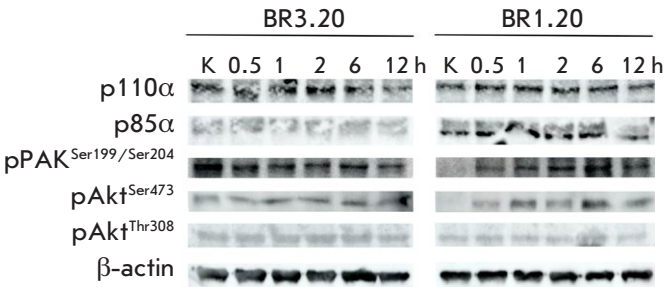

Fig. 5. Analysis of the p85α, p110α, pAKT^{Ser473}, pAKT^{Thr308}, and pPAK1$^{Ser199/204}$ proteins in the cells of patient-derived cultures BR1.20 and BR3.20. Western blot. Lanes: K – lysates of control cells; 0.5, 1, 2, 6, and 12 h – lysates of cells incubated with VV-GMCSF-Lact for different periods of time

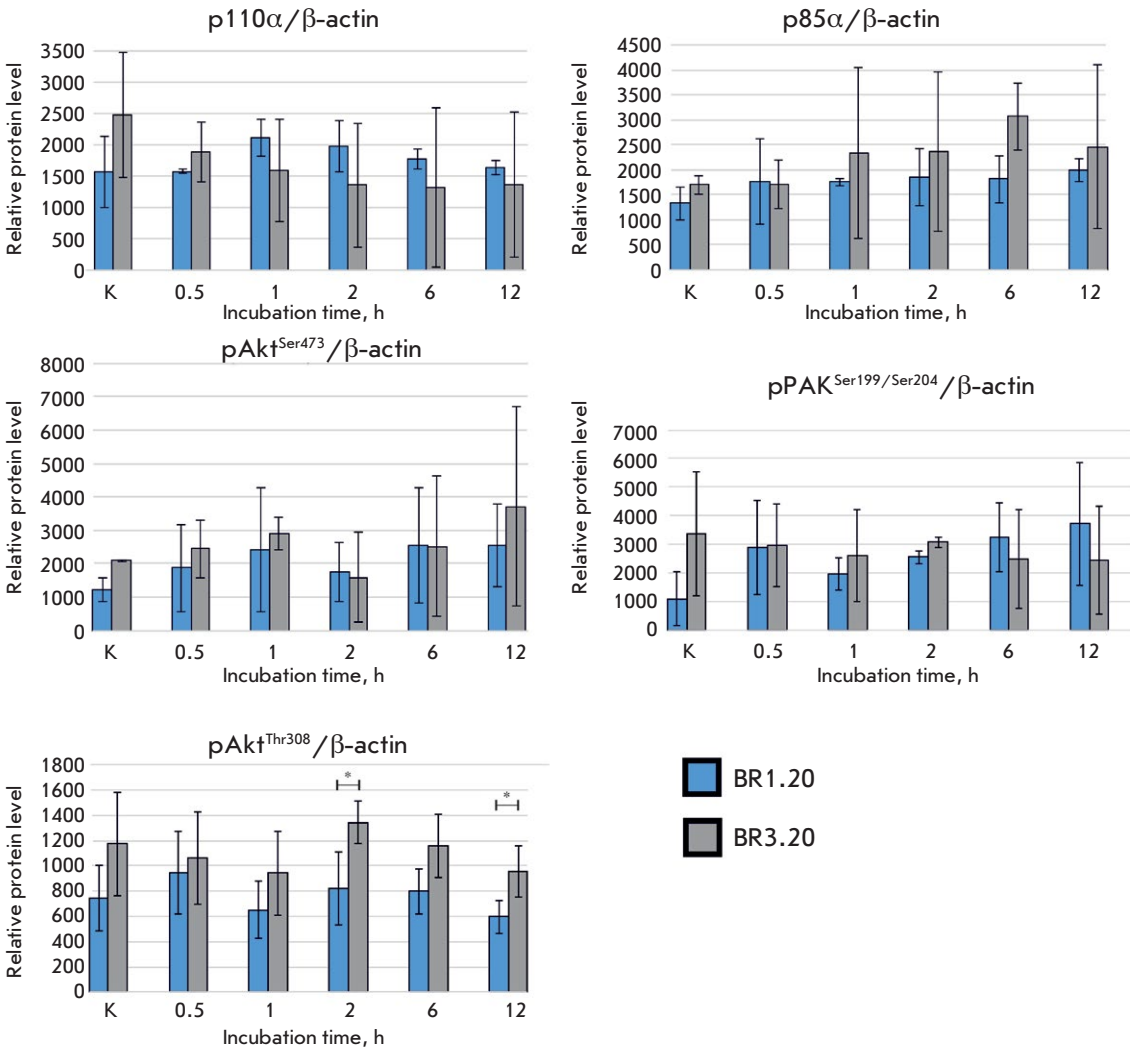

Fig. 6. The relative levels of the p85α, p110α, pAKT^{Ser473}, pAKT^{Thr308}, and pPAK1$^{Ser199/204}$ proteins in the cells of patient-derived cultures BR1.20 and BR3.20 before and after incubation with VV-GMCSF-Lact. (* $p < 0.05$)

kinase inhibiting the mitochondrial pathway of apoptosis, which probably reduces the cytotoxic effect of the recombinant virus expressing the transgene lactaptin that is an inductor of the mitochondrial apoptotic pathway.

CONCLUSIONS

Our results suggest that human glioblastoma cells sensitive to the oncolytic virus VV-GMCSF-Lact are characterized by a low level of disturbance in the programmed cell death cascade. The mechanisms of glioblastoma resistance to standard therapy are being intensively studied. However, the issue of its resistance to oncolytic viruses still remains open [6, 7]. The mechanisms of action of the vaccinia virus, which was used to generate the recombinant strain VV-GMCSF-Lact, are well studied. The processes occurring in the host cell upon pathogen entry were also investigated. Tumor cells, and CSCs in particular, are characterized by disturbances in many signaling pathways, regulation of the cell cycle, and cascades of programmed cell death. A detailed study of the mechanisms contributing to the efficacy of VV-GMCSF-Lact-based therapy will help identify potential markers of tumors that are sensitive to the virus and possible targets for combined therapy with VV-GMCSF-Lact. ●

The reported study was funded by RFBR according to the research project № 20-34-90041. This work was partially supported by the Russian state-funded project for ICBFM SB RAS (grant number 122022100238-7).

REFERENCES

1. Tan A.C., Ashley D.M., López G.Y., Malinzak M., Friedman H.S., Khasraw M. // CA Cancer J. Clin. 2020. V. 70. № 4. P. 299–312.
2. Kochneva G., Sivolobova G., Tkacheva A., Grazhdantseva A., Troitskaya O., Nushtaeva A., Tkachenko A., Kuligina E., Richter V., Koval O. // Oncotarget. 2016. V. 7. № 45. P. 74171–74188.
3. Vasileva N., Ageenko A., Dmitrieva M., Nushtaeva A., Mishinov S., Kochneva G., Richter V., Kuligina E. // Life. 2021. V. 11. № 10. P. 1084.
4. Mao P., Joshi K., Li J., Kim S.-H., Li P., Santana-Santos L., Luthra S., Chandran U.R., Benos P.V., Smith L., et al. // Proc. Natl. Acad. Sci. USA. 2013. V. 110. № 21. P. 8644–8649.
5. Bhat K.P.L., Balasubramaniyan V., Vaillant B., Ezhilarasan R., Hummelink K., Hollingsworth F., Wani K., Heathcock L., James J.D., Goodman L.D., et al. // Cancer Cell. 2013. V. 24. № 3. P. 331–346.
6. Zhang Q., Liu F. // Cell Death Dis. 2020. V. 11. № 6. P. 485.
7. Raja J., Ludwig J.M., Gettinger S.N., Schalper K.A., Kim H.S. // J. Immunother. Canc. 2018. V. 6. № 1. P. 140.
8. Moss B. // Virology. 2006. V. 344. № 1. P. 48–54.
9. Sobhy H. // Arch. Virol. 2017. V. 162. № 12. P. 3567–3585.
10. Mercer J., Helenius A. // Science. 2008. V. 320. № 5875. P. 531–535.
11. Mercer J., Helenius A. // Nat. Cell Biol. 2009. V. 11. № 5. P. 510–520.
12. Bahadur S., Sahu A.K., Baghel P., Saha S. // Oncol. Rev. 2019. V. 13. № 2. P. 114–124.
13. Skaga E., Kulesskiy E., Brynjulvsen M., Sandberg C.J., Potdar S., Langmoen I.A., Laakso A., Gaál-Paavola E., Perola M., Wennerberg K., et al. // Clin. Translat. Med. 2019. V. 8. № 1. P. 33.
14. Prager B.C., Bhargava S., Mahadev V., Hubert C.G., Rich J.N. // Trends Cancer. 2020. V. 6. № 3. P. 223–235.
15. Wang J., Wakeman T.P., Lathia J.D., Hjelmeland A.B., Wang X.-F., White R.R., Rich J.N., Sullenger B.A. // Stem Cells. 2009. V. 28. № 1. P. 17–28.
16. Hassn Mesrati M., Behrooz A.B., Abuhamad Y.A., Syahir A. // Cells. 2020. V. 9. № 5. P. 1236.
17. Lauko A., Lo A., Ahluwalia M.S., Lathia J.D. // Semin. Cancer Biol. 2021. P. S1044579X21000493.
18. Capela A., Temple S. // Neuron. 2002. V. 35. № 5. P. 865–875.
19. Son M.J., Woolard K., Nam D.-H., Lee J., Fine H.A. // Cell Stem Cell. 2009. V. 4. № 5. P. 440–452.
20. Moos M., Tacke R., Scherer H., Teplow D., Früh K., Schachner M. // Nature. 1988. V. 334. № 6184. P. 701–703.
21. Mohanan V., Temburni M.K., Kappes J.C., Galileo D.S. // Clin. Exp. Metastasis. 2013. V. 30. № 4. P. 507–520.
22. Cheng L., Wu Q., Huang Z., Guryanova O.A., Huang Q., Shou W., Rich J.N., Bao S. // EMBO J. 2011. V. 30. № 5. P. 800–813.
23. Held-Feindt J., Schmelz S., Hattermann K., Mentlein R., Mehdorn H.M., Sebens S. // Neurochem. Internat. 2012. V. 61. № 7. P. 1183–1191.
24. Bao S., Wu Q., Li Z., Sathornsumetee S., Wang H., McLendon R.E., Hjelmeland A.B., Rich J.N. // Cancer Res. 2008. V. 68. № 15. P. 6043–6048.
25. Li Z. // Exp. Hematol. Oncol. 2013. V. 2. № 1. P. 17.
26. Bao S., Wu Q., McLendon R.E., Hao Y., Shi Q., Hjelmeland A.B., Dewhirst M.W., Bigner D.D., Rich J.N. // Nature. 2006. V. 444. № 7120. P. 756–760.
27. Wei Y., Jiang Y., Zou F., Liu Y., Wang S., Xu N., Xu W., Cui C., Xing Y., Liu Y., et al. // Proc. Natl. Acad. Sci. USA. 2013. V. 110. № 17. P. 6829–6834.
28. Soares J.A.P., Leite F.G.G., Andrade L.G., Torres A.A., De Sousa L.P., Barcelos L.S., Teixeira M.M., Ferreira P.C.P., Kroon E.G., Souto-Padrón T., et al. // J. Virol. 2009. V. 83. № 13. P. 6883–6899.
29. Diehl N., Schaal H. // Viruses. 2013. V. 5. № 12. P. 3192–3212.
30. El-Jesr M., Teir M., Maluquer de Motes C. // Front. Immunol. 2020. V. 11. P. 568412.
31. Lei M., Lu W., Meng W., Parrini M.-C., Eck M.J., Mayer B.J., Harrison S.C. // Cell. 2000. V. 102. № 3. P. 387–397.
32. Meshki J., Douglas S.D., Hu M., Leeman S.E., Tuluc F. // PLoS One. 2011. V. 6. № 9. P. e25332.
33. Moore S.F., Hunter R.W., Hers I. // J. Biol. Chem. 2011. V. 286. № 28. P. 24553–24560.
34. Meade N., Furey C., Li H., Verma R., Chai Q., Rollins M.G., DiGiuseppe S., Naghavi M.H., Walsh D. // Cell. 2018.

V. 174. № 5. P. 1143–1157.e17.
35. Alessi D.R., James S.R., Downes C.P., Holmes A.B., Gaffney P.R.J., Reese C.B., Cohen P. // Curr. Biol. 1997. V. 7. № 4. P. 261–269.
36. Manning B.D., Cantley L.C. // Cell. 2007. V. 129. № 7. P. 1261–1274.
37. Memmott R.M., Dennis P.A. // Cell. Signal. 2009. V. 21. № 5. P. 656–664.
38. Zhou H., Li X.-M., Meinkoth J., Pittman R.N. // J. Cell Biol. 2000. V. 151. № 3. P. 483–494.
39. Fomin A.S., Koval O.A., Semenov D.V., Potapenko M.O., Kuligina E.V., Kit Yu.Ya., Richter V.A. // Bioorganic Chemistry. 2012. V. 38. №. 1. P. 1–7.
40. Cetintas V.B., Batada N.N. // J. Transl. Med. 2020. V. 18. № 1. P. 45.
41. Smith J.S., Tachibana I., Passe S.M., Huntley B.K., Borell T.J., Iturria N., O'Fallon J.R., Schaefer P.L., Scheithauer B.W., James C.D., et al. // J. Natl. Cancer Inst. 2001. V. 93. № 16. P. 1246–1256.
42. Geue S., Aurbach K., Manke M.-C., Manukjan G., Münzer P., Stegner D., Brähler C., Walker-Allgaier B., Märklin M., Borst C.E., et al. // Blood. 2019. V. 134. № 21. P. 1847–1858.
43. Han J.E., Lim P.W., Na C.M., Choi Y.S., Lee J.Y., Kim Y., Park H.W., Moon H.E., Heo M.S., Park H.R., et al. // Exp. Neurobiol. 2017. V. 26. № 5. P. 295–306.
44. Velpula K.K., Tsung A.J. // CNS Oncology. 2014. V. 3. № 3. P. 177–179.

Imidazole Derivative As a Novel Translation Inhibitor

D. A. Lukianov[1,6*], V. S. Buev[2], Y. A. Ivanenkov[3,4], V. G. Kartsev[5], D. A. Skvortsov[6,7], I. A. Osterman[1,6,8], P. V. Sergiev[1,2,6,9]

[1]Skolkovo Institute of Science and Technology, Center of Life Sciences, Skolkovo, 143028 Russia
[2]Lomonosov Moscow State University, Faculty of Bioengineering and Bioinformatics, Moscow, 119991 Russia
[3]Institute of Biochemistry and Genetics Russian Academy of Science (IBG RAS), Ufa Scientific Centre, Ufa, 450054 Russia
[4]The Federal State Unitary Enterprise Dukhov Automatics Research Institute, Moscow, 127055 Russia
[5]InterBioScreen Ltd, Chernogolovka, 142432 Russia
[6]Lomonosov Moscow State University, Chemistry Department, Moscow, 119991 Russia
[7]Higher School of Economics, Faculty of biology and biotechnologies, Moscow, 101000 Russia
[8]Sirius University of Science and Technology, Genetics and Life Sciences Research Center, Sochi, 354340 Russia
[9]Lomonosov Moscow State University, Institute of functional genomics, Moscow, 119991 Russia
*E-mail: Dmitrii.Lukianov@skoltech.ru

Received: December 18, 2021; in final form, March 10, 2022
DOI: 10.32607/actanaturae.11654

ABSTRACT **Searching for novel compounds with antibiotic activity and understanding their mechanism of action is extremely important. The ribosome is one of the main targets for antibiotics in bacterial cells. Even if the molecule does not suit the clinical application for whatever reasons, an investigation of its mechanism of action can deepen our understanding of the ribosome function. Such data can inform us on how the already used translational inhibitors can be modified. In this study, we demonstrate that 1-(2-oxo-2-((4-phenoxyphenyl)amino)ethyl)-3-(*p*-tolyl)-6,7-dihydro-5H-pyrrolo[1,2-a]imidazol-1-ium chloride inhibits protein synthesis both *in vivo* and *in vitro*.**

KEYWORDS **translation, bacteria, translation inhibitor, compounds with antibiotic activity, imidazole derivatives.**

INTRODUCTION

The coronavirus pandemic has highlighted the problem of human vulnerability to pathogens. The outlook for the expansion of antibiotic resistance in bacteria is also unfavorable. According to the Organization for Economic Cooperation and Development (OECD), approximately 17% of infectious diseases in OECD member countries were rooted in antibiotic resistance of bacteria in 2015. In the Russian Federation, the percentage of such diseases exceeds 40% [1]. As of 2016, ~700,000 people die each year from infections caused by antibiotic-resistant bacteria. According to a prediction published in 2016, the number of deaths caused by resistant bacteria may be as high as 10 million people by 2050 [2]. Hence, modern science currently faces the challenge of coming up with novel antibiotics.

The protein synthesis occurring on ribosomes is the vital process through which the genetic information in the mRNA is translated into the amino acid sequence of a protein. The bacterial ribosome consists of three ribosomal RNAs (16S, 23S, and 5S) and more than 50 proteins, forming two subunits; the small, 30S, subunit and the large, 50S, one; they combine to form the 70S ribosome. Each of these subunits and the exit tunnel through which the newly synthesized peptide is released are targets for a large number of antibiotics [3]. Thus, tetracycline [4], streptomycin [5], pactamycin [6], and amicoumacin A [6] bind to the small ribosomal subunit. The structure of the complex formed be-

tween the ribosome and each of these antibiotics has been determined. Chloramphenicol [7], clindamycin [8], and blasticidin C [9] can bind to the large ribosomal subunit, thus leading to protein synthesis arrest. The antibiotics tetracenomycin X [10], klebsazolicin [11], and erythromycin [7] inhibit peptide release from the ribosome. According to published data, more than half of all drugs used to treat infections belong to the class of protein synthesis inhibitors [12]. Therefore, understanding the ribosome function can be crucial both in the search for novel drugs and in improving the ones that are already in our possession. We have described a novel translation inhibitor, and understanding of its mechanism of action can be highly valuable both in fundamental science and, after we master it, in the real-world healthcare system.

EXPERIMENTAL

Application of a dual reporter system for analyzing the mechanism of action of antibiotics

The mechanism of antibiotic action was studied using the pDualrep2 reporter system [13]. For conducting the assay, an overnight culture of *Escherichia coli* JW5503 cells [14] frozen in 50% glycerol was diluted tenfold in LB liquid broth and inoculated in Petri dishes containing 1.5% LB agar and ampicillin (50 μg/mL) to obtain a bacterial lawn. The culture dishes were dried, and 96 samples of different molecules (*Fig. 1*) were applied onto their surface using a Janus robotic workstation (Perkin Elmer, USA). Before their application, the compounds were dissolved in dimethyl sulfoxide (DMSO, PharmaMed, Russia) to a concentration of 20 mg/mL. Each compound (30 μg) was applied. The culture dishes, containing cells, were then incubated for 18 h at 37°C. To visualize the results, the culture dishes were scanned using a ChemiDoc imaging system (Bio-Rad, USA) in Cy3 (for TurboRFP detection) and Cy5 channels (for Katushka2S detection).

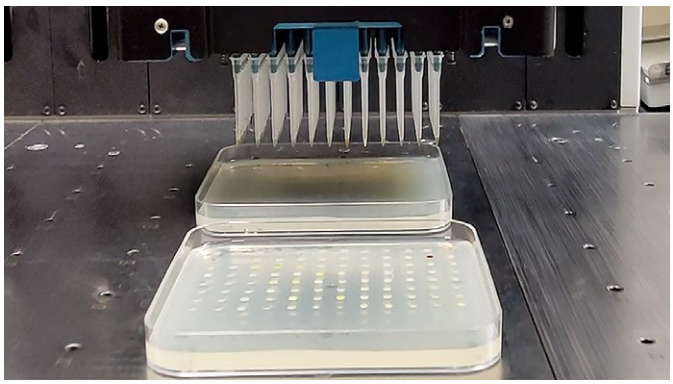

Fig. 1. Transferring 96 individual molecules onto the cell lawn

Measuring the minimum inhibitory concentration

The minimum inhibitory concentration was measured in 96-well plates. Plate rows (1–11) were filled with a *E. coli* (JW5503) cell suspension obtained by diluting the overnight culture 200-fold. 200 μL of the cells was added to the first row, and 100 μL of the cells was added to the subsequent rows. The last plate row (row 12) was filled with the LB culture medium without cells to control for the validity of the experiment.

The test compound (2 μL; concentration, 20 mg/mL) was added to the cells of row 1, followed by a series of twofold dilutions in the subsequent rows (up to row 10). For this purpose, 100 μL of the mixture was transferred from the first well to the second one using an eight-channel pipette, mixed, and the procedure was repeated up to row 10. Erythromycin (2 μL; concentration, 5 mg/mL) was added to one of the rows of each plate instead of the test substance as a control. The plates were then subjected to aeration incubation at 37°C overnight at 200 rpm. Cell concentration was estimated according to the absorbance (A_{600}). The measurements were performed on a Victor X5 2030 plate reader (Perkin Elmer).

The lowest concentration of the test compound that completely inhibited bacterial growth was considered the minimum inhibitory concentration.

Cytotoxicity test

The cytotoxicity of the test compound was verified using the MTT method (3-(4,5-dimethylthiazol-2-yl)-2,5-diphenyl-tetrazolium bromide) [15], with the certain modifications. Some 2,500 cells per well for MCF7, HEK293T, and A549 cell lines or 4,000 cells per well for the VA-13 cell line were inoculated into 135 μL of the DMEM-F12 medium (Gibco, USA) in a 96-well plate and incubated in a 5% CO_2 incubator for the first 16 h without any treatment. Next, 15 μL of a mixture of the medium and a solution of the test compound in DMSO (final DMSO concentrations in the media were ⩽ 1%) were added to the cells; the cells were treated for 72 h in the presence of the test compounds in eight dilutions (100 ng/mL – 200 μg/mL); three replicates were made for each dilution; doxorubicin was used as a control substance. MTT was then added to the cells (OJSC PanEco, Russia) to a final concentration of 0.5 g/L (a supernatant fluid diluted in PBS tenfold

was used), and the cells were incubated for 2 h in an incubator in an atmosphere of 5% CO_2 at 37°C. The MTT solution was then removed, and 140 μL of DMSO (OJSC Pharmamed, Russia) was added. The plates were shaken (80 rpm) to let formazan dissolve. Absorbance was measured using a Victor X5 2030 plate reader (Perkin Elmer) at 565 nm (for measuring formazan concentration). The results were used to plot the dose–response relationships and assess the IC50 value (GraphPad Software, Inc., USA).

In vitro translation

The ability of the tested compound to inhibit translation was determined using a *E. coli* S30 Extract System for Linear Templates kit (Promega, USA).

The reaction was conducted in 5 μL of the mixture having the following composition: 2 μL of S30 Premix, 1.5 μL of S30 from the *E. coli* cell extract, 0.5 μL of the amino acid mixture (concentration of each amino acid, 1 mM), 0.5 μL of mRNA (Fluc 200 ng/μL), 0.2 mM *D*-luciferin, 0.1 μL of the RiboLock RNase inhibitor, and 0.5 μL of the test compound. The reaction mixture (except for mRNA) was pre-mixed on ice and then incubated at room temperature for 5 min to give the antibiotic ample time to bind to the ribosome before the initiator complex assembly; the mixture was then returned on ice, and the template was added.

Translation was carried out for 20 min at 37°C. The signal was then detected on a Victor X5 2030 plate reader (Perkin Elmer).

Toeprinting assay

The toeprinting assay was conducted according to the protocol described by Orelle et al. [16].

At the first stage, the primers were labeled with [γ-^{32}P]ATP polynucleotide kinase (ThermoFisher, USA) according to the manufacturer's protocol. Next, *in vitro* translation of the short-model mRNA was performed using a PURExpress® *In Vitro* Protein Synthesis Kit (New England Biolabs, USA). The reaction mixture (volume, 5 μL) contained 2 μL of solution A, 1 μL of solution B, 0.2 μL of RiboLock (ThermoFisher), 0.5 μL of the test compound, 0.5 μL of DNA template (0.2 mmol/μL), and 0.5 μL of the radiolabeled primer. The mixture was incubated at 37°C for 20 min, and 1 μL of the reverse transcription mix from the Titan One Tube RT-PCR System kit (Roche, Switzerland) was added. Reverse transcription was conducted for 15 min at 37°C. The reaction was stopped by adding 1 μL of 10 M NaOH, followed by incubation at 37°C for 15 min. The neutralization was performed by adding 1 μL of 10 N HCl. Next, 200 μL of the resuspension buffer as added.

The resulting samples were purified using a QIAquick PCR purification kit (Qiagen, Germany).

The sequence mixtures were prepared using a USB® Thermo Sequenase Cycle Sequencing Kit (Affymetrix, USA) according to the manufacturer's protocol.

Electrophoresis was carried out in 6% polyacrylamide gel (60 × 40 × 0.03 cm) containing 19% acrylamide, 1% N,N'-methylenebisacrylamide, and 7 M urea in TBE buffer for 2–3 h. The specimens and products of the sequencing reactions (2 and 1.5 μL, respectively) were applied onto the gel.

The gel was transferred onto 3-mm paper, dried, and exposed to a sensory screen for 18 h. The screen was scanned using a Typhoon FLA 9500 Biomolecular Imager (GE Healthcare, USA).

The RST1 template for this experiment was obtained by PCR amplification using a Taq-DNA-polymerase kit (ThermoFisher), according to the standard protocol. The template sequence was as follows: ACTAATACGACTCACTATAGGGCTTAAGTATAAGGAGGAAAACATATGTATTGGGTAACCTCACGTCAGCCGAATATGCTGAAAATCCATGGCTTCGAAGACTGCGCCTAATAATAATAAAAAAAGTGATAGAATTCTATCGTTAATAAGCAAAATTCATTATAAC. The forward primer GTAAAACGACGGCCAGT, reverse primer CAGGAAACAGCTATGAC, and primer for reverse transcription GGTTATAATGAATTTTGCTTATTAAC were used.

RESULTS AND DISCUSSION

High-throughput screening for compounds exhibiting antimicrobial activity

An *E. coli* JW5503 strain with *tolC* deletion [14] transformed with plasmid pDualrep2 [13] was used for screening for compounds exhibiting antimicrobial activity (*Fig. 2A*). The *tolC* gene is responsible for the synthesis of the AcrAB-TolC component of the efflux system, and its deletion renders cells more sensitive to the test compounds [17]. The reporter system functions according to the following principle: if a compound inhibits protein synthesis in the cell, it results in ribosomal stalling on the modified tryptophan operon sequence (trpL-2-Ala), which induces the synthesis of the far-red fluorescent protein Katushka2S (*Fig. 2B*, red pseudo-color). DNA damage-inducing compounds elicit the SOS response in the cell, thus causing dissociation of the LexA repressor protein from the *sulA* promoter and initiation of the expression of the gene encoding the TurboRFP red fluorescent protein (*Fig. 2B*, green pseudo-color).

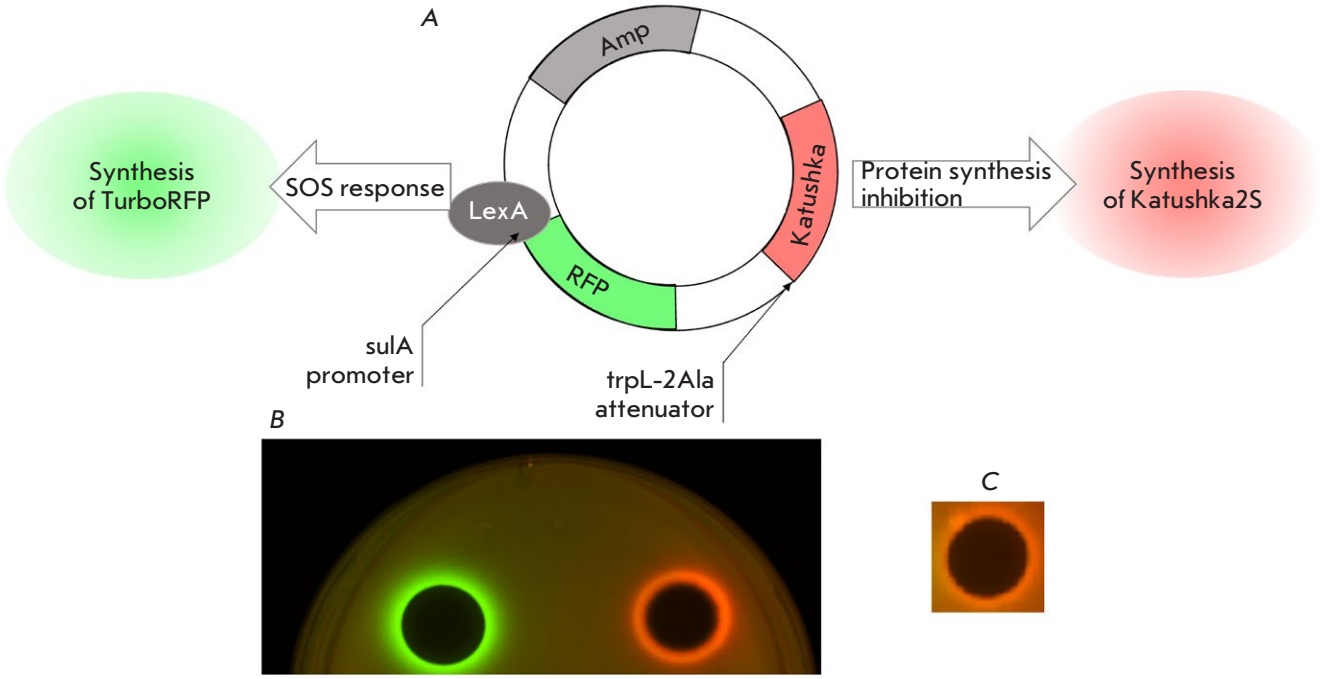

Fig. 2. (*A*) – the composition of the pDualrep2 reporter plasmid. (*B*) – induction of a two-color dual-reporter system sensitive to inhibitors of ribosome progression or DNA replication. Drops of erythromycin (right-hand side, 2 μg) and levofloxacin (left-hand side, 0.05 μg) were placed on the surface of an agar plate containing *E. coli* JW5503 cells transformed with the pDualrep2 plasmid. Expression of Katushka2S (red) is induced by translation inhibitors, whereas RFP expression (green) is induced upon DNA damage. (*C*) – induction of a two-color dual-reporter system induced by 1-(2-oxo-2-((4-phenoxyphenyl)amino)ethyl)-3-(*p*-tolyl)-6,7-dihydro-5H-pyrrolo[1,2-a]imidazol-1-ium chloride (30 μg)

During the high-throughput screening libraries of the chemical compounds provided by InterBioScreen Ltd., among the compounds with antimicrobial activity, we found a molecule that both inhibited growth of the *E. coli* strain JW5503 transformed with plasmid pDualrep2 and induced the expression of the *Katushka2S* gene that is typical of translation inhibitors (*Fig. 2C*). The formula of this molecule, 1-(2-oxo-2-((4-phenoxyphenyl)amino)ethyl)-3-(*p*-tolyl)-6,7-dihydro-5H-pyrrolo[1,2-a]imidazol-1-ium chloride, is shown in *Fig. 3A* (STOCK4S-33513). During screening, two analogs of this molecule were tested: 1-(2-((2,5-dimethoxyphenyl)amino)-2-oxoethyl)-3-(*p*-tolyl)-6,7-dihydro-5H-pyrrolo[1,2-a] imidazol-1-ium chloride (STOCK4S-37310, *Fig. 3B*) and 1-(2-((2-methoxyphenyl)amino)-2-oxoethyl)-3-(*p*-tolyl)-6,7-dihydro-5H-pyrrolo[1,2-a]imidazol-1-ium chloride (STOCK4S-72264, *Fig. 3C*). These molecules did not yield growth inhibition zones for the *E. coli* JW5503 strain transformed with plasmid

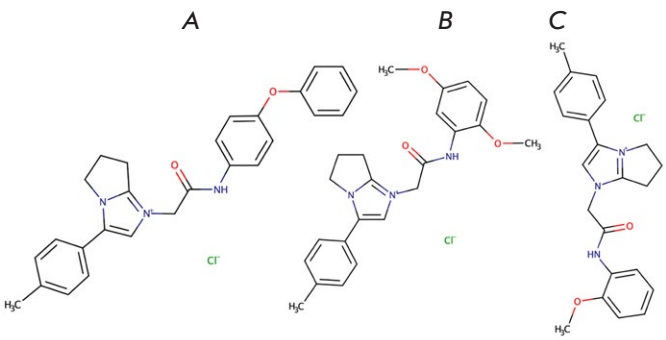

Fig. 3. (*A*) – structural formula of the active compound 1-(2-oxo-2-((4-phenoxyphenyl)amino)ethyl)-3-(*p*-tolyl)-6,7-dihydro-5H-pyrrolo[1,2-a]imidazol-1-ium chloride (STOCK4S-33513). (*B*) – structural formula of the active compound analog 1-(2-((2,5-dimethoxyphenyl)amino)-2-oxoethyl)-3-(*p*-tolyl)-6,7-dihydro-5H-pyrrolo[1,2-a]imidazol-1-ium chloride (STOCK4S-37310). (*C*) – structural formula of the active compound analog 1-(2-((2-methoxyphenyl)amino)-2-oxoethyl)-3-(*p*-tolyl)-6,7-dihydro-5H-pyrrolo[1,2-a]imidazol-1-ium chloride (STOCK4S-72264)

pDualrep2 in the solid agar medium test; therefore, further experiments were conducted using exclusively 1-(2-oxo-2-((4-phenoxyphenyl)amino)ethyl)-3-(*p*-tolyl)-6,7-dihydro-5H-pyrrolo[1,2-a]imidazol-1-ium chloride.

This compound was inactive in the test for the *E. coli* BW25113 strain transformed with the reporter plasmid.

Measuring the minimum inhibitory concentration

The minimum inhibitory concentration was measured using the serial dilution method for the *E. coli* JW5503 strain with *tolC* deletion [14]. The minimum inhibitory concentration of 1-(2-oxo-2-((4-phenoxyphenyl)amino)ethyl)-3-(*p*-tolyl)-6,7-dihydro-5H-pyrrolo[1,2-a]imidazol-1-ium chloride is 3.1 μg/mL. It is comparable with that of erythromycin, a natural protein synthesis inhibitor whose minimum inhibitory concentration for this strain was 3.1 μg/mL.

Measuring cytotoxicity in eukaryotic cells

The toxicity of this compound was tested in several human cell cultures using the MTT assay. Unfortunately, it was found to be more toxic to human cells compared to bacterial ones; so, this compound cannot be used as a drug, at least in the tested form. The data are summarized in *Table*.

Translation in the cell-free system

The translation reaction in the cell-free system was carried out using a *E. coli* S30 Extract System for Linear Templates kit (Promega). Synthesis of firefly luciferase in this experiment was determined using the reaction of luciferin oxidation to oxyluciferin. If the reaction mixture contains a translation inhibitor, luciferase is not synthesized and luciferin is not degraded. The results of each experiment were normalized with respect to the added solvent (dimethyl sulfoxide), whose volume was identical to that of the test compound. The data for 1-(2-oxo-2-((4-phenoxyphenyl)amino)ethyl)-3-(*p*-tolyl)-6,7-dihydro-5H-pyrrolo[1,2-a]imidazol-1-ium chloride (STOCK4S-33513) are presented in *Fig. 4*.

According to the results, it appears fair to say that the compound 1-(2-oxo-2-((4-phenoxyphenyl)amino)ethyl)-3-(*p*-tolyl)-6,7-dihydro-5H-pyrrolo[1,2-a]imidazol-1-ium chloride (STOCK4S-33513) is a translation inhibitor.

Analysis of the ribosome stall sites

Not only does the toeprinting assay allow one to verify whether a compound inhibits protein synthesis, or not, but it also makes it possible to hypothesize regarding the stage at which translation was stalled. The working principle of the method is as follows: in a cell-free system that is based on individually isolated translation components, a short peptide is synthesized in the presence of the test compound. A radiolabeled primer (complementary to the 3'-terminus of mRNA), RNA-dependent DNA

The MTT assay results for 1-(2-oxo-2-((4-phenoxyphenyl)amino)ethyl)-3-(*p*-tolyl)-6,7-dihydro-5H-pyrrolo[1,2-a]imidazol-1-ium chloride

Cell line	Concentration*, μg/mL
HEK293T	0.2 ± 0.1
MCF7	1.8 ± 0.5
A549	0.5 ± 0.1
Va-13	0.4 ± 0.2

*Concentration of the test compound toxic to cells, μg/mL.

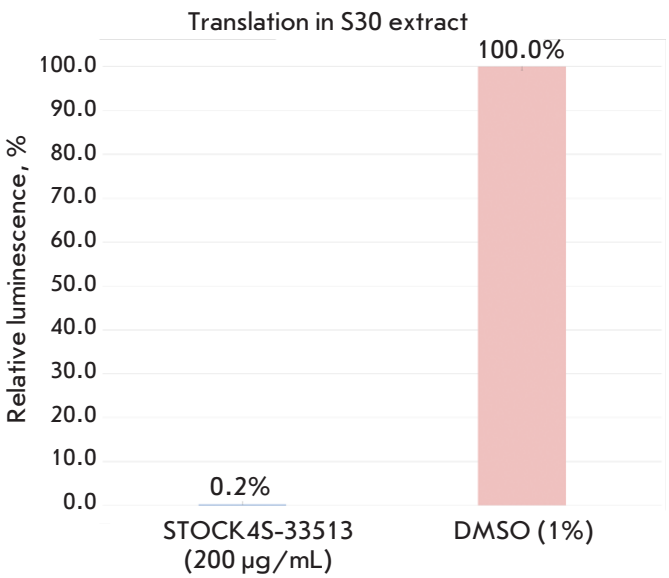

Fig. 4. Protein synthesis inhibition with 200 μg/mL of 1-(2-oxo-2-((4-phenoxyphenyl)amino)ethyl)-3-(*p*-tolyl)-6,7-dihydro-5H-pyrrolo[1,2-a]imidazol-1-ium chloride using an *in vitro* cell-free translation system. The activity of luciferase synthesised using an *in vitro* cell-free translation system without translation inhibitors is taken as 100%

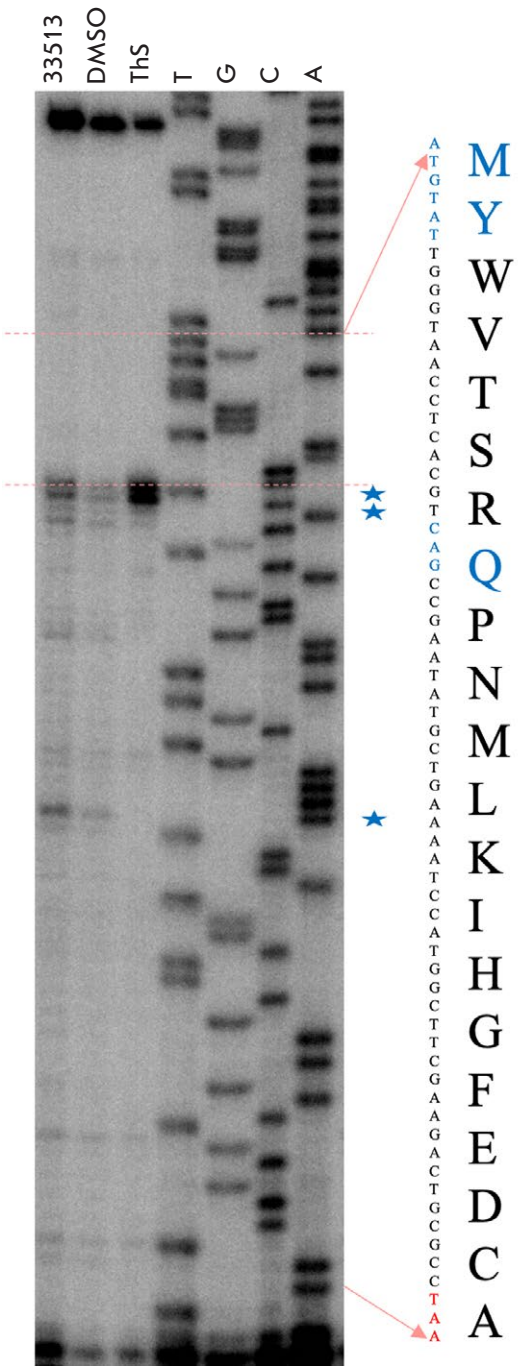

Fig. 5. The scheme of toeprinting assay on the RST1 template: lane 1 (STOCK4S-33513) corresponds to the *in vitro* cell-free translation system supplemented with 200 μg/mL 1-(2-oxo-2-((4-phenoxyphenyl)amino)ethyl)-3-(*p*-tolyl)-6,7-dihydro-5H-pyrrolo[1,2-a]imidazol-1-ium chloride; lane 2 (DMSO) corresponds to the negative control (1% DMSO); lane 3 (Ths) corresponds to 50 μM thiostrepton (Ths inhibits translation at the start codon [18]); T, G, A, C are the lanes corresponding to sequencing reactions with serial stops at the corresponding nucleotides

polymerase, and 2'-deoxynucleoside-5'-triphosphates are added to the reaction mixture. Next, template RNA-directed primer extension takes place until RNA-dependent DNA polymerase either meets the ribosome or reaches the template end. If a protein synthesis inhibitor is added to the mixture, the ribosome will stall on the template and will not allow RNA-dependent DNA polymerase to reach the end of the template; so, the cDNA fragment will be short. The exact length of the cDNA fragment and the ribosome stall site on mRNA can be calculated according to the RNA sequence and position of the reverse transcription product in the gel with respect to the Sanger sequencing products being separated in the respective gel lanes. In a typical experimental run, we also compared the sites of ribosome stalling induced by the novel and already known translation inhibitors. The distance between the first nucleotide of the P site of the ribosome blocked on mRNA and the last synthesized cDNA nucleotide is 16 nucleotides long. It is convenient to use the thiostrepton antibiotic for comparison as it is known to induce ribosome stalling at the first translation step, right when the start codon AUG resides at the ribosomal P site. Based on these data, we have performed computations for the codons residing at the P site at the instant of ribosomal stalling (*Fig. 5*). These codons were 1-AUG (M), 2-UAU (Y), and 8-CAG (Q). However, in the control experiment without the DMSO antibiotic added, one can see the same short pauses (but less pronounced) at the same spots. Therefore, a hypothesis can be put forward that this translation inhibitor can affect the kinetics of protein synthesis at mRNA regions that are difficult for the ribosome to traverse.

CONCLUSIONS

We have investigated a novel inhibitor of bacterial translation, 1-(2-oxo-2-((4-phenoxyphenyl)amino) ethyl)-3-(*p*-tolyl)-6,7-dihydro-5H-pyrrolo[1,2-a]imidazol-1-ium chloride, retrieved from the chemical library. This compound was shown to induce the reporter system and act as an *in vivo* translation inhibitor. It was revealed that it can inhibit *in vitro* translation and potentiate ribosomal stalling during the synthesis of small peptides. Although this compound is highly toxic to human cells and, thus, cannot be used as a drug, a more thorough examination of this molecule may provide a deeper insight into the functioning of such an important molecular machine as ribosome. ●

This work was supported by the Russian Foundation for Basic Research (project No. 20-34-90048).

REFERENCES
1. Stemming the Superbug Tide. Paris: OECD Publishing, 2018. 224 p.
2. O'Neill J. Tackling drug-resistant infections globally. L.: Government of the United Kingdom, 2016. 84 p.
3. Ramakrishnan V. // Cell. 2002. V. 108. № 4. P. 557–572.
4.Jenner L., Starosta A.L., Terry D.S., Mikolajka A., Filonava L., Yusupov M., Blanchard S.C., Wilson D.N., Yusupova G. // Proc. Natl. Acad. Sci. USA. 2013. V. 110. № 10. P. 3812–3816.
5. Demirci H., Murphy F., Murphy E., Gregory S.T., Dahlberg A.E., Jogl G. // Nat. Commun. 2013. V. 4. P. 1355.
6. Polikanov Y.S., Osterman I.A., Szal T., Tashlitsky V.N., Serebryakova M.V., Kusochek P., Bulkley D., Malanicheva I.A., Efimenko T.A., Efremenkova O.V., et al. // Mol. Cell. 2014. V. 56. № 4. P. 531–540.
7. Bulkley D., Innis C.A., Blaha G., Steitz T.A. // Proc. Natl. Acad. Sci. USA. 2010. V. 107. № 40. P. 17158–17163.
8. Dunkle J.A., Xiong L., Mankin A.S., Cate J.H. // Proc. Natl. Acad. Sci. USA. 2010. V. 107. № 40. 17152–17157.
9. Svidritskiy E., Ling C., Ermolenko D.N., Korostelev A.A. // Proc. Natl. Acad. Sci. USA. 2013. V. 110. № 30. P. 12283–12288.
10. Osterman I.A., Wieland M., Maviza T.P., Lashkevich K.A., Lukianov D.A., Komarova E.S., Zakalyukina Y.V., Buschauer R., Shiriaev D.I., Leyn S.A., et al. // Nat. Chem. Biol. 2020. V. 16. № 10. P. 1071–1077.
11. Metelev M., Osterman I.A., Ghilarov D., Khabibullina N.F., Yakimov A., Shabalin K., Utkina I., Travin D.Y., Komarova E.S., Serebryakova M., et al. // Nat. Chem. Biol. 2017. V. 13. № 10. P. 1129–1136.
12. Lin J., Zhou D., Steitz T.A., Polikanov Y.S., Gagnon M.G. // Annu. Rev. Biochem. 2018. V. 87. P. 451–478.
13. Osterman I.A., Komarova E.S., Shiryaev D.I., Korniltsev I.A., Khven I.M., Lukyanov D.A., Tashlitsky V.N., Serebryakova M.V., Efremenkova O.V., Ivanenkov Y.A., et al. // Antimicrob. Agents Chemother. 2016. V. 60. № 12. P. 7481–7489.
14. Baba T., Ara T., Hasegawa M., Takai Y., Okumura Y., Baba M., Datsenko K.A., Tomita M., Wanner B.L., Mori H. // Mol. Syst. Biol. 2006. V. 2. P. 2006.0008.
15. Mosmann T. // J. Immunol. Methods. 1983. V. 65. № 1–2. P. 55–63.
16. Orelle C., Szal T., Klepacki D., Shaw K.J., Vázquez-Laslop N., Mankin A.S. // Nucl. Acids Res. 2013. V. 41. № 14. P. e144.
17. Li X.Z., Plésiat P., Nikaido H. // Clin. Microbiol. Rev. 2015. V. 28. № 2. P. 337–418.
18. Orelle C., Carlson S., Kaushal B., Almutairi M.M., Liu H., Ochabowicz A., Quan S., Pham V.C., Squires C.L., Murphy B.T., et al. // Antimicrob. Agents Chemother. 2013. V. 57. № 12. P. 5994–6004.

Ras Participates in the Regulation of the Stability of Adenoviral Protein E1A via MAP-kinase ERK

A. V. Morshneva*, O. O. Gnedina, D. N. Kindt, M. V. Igotti
Institute of Cytology, Russian Academy of Sciences, St. Petersburg, 194064 Russia
*E-mail: 1195alisa@gmail.com
Received: December 30, 2021; in final form, March 18, 2022
DOI: 10.32607/actanaturae.11675

ABSTRACT **The E1A adenoviral protein required for the initiation of the viral life cycle is being actively studied as a sensitizing agent in the combination therapy of cancer, and tumors with activated Ras in particular. We investigated the role played by the Ras signaling pathway in the regulation of E1A protein stability and showed that overexpression of activated Ras increases the basal level of E1A, but enhances the degradation of the E1A protein under treatment with histone deacetylase inhibitors (HDIs). It has been found that the MAP kinase ERK is the key factor in E1A stabilization, and ERK inactivation upon HDI treatment reduces the E1A protein level. Our results indicate that the combination treatment of tumors with activated Ras using adenoviral E1A and HDI has limitations attributed to intense HDI-dependent degradation of E1A. Nevertheless, the established contribution of ERK kinase to the regulation of E1A stability can be used to search for new effective drug combinations based on the adenoviral E1A protein.**
KEYWORDS **molecular oncology, Ras, E1A, combination therapy, histone deacetylase inhibitors.**
ABBREVIATIONS: HDI – histone deacetylase inhibitors; E1A – protein encoded by the adenovirus early region 1A gene; LC – lactacystin (a proteasome inhibitor); WM – wortmannin (a PI3 kinase inhibitor); NaBut – sodium butyrate; Ac-Lys – acetylated lysine.

INTRODUCTION

The early region 1A (*E1A*) gene of human adenovirus type 5 (Ad5) is the first gene to be expressed during adenovirus infection, and the E1A protein is a critical regulator of viral replication. The E1A protein orchestrates the expression of other adenoviral genes and ensures the necessary conditions for viral replication; namely, it stimulates the transition of infected cells to the S phase of the cell cycle (DNA synthesis phase) [1]. E1A *per se* cannot directly interact with DNA, but, being a cofactor of many transcription factors and coactivators, it alters the activity of such proteins as Rb, the inhibitor of cyclin-dependent kinases p21/Waf; acetyltransferase CBP/p300; the transcription factors ATF, AP1, Sp1, etc. [2]. Despite the viral nature of E1A, its scientific significance goes far beyond virology. Expression of the *E1A* gene immortalizes primary cells due to the stimulation of S-phase progression and suppression of replicative senescence [3]. In primary rodent cells, E1A promotes oncogenic transformation in combination with activated *ras* [4] or other complementary oncogenes (e.g., another Ad5 early region gene *E1B*) [5]. However, E1A is not oncogenic in human cells [6, 7].

Abundant experimental data points to the tumor-suppressive properties of E1A in various types of human cancer cells: carcinoma, fibrosarcoma, and melanoma. These observations seem surprising, given the diversity of genetic changes in these three types of tumors. Several mechanisms of E1A-mediated tumor growth suppression have been established, including the reduction of the metastatic potential, as well as apoptosis induction [8, 9].

Later studies have shown that *E1A* expression increases the sensitivity of cancer cells to a number of cytotoxic agents used in antitumor therapy, such as etoposide, cisplatin, taxanes, etc. [10, 11]. It should be noted that adenoviral E1A selectively sensitizes multiple cancer cells, but not normal cells [12, 13]. Therefore, adenoviral E1A is considered a promising sensitizing component of combination cancer therapy.

We investigated the possibility of using E1A in combination chemotherapy with histone deacetylase inhibitors (HDIs). HDI aims at increasing histone

acetylation, which is an epigenetic modification regulating such fundamental cellular processes as gene expression, DNA replication, and genome stability [14]. It has been shown that E1A sensitizes tumor cells with respect to HDIs (SAHA, TSA) more effectively than with respect to other chemotherapy drugs (5-fluorouracil, cisplatin, etoposide, or paclitaxel) [13]. However, as we have shown earlier, HDI induced degradation of E1A [15].

In our study, we used sodium butyrate, which is a broad-spectrum HDI inhibiting all histone deacetylases, except for HDAC6 and HDAC10 belonging to class II and class III histone deacetylases, respectively [16]. Sodium butyrate is a natural metabolite formed in the mammalian body [17]. Therefore, it has low cytotoxicity against normal cells and selectively kills cancer cells [18].

The E1A protein, like the products of other oncogenes, has a short half-life of approximately 40 min [19]. Normally, the intracellular level of regulatory proteins with a short half-life, such as cyclins, p53, beta-catenin, p27/kip and Myc, is controlled by the ubiquitin-proteasome system. Accordingly, it can be assumed that the E1A protein is degraded by the same mechanism. However, the exact pathways for the E1A stability regulation have not yet been elucidated. It has been shown that degradation of the E1A protein is triggered through phosphorylation of its C-terminal amino acid residues rather than through ubiquitination [20]. Notably, the E1A protein itself acts as a proteasome regulator that can both suppress the ubiquitin–proteasome system by direct binding of its N-terminal region to the 26S proteasome subunit [20] and to stimulate the ubiquitination of individual proteins [21].

Previously, we showed that there was a difference in the dynamics of HDI-induced E1A degradation in cells expressing wild-type Ras or a mutant Ras protein [15]. These observations suggest that there is a role played by the Ras protein in the regulation of E1A stability. The small GTPase Ras is a key regulator of cell growth [22]. Normally, Ras is activated in response to extracellular stimuli and initiates the proliferation programs. However, some pathologies are accompanied by constitutive activation of the Ras protein, leading to the permanent activation of underlying Ras-dependent signaling pathways, which results in cell division independent of environmental signals and carcinogenesis induction [23]. Ras gene mutations leading to a constitutive activity of the Ras protein have been found in many tumor types, including aggressive and difficult-to-treat cancers such as melanoma, colorectal cancer, and lung cancer [24]. Therefore, searching for therapy methods for tumors carrying Ras mutations is critical in molecular biology.

The aim of this study is to reveal the role of activated Ras in the regulation of E1A stability in untreated or HDI-treated cells in order to determine the rationality of combination therapy with E1A and HDI for treating Ras-mutated tumors.

MATERIALS AND METHODS

Cell lines

The E1A+Ras cell line was obtained by transformation of mouse embryonic fibroblasts with complementary oncogenes: the early region E1A gene of human adenovirus type 5 (Ad5) and cHa-ras carrying the activating mutations in codons 12 and 61 [25]. The E1A+E1B line was obtained by transformation of rat embryonic fibroblasts with the Ad5 HindIII region encoding the E1A and E1B proteins. Human embryonic kidney cells transformed with adenovirus type 5 (HEK293) were obtained from the Center for Collective Use "Collection of Vertebrate Cell Cultures".

The cells were cultured at 37°C and 5% CO_2 in a DMEM medium supplemented with 10% FCS. The cells were treated with 4 mM sodium butyrate (Calbiochem, USA) and/or 1–2 μM lactacystin (Calbiochem).

RT-PCR

RNA was isolated from the cells using the Trizol reagent (Invitrogen, USA). Reverse transcription was performed with 2 μg of RNA and 1 μg of random hexaprimers. The PCR reaction was carried out on a PCR cycler (Eppendorf Mastercycler Personal, AG 22331) in the presence of 100 ng primers to cDNA of the genes of interest (*E1A*: 5′-CTTTCCACCCAGTGACGACG-3′/5′-TGTCGGGCGTCTCAGGATAG-3′; *gapdh*: 5′-TCATCAGCAATGCCTCCTGCACC-3′/5′-ACAGTTTCCCGGAGGGGCCA-3′) for 22–32 cycles: denaturation for 30 s (95°C), primer annealing for 30 s (61°C E1A, 58°C gapdh), and elongation for 1 min (72°C).

Fractionation of cell extracts

The cells were suspended in 10 mM HEPES-KOH (pH 7.9); 0.4% NP-40 was then added. The cells were centrifuged at 5,000 rpm to obtain cytoplasmic extracts. The pellets were lysed in 20 mM HEPES-KOH (pH 7.9) and then centrifuged at 15,000 rpm to obtain nuclear extracts.

Immunoprecipitation and immunoblotting

The cells were lysed in a buffer containing 0.5% NP-40, 1% Triton X-100, protease and phosphatase inhibitors (a buffer containing 1% NP-40, 0.5% sodium

deoxycholate, 0.1% sodium dodecyl sulfate (SDS) was used for immunoprecipitation). Proteins were separated in a 10–12% polyacrylamide gel, transferred to a PVDF membrane (Millipore, USA), and analyzed with specific antibodies, detected by enhanced chemiluminescence (ECL, Amersham Biosciences, UK) and visualized using a Syngene PXi6 Access system. We used antibodies against proteins E1A sc-25 G1713 1 : 1000 (Santa Cruz Biotechnology, Inc., USA), pan-Ras OP40 1 : 1000 (Calbiochem), pERK1/2 #4377 1 : 800 (Cell Signaling, USA), pAkt (Ser 473) #4060 1 : 1000 (Cell Signaling), p-p38 #9211 1 : 1000 (Cell Signaling), p-JNK #9251 1 : 500 (Cell Signaling), acetylated lysine #9441 1 : 500 (Cell Signaling), α-tubulin sc-32293 1 : 10000 (Santa Cruz Biotechnology, Inc.), and Gapdh 2118 1 : 1000 (Cell Signaling). Immunoblotting for each protein was performed at least in triplicate. The ImageJ software was used for densitometric analysis. The diagrams show the values normalized to the loading control (Gapdh) and reduced to relative units of measurement. The diagrams show the average values for the 3–5 experiments; the error bars represent the standard error of the mean (SEM).

Transient transfection

For transfection, the cells were plated onto a 12-well plate (DMEM supplemented with 10% FCS without antibiotic) at a density of 150 × 10^3 cells per well. Transfection of pcDNA3 (Addgene) and pSV2-ras vectors encoding cHa-ras (Addgene) was performed with Lipofectamine-2000 (Invitrogen) according to the manufacturer's protocol.

RESULTS

The influence of HDI sodium butyrate on the dynamics of E1A degradation in cells with different Ras protein status

To study the impact of the Ras signaling pathway on the E1A stability, we used two E1A-expressing transformed cell lines differing in the activity status of the Ras protein: the E1A+Ras cell line expressing cHa-*ras* with activating mutation and the E1A+E1B line expressing wild-type *ras*.

The RT-PCR and immunoblotting data show that sodium butyrate (NaBut) does not affect the transcription of the *E1A* gene (*Fig. 1A*), while its protein product is degraded in both cell lines, but with different dynamics and intensities (*Fig. 1B*). In E1A+Ras cells, the E1A protein degrades rapidly under NaBut treatment. Whereas E1A can be detected even after 72 h of exposure of E1A+E1B cells to NaBut. Similar dynamics of the moderate decline in the E1A expression upon treatment with NaBut is also observed in HEK293 cells expressing the wild-type *ras* gene (*Fig. 1C*).

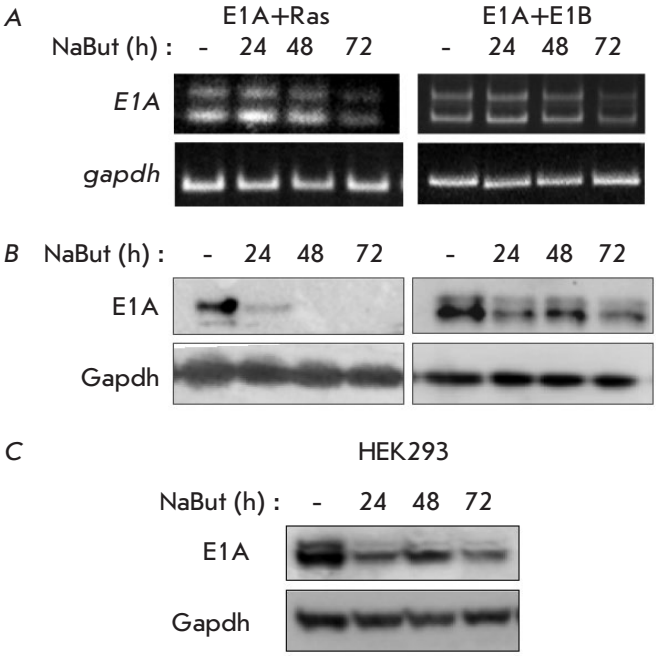

Fig. 1. NaBut causes the degradation of the E1A protein, which is most pronounced in cells with activated Ras. (*A*) Analysis of e1a transcription by RT-PCR. Amount of the E1A protein product (immunoblotting) in E1A-expressing rodent (*B*) and human (*C*) cells. The gapdh gene and its protein product were used as a loading control in RT-PCR and immunoblotting, respectively

Expression of activated Ras increases the E1A protein level but leads to E1A destabilization upon treatment with sodium butyrate

To confirm the role played by activated Ras in the regulation of the E1A protein stability, an expression vector encoding cHa-Ras with activating mutations was introduced into HEK293 cells. Immunoblotting reveals an increased phosphorylation state of MAP kinase ERK in cells transfected with mutant cHa-ras, compared to that in cells transfected with a control vector pcDNA3, thus confirming the activated state of exogenous Ras (*Fig. 2A*). Expression of activated Ras is accompanied by the accumulation of the adenoviral E1A protein (*Fig. 2A*). Thus, our results show a stabilizing effect of activated Ras signaling on the adenovirus E1A protein.

According to the immunoblotting data, the adenoviral E1A protein degrades faster upon exposure to NaBut in cells transfected with mutant cHa-ras than in cells transfected with the control vector pcDNA3

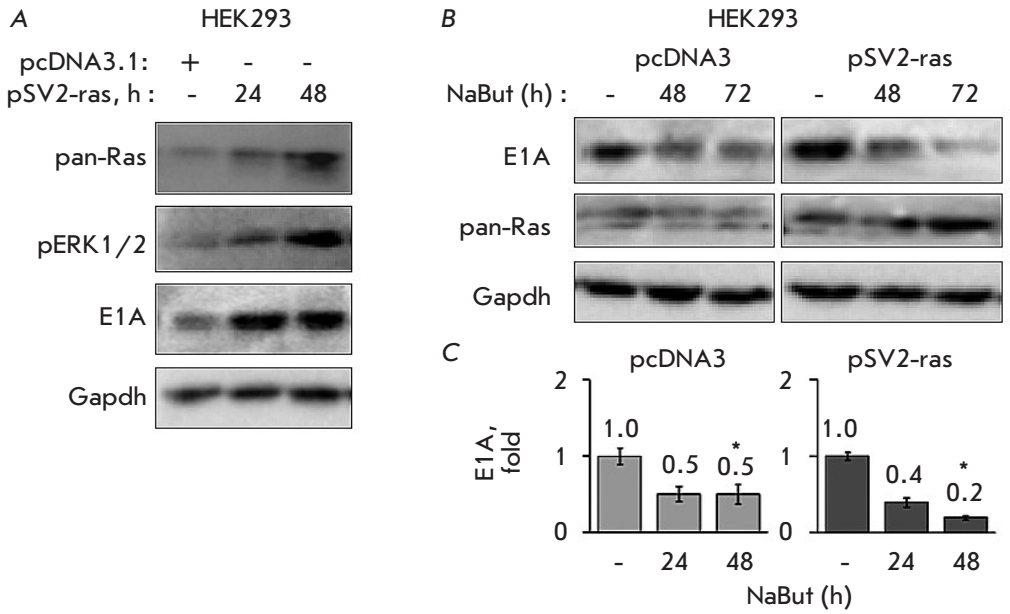

Fig. 2. Activated Ras stabilizes E1A, but also enhances its degradation under the action of NaBut. Immunoblotting of proteins from HEK293 cells (*A*) transfected with pcDNA3 (control vector) or pSV2-ras vectors with antibodies against E1A, pERK, and pan-Ras and (*B*) transfected with pcDNA3 (control vector) or pSV2-ras vectors, and treated with 4 mM NaBut for 0–72 h, with antibodies against E1A and pan-Ras. Gapdh is used as the loading control. (*C*) Bar plots of the average E1A level in transfected HEK293 cells under the action of NaBut, obtained by densitometric analysis of loading-control-normalized (Gapdh) immunoblotting data; the amount of E1A in untreated cells is taken to be unity. Error bars are based on the standard error of the mean (SEM). The Mann–Whitney test was used for comparing the values for two vectors within each timepoint (*$p < 0.05$)

(*Figs. 2B,C*). Thus, overexpression of activated Ras leads to the accumulation of the E1A protein but makes E1A more sensitive to NaBut-induced degradation.

The mechanisms of Ras-dependent E1A stabilization were identified using chemical inhibitors of the downstream kinases in the Ras signaling pathways. Immunoblotting reveals that suppression of exclusively ERK kinase activity by specific inhibitors PD098059 or PD0325901 leads to the destabilization of E1A in E1A+Ras cells, like in the case of NaBut (*Fig. 3A*).

To elucidate the mechanisms of HDI-induced E1A protein degradation, we compared the effect of NaBut on the activity/phosphorylation status of various Ras-dependent kinases in cells with different Ras status. According to immunoblotting with phosphospecific antibodies, NaBut changes the activity of the p38 and JNK kinases in cells with normal and activated Ras in a similar manner, whereas NaBut affects the activities of the ERK and PKB/Akt kinases differently, depending on the Ras status in the cell (*Fig. 3B*). Therefore, NaBut reduces the activity of the ERK and PKB/Akt kinases in E1A+Ras cells with activated Ras, while activity of these kinases increases in HEK293 cells expressing normal Ras (*Fig. 3B*). These data imply the involvement of the ERK and PKB/Akt kinases in the regulation of both the basal E1A protein level and NaBut-induced decline of the E1A protein level.

Proteasome inhibition does not abolish NaBut-induced E1A level reduction

In order to reveal the role of the ubiquitin–proteasome system in the HDI-dependent reduction of the E1A level, E1A+Ras cells were treated with a proteasome inhibitor lactacystin (LC). LC treatment was accompanied by a dose-dependent increase in E1A protein level (*Fig. 4A*).

To test the possibility of preventing the NaBut-induced degradation of E1A by suppressing proteasome activity, E1A+Ras cells were treated with either NaBut or its combination with LC for 24–48 h. Immunoblotting data showed that after 24 h, LC had a slight stabilizing effect on both the control and NaBut-treated cells; however, upon prolonged exposure the amount of the E1A protein decreased regardless of the presence of LC (*Fig. 4B*).

Therefore, we have shown that LC increases the basal level of the E1A protein but does not prevent its degradation during a prolonged action of NaBut.

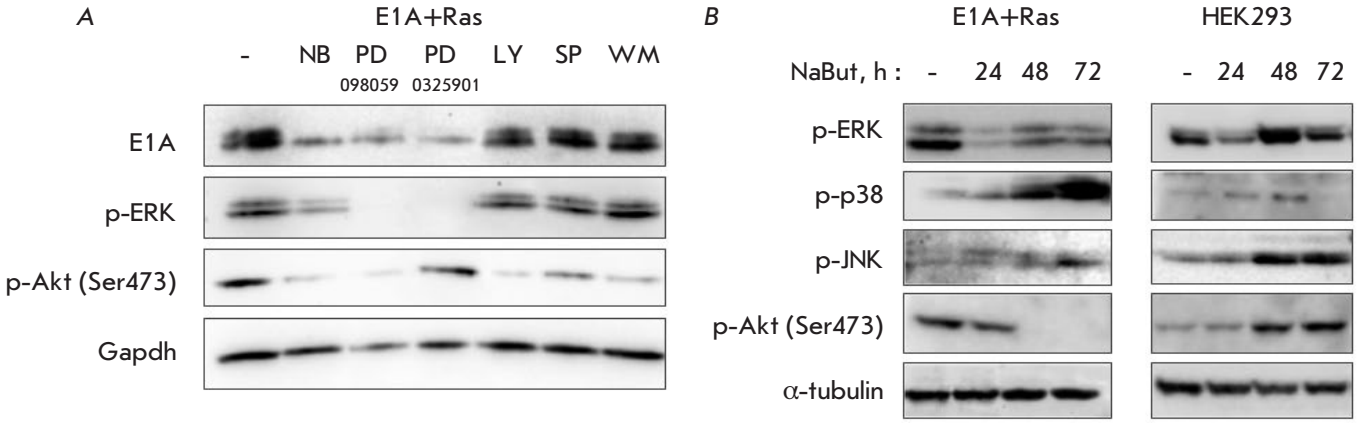

Fig. 3. Akt and ERK kinases as E1A stabilizing factors in Ras-expressing cells. (*A*) The dynamics of the E1A protein product in Ras-activated E1A-expressing cells upon treatment with 4 mM NaBut and inhibitors of Ras-dependent kinases (50 μM PD098059 and PD0325901 – ERK inhibitors, 20 μM LY and 10 μM WM – PI3K inhibitors, 10 μM SP – JNK inhibitor) for 24 h. (*B*) The dynamics of kinase phosphorylation under the action of NaBut in cells with activated and normal Ras. Immunoblotting of proteins from E1A+Ras and HEK293 cells untreated or treated with 4 mM NaBut for 0–48 h. Gapdh/α-tubulin are used as a loading control

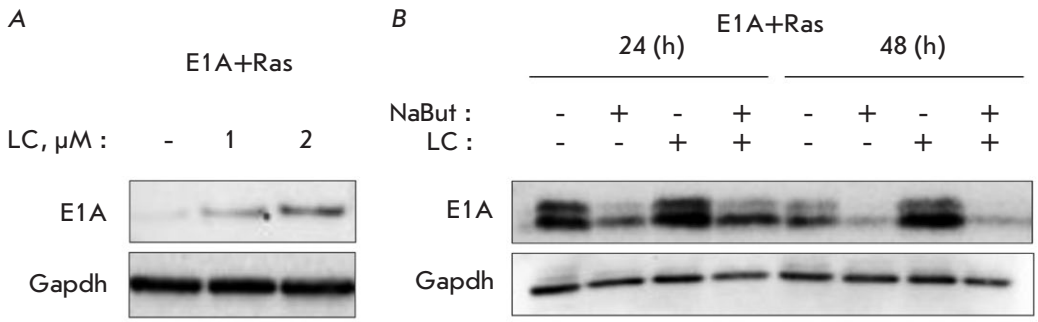

Fig. 4. Immunoblotting of E1A+Ras cells (*A*) treated with the proteasome inhibitor lactacystin (1 μM and 2 μM LC) or (*B*) co-treated with NaBut and/or 2 μM LC, with anti-E1A antibodies, for 24–48 h. Gapdh is used as a loading control

For protein degradation to occur, the protein needs to be located in the cytoplasm. It was shown previously that E1A relocalization can be affected by its acetylation [26]. In this regard, the effect of NaBut on the E1A acetylation level and its intracellular localization was studied. According to the results of immunoblotting performed after immunoprecipitation with acetylated-lysine antibodies, NaBut causes the accumulation of acetylated E1A in E1A+Ras cells during the first 24 h, but then the E1A protein is no longer detected (*Fig. 5A*). Meanwhile, the immunoblotting data for fractionated cell extracts indicate that the E1A protein, which is predominantly localized in the nucleus, is released from it under the action of NaBut (*Fig. 5B*). This suggests that NaBut enhances the acetylation of the E1A protein, thus leading to its relocalization from the nucleus to the cytoplasm, where it undergoes rapid degradation.

DISCUSSION

The ability of HDI to cause degradation of the adenoviral E1A protein has been demonstrated [13, 26–28], but the mechanisms of E1A degradation, as well as E1A stabilization factors, have not yet been elucidated. We have previously shown that HDIs sodium butyrate, trichostatin A, and vorinostat (SAHA) cause degradation of the adenoviral E1A protein, while the dynamics of reduction of the HDI-induced E1A level correlates with the activity of the Ras protein in cells [29].

In this paper, we studied the contribution of Ras-signaling pathway proteins to the stability of adenoviral E1A. We have demonstrated for the first time that overexpression of activated Ras leads to an accumulation of the E1A protein. According to our data, ERK1/2 kinases play a decisive role in the Ras-dependent stabilization of E1A. Thus, the accumula-

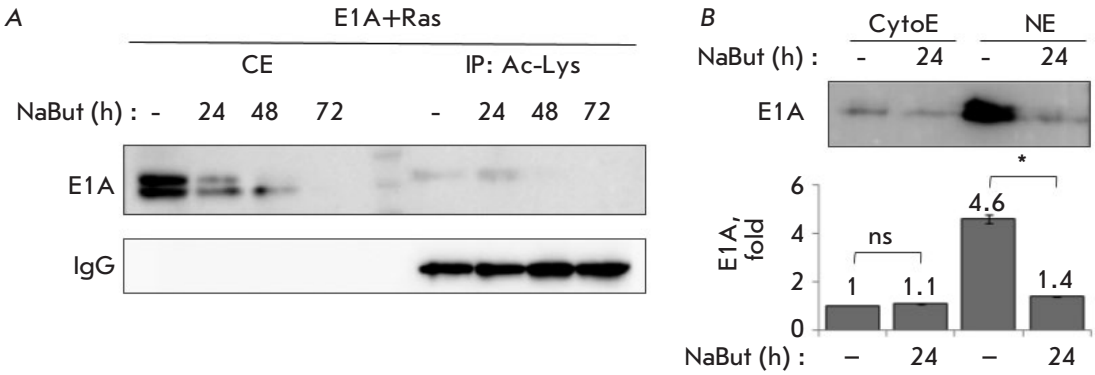

Fig. 5. Acetylation and relocalization of E1A under the action of NaBut. (*A*) Immunoprecipitation with acetylated lysine antibodies (IP: Ac-Lys), followed by immunoblotting with anti-E1A antibodies. Immunoglobulins G (IgG) were used as a loading control. (*B*) Immunoblotting of fractionated cell extracts (CytoE – cytoplasmic extracts, NE – nuclear extracts) with anti-E1A antibodies. The extracts were obtained from cells either untreated or treated with 4 mM NaBut for 24 h. The bar plot shows the average amount of E1A obtained by densitometric analysis of the immunoblotting data normalized to lane loading signal intensity (Ponceau S); the amount of E1A in the untreated NaBut cytoplasmic extract was taken to be unity. Error bars are based on the standard error of the mean (SEM). The Mann–Whitney test was used to check the significance of the differences (ns $p > 0.05$, $^{*}p < 0.05$)

tion of the adenoviral E1A protein induced by overexpression of activated Ras is accompanied by ERK1/2 activation (*Fig. 2A*) and the suppression of the MEK/ERK pathway activity by pharmacological inhibitors reduces the E1A level (*Fig. 3B*).

HDI-induced degradation of E1A is also mediated by ERK kinases. The HDI-induced decrease in the E1A protein level is accompanied by inactivation of ERK kinase (*Fig. 3A*). NaBut also inactivates PKB/Akt kinase in cells with activated Ras. However, reduction of the PKB/Akt activity does not affect E1A expression, as demonstrated in the experiments using specific Akt inhibitors (*Fig. 3A*).

The involvement of Ras signaling in the E1A regulation is not surprising, since during infection, viruses induce signal transduction through the MAP kinase cascade [30] and, in particular, through the ERK kinase [31]. It is known that adenovirus enhances ERK activity both in the early and late phases of the infection [32].

Understanding the interplay between the virus and the Ras signaling pathway can be crucial for constructing oncolytic viruses replicating specifically in cancer cells, as well as for developing new adenovirus-based strategies for cancer therapy.

Phosphorylation at serine residues plays an important role in the regulation of E1A protein activity. Thus, ERK1/2-mediated phosphorylation of E1A at the Ser185 and Ser188 residues increases gene expression from the E4 promoter [33]. However, the role of phosphorylation in the stability of the E1A protein has not been sufficiently studied yet. So far, only two studies have shown that both the expression and functions of the E1A protein are strongly dependent on the MEK/ERK kinase cascade [32, 33]. Meanwhile, it is assumed that the Ras/MEK/ERK signaling pathway affects the efficiency of E1A translation rather than the rate of E1A protein degradation.

Using the proteasome inhibitor lactacystin, we found that the basal level of E1A protein increases under exposure to a proteasome inhibitor, thus confirming that E1A is normally utilized through the proteasome pathway; these findings are consistent with the results demonstrating the role played by proteasomes in the degradation of E1A isoforms [34]. However, lactacystin did not abolish the HDI-induced reduction in the E1A protein level, in contrast to the basal level of the E1A protein, thus suggesting that HDI-dependent degradation of E1A occurs not through the ubiquitin-proteasome pathway, but rather through an alternative mechanism of E1A destabilization induced by HDI in Ras-transformed cells. Sodium butyrate, an inhibitor of a wide class of histone deacetylase, can also use non-histone proteins as a substrate, and, accordingly, affect the level of E1A protein acetylation. The E1A protein is acetylated at Lys239 in the C-terminal domain by acetyltransferases CBP, p300, and pCAF, which impedes the nuclear localization of E1A through impaired binding to importin-α [26], making E1A accessible to degradation systems.

It is known that constant activation of the Ras signaling pathway leads to the induction of the transcription factor HSF1, which controls the expression of heat shock proteins [35], which allows one to suggest that the Hsp-dependent degradation mechanism [36] might be involved in the HDI-induced destabilization of the E1A protein. However, the contribution of chaperone-mediated autophagy to the utilization of the E1A protein requires further research.

CONCLUSIONS

1. Activated Ras stabilizes E1A through the activation of downstream kinase ERK.

2. The E1A protein level drops significantly after exposure to NaBut in cells with activated Ras as a result of HDI-dependent inactivation of ERK kinase.

3. Normally, E1A is utilized in proteasome degradation; however, under a prolonged action of sodium butyrate, E1A degradation is observed even upon proteasome inhibition, which means that HDI-dependent degradation of E1A does not occur via the ubiquitin-proteasome pathway.

4. HDI-induced degradation of E1A, which was shown to take place in cells with activated Ras, implies that the application of combination therapy with E1A and HDI in the treatment of tumors with mutant Ras is limited. ●

This work was supported by the Russian Science Foundation (grant No. 22-25-20229) and partly by the Fund of the Director of the Institute of Cytology, Russian Academy of Sciences. Cells were obtained from the shared research facility "Vertebrate Cell Culture Collection" supported by the Ministry of Science and Higher Education of the Russian Federation (Agreement No. 075-15-2021-683).

REFERENCES

1. Berk A.J. // Cancer Surv. 1986. V. 5. № 2. P. 367–387.
2. Pelka P., Ablack J.N.G., Torchia J., Turnell A.S., Grand R.J.A., Mymryk J.S. // Nucl. Acids Res. 2009. V. 37. № 4. P. 1095–1106.
3. Deng Q., Li Y., Tedesco D., Liao R., Fuhrmann G., Sun P. // Cancer Res. 2005. V. 65. № 18. P. 8298–8307.
4. Reed J.C., Haldar S., Croce C.M., Cuddy M.P. // Mol. Cell. Biol. 1990. V. 10. № 8. P. 4370–4374.
5. Cuconati A., Degenhardt K., Sundararajan R., Anschel A., White E. // J. Virol. 2002. V. 76. № 9. P. 4547–4558.
6. Byrd P.J., Grand R.J., Gallimore P.H. // Oncogene. 1988. V. 2. № 5. P. 477–484.
7. Gallimore P.H., Grand R.J., Byrd P.J. // Anticancer Res. 1986. V. 6. № 3. P. 499–508.
8. Chang Y.-W., Hung M.-C., Su J.-L. // Arch. Immunol. Ther. Exp. (Warsz.). 2014. V. 62. № 3. P. 195–204.
9. Frisch S.M., Reich R., Collier I.E., Genrich L.T., Martin G., Goldberg G.I. // Oncogene. 1990. V. 5. № 1. P. 75–83.
10. Liao Y., Hung M.-C. // Cancer Res. 2004. V. 64. № 17. P. 5938–5942.
11. Radke J.R., Siddiqui Z.K., Figueroa I., Cook J.L. // Cell Death Discov. 2016. V. 2. P. 16076–16076.
12. Sánchez-Prieto R., Quintanilla M., Cano A., Leonart M.L., Martin P., Anaya A., Ramón y Cajal S. // Oncogene. 1996. V. 13. № 5. P. 1083–1092.
13. Yamaguchi H., Chen C.-T., Chou C.-K., Pal A., Bornmann W., Hortobagyi G.N., Hung M.-C. // Oncogene. 2010. V. 29. № 41. P. 5619–5629.
14. Seto E., Yoshida M. // Cold Spring Harb. Perspect. Biol. 2014. V. 6. № 4. P. a018713.
15. Morshneva A., Gnedina O., Marusova T., Igotti M. // Cells. 2019. V. 9. № 1. P. 97.
16. Davie J.R. // J. Nutr. 2003. V. 133. № 7 Suppl. P. 2485S–2493S.
17. Liu H., Wang J., He T., Becker S., Zhang G., Li D., Ma X. // Adv. Nutr. Bethesda Md. 2018. V. 9. № 1. P. 21–29.
18. Wang W., Fang D., Zhang H., Xue J., Wangchuk D., Du J., Jiang L. // OncoTargets Ther. 2020. V. 13. P. 4691–4704.
19. Slavicek J.M., Jones N.C., Richter J.D. // EMBO J. 1988. V. 7. № 10. P. 3171–3180.
20. Turnell A.S., Grand R.J.A., Gorbea C., Zhang X., Wang W., Mymryk J.S., Gallimore P.H. // EMBO J. 2000. V. 19. № 17. P. 4759–4773.
21. Guan H., Ricciardi R.P. // J. Virol. 2012. V. 86. № 10. P. 5594–5602.
22. Song S., Cong W., Zhou S., Shi Y., Dai W., Zhang H., Wang X., He B., Zhang Q. // Asian J. Pharm. Sci. 2019. V. 14. № 1. P. 30–39.
23. Downward J. // Nat. Rev. Cancer. 2003. V. 3. № 1. P. 11–22.
24. Fernández-Medarde A., Santos E. // Genes Cancer. 2011. V. 2. № 3. P. 344–358.
25. Pospelova T.V., Kislyakova T.V., Medvedev A.V., Svetlikova S.B., Pospelov V.A. // Tsitologiya. 1990. V. 32. № 2. P. 148–155.
26. Madison D.L., Yaciuk P., Kwok R.P.S., Lundblad J.R. // J. Biol. Chem. 2002. V. 277. № 41. P. 38755–38763.
27. Igotti M.V., Svetlikova S.B., Pospelov V.A. // Acta Naturae. 2018. V. 10. № 4. P. 70–78.
28. Saha B., Parks R.J. // J. Virol. 2019. V. 93. № 12. P. e00088-19.
29. Morshneva A., Gnedina O., Svetlikova S., Pospelov V., Igotti M. // AIMS Genet. 2018. V. 5. № 1. P. 41–52.
30. Popik W., Pitha P.M. // Virology. 1998. V. 252. № 1. P. 210–217.
31. Bruder J.T., Kovesdi I. // J. Virol. 1997. V. 71. № 1. P. 398–404..
32. Schümann M., Dobbelstein M. // Cancer Res. 2006. V. 66. № 3. P. 1282–1288.
33. Whalen S.G., Marcellus R.C., Whalen A., Ahn N.G., Ricciardi R.P., Branton P.E. // J. Virol. 1997. V. 71. № 5. P. 3545–3553.
34. Radko S., Jung R., Olanubi O., Pelka P. // PLoS One. 2015. V. 10. № 10. P. e0140124.
35. Dai C. // Philos. Trans. R. Soc. B Biol. Sci. 2018. V. 373. № 1738. P. 20160525.
36. Cuervo A.M. // Trends Endocrinol. Metab. 2010. V. 21. № 3. P. 142–150.

Antibodies Against Unusual Forms of Sialylated Glycans

P. S. Obukhova[1,2], M. M. Ziganshina[2], N. V. Shilova[1,2], A. A. Chinarev[1], G. V. Pazynina[1], A. Y. Nokel[1,2], A. V. Terenteva[2], N. R. Khasbiullina[2], G. T. Sukhikh[2,3], A. A. Ragimov[3], E. L. Salimov[3], V. I. Butvilovskaya[4], S. M. Polyakova[1,5], J. Saha[6], N. V. Bovin[1,7*]

[1]Shemyakin-Ovchinnikov Institute of Bioorganic Chemistry of the Russian Academy of Sciences, Moscow, 117997 Russia

[2]National Medical Research Center for Obstetrics, Gynecology and Perinatology named after V.I. Kulakov of the Ministry of Health care of Russian Federation, Moscow, 117997 Russia

[3]I.M. Sechenov First Moscow State Medical University of the Ministry of Health care of the Russian Federation (Sechenov University), Moscow, 119991 Russia

[4]Engelhardt Institute of Molecular Biology of the Russian Academy of Sciences, Moscow, 119991 Russia

[5]Synthaur LLC, Moscow, 117997 Russia

[6]Centre of Biomedical Research, Sanjay Gandhi PostGraduate Institute of Medical Science, Lucknow, 226014 India

[7]Centre for Kode Technology Innovation, Auckland University of Technology, Auckland, 1010 New Zealand

*E-mail: professorbovin@yandex.ru

Received: November 11, 2021; in final form, March 22, 2022

DOI: 10.32607/actanaturae.11631

ABSTRACT **Previous studies have shown that in the blood of healthy donors (1) there are no natural antibodies against sialylated glycoproteins, which contain Neu5Acα (N-acetylneuraminic acid) as the most widespread form of human sialic acid, and (2) there is a moderate level of antibodies capable of binding unnatural oligosaccharides, where Neu5Ac is beta-linked to a typical mammalian glycan core. In the present study, we investigated antibodies against βNeu5Ac in more detail and verified the presence of Kdn (2-keto-3-deoxy-D-glycero-D-galacto-nonulosonic acid) as a possible cause behind their appearance in humans, taking into account the expected cross-reactivity to Kdn glycans, which are found in bacterial glycoconjugates in both the α- and β-forms. We observed the binding of peripheral blood immunoglobulins to sialyllactosamines (where "sialyl" is Kdn or neuraminic acid) in only a very limited number of donors, while the binding to monosaccharide Kdn occurred in all samples, regardless of the configuration of the glycosidic bond of the Kdn moiety. In some individuals, the binding level of some of the immunoglobulins was high. This means that bacterial Kdn glycoconjugates are very unlikely to induce antibodies to βNeu5Ac glycans in humans. To determine the reason for the presence of these antibodies, we focused on noninfectious pathologies, as well as on a normal state in which a significant change in the immune system occurs: namely, pregnancy. As a result, we found that 2/3 of pregnant women have IgM in the blood against Neu5Acβ2-3Galβ1-4GlcNAcβ. Moreover, IgG class antibodies against Neu5Acβ2-3Galβ1-4GlcNAcβ and Neu5Acβ2-6Galβ1-4GlcNAcβ were also detected in eluates from the placenta. Presumably, these antibodies block fetal antigens.**

KEYWORDS **sialylated glycans, Kdn, human natural antibodies, pregnancy, glycoarray.**

ABREVIATIONS **FGR – fetal growth restriction; Gal – galactose; GalNAc – N-acetylgalactosamine; GlcNAc – N-acetylglucosamine; Kdn – 2-keto-3-deoxy-D-glycero-D-galacto-nonulosonic acid; LN – N-acetyllactosamine Galβ1-4GlcNAcβ; Neu5Ac – N-acetylneuraminic acid; Neu5Gc – N-glycolylneuraminic acid; PE – preeclampsia; PGA – printed glycan array; RFU – relative fluorescent units; SLN – sialyllactosamine.**

INTRODUCTION

Within animal cells, sialic acids (N-acetylneuraminic acid, Neu5Ac, and N-glycolylneuraminic acid, Neu5Gc, the two most abundant forms) in glycoproteins are normally found at the terminal positions of complex glycans linked by α2,3 or α2,6 to Gal or α2,6 to GalNAc penultimate residues. Sialylated glycans are involved in numerous biological recognition processes [1]; so, it

is not surprising that antibodies (i.e., autoantibodies) against Neu5Acα-glycans are not found in healthy individuals [2]. However, antibodies against some oligosaccharides terminated by β-form Neu5Ac, not found in nature, have been documented [2]. To explain their origin and predetermination, it has been hypothesized that formal antibodies against βNeu5Ac actually target fragments of bacterial polysaccharides/lipopolysaccharides of *Streptomyces*, *Klebsiella*, etc. (according to http://csdb.glycoscience.ru/database/), which often contain structurally similar sialic acid; namely, the β-anomer of 2-keto-3-deoxy-D-glycero-D-galacto-nonulosonic acid (Kdn) [2, 3]. In support of this idea there was the presence of antibodies in healthy donor blood against Kdn-glycans typical of the lipopolysaccharide core motif [4]. Therefore, we investigated human antibodies against Kdn glycans using synthetic spacer-armed α- and β-Kdn monosaccharides [5], Kdn-form of 6'- and 3'-sialyllactosamines, as well as the corresponding Neu5Acα- and β-derivatives in parallel (*Scheme 1*), by immobilizing them together with other glycans on a microchip. Blood sera from healthy donors, healthy pregnant women, and women with complicated pregnancies were studied using this "sialic" printed glycan array (sialic PGA). In this article, we discuss the possible causes of the emergence of antibodies directed to the β-form of sialic acids.

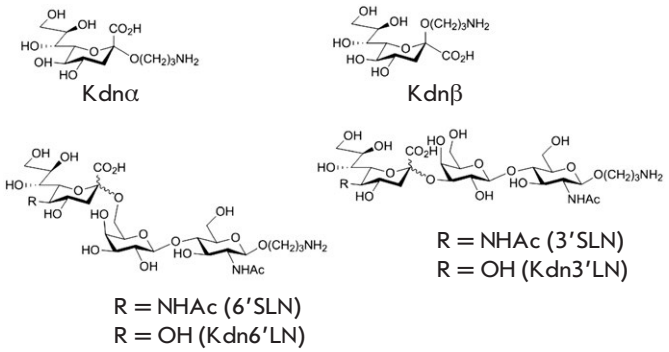

Scheme 1. The structure of the synthetic Kdn-glycans used in this work (in the composition of sialic PGA) and parent Neu5Ac-trisaccharides

EXPERIMENTAL

Kdn-glycans

Kdn-glycans were obtained [5] as individual anomers (of 95% purity according to HPLC and NMR), and their anomeric stereochemistry was determined based on chemical shifts and coupling constants for Kdn H-3 protons, as previously described [5].

Donors and patients

We examined biological samples from 104 individuals. The original cohort (Group 1), which consisted of 16 donors (8 women and 8 men) from I.M. Sechenov First Moscow State Medical University (Moscow, Russia), and a retrospective cohort consisting of 88 patients from the National Medical Research Center for Obstetrics, Gynecology and Perinatology (Moscow, Russia) met the inclusion criteria and were selected for participation in the study (*Table 1*). In the retrospective cohort, 26 healthy nonpregnant women applied to a pregnancy planning center (Group 2); 30 patients with normal pregnancies (Group 3); and 32 patients with complicated pregnancies (Group 4), in-

Table 1. Samples and corresponding versions of glycochips

Cohorts		Number of individuals	Biomaterials	Number of samples	PGA version	Sources of biomaterials
1	Healthy donors	16	Blood sera	16	#1 sialic PGA (17 oligosaccharides)	I.M. Sechenov First Moscow State Medical University of the Ministry of Health care of the Russian Federation (Sechenov University), Moscow, 119991 Russia
2	Healthy fertile women (donors)	26	Blood sera	26	#3 (441 oligosaccharides and 219 bacterial polysaccharides)	National Medical Research Center for Obstetrics, Gynecology and Perinatology named after V.I. Kulakov of the Ministry of Health care of Russian Federation, Moscow, 117997 Russia
3	Healthy pregnant women	30	Blood sera	26	#2 (381 oligosaccharides)	
			Eluates from placentas	30		
4	Patients with pregnancy complications	32	Blood sera	29		
			Eluates from placentas	32		

Table 2. Clinical characteristics of the study groups

Features	Group 1 healthy donors	Group 2 nonpregnant healthy women	Group 3 women with normal pregnancy	Group 4 women with complicated pregnancy	*p* value*
Age (years)**	33.0 (18–62)	30.0 (24–44)	32.5 (23–40)	34.5 (24–45)	0.2253
Systolic arterial blood pressure (mm Hg)**	–	118.0 (110–120)	110 (103–130)	150.0 (110–210)	<0.0001
Diastolic arterial blood pressure (mm Hg)**	–	75.0 (70–82)	70.0 (60–80)	95.0 (70–115)	<0.0001
Newborns' gestational age at delivery (weeks)***	–	–	39.2 (39.0–40.0)	34.8 (30.40–37.20)	<0.0001
Newborns' weight, g**	–	–	3462.0 (2800–4180)	1997.0 (440–3300)	<0.0001
Newborns' Apgar Scores**	–	–	8.0 (8)	7.0 (2–8)	<0.0001

* Groups 3 and 4 comparison.
** data are presented as a median with min. and max. values, Mann–Whitney test.
*** data are presented as a median with interquartile range, Mann–Whitney test.

cluding 41% with preeclampsia (PE), 25% with fetal growth restriction (FGR), and 34% with PE accompanied by FGR. The inclusion criteria for Group 1 were as follows: age greater than or equal to 18, the absence of absolute contraindications for donation, normal blood tests, biochemical blood analysis, coagulogram and blood pressure. The inclusion criteria for Group 2 were as follows: more than one pregnancy, occurring in the natural cycle without assisted reproduction technology, normal menstrual cycle and absence of hormonal dysregulation. Inclusion criteria for Group 3 were the absence of any chronic gynecological or somatic disease, no threat of abortion, early toxicosis, inflammatory disease, PE or FGR, no medical therapy (except for vitamins or mineral supplements), normal vaginal flora, and normal ultrasonography and Doppler ultrasonography during current pregnancy. The inclusion criteria for Group 4 were pregnancy complicated by PE, and/or FGR. All pregnant women had spontaneous singleton pregnancies and gave birth by cesarean section. Pregnant women with the HELLP syndrome (an atypical form of severe preeclampsia, which is characterized by symptoms: H – hemolysis, EL – elevated liver enzymes, LP – low platelet count in the blood) were excluded from the study. The exclusion criteria for all groups were severe somatic diseases, including autoimmune diseases, acute and chronic inflammatory diseases, acute and chronic inflammatory diseases in the acute stage, a history of blood transfusion or organ transplantation, immunotherapy, hormone therapy, and the use of drugs that affect antibody production and bioavailability, including low-molecular-weight heparins. All subjects provided written informed consent before participation. The study protocol was approved by the local ethical committee of the related medical organizations.

Diagnostic evaluation of pregnancy disorders

Patients were included in the groups according to the criteria of the International Society for the Study of Hypertension in Pregnancy (ISSHP) [6]. The prenatal diagnosis of FGR was based on the criteria described in [7]. The clinical characteristics of the study groups are shown in *Table 2*.

Blood serum sample collection

In the original cohort (Group 1), serum samples were collected in vacuum blood collection tubes VACUETTE® Serum, cap red, with clotting activator and gel for separation (4 ml, L×Ø =75 × 13 mm). In the retrospective cohort, serum samples were collected in vacuum blood collection tubes S-Monovette® Serum, cap white, with clotting activator (4.9 ml, L×Ø = 90 × 13 mm). Within 1 h of blood collection, the samples were centrifuged for 10 min at 2,000 *g* and stored at −80°C until antibody analysis.

Elution of antibodies from the placenta

The placenta was obtained from patients in Groups 3 and 4 during cesarean section, and placenta-associated antibodies were eluted, as previously de-

scribed [8], using 10.0 g of placental tissue (mainly the villous chorion, basal, and chorial lamina were taken). An equal amount of placental tissue was collected from each patient. Samples of eluates with the SIGMAFAST protease inhibitor (S8820, Sigma–Aldrich, MO, USA) at the concentration recommended by the manufacturer were stored for a maximum of 7 days at 4°C before the analysis. Analysis of the eluted antibodies was performed using PGA as described below, with only IgG detection. Placental eluates were applied to the glycochip without dilution, and the concentration of the eluted antibodies was standardized by means of the same amount of placental tissue and identical elution procedures.

PGA assay

Glycochips of three formats were used (Semiotik LLC, Russia): #1 – containing only sialylated glycans (approximately 20 glycans, this version of the glycochip was called "sialic PGA"), #2 – containing 381 oligosaccharides, #3 – containing 441 oligosaccharides and 219 bacterial polysaccharides; the second and third versions included all the sialylated glycans of the first. The purity of the glycans was 95-98%, according to HPLC and NMR data. Glycan printing was carried out in accordance with international rules, as previously described [4]. Each ligand on the array was applied in 6-12 repeats; ligand immobilization on the array was monitored using human serum, monoclonal and affine-purified polyclonal antibodies and plant lectins according to the manufacturer's quality control protocol.

The analysis of blood sera and the eluates from the placenta using PGA was performed as previously described [4, 8]. The correspondence of the samples and formats of the glycochips is presented in *Table 1*. Signals were measured as the medians of relative fluorescence units (RFU) for replicates with median absolute deviations. The background value was determined as the signal from the ligand-free spot. The background value multiplied by a factor of 10 was taken as the cutoff. Signals above the cutoff were considered significant. The frequency of the specific anti-glycan antibody occurrence was calculated as a percentage (%) of the number of individuals in whom the median RFU for the corresponding glycan as a result of blood serum analysis in PGA was higher than the cutoff.

Statistical analysis

The Mann–Whitney U test was performed for intergroup comparison using the MedCalc software version 16.4 (MedCalc, Belgium). Differences were considered significant if the p value was below 0.05.

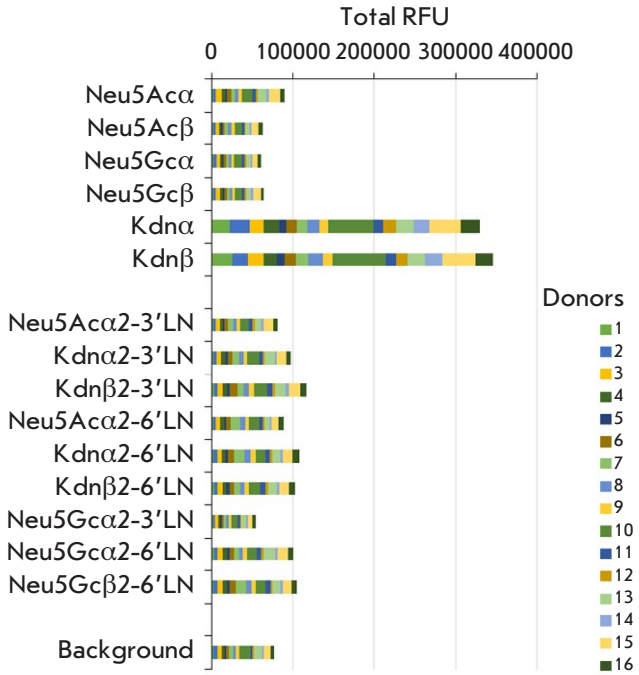

Fig. 1. Binding of human IgG antibodies (sera from 16 donors) to sialylated glycans. The sialic PGA (format #1) data are presented as a stacked chart. The RFU values for all donors are summarized

RESULTS AND DISCUSSION

2-Keto-3-deoxy-D-glycero-D-galacto-nonulosonic acid (Kdn) is found in noticeable amounts in bacteria and ectothermic vertebrates. From a molecular perspective, these are glycolipids, glycoproteins, bacterial capsular polysaccharides, and bacterial lipopolysaccharides, where Kdn is linked as a 2,3-, 2,4-, 2,6- or 2,8-substituent. In humans, Kdn has been found in very small amounts; 0.1–1% of total sialic acid, in all types of glycoconjugates in various organs [9]. It is believed that Kdn enters the human metabolic system from the outside through food, similar to Neu5Gc [10]; slightly increased Kdn expression was found in human fetal red blood cells compared to adult cells and in ovarian tumor tissues [9]. Kdn is widespread in organisms with which humans come into contact and is definitely an alien monosaccharide to humans, even in its α-linked form.

When testing 16 blood serum samples from healthy donors (Group 1) using sialic PGA, we did not detect IgG antibodies against either Kdnα2-3Galβ1-4GlcNAcβ (Kdnα2-3'LN) or Kdnα2-6Galβ1-4GlcNAcβ(Kdnα2-6'LN), or against their corresponding Kdnβ-versions (*Fig. 1*).

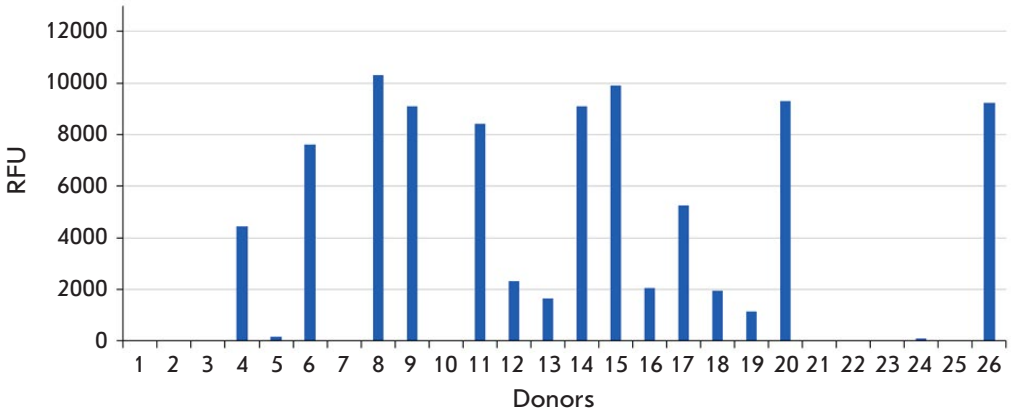

Fig. 2. Fifteen out of twenty-six healthy donors had antibodies (IgM) against the trisaccharide Kdnα2-3Galβ1-4GlcNAcβ. The data of the PGA of format #3 are presented. The cutoff value was subtracted

However, in this small cohort, we did not observe antibodies against the α-linked form of Kdn, Kdnα2-3Galβ1-4GlcNAc, although A. Varki's group detected IgG antibodies against it in a limited number of donors using a similar PGA [10, 11]. To address this inconsistency, we extracted data from our archives corresponding to the data for contingently healthy women, where the full version of PGAs was used, which included the trisaccharide Kdnα2-3Galβ1-4GlcNAc. According to these data, compiled in *Fig. 2*, 15 out of 26 donors did have antibodies against the trisaccharide, but this only applies to IgM, as IgG antibodies were not detected. Information about the samples studied and the corresponding versions of the PGA is given in *Table 1*.

We believe the discrepancy above between the results is due to the fact that antibodies capable of binding to the Kdn-form of sialyllactosamine are formed in response to bacterial infections (i.e., we deal with adaptive immunoglobulins), which emerge with different frequencies in different small-sized cohorts, depending on the region, season, etc.

In contrast to antibodies directed to Kdn-trisaccharides, a moderate (or sporadically high) level of IgG antibodies against the monosaccharide Kdn was observed in most donors (*Fig. 3*), interestingly, almost indentical for both the α- and β-form.

The observed RFU values for the Kdn monosaccharide in highly responsive donors were close to the values for L-rhamnose, which is used here as a high binding reference, while no antibodies were found against the Neu5Ac monosaccharide (both α- and β-) (*Fig. 1*), which is confirmed by previously published data [4]. Apparently, the immunoglobulins that bind to the monosaccharide Kdn broadly recognize antibodies against bacterial polysaccharides, to the main chain of which Kdn is attached as a pendant residue.

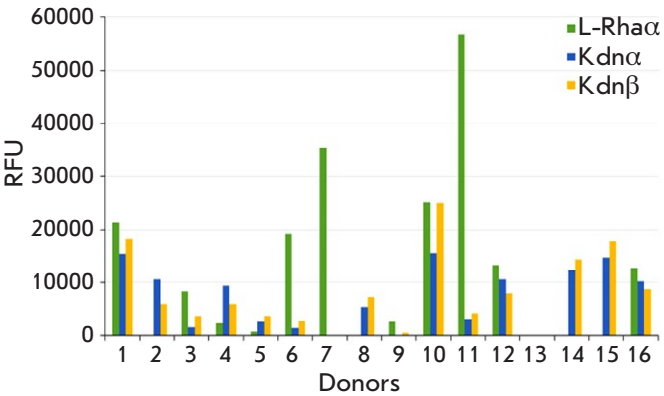

Fig. 3. Binding of human IgG-class serum antibodies (from 16 donors) to Kdn monosaccharide in its α- and β-spacer form compared to αL-rhamnose (L-Rhaα). The sialic PGA (format #1) data are presented. The cutoff value was subtracted

The absence of antibodies to trisaccharides, in which the Kdn residue is linked by a β-glycosidic bond, indicates that Kdn-containing lipopolysaccharides are unlikely to trigger the appearance in humans of the previously observed (see above) antibodies against glycans containing β-linked N-acetylneuraminic acid.

However, anti-Kdn antibodies were not the subject of this study. In this study, a critical issue for us was to explain the origin and biological significance of previously identified antibodies against Neu5Acβ-glycans [2]. As noted above, the assumption that lipopolysaccharides are a trigger of and target for them is inconsistent with new experimental data; namely, the absence of any evidence of their binding to Kdn-lactosamines in the overwhelming number of donors and the inability to distinguish between the α- and β-forms of the monosaccharide Kdn. Therefore, an alternate explanation for the origin and function of

antibodies to Neu5Acβ-glycans is warranted. Our first attempt at this is outlined below.

We investigated how often antibodies against Neu5Acβ2-3Galβ1-4GlcNAcβ and Neu5Acβ2-6Galβ1-4GlcNAcβ (β-forms of 3′SLN and 6′SLN) in the blood of healthy pregnant women are encountered, as well as how often they are encountered in the blood of patients with pregnancy complications caused by PE and FGR. These complications are the great obstetrical syndromes associated with the disorders of deep placentation and impaired immune response to alloantigens [12, 13]. In addition to blood antibodies, eluates from the placentas of Groups 3 and 4 were also examined (*Table 3, Fig. 4*).

The observed frequency was surprisingly high (*Table 3, Fig. 4*), especially for the occurrence of antibodies against the β2-3 isomer of SLN, Neu5Acβ2-3Galβ1-4GlcNAcβ. As mentioned above [2, 14], antibodies against the corresponding α-sialylated glycans were practically absent in healthy subjects. They were rarely found in women with normal pregnancies and were found more frequently in individuals with pregnancy complications, which are apparently associated with a general impaired immune response [15] and impaired tolerance of the fetus. New data have confirmed this observation. Notably, antibodies against Neu5Acβ-glycans were also detected quite often (20-30% of cases) in eluates from the placenta (*Table 3*). Indeed, this is only IgG, since IgM is absent in the placenta. At the same time, anti-Neu5Acβ2-3Galβ1-4GlcNAcβ IgM antibodies were found with a high frequency in the blood of these patients whereas IgG antibodies with this specificity were absent in their blood. Since the antigens of both parents may be present in the placenta [16], we assume that these placental immunoglobulins G located in resident in the placenta and found in eluates play the role of protectors against the maternal immune system by binding to alloantigens in the placenta. This is supported by their lower incidence in patients with complicated pregnancies. Apparently, in PE and FGR, the mecha-

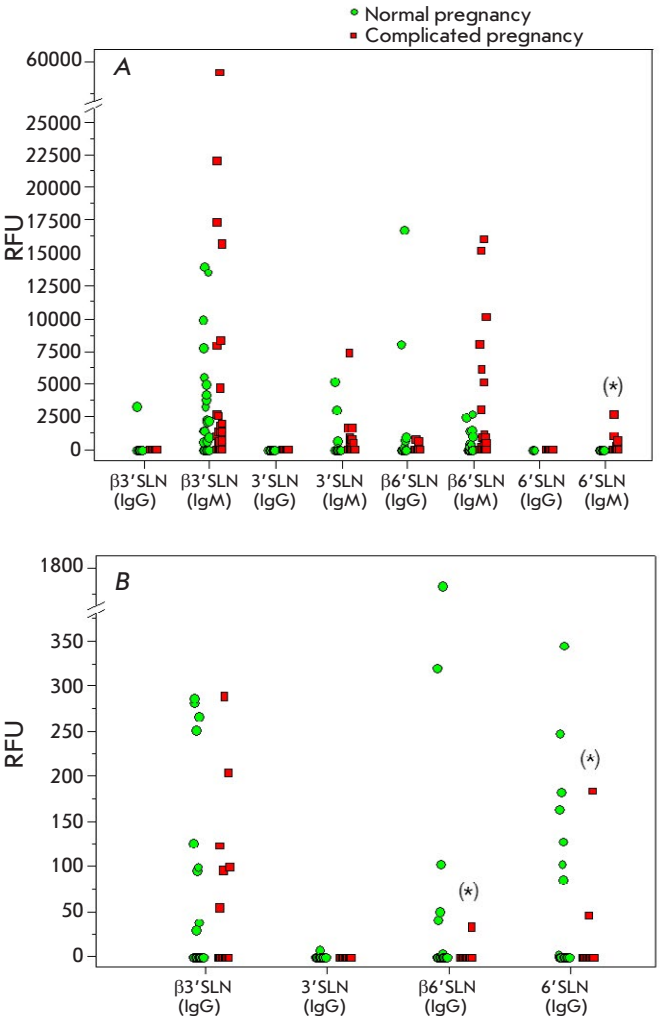

Fig. 4. Binding of serum IgG and IgM antibodies (*A*) and eluated placenta-associated IgG antibodies (*B*) to 3′SLN and 6′SLN trisaccharides (comparison of their Neu5Acβ- *vs*. Neu5Acα-forms). The data of the PGA of format #2 for 30 healthy pregnant women and 32 women with pregnancy complications (preeclampsia and fetal growth restriction). The cutoff value was calculated for each group separately (for sera and eluates, for IgG and IgM) as described in the Materials and Methods section. (*) - the intergroup difference was significant (U test, $p < 0.05$)

Table 3. The occurrence frequency of the corresponding antibodies recognizing sialylated glycans (this parameter is a % of individuals whose RFU was higher than cutoff)

Sialylated glycans	% in women with normal pregnancy (blood)		% in women with complicated pregnancy (blood)		% in women with normal pregnancy (placenta)	% in women with complicated pregnancy (placenta)
Structure	IgG	IgM	IgG	IgM	IgG	IgG
Neu5Acβ2-3Galβ1-4GlcNAcβ (β3′SLN)	4	65	0	69	30	19
Neu5Acα2-3Galβ1-4GlcNAcβ (3′SLN)	0	15	0	35	0	0
Neu5Acβ2-6Galβ1-4GlcNAcβ (β6′SLN)	19	31	7	45	20	3
Neu5Acα2-6Galβ1-4GlcNAcβ (6′SLN)	0	0	0	17	27	6

nism of masking alloantigens by placental antibodies is impaired. This assumption is consistent with the concept that the production of other protective antibodies during pregnancy masks fetal alloantigens in the placenta from an attack by the mother's immune system [17, 18]. J. Gu et al. [19] demonstrated that protective IgG antibodies are generated by placental cells and regulate local immune reactions. The second (and more plausible in our opinion) explanation for the fact that antibodies are found in the placental tissue but are absent in the peripheral blood is their complete - or almost complete - harboring on the placental antigens, as a result of which their content in the blood drops below the sensitivity threshold of the detection method. While there are no direct data available, we believe that for the observed antibodies, β-sialosides are mimotopes of protein antigens. Identifying the true epitopes is the next challenge.

CONCLUSION

The profiling of human antibodies using a comprehensive glycan array reveals a number of immunoglobulins with unexpected specificities, which include antibodies to β-linked sialic acid. The search for what is behind the presence and function of these antibodies was the aim of this study. We assumed that the identified antibodies are directed to Kdn-containing glycoconjugates of bacterial origin, which occur in both α- and β-linked forms. However, this hypothesis is not supported by the new data presented here; that is, the true target antigens and the physiological role of these antibodies have yet to be determined. At the same time, we found antibodies in the blood (IgM) and placental tissue (IgG) of pregnant women, which provides grounds for searching for a physiological role for antibodies to the β-form of sialic acid (or its antigen-mimetic) in reproductive immunology.

ACKNOWLEDGMENTS

The experiments were partially carried out using equipment provided by the Shemyakin-Ovchinnikov Institute of Bioorganic Chemistry (IBCh) core facility (CKP IBCh, supported by the Russian Ministry of Education and Science [agreement No. RFMEFI 621117X0018]). The authors wish to thank the Laboratory for Collection and Storage of Biological Material (Biobank) of the National Medical Research Center for Obstetrics, Gynecology and Perinatology named after V.I. Kulakov for providing the blood samples. ●

This work was supported by the Russian Foundation for Basic Research [No. 18-53-45008 to N.V. Shilova, A.A. Chinarev, G.V. Pazynina, N.V. Bovin and No. 19-015-00102 to M.M. Ziganshina, N.R. Khasbiullina], and the Ministry of Science and Technology of the Government of India project [No. INT/RUS/RFBR/P-321 to J. Saha] in the frame of the DST-RFBR cooperation.

The authors declare no conflicts of interest.

REFERENCES

1. Varki A. // Nature. 2007. V. 446. № 7139. P. 1023–1029. https://doi.org/10.1038/nature05816.
2. Shilova N., Huflejt M.E., Vuskovic M., Obukhova P., Navakouski M., Khasbiullina N., Pazynina G., Galanina O., Bazhenov A., Bovin N. // Top. Curr. Chem. 2015. V. 366. P. 169–181.
3. Deng L., Chen X., Varki A. // Biopolymers. 2013. V. 99. № 10. P. 650–665. https://doi.org/10.1002/bip.22314.
4. Obukhova P., Tsygankova S., Chinarev A., Shilova N., Nokel A., Kosma P., Bovin N. // Glycobiology. 2020. V. 30. № 6. P. 395–406. https://doi.org/10.1093/glycob/cwz107.
5. Chinarev A.A., Sablina M.A., Kunetskiy R.A., Shilova N.V., Polyakova S.V., Paramonov A.S., Saha J., Bovin N.V. // Mendeleev Commun. 2021. V. 31. № 4. P. 490–492.
6. Brown M.A., Magee L.A., Kenny L.C., Karumanchi S.A., McCarthy F.P., Saito S., Hall D.R., Warren C.E., Adoyi G., Ishaku S. // Pregn. Hypert. 2018. V. 13. P. 291–310. https://doi.org/10.1016/j.preghy.2018.05.004.
7. Ziganshina M.M., Kulikova G.V., Fayzullina N.M. Yarotskaya E.L., Shchegolev A.I., Le Pendu J., Breiman A., Shilova N.V., Khasbiullina N.R., Bovin N.V., et al. // Placenta. 2020. V. 90. P. 98–102. https://doi.org/10.1016/j.placenta.2019.12.005.
8. Ignat'eva N.V., Ziganshina M.M., Shilova N.V., Khasbiullina N.R., Bovin N.V., Tyutyunnik V.L., Sukhikh G.T. // Bull. Exp. Biol. Med. 2019. V. 167. № 1. P. 120–122. https://doi.org/10.1007/s10517-019-04474-4.
9. Inoue S., Kitajima K. // Glycoconj. J. 2006. V. 23. № 5–6. P. 277–290. https://doi.org/10.1007/s10719-006-6484-y.
10. Kawanishi K., Saha S., Diaz S. Vaill M., Sasmal A., Siddiqui S.S., Choudhury B., Sharma K., Chen X., Schoenhofen I.C., et al. // J. Clin. Invest. 2021. V. 131. № 5. P. e137681. https://doi.org/10.1172/JCI137681.
11. Saha S., Coady A., Sasmal A., Kawanishi K., Choudhury B., Yu H., Sorensen R.U., Inostroza J., Schoenhofen I.C., Chen X., et al. // mBio. 2021. V. 12. № 1. P. e03226–20. https://doi.org/10.1128/mBio.03226-20.
12. Brosens I., Pijnenborg R., Vercruysse L., Romero R. // Am. J. Obstet. Gynecol. 2011. V. 4. № 3. P. 193–201. https://doi.org/10.1016/j.ajog.2010.08.009.
13. Wilczynski J.R. // Hum. Immunol. 2006. V. 67. № 7. P. 492–511. https://doi.org/10.1016/j.humimm.2006.04.007.
14. Huflejt M.E., Vuskovic M., Vasiliu D., Xu H., Obukhova P., Shilova N., Tuzikov A., Galanina O., Arun B., Lu K., et al. // Mol. Immunol. 2009. V. 46. № 15. P. 3037–3049. https://doi.org/10.1016/j.molimm.2009.06.010.
15. Yang X., Zhang C., Chen G., Sun C., Li J. // J. Obstet.

Gynaecol. Res. 2019. V. 45. № 1. P. 39–46. https://doi.org/10.1111/jog.13839.
16. Deshmukh H., Way S.S. // Annu. Rev. Pathol. 2019. V. 14. P. 185–210. https://doi.org/10.1146/annurev-pathmechdis-012418-012743.
17. Barrientos G., Fuchs D., Schrocksnadel K., Ruecke M., Garcia M.G., Klapp B.F., Raghupathy R., Miranda S., Arck P.C., Blois S.M. // J. Reprod. Immunol. 2009. V. 79. № 2. P. 201–210. https://doi.org/10.1016/j.jri.2008.11.002.
18. Malan Borel I., Gentile T., Angelucci J., Pividori J., Guala M.C., Binaghi R.A., Margni R.A. // J. Reprod. Immunol. 1991. V. 20. № 2. P. 129–240. https://doi.org/10.1016/0165-0378(91)90029-p.
19. Gu J., Lei Y., Huang Y., Zhao Y., Li J., Huang T., Zhang J., Wang J., Deng X., Chen Z., et al. // Hum. Reprod. 2015. V. 30. № 2. P. 380–391. https://doi.org/10.1093/humrep/deu323.

Isolation and Biochemical Characterization of Recombinant Transketolase from *Mycobacterium tuberculosis*

T. A. Shcherbakova[1], S. M. Baldin[1], M. S. Shumkov[2], I. V. Gushchina[3], D. K. Nilov[1], V. K. Švedas[1,3*]
[1]Lomonosov Moscow State University, Belozersky Institute of Physicochemical Biology, Moscow, 119991 Russia
[2]Federal Research Centre «Fundamentals of Biotechnology», Russian Academy of Sciences, Moscow, 119071 Russia
[3]Lomonosov Moscow State University, Faculty of Bioengineering and Bioinformatics, Moscow, 119991 Russia
*E-mail: vytas@belozersky.msu.ru
Received: March 30, 2022; in final form, May 25, 2022
DOI: 10.32607/actanaturae.11713

ABSTRACT **Transketolase, an enzyme of the pentose phosphate pathway, plays an important role in the functioning of mycobacteria. Using plasmid pET-19b carrying the *Rv1449c* gene of transketolase from *Mycobacterium tuberculosis* and an additional histidine tag, we isolated and purified recombinant transketolase and determined the conditions for obtaining the apoform of the protein. The Michaelis constants were evaluated for the thiamine diphosphate cofactor in the presence of magnesium and calcium ions. We found that the affinity of mycobacterial transketolase for thiamine diphosphate is by three orders of magnitude lower than that of the human enzyme. Analysis of the structural organization of the active centers of homologous enzymes showed that this difference is due to a replacement of lysine residues by less polar amino acid residues.**

KEYWORDS **transketolase, thiamine diphosphate, xylulose 5-phosphate, ribose 5-phosphate, mycobacteria.**

ABBREVIATIONS **TK – transketolase; hTK – human transketolase; mbTK – mycobacterial transketolase; yTK – yeast transketolase; TDP – thiamine diphosphate; X5P – xylulose 5-phosphate; R5P – ribose 5-phosphate.**

INTRODUCTION

Tuberculosis is a common infectious disease caused by *Mycobacterium tuberculosis*. Despite the centuries-long fight against tuberculosis, there are still no drugs that provide quick and safe treatment of this infectious disease. Therefore, the search for new molecular targets important for the vital function of mycobacteria and the development of selective inhibitors remain a priority. A genomic analysis of the H37Rv strain [1] has made it possible to identify the key biosynthetic processes involved; among them, the pentose phosphate pathway of carbohydrate metabolism is worth mentioning.

Transketolase (TK; [EC 2.2.1.1]) is a crucial enzyme of the pentose phosphate pathway that is involved in ketose (the donor substrate) cleavage and the subsequent transfer of a two-carbon fragment to aldose (the acceptor substrate). The enzyme is found in almost all animal and plant tissues, as well as in many microorganisms [2–4]. There are reasons to believe that *M. tuberculosis* TK (mbTK) participates in the synthesis of the carbohydrates that form the bacterial cell wall [5]. However, the biological properties of mbTK are still poorly understood, which makes difficult a search for effective enzyme inhibitors. Preliminary data on mbTK substrate specificity have been published, and a crystal structure has been determined (PDB ID 3rim) [6]. The aim of this study was to obtain a purified recombinant mbTK, characterize it biochemically, and study enzyme binding with the cofactor thiamine diphosphate (TDP) and the substrates xylulose 5-phosphate (X5P) and ribose 5-phosphate (R5P).

EXPERIMENTAL

Recombinant mbTK was obtained using the *Escherichia coli* strain BL21(DE3). Cells were transformed using a pET-19b plasmid carrying the

Rv1449c gene with a histidine tag and the ampicillin resistance gene. The transformed strain was grown in a LB medium for 12 h, transferred to a shake flask with a medium containing ampicillin (100 μg/mL) and incubated for 6–7 h at 180 rpm and 37°C. Expression of mbTK was initiated by lowering the temperature to 15°C, adding either $MgCl_2$ or $CaCl_2$ (2 mM), TDP (2 mM), isopropyl-β-*D*-1-thiogalactopyranoside (0.2 mM), and glycerol (2% v/v); the expression was conducted for 24 h. The cells were pelleted by centrifugation for 15 min at 4,000 g and 4°C, then resuspended in a phosphate buffer (50 mM NaH_2PO_4, pH 8.0; 0.3 M NaCl). After this, lysozyme (1 mg/mL) was added and the solution was incubated for 30 min. The cells were sonicated at 0°C. The resulting lysate was centrifuged for 30 min at 12,000 g and 4°C. The mbTK protein containing the decahistidine fragment was purified using Protino Ni-TED 1000 kit columns (Macherey-Nagel), according to the manufacturer's instructions. The purity of the resulting mbTK sample was analyzed by polyacrylamide gel electrophoresis [7].

The activity of mbTK was measured by the coupled reaction of NAD^+ reduction, catalyzed by glyceraldehyde 3-phosphate dehydrogenase from rabbit muscle [8]. The composition of the reaction system for measuring activity at pH 7.6 and 25°C was as follows: glyceraldehyde 3-phosphate dehydrogenase (3 U), glycylglycine (50 mM), dithiothreitol (3.2 mM), sodium arsenate (10 mM), magnesium or calcium chloride (2.5 mM), TDP (200 μM), X5P (500 μM), R5P (2,800 μM), and NAD^+ (370 μM). The reaction was initiated by adding the mbTK solution. The reaction rate was monitored as an increase in the optical density of the solution for 3–5 min at 340 nm. A Shimadzu UV-1800 spectrophotometer was used to measure the reaction rate.

In order to generate the apo form of mbTK, the cofactors were removed according to the technique described in [9]. A saturated solution of ammonium sulfate (pH 3.5) was added to the mbTK holoenzyme solution (0.2 mg/mL) in a 10 mM glycylglycine buffer (pH 7.4) at a 2 : 3 ratio. The mixture was incubated on ice for 5 min and then centrifuged for 15 min at 12,000 g and 4°C. The precipitated protein was dissolved in a 50 mM glycylglycine buffer (pH 7.4). In order to determine the TDP binding constant, the mbTK apoenzyme was incubated in a 50 mM glycylglycine buffer (pH 7.6) in the presence of a 2.5 mM divalent cation (either Mg^{2+} or Ca^{2+}) and TDP at different concentrations (0–200 μM) for 45–60 min at 25°C. Bovine serum albumin (1 mg/mL) was added to the sample to stabilize the protein. Other components necessary for measuring mbTK activity were added to the cuvette, and the reaction was initiated by adding a mixture of substrates. The Michaelis constant was calculated using the dependence of the reaction rate on the cofactor concentration plotted in Lineweaver–Burk coordinates.

Substrate binding constants were determined using a standard method by varying the substrate concentration within the ranges of 0–100 and 0–215 μM for X5P and R5P, respectively. The concentration of the second substrate was constant: 320 μM. The Michaelis constants were calculated by plotting the dependence of the reaction rate on substrate concentration in Lineweaver–Burk coordinates.

To compare the active centers of TKs from different organisms, we used the crystal structures of mbTK [6], yeast TK (yTK) [10], and human TK (hTK) [11]. The TK sequences were aligned using the Matt 1.0 software [12]. The crystal structures were visualized using the VMD 1.9.2 software [13].

RESULTS AND DISCUSSION

A recombinant protein for studying the biochemical properties of mbTK was obtained by transforming the *E. coli* strain BL21(DE3) with a plasmid carrying the *Rv1449c* gene. A significant portion (about 50%) of the resulting protein was found to be the apoenzyme, which rapidly loses its activity during isolation and purification. Addition of the TDP cofactor during expression made it possible to increase the holoenzyme content to 75%, which led to enhanced specific activity of the resulting recombinant mbTK, and made it possible to isolate the required amount of active enzyme. It should be noted that the active center of this family of enzymes contains a divalent metal ion: hTK contains a magnesium ion, yTK contains a calcium ion (the metal ion can be replaced when obtaining the TK holoenzyme from the apoenzyme) [9, 14–16]. The only crystal structure of mbTK available to date contains Mg^{2+} [6]. However, the preferred metal ion under physiological conditions has yet to be determined. When optimizing conditions for obtaining recombinant mbTK, we found that the type of the metal ion (Mg^{2+} or Ca^{2+}) used for cultivation and expression does not affect the final yield of the active enzyme.

The apo form of the enzyme was required to study mbTK affinity to the cofactor. Various methods for cofactor removal have been reported: dialysis, chromatography, and precipitation with ammonium sulfate. In the case of the east enzyme yTK, the cofactor dissociates from the protein during dialysis in a slightly alkaline medium [17], while hTK cofactors can be removed only by precipitation with ammonium sulfate in an acidic medium [9]. We managed to purify mbTK from the cofactor by precipitation with ammonium

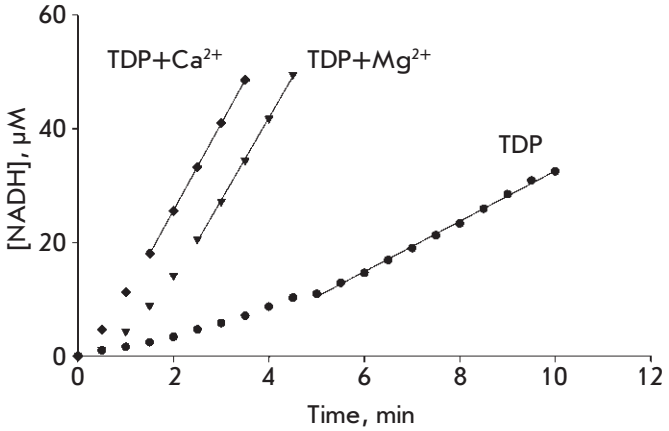

Fig. 1. Time dependence of enzymatic activity recovery after the addition of TDP (200 μM) and either Mg^{2+} or Ca^{2+}ion (2.5 mM) to the mbTK apoenzyme

Table 1. Recovery of enzymatic activity upon activation of the mbTK apoenzyme in the presence and absence of metal ions and TDP

Mg^{2+}/Ca^{2+} (2.5 mM)	TDP (200 μM)	Residual activity, %
–	–	5
+	–	5
–	+	30
+	+	100

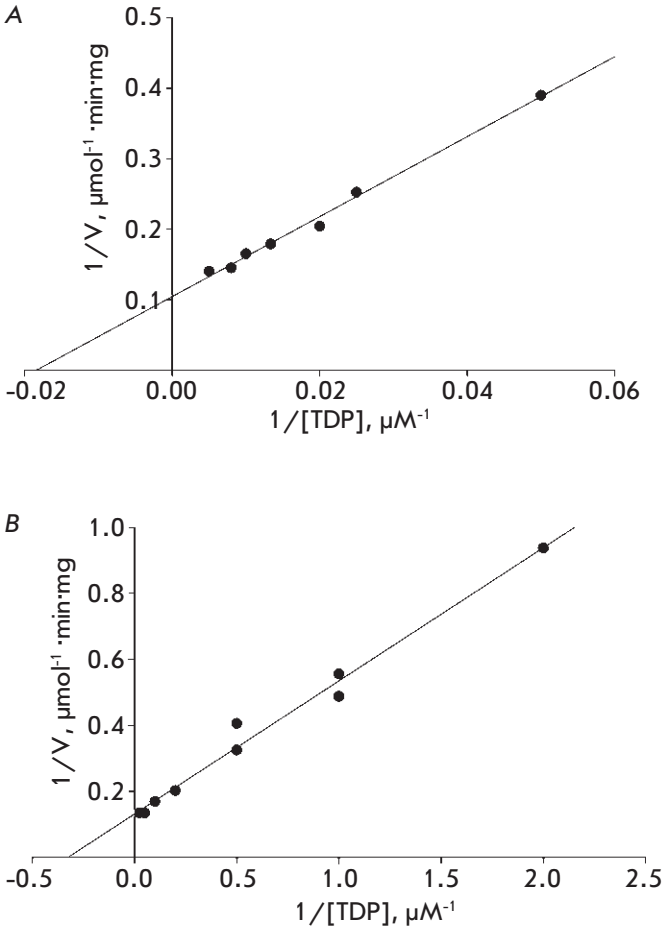

Fig. 2. Dependence of the initial rate of the reaction catalyzed by mbTK on the TDP concentration and evaluation of the Michaelis constant in the presence of Mg^{2+} (*A*) and Ca^{2+} ions (*B*)

Table 2. K_m values for TDP in reactions catalyzed by TKs from different organisms in the presence of Mg^{2+} and Ca^{2+} ions

Enzyme	K_m (Mg^{2+}), μM	K_m (Ca^{2+}), μM
hTK	0.074 [9]	not defined
yTK	0.22–4.4 [18]	0.032–0.250 [4, 14]
mbTK	57	3

sulfate in acidic medium (pH 3.5). Apoenzyme activation and proper mbTK function require a simultaneous presence of a metal ion and a TDP molecule in the active center (see *Table 1*). It should be noted that the rates of apoenzyme activation and holoenzyme formation are higher in the presence of Ca^{2+} ions than in the presence of Mg^{2+} ions (*Fig. 1*). In addition, reconstitution of the mbTK holo form in the presence of cofactors is much more efficient at 25°C (compared to 0°C).

In order to determine the Michaelis constant for TDP, the mbTK apoenzyme was preliminarily incubated in a solution containing a divalent metal ion and the cofactor at different concentrations. The K_m value was 57 and 3 μM in the presence of Mg^{2+} and Ca^{2+} ions, respectively (*Fig. 2*). It should be noted that mbTK affinity to the cofactor is significantly lower than that of homologous eukaryotic enzymes (*Table 2*). Thus, the K_m values for TDP were an order and three orders of magnitude lower for yeast yTK and human hTK, respectively. In order to determine what type of interactions in the active site has such a significant effect on the cofactor binding efficiency, we analyzed the structural organization of the cofactor binding sites in the mbTK (3rim), yTK (1ngs), and hTK (3mos) crystal structures.

In the human enzyme hTK, the Lys75 and Lys244 residues make a significant contribution to the binding energy due to direct electrostatic interaction with the TDP pyrophosphate group. In yTK Lys75 is replaced by Asn67, which interacts with the pyrophos-

Table 3. Affinity to the X5P and R5P substrates in reactions catalyzed by TKs from different organisms in the presence of Mg^{2+} ions

Enzyme	K_m (X5P), μM	K_m (R5P), μM
hTK	11 [9]	63 [9]
yTK	71 [9]	400 [20]
mbTK	30	134

phate group via water molecules, and in mbTK it is replaced by Ala83 that does not interact with TDP (*Fig. 3*). The polar residue Lys244 in hTK is replaced by hydrophobic Ile250 in yTK and Ile269 in mbTK. The Ile416 residue in yTK forms a stronger hydrophobic interaction with the thiazole fragment of the TDP molecule compared to Val439 in mbTK (*Fig. 3*). We assume that these substitutions make a key contribution to the decreased affinity to TDP in the series hTK > yTK > mbTK. Meanwhile, a group of variable residues, Ser40/Ala33/Thr48, Gly154/Gly156/Ser176, and Glu157/Cys159/Asp179 (hTK/yTK/mbTK), either directly or indirectly forms two hydrogen bonds with the TDP pyrophosphate group in all three proteins.

The properties of the substrate binding sites in enzymes of differing origin vary less than those of the cofactor binding sites. This conclusion is supported by the K_m values determined for two substrates, X5P and R5P, in mbTK catalyzed reactions in the presence of magnesium ions. We have studied the dependence of the enzymatic reaction rate on the concentration of one of the substrates in an excess of the second substrate, with the concentration of the second substrate not exceeding the maximum concentration of the variable component by more than 3.5-fold. This limitation was due to possible competition between the substrates for binding to the active site, which was noted for yTK [19]. The obtained K_m values – 30 μM for X5P and 134 μM for R5P – are comparable with the K_m values for these substrates in reactions catalyzed by hTK and yTK (*Table 3*), which is consistent with the sequence conservation of the binding site.

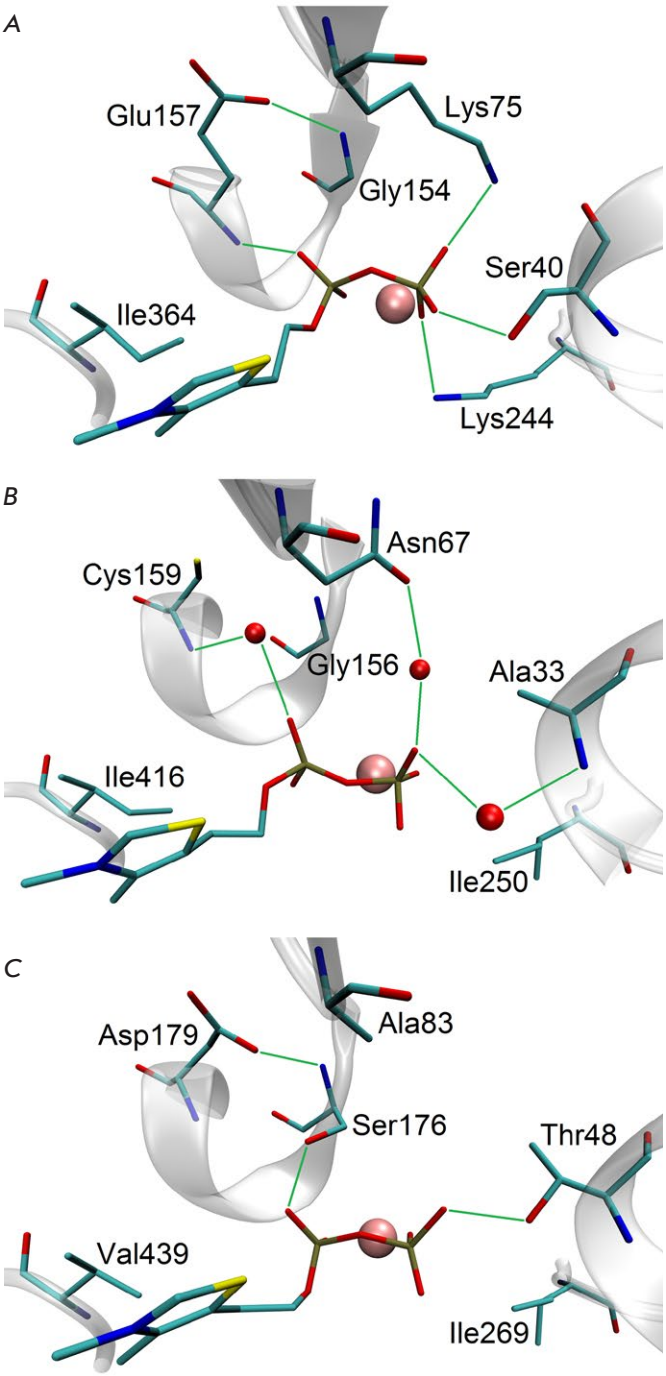

Fig. 3. Interactions of the TDP cofactor with variable residues in the active sites of the homologous enzymes hTK (*A*), yTK (*B*), and mbTK (*C*). The pyrimidine fragment of the TDP molecule is not shown. The divalent metal ion is shown in pink; hydrogen bonds are shown in green

CONCLUSIONS

We obtained holo, as well as apo, forms of mycobacterial transketolase mbTK using a pET-19b plasmid carrying the *Rv1449c* gene, and isolated and purified the recombinant enzyme. The biochemical characteristics of mycobacterial transketolase mbTK were shown to differ significantly from those of both the homologous human enzyme hTK and the yeast enzyme yTK due to a substitution of lysine residues in

the active center by less polar amino acid residues. The affinity of mbTK to the cofactor was found to be almost three orders of magnitude lower than that of hTK. Therefore, it is easier for low-molecular-weight compounds to compete for the TDP binding site in the active center of mycobacterial TK. This feature makes it possible to develop a new class of antibacterial inhibitors that selectively inhibit mbTK activity while exerting no significant effect on hTK. ●

This study was supported by the Russian Science Foundation (grant No. 15-14-00069-P).

REFERENCES

1. Cole S.T., Brosch R., Parkhill J., Garnier T., Churcher C., Harris D., Gordon S.V., Eiglmeier K., Gas S., Barry C.E. 3rd, et al. // Nature. 1998. V. 393. P. 537–544.
2. Schenk G., Duggleby R.G., Nixon P.F. // Int. J. Biochem. Cell Biol. 1998. V. 30. P. 1297–1318.
3. Sevostyanova I.A., Selivanov V.A., Yurshev V.A., Solovjeva O.N., Zabrodskaya S.V., Kochetov G.A. // Biochemistry (Mosc.). 2009. V. 74. P. 789–792.
4. Kochetov G.A., Solovjeva O.N. // Biochim. Biophys. Acta. 2014. V. 1844. P. 1608–1618.
5. Wolucka B.A. // FEBS J. 2008. V. 275. P. 2691–2711.
6. Fullam E., Pojer F., Bergfors T., Jones T.A., Cole S.T. // Open Biol. 2012. V. 2. P. 110026.
7. Laemmly U.K., Favre M. // J. Mol. Biol. 1973. V. 80. P. 575–599.
8. Kochetov G.A. // Methods Enzymol. 1982. V. 90. P. 209–223.
9. Meshalkina L.E., Solovjeva O.N., Khodak Y.A., Drutsa V.L., Kochetov G.A. // Biochemistry (Mosc.). 2010. V. 75. P. 873–880.
10. Nilsson U., Meshalkina L., Lindqvist Y., Schneider G. // J. Biol. Chem. 1997. V. 272. P. 1864–1869.
11. Mitschke L., Parthier C., Schröder-Tittmann K., Coy J., Lüdtke S., Tittmann K. // J. Biol. Chem. 2010. V. 285. P. 31559–31570.
12. Menke M., Berger B., Cowen L. // PLoS Comput. Biol. 2008. V. 4. P. e10.
13. Humphrey W., Dalke A., Schulten K. // J. Mol. Graph. 1996. V. 14. P. 33–38.
14. Kochetov G.A., Philippov P.P. // Biochem. Biophys. Res. Commun. 1970. V. 38. P. 930–933.
15. Datta A.G., Racker E. // J. Biol. Chem. 1961. V. 236. P. 617–623.
16. Kochetov G.A. // Biochemistry (Mosc.). 1986. V. 51. P. 2010–2029.
17. Sprenger G.A., Schörken U., Sprenger G., Sahm H. // Eur. J. Biochem. 1995. V. 230. P. 525–532.
18. Esakova O.A., Meshalkina L.E., Golbik R., Hübner G., Kochetov G.A. // Eur. J. Biochem. 2004. V. 271. P. 4189–4194.
19. Solov'eva O.N., Meshalkina L.E., Kovina M.V., Selivanov V.A., Bykova I.A., Kochetov G.A. // Biochemistry (Mosc.). 2000. V. 65. P. 1202–1205.
20. Kochetov G.A., Sevostyanova I.A. // IUBMB Life. 2010. V. 62. P. 797–802.

High-Affinity Single-Domain Antibodies for Analyzing Human Apo- and Holo-Transferrin

S. V. Tillib*, O. S. Goryainova, A. M. Sachko, T. I. Ivanova
Institute of Gene Biology, Russian Academy of Sciences, Moscow, 119334 Russia
*E-mail: tillib@genebiology.ru
Received: December 14, 2021; in final form, May 30, 2022
DOI: 10.32607/actanaturae.11663

ABSTRACT **A highly efficient technology for generating new monoclonal single-domain recombinant antibodies (nanobodies) was used to obtain a panel of nanobodies recognizing human apo- and/or holo-transferrin. This article is devoted to the primary analysis of the properties of two different variants of the new nanobodies obtained by us, as well as to the demonstration of the unique potential of their application for diagnostic studies. The simultaneous use of immunosorbents based on these nanobodies apparently makes it possible to detect changes in the relative abundance of apo- and holo-transferrin in human biological fluids. Such changes could potentially be indicative of an increased risk or degree of development of pathological processes, such as malignant neoplasms in humans.**
KEYWORDS **single-domain antibody, nanobody, apo- and holo-transferrin, immunosorbent, affinity chromatography, diagnosis.**
ABBREVIATIONS **Holo-Tf and apo-Tf – the iron-containing and iron-free transferrin protein; nanobody – a recombinant protein corresponding to the variable domain of specific camel antibodies, consisting of a homodimer of truncated heavy chains in the absence of immunoglobulin light chains; HA tag is a 9 amino acid fragment of YPYDVPDYA to which commercial antibodies are available.**

INTRODUCTION

Iron is a vital element for a number of key biological processes. Transferrin (Tf) and its receptors (TfR1 and TfR2) are the key proteins regulating iron metabolism in the human body [1]. The high proliferation rate of most tumor cells depends on a supply of sufficient iron and is often associated with increased TfR1 expression [2]. Tf is an 80 kDa glycoprotein composed of two subunits (the N- and C-subunits, 40 kDa each). Each subunit can bind one free ferric ion (Fe^{3+}); i.e., up to two iron ions can be attached to Tf. The iron-saturated form of Tf is referred to as holo-Tf. An iron-free form of Tf is known as apo-Tf. The apo-Tf binds Fe^{3+} in blood with high efficiency and transports it to the cell surface for internalization through interaction with TfR [3]. The cell receptor TfR1 binds holo-Tf with high affinity (K_d1 < 0.1 nM, K_d2 = 3.8 nM, pH 7.4), while the affinity in case of apo-Tf is ~ 100 times lower (K_d1 = 49 nM, K_d2 = 344 nM, pH 7.4) [4]. The complex of iron-bound Tf and receptor formed on the cell surface is internalized by clathrin-mediated endocytosis. The work of the proton pump in the endosomal membrane reduces pH to 5.5 (acidification of the endosome), which triggers conformational changes in both Tf and TfR1, thus leading to the subsequent release of iron from Tf. The ferric iron (Fe^{3+}) is converted to ferrous iron (Fe^{2+}); the receptor/apo-Tf complex then returns to the cell surface, where apo-Tf is released from its bonding with the receptor at neutral pH [5].

The transferrin iron saturation ratio is a widely used clinical parameter, which is calculated as the ratio between the iron content in the patient's blood and the indicator of the total iron-binding capacity of serum [6]. It is a rather general characteristic, which does not allow one to capture subtle changes in the relative representation of different forms of transferrin in blood during pathological processes. Specific antibodies may be a more adequate tool for investigating such likely subtle changes. In this work, we describe single-domain antibodies (nanobodies) against various forms of transferrin obtained using a technology developed and used in our laboratory for many years [7–10].

EXPERIMENTAL

The peripheral blood plasma of three patients diagnosed with FIGO stage IV ovarian cancer and a urine sample of one patient with invasive bladder cancer were kindly provided by the National Medical Research Center for Radiology of the Ministry of Health of the Russian Federation. Blood plasma from healthy donors was obtained from blood samples taken from employees at a medical laboratory, with their consent, according to the standard protocol. The previously obtained libraries of sequences encoding nanobodies [9] were used in new selection procedures using a modified phage display technique as described previously [7–9]. Commercial preparations holo-Transferrin human (holo-Tf) and apo-Transferrin human (apo-Tf) procured from Sigma-Aldrich (USA) were used as target antigens. The initially selected sequences of single-domain antibodies were re-cloned and formatted; the nanobodies were then generated in the bacterial periplasm, isolated, and purified. The isolated nanobodies were characterized using electrophoresis and immunoassay (ELISA) [7–9]. In ELISA, 1-Step Ultra TMB-ELISA reagent (Thermo Scientific, USA) was used for final detection of the secondary HA tag antibodies conjugated to HRP; 2 M sulfuric acid was added, and optical density (OD) was measured at 450 nm. The nanobodies obtained by adaptive re-cloning contain a long linker sequence at the C-terminus (28 amino acid residues of the long variant of the non-canonical camel antibody hinge region), followed by two peptide fragments: a fragment of nine amino acids YPYDVPDYA (HA-tag) and a sequence of six histidine residues (His-tag). The linker linear region contains four conveniently located and easily accessible lysine residues. Using these residues, it is very convenient to carry out chemical reactions to sew other molecules, including the immobilization of a nanobody on BrCN-Sepharose. The nanobodies were cross-linked to CNBr-activated Sepharose 4B (GE Healthcare Life Sciences, USA) according to the manufacturer's recommendations and as described previously [8, 9]. Hence, new immunosorbents (immunoaffinity columns) were obtained whose specificity depended on the properties of the immobilized nanobody. Immunosorbents with immobilized nanobodies were used to isolate bound proteins as described previously [8, 9].

The binding constants of nanobodies to each form of transferrin (holo-Tf and apo-Tf) in standard phosphate-buffered saline (PBS, pH 7.4) were determined on a MicroCal PEAQ-ITC microcalorimeter (Malvern, Switzerland) using the MicroCal PEAQ-ITC Analysis Software at the Shared Use Center of the Institute of Gene Biology. The fitting model (two sequential binding sites) was unambiguous from the data.

To perform an electrophoretic analysis of the proteins, aliquots of the eluates were collected and analyzed in a 5–19% gradient SDS polyacrylamide gel according to Laemmli. We used the MiniProtean 3 device (Bio-Rad, USA); the power source was Elf-4 (DNA-Technology, Russia). Spectra Multicolor Broad Range Protein Ladder (Thermo Fisher Scientific, USA) was used as a protein marker.

"Native" polyacrylamide gel electrophoresis developed by Novakovsky et al. [11] was adapted for efficient separation of holo-Tf and apo-Tf (in the modification presented on the BraunLab web page – https://braunlab.de/?page_id=176). The 10% separating and 4% concentrating gels were used. The samples for analysis were prepared by adding 4× loading buffer containing 400 mM Tris-HCl, 600 mM Tris-base, 0.075% Coomasie G-250, 0.025% bromophenol, and 40% glycerol. Only the marker was warmed up before application (in a standard Laemmli SDS buffer). Electrophoresis was carried out at 150 V and cooling (+4°C). At the end of the electrophoresis, the gel was washed in distilled water (three times for 5 min); the proteins were then stained in Imperial™ Protein Stain (Thermo Fisher Scientific).

RESULTS AND DISCUSSION

Using commercially available transferrin preparations, we selected two markedly different major variants of high-affinity nanobodies which had relatively different affinities for holo-Tf and apo-Tf and, apparently, recognized different transferrin epitopes (*Fig. 1*, *Table*).

Whereas the difference in binding of different forms of transferrin by the resulting nanobodies was only slightly noticeable in ELISA (*Fig. 1A*), these

Determining the binding constants of aTf-1 and aTf-2 nanobodies with two forms of transferrin (holo-Tf and apo-Tf) in solution at pH 7.4 using a MicroCal PEAQ-ITC microcalorimeter (Malvern)

Nanobody name	Binding to holo-Tf*	Binding to apo-Tf*
aTf1	K_D1≈ 0.44 nM; K_D2 ≈1.44 nM	K_D1≈ 99.4 nM; K_D2 (not determined)
aTf2	K_D1≈ 0.94 nM; K_D2 ≈ 0.75 nM	K_D1≈ 0.82 nM; K_D2 ≈ 14.5 nM

* Fitting model: sequential binding sites, number of sites – 2.

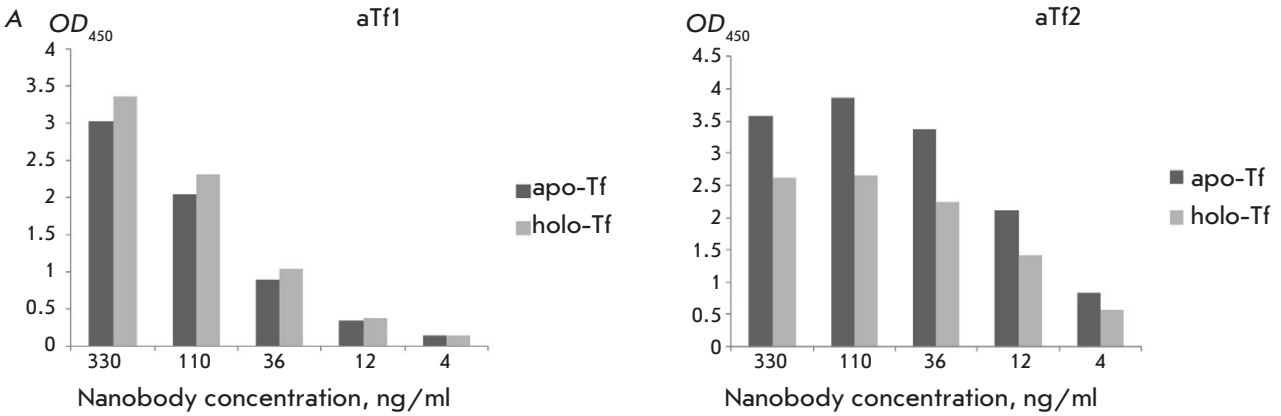

B

aTf1 MAQVQLVESGGGLVQPGGSLTLSCAAS**GFTFSTYAMK**WVRQAPGMGLEYVA**SINNGGTSTFYSASVKG**
RFTISRDNAKNTLYLQLNSLKTEDTAMYYC**ARINEYSTR**GQGTQVTVSS

aTf2 MAQVQLVESGGGSVQAGGSLRLSCAVS**GYMYSTNCMG**WFRQAPGKEREGVA**AIYTGGGSTYYPDSVKG**
RFTISQDNAKNTVYLQMNSLKPEDTAMYYC**AAMRHCPYGGNWDHPVNYL**GQGTQVTVSS

Fig. 1. Characteristics of two new anti-human transferrin nanobodies: (*A*) Immunofluorescent analysis of binding of aTf1 and aTf2 nanobodies in different dilutions to apo-transferrin (apo-Tf, dark bar) or holo-transferrin (holo-Tf, light bar) immobilized in wells of an immunological plate. OD_{450} absorbance values (Y axis) correspond to the number of bound nanobodies and are shown as the average of duplicates with less than 5% variation (the mean background value ~ 0.06 for control wells was subtracted). (*B*) Amino acid sequences derived from the determined cDNA sequences of the resulting two anti-human transferrin nanobodies. The hypervariable regions of CDR1, CDR2, and CDR3 are underlined. Cysteine residues are detected in the CDR1 and CDR3 regions of the aTf2 nanobody (highlighted in gray)

nanobodies worked unexpectedly selectively in the solution (*Table*) and as a part of an immunosorbent (*Fig. 2A*). The aTf1 nanobody in solution (PBS) at pH 7.4 binds holo-Tf with a very high affinity, while binding apo-Tf is 100 times weaker. Interestingly, the TfR1 receptor interacts with transferrin in a similar manner [4]. Another nanobody, aTf2, binds both forms of transferrin in the solution, but it appears to bind apo-Tf particularly well.

The sequences of these two nanobodies are very different (*Fig. 1B*). In the case of aTf2, CDR3 is significantly increased and there appears to be an additional Cys–Cys bond between CDR1 and CDR3. Both variants of nanobodies were adapted, produced in bacterial periplasm, and purified as described previously [7–9]. The adapted nanobodies were immobilized on CNBr-sepharose [8, 9], giving rise to two new immunosorbents. The specificities of binding of these immunosorbents to commercial transferrins (apo- and holo-) were tested. We adapted and successfully used a special variant of SDS-free polyacrylamide gel electrophoresis to separate iron-bound and non-iron-bound transferrins (*Fig. 2A*). To our surprise, in the column format, the aTf2 nanobody barely binds holo-Tf while binding apo-Tf very efficiently. In contrast, the aTf1 nanobody binds holo-Tf very well and binds the purified apo-Tf much weaker than aTf2. Next, immunosorbents in a column format were used in parallel to test potential differences in the relative abundances of the bound forms of transferrin in normal and pathological conditions. The first results of such testing are presented in *Fig. 2*. One can see that while for blood plasma samples from healthy donors (samples 1, 2, and 3) the eluates from both columns contain approximately the same amount of transferrin, for the samples obtained from cancer patients (at advanced stages of ovarian cancer, samples 4–6), one can clearly see that more protein is bound and then eluted in the case of aTf2 nanobodies. A very similar situation is observed when analyzing transferrin in the urine of a patient with an invasive form of bladder cancer (sample 7). In healthy donors, the urinary level of transferrin is ten times lower, and, according to our preliminary observations, we do not see noticeable differences in the amounts of transferrin bound by these two immunosorbents. Hence, this test makes

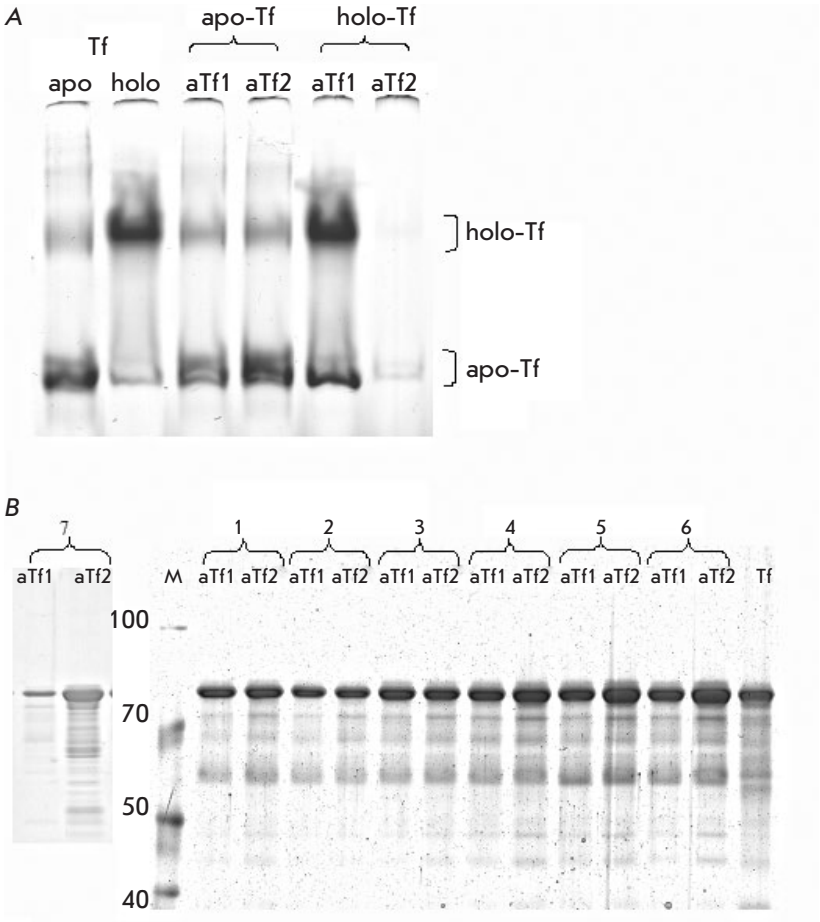

Fig. 2. Demonstration of specific binding of different forms of transferrin by nanobodies cross-linked to Sepharose. (*A*) Gel electrophoresis under conditions preserving the integrity of the transferrin complex with iron ions is used to demonstrate the selective binding of different forms of transferrin (apo-Tf and holo-Tf) to immobilized nanobodies (aTf1 or aTf2). Original transferrins were loaded on two lanes on the left-hand side. (*B*) Electrophoretic fractionation in 5–19% gradient SDS-polyacrylamide gel of blood (or urine) proteins bound to immunosorbents under physiological conditions and then eluted. Identification of quantitative differences in the representation of transferrin forms apparently differing in iron saturation (all transferrin forms are localized in a given electrophoretic fractionation in one major band) in transferrin fractions isolated simultaneously in parallel using two immunosorbents containing the immobilized nanobodies aTf1 or aTf2 in healthy people (from blood samples denoted by numbers 1, 2, and 3) and cancer patients (with stage 4 ovarian cancer – 4, 5, 6 or in the urine of a patient with muscle-invasive bladder cancer –7). The sizes of the marker bands are indicated in kDa. Tf – transferrin (commercial)

it possible to detect changes in the relative amounts – and availability for binding – of certain epitopes of different transferrin forms using nanobodies. This could probably have a diagnostic potential, including for cancer monitoring; however, the reliability and reproducibility of the proposed test needs to be evaluated on a larger number of samples.

For now, we can only speculate what the observed effects might mean. The immunosorbent with the aTf2 nanobody makes it possible to selectively isolate apo-Tf. Normally, this corresponds to approximately 2/3 of all transferrin subunits contained in blood. The immunosorbent with the aTf1 nanobody preferentially binds holo-Tf and a part (about half) of apo-Tf (this may be Tf with one bound iron ion). As a result, both immunosorbents bind approximately 2/3 of the total plasma transferrin (differing in composition). Cancer cells are known to consume iron particularly efficiently, which can lead to iron deficiency in the biological fluids surrounding the tumor and a relative increase in the proportion of apo-Tf. On the other hand, holo-Tf, unlike apo-Tf, binds very efficiently to the TfR1 receptor on the cell surface. However, TfR1 is also detected in free, extracellular form (as soluble sTfR1 [12]). It cannot be ruled out that in pathological processes such holo-Tf–TfR1 interactions can shield a portion of holo-Tf from binding to the aTf1 nanobody. Taken together, we observe the effect of a prominent increase in the form of transferrin to which the aTf2 nanobody binds but does not bind at all or poorly binds the aTf1 nanobody. We can hypothesize that the exosome-associated increase in apo-Tf in the biological fluid may result from intensive iron consumption by tumor cells.

In conclusion, we note that in this study we have obtained new single-domain antibodies and immunosorbents based on them which differently bind forms of transferrin differing in iron saturation. This ability of differential binding of the resulting immunosorbents makes it possible to observe relative changes in the representation of different transferrin forms that are either directly or indirectly associated with cancer. ●

This work was supported by Russian Science Foundation (grant No. 20-14-00305) and the Russian Foundation for Basic Research (grant No. 19-015-00487).

REFERENCES
1. Torti S.V., Torti F.M. // Mol Aspects Med. 2020. V. 75. P. 100860.
2. Candelaria P.V., Leoh L.S., Penichet M.L., Daniels-Wells T.R. // Front. Immunol. 2021. V. 12. P. 607692.
3. André M.N., Silva A.M.N., Moniz T., de Castro B., Rangel M. // Coordination Chem. Rev. 2021. V. 449. P. 214186.
4. Kleven M.D., Jue S., Enns C.A. // Biochemistry. 2018. V. 57. P. 1552–1559.
5. Yiannikourides A., Latunde-Dada G.O. // Medicines (Basel). 2019. V. 6. P. 85.
6. Elsayed M.E., Sharif M.U., Stack A.G. // Adv. Clin. Chem. 2016. V. 75. P. 71–97.
7. Tillib S.V., Ivanova T.I., Vasilev L.A. // Acta Naturae. 2010. V. 2. P. 85–93.
8. Tillib S.V., Privezentseva M.E., Ivanova T.I., Vasilev L.F., Efimov G.A., Gurskiy Ya.G., Georgiev G.P., Goldman I.L., Sadchikova E.R. // J. Chromatogr. B. 2014. № 949–950. P. 48–57.
9. Goryainova O.S., Ivanova T.I., Rutovskaya M.V., Tillib S.V. // Mol. Biol. 2017. V. 51. P. 855–864.
10. Tillib S.V. // Mol. Biol. 2020. V. 54. P. 317-326.
11. Nowakowski A.B., Wobig W.J., Petering D.H. // Metallomics. 2014. V. 6. P. 1068–1078.
12. Speeckaert M.M., Speeckaert R., Delanghe J.R. // Crit. Rev. Clin. Lab. Sci. 2010. V. 47. № 5–6. P. 213–228.

GENERAL RULES

Acta Naturae publishes experimental articles and reviews, as well as articles on topical issues, short reviews, and reports on the subjects of basic and applied life sciences and biotechnology.

The journal *Acta Naturae* is on the list of the leading periodicals of the Higher Attestation Commission of the Russian Ministry of Education and Science. The journal Acta Naturae is indexed in PubMed, Web of Science, Scopus and RCSI databases.

The editors of *Acta Naturae* ask of the authors that they follow certain guidelines listed below. Articles which fail to conform to these guidelines will be rejected without review. The editors will not consider articles whose results have already been published or are being considered by other publications.

The maximum length of a review, together with tables and references, cannot exceed 50,000 characters with spaces (approximately 30 pages, A4 format, 1.5 spacing, Times New Roman font, size 12) and cannot contain more than 16 figures.

Experimental articles should not exceed 30,000 symbols (approximately 15 pages in A4 format, including tables and references). They should contain no more than ten figures.

A short report must include the study's rationale, experimental material, and conclusions. A short report should not exceed 12,000 symbols (5–6 pages in A4 format including no more than 12 references). It should contain no more than three figures.

The manuscript and all necessary files should be uploaded to www.actanaturae.ru:

1) text in Word 2003 for Windows format;
2) the figures in TIFF format;
3) the text of the article and figures in one pdf file;
4) the article's title, the names and initials of the authors, the full name of the organizations, the abstract, keywords, abbreviations, figure captions, and Russian references should be translated to English;
5) the cover letter stating that the submitted manuscript has not been published elsewhere and is not under consideration for publication;
6) the license agreement (the agreement form can be downloaded from the website www.actanaturae.ru).

MANUSCRIPT FORMATTING

The manuscript should be formatted in the following manner:

- Article title. Bold font. The title should not be too long or too short and must be informative. The title should not exceed 100 characters. It should reflect the major result, the essence, and uniqueness of the work, names and initials of the authors.
- The corresponding author, who will also be working with the proofs, should be marked with a footnote *.
- Full name of the scientific organization and its departmental affiliation. If there are two or more scientific organizations involved, they should be linked by digital superscripts with the authors' names. Abstract. The structure of the abstract should be very clear and must reflect the following: it should introduce the reader to the main issue and describe the experimental approach, the possibility of practical use, and the possibility of further research in the field. The average length of an abstract is 20 lines (1,500 characters).
- Keywords (3 – 6). These should include the field of research, methods, experimental subject, and the specifics of the work. List of abbreviations.
- INTRODUCTION
- EXPERIMENTAL PROCEDURES
- RESULTS AND DISCUSSION
- CONCLUSION

  The organizations that funded the work should be listed at the end of this section with grant numbers in parenthesis.
- REFERENCES

  The in-text references should be in brackets, such as [1].

RECOMMENDATIONS ON THE TYPING AND FORMATTING OF THE TEXT

- We recommend the use of Microsoft Word 2003 for Windows text editing software.
- The Times New Roman font should be used. Standard font size is 12.
- The space between the lines is 1.5.
- Using more than one whole space between words is not recommended.
- We do not accept articles with automatic referencing; automatic word hyphenation; or automatic prohibition of hyphenation, listing, automatic indentation, etc.
- We recommend that tables be created using Word software options (Table → Insert Table) or MS Excel. Tables that were created manually (using lots of spaces without boxes) cannot be accepted.
- Initials and last names should always be separated by a whole space; for example, A. A. Ivanov.
- Throughout the text, all dates should appear in the "day.month.year" format, for example 02.05.1991, 26.12.1874, etc.
- There should be no periods after the title of the article, the authors' names, headings and subheadings, figure captions, units (s – second, g – gram, min – minute, h – hour, d – day, deg – degree).
- Periods should be used after footnotes (including those in tables), table comments, abstracts, and abbreviations (mon. – months, y. – years, m. temp. – melting temperature); however, they should not be used in subscripted indexes (T_m – melting temperature; $T_{p.t}$ – temperature of phase transition). One exception is mln – million, which should be used without a period.
- Decimal numbers should always contain a period and not a comma (0.25 and not 0,25).
- The hyphen ("-") is surrounded by two whole spaces, while the "minus," "interval," or "chemical bond" symbols do not require a space.
- The only symbol used for multiplication is "×"; the "×" symbol can only be used if it has a number to its

right. The "·" symbol is used for denoting complex compounds in chemical formulas and also noncovalent complexes (such as DNA·RNA, etc.).
- Formulas must use the letter of the Latin and Greek alphabets.
- Latin genera and species' names should be in italics, while the taxa of higher orders should be in regular font.
- Gene names (except for yeast genes) should be italicized, while names of proteins should be in regular font.
- Names of nucleotides (A, T, G, C, U), amino acids (Arg, Ile, Val, etc.), and phosphonucleotides (ATP, AMP, etc.) should be written with Latin letters in regular font.
- Numeration of bases in nucleic acids and amino acid residues should not be hyphenated (T34, Ala89).
- When choosing units of measurement, SI units are to be used.
- Molecular mass should be in Daltons (Da, KDa, MDa).
- The number of nucleotide pairs should be abbreviated (bp, kbp).
- The number of amino acids should be abbreviated to aa.
- Biochemical terms, such as the names of enzymes, should conform to IUPAC standards.
- The number of term and name abbreviations in the text should be kept to a minimum.
- Repeating the same data in the text, tables, and graphs is not allowed.

GUIDENESS FOR ILLUSTRATIONS

- Figures should be supplied in separate files. Only TIFF is accepted.
- Figures should have a resolution of no less than 300 dpi for color and half-tone images and no less than 600 dpi.
- Files should not have any additional layers.

REVIEW AND PREPARATION OF THE MANUSCRIPT FOR PRINT AND PUBLICATION

Articles are published on a first-come, first-served basis. The members of the editorial board have the right to recommend the expedited publishing of articles which are deemed to be a priority and have received good reviews.

Articles which have been received by the editorial board are assessed by the board members and then sent for external review, if needed. The choice of reviewers is up to the editorial board. The manuscript is sent on to reviewers who are experts in this field of research, and the editorial board makes its decisions based on the reviews of these experts. The article may be accepted as is, sent back for improvements, or rejected.

The editorial board can decide to reject an article if it does not conform to the guidelines set above.

The return of an article to the authors for improvement does not mean that the article has been accepted for publication. After the revised text has been received, a decision is made by the editorial board. The author must return the improved text, together with the responses to all comments. The date of acceptance is the day on which the final version of the article was received by the publisher.

A revised manuscript must be sent back to the publisher a week after the authors have received the comments; if not, the article is considered a resubmission.

E-mail is used at all the stages of communication between the author, editors, publishers, and reviewers, so it is of vital importance that the authors monitor the address that they list in the article and inform the publisher of any changes in due time.

After the layout for the relevant issue of the journal is ready, the publisher sends out PDF files to the authors for a final review.

Changes other than simple corrections in the text, figures, or tables are not allowed at the final review stage. If this is necessary, the issue is resolved by the editorial board.

FORMAT OF REFERENCES

The journal uses a numeric reference system, which means that references are denoted as numbers in the text (in brackets) which refer to the number in the reference list.

For books: the last name and initials of the author, full title of the book, location of publisher, publisher, year in which the work was published, and the volume or issue and the number of pages in the book.

For periodicals: the last name and initials of the author, title of the journal, year in which the work was published, volume, issue, first and last page of the article. Must specify the name of the first 10 authors. Ross M.T., Grafham D.V., Coffey A.J., Scherer S., McLay K., Muzny D., Platzer M., Howell G.R., Burrows C., Bird C.P., et al. // Nature. 2005. V. 434. № 7031. P. 325–337.

References to books which have Russian translations should be accompanied with references to the original material listing the required data.

References to doctoral thesis abstracts must include the last name and initials of the author, the title of the thesis, the location in which the work was performed, and the year of completion.

References to patents must include the last names and initials of the authors, the type of the patent document (the author's rights or patent), the patent number, the name of the country that issued the document, the international invention classification index, and the year of patent issue.

The list of references should be on a separate page. The tables should be on a separate page, and figure captions should also be on a separate page.

The following e-mail addresses can be used to contact the editorial staff: actanaturae@gmail.com, tel.: (495) 727-38-60.